Mechanical Analysis and Simulation of the Nitinol Ring-Stent:

Assessing the Radial Strength, Fatigue Safety and Compaction Strains

David Russell Bow

Department of Mechanical & Aerospace Engineering

University of Strathclyde, Glasgow

August 2018

Submitted to the Department of Mechanical & Aerospace Engineering

in partial fulfilment of the requirements of

Doctor of Philosophy

Abstract

Disease of the vascular system is often treated by 'minimally invasive' endovascular methods, which are less traumatic than conventional 'open surgery'. The endovascular treatments, including implants, are delivered to the target area by catheter devices. The aorta, the largest artery in the body which stems from the heart, is susceptible to aneurysms and dissection of the arterial wall layers, which can both be fatal if left untreated. These specific conditions are often treated with endovascular stent-graft implants: flexible polymer conduits supported by metallic structures. *Vascutek*, a company based near Glasgow, is unique in designing and producing stent-grafts based on the 'ring-stent' technology: the structural annular components being formed of multiple turns of a superelastic alloy called Nitinol. Competitors in the stent-graft market mainly implement the more common 'Z-stent' structure, also usually with Nitinol.

The work of this thesis addresses the requirement of *Vascutek* to have advanced methods of analysing the mechanical performance of ring-stents in terms of: the loading which they apply to vessels; their fatigue performance in the pulsatile environment of the cardiac cycle, and the ability to compact into small diameter delivery systems without incurring detrimental levels of material strain.

Building on previous efforts at The University of Strathclyde, the work presented here represents the first complete development, and thorough validation, of a Finite Element simulation methodology which captures the 'bundle' geometry and mechanical response of the multiple-strand ring-stent technology. A unique method has been devised to capture and simulate the non-linear response of human aortic tissue, specific to thoracic or abdominal locations and for a range of patient ages. Currently, there exists no standard approach in the industry to mechanically represent artery, partly due to the variability and difficulty of obtaining data.

The bespoke Finite Element Analysis capabilities have provided the first quantification of the 'radial strength' of ring-stents, and knowledge of how the radial force is distributed on the artery wall. This includes evidence that if devices are implanted at high 'oversize', distribution is less uniform and there is no significant increase in total radial force. Furthermore; the first reliable simulation of the ring-stents interacting with the non-linear arterial response has been executed; the results showing a significant reduction to the

vessels' physiological motion and a corresponding increase in factor of safety when compared to assessments made assuming linear elastic artery. The latter goes beyond current standard practice for fatigue, and will allow justification of design of new products which are in development. An understanding, and verification, of how classic beam theory can be used to inform ring-stent design has also been provided.

The methodology devised here has also been used to inform and analyse a component level Nitinol wire fatigue-to-failure test programme required to attain the strain based limits, against which the device simulations are assessed. This combined work (empirical side undertaken by colleagues at *Vascutek*) is a unique study, which successfully defines the fatigue strength of Nitinol wire at multiple 'non-zero' mean-strain states.

Regarding the analysis on compaction of ring-stents, geometric mathematical tools and Micro Computed Tomography X-Ray imaging have been implemented in the design process, providing fidelity in measuring strain levels and insight to optimise the designs to allow the highly desirable reduction in catheter profile. To truly optimise the profile of delivery systems, a more complete understanding of the effects of straining Nitinol to high levels is required, which is ongoing in further research collaborations with The University of Strathclyde.

Declaration of Authenticity and Author's / Companies' Rights

This thesis is the result of the author's original research. It has been composed by the author and has not been previously submitted for examination which has led to the award of a degree.

Signed:

Date:

Acknowledgements

First, I would like to thank my academic supervisors, Prof David Nash and Dr Bill Dempster, for the opportunity, their guidance, encouragement and technical input towards this piece of work.

I am grateful to my initial company supervisors David Stevenson and Tim Ashton, who had patience, trust and a wealth of experience and expertise in stent-graft technology. More recently at Vascutek, I owe gratitude to Vincent Nelis and Mark Steckel for their encouragement and enthusiasm with regards to this endeavour, and I thank Robbie Brodie who has been an accomplice and a support, himself completing a PhD thesis in parallel.

I appreciate the preceding PhD work carried out at the University of Strathclyde by Emma Henderson (formerly McCummiskey) and Martin van Zyl, which gave valuable direction to this project.

However, above all, I owe the most to my wife, Giorgia, for her extreme patience and encouragement throughout this journey, not to mention the many hours of childcare to which I am in debt. Finally, my young daughters, Bonnie and Isla, have unwittingly helped me to keep things in perspective, mentally speaking.

Contents

List of Figures

List of Tables

Abbreviations

AAA	Abdominal Aortic Aneurysm
ART	Adjustable Rigid Torus
ASTM	American Society of Testing and Materials
CE	Conformité Européene
CFD	Computation Fluid Dynamics
CNORMF	*Abaqus* abbreviation for 'Contact Normal Force'
CoF	Coefficient of Friction
CT	Computed Tomography
DIC	Digital Image Correlation
FE	Finite Element
FEA	Finite Element Analysis
FPS	Frames per Second
FSI	Fluid-Structure Interaction
HGO	Holzapfel-Gasser-Ogden
HY	Hybrid (Thoraflex Hybrid device)
ID	Inner Diameter
ODB	Output Database
OLB	One-Lok Body
PTFE	Polytetrafluoroethylene
RAM	Random Access Memory
RSD	Relative Standard Deviation
STL	Standard Tessellation Language
UMAT	*Abaqus* abbreviation for 'User defined Material'

1
Introduction

1.1 Background and Context

The Aorta is the largest artery in the body, taking oxygenated blood from the heart, and distributing it to peripheral arteries which supply the whole body. Figure 1 (A) depicts the full aorta which stems from the top of the heart, turns in the 'aortic arch', and then descends through the chest and abdomen close to the spine. The aorta bifurcates into the iliac arteries which supply the lower body. In contrast to the smaller peripheral arteries, which often suffer from blockages caused by atherosclerosis, vascular disease in the aorta

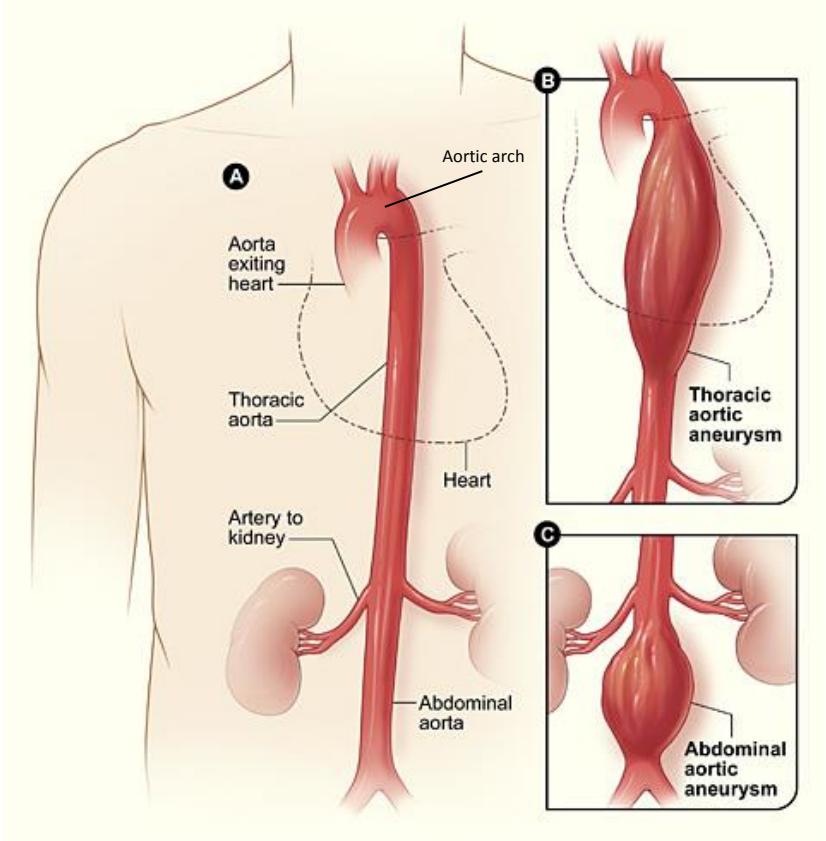

Figure 1 - A depiction of the healthy human aorta (A), and diseased states in the insets of a thoracic and abdominal aortic aneurysms in (B) and (C) respectively. Used with additional annotation from: National Institutes of Health (public domain), via Wikimedia Commons.

can manifest as an aneurysm: a ballooning of the vessel wall which can ultimately rupture if left untreated. The condition represents a prevalent health issue in modern society, particularly for males: ruptured aneurysms are the 10th most common cause of death in elderly men in the United States [1]. The three broad classifications of aneurysms in the aorta are: the Thoracic Aortic Aneurysm (TAA) (Figure 1 (B)), Abdominal Aortic Aneurysm (AAA) (Figure 1 (C)) and the Thoraco-Abdominal Aortic Aneurysm (TAAA) if extending from chest to abdomen. Each type represents a different clinical challenge in order to be treated. Another common vascular disease condition in the aorta is 'dissection', where the inner most layer of tissue has tears, allowing blood to flow behind, opening up a 'false lumen' between layers.

Both aneurysms and dissections of the aorta can be fatal if left untreated and allowed to develop. Conventional treatment for severely diseased aorta is by 'open repair' surgery, in which the diseased length of aorta is removed and replaced with a prosthetic tubular fabric graft. While these surgeries provide a very robust repair of the aorta, the procedure is highly invasive and for some elderly or frail patients it is either too risky or not an option at all. The alternative 'minimally invasive' technique is to implant stent-grafts by endovascular (through the vessel) delivery, using X-ray fluoroscopy to visualise the position of the devices.

The stent-grafts for treating the aorta are usually fundamentally constructed from tubular fabric graft with a 'self-expanding' metallic stent structure. They are compacted into small diameter, catheter-like systems for delivery via an access point, often at the femoral artery near the hip. Once the endovascular stent-graft has been deployed and positioned within the artery it is designed to act as a conduit for blood flow between the healthy artery above the aneurysm to healthy artery below, thus excluding the aneurysm from the cyclic blood pressure loading and reducing the risk of the aneurysm rupturing. The ability of the device to seal with the vessel at either end is provided by the outward 'radial force' of the stent components.

Numerous stent-grafts have been developed and are commercially available; however the work of this thesis is solely focused on analysing the unique 'ring-stent' technology of *Vascutek Ltd*. (a manufacturer and developer of vascular prosthetics based in Renfrewshire, Scotland).

The concept of using a multi-strand 'ring-stent' in treating vascular disease was successfully commercialised by *Vascutek Ltd*. in 2005 when the *Anaconda Stent Graft System* was CE marked. Product development had started in 1997 and clinical trials for two early design generations had been underway since 1999. The modular system comprises a polyester fabric graft supported primarily by the ring-stent wire structures, which are constructed from multiple turns of Nitinol wire. The three modular parts of a current generation '*Anaconda One-Lok*' product are shown in Figure 2, and will be introduced further in Chapter 2.

Nitinol, a Nickel-Titanium alloy, is a complex material which exhibits both 'superelastic' and 'shape-memory' behaviour, excellent biocompatibility and fatigue resistance [2]. The superelastic property refers to the material's ability to undergo and recover from large deformations, enabled by transformation of the molecular lattice structure, and is what enables devices such as the *Anaconda* to treat diseased aorta in a 'minimally-invasive' manner. The 'minimally-invasive' procedure is endovascular: a stent-graft, compacted into a small diameter sheath during manufacture, can be passed through the vascular system to

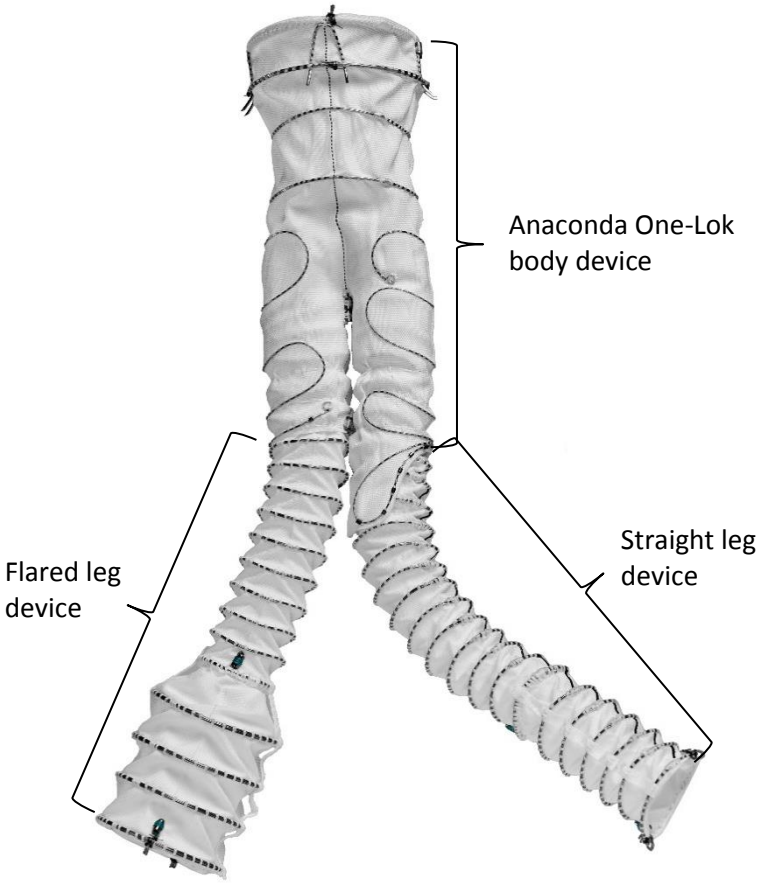

Figure 2 - The *Anaconda One-Lok* body device docked with straight and flared leg devices.

the aorta on a catheter by an incision into the iliac artery, at a location where it is relatively near the surface in the groin region.

A stent-graft in the aorta will experience high cyclic loading during its lifetime as it interacts with the compliant wall of the aorta during the pulsatile blood pressure load applied from each heartbeat. These devices must therefore be designed with fatigue resistance as a primary requirement, and indeed as the international standards on medical devices demand [3], [4].

The non-linear material, high levels of deformation and interaction between metal structure and compliant artery lead to a complex structural problem, hence the requirement for Finite Element Analysis (FEA) as will be described in this thesis.

1.2 Project Objectives

Considering the fundamental structural system to be the superelastic ring-stent in interaction with the human aortic artery, there is a requirement to understand and quantify the radial loading applied by a Nitinol ring on the vessel. The radial force behaviour is non-trivial due to the complexity of the Nitinol stress-strain relation, and the large deflections which the ring structures are subjected to, as will be explored in the following chapters.

Subsequent to considering the structural loading of a Nitinol ring component in a hypothetically static situation, analysis of cyclic motion will be considered, with a new approach to take account of the non-linear elastic behaviour of human aorta. This will be predominantly to analyse the fatigue resistance of the Nitinol rings from a cyclic strain amplitude perspective. The fatigue safety case needs to be updated from the current approach, based mainly on classic mechanics, to an FEA informed approach to allow product development of ring-stents to continue with confidence and also to satisfy future regulatory requirements.

The compaction of a ring-stent device into a delivery system subjects the Nitinol ring to significant bending at four points in the circumference which induces high material strains and challenges the recoverability of the superelastic Nitinol on deployment. There is a requirement to quantify the strain levels in compaction to enable future development iterations to optimise the design for compaction in terms of both ring configuration and sheath size. Smaller sheath sizes will provide significant clinical benefits and competitive advantage over alternative stent-grafts.

The objectives are to provide new knowledge in the areas outlined above, but also to provide the tools, to be used in product development, to assess and optimise new ring-stent devices for radial strength, fatigue resistance and compaction.

1.3 Thesis Outline

The preceding work to this thesis included different approaches to theoretically analyse the stress-strain state of Nitinol rings: from a classic structural mechanics approach [5], to the development of FE methods using the commercial packages *ANSYS* [6], and *Abaqus* more recently [7].

This thesis describes how the initial methodology devised by van Zyl [7] has been progressed to simulate and validate multi-strand Nitinol ring models. The complexity of artery modelling required has been investigated, resulting in a solution which is a compromise between modelling the detail of artery construct and achieving a practical method which is able to capture the overall non-linear arterial response. Combining the multi-strand ring modelling with artery representation now allows the radial strength and fatigue life of these devices to be analysed and quantified for the safety case and future product development.

Through experimental investigation, scanning sample devices using Micro Computed Tomography X-Ray imaging (abbreviated to 'Micro CT'), the levels of deformation due to device compaction, and the resulting material strain levels, have been investigated. A theoretical approach using 'circle packing theory' (see 4.2.8) has also been developed to optimise the wire diameter and number of turns of a ring-stent for minimal compaction strain.

The objectives and approaches discussed above are outlined in this thesis' chapters as follows:

- Chapter 2 – **Literature Review and Technology Background**: an introduction to the Nitinol ring-stent and the products thereof; a literature review of Nitinol's behaviour and fatigue characteristics, an overview of aortic tissue structure and literature on its mechanical characterisation; and an overview of the preceding work to this thesis carried out at the University of Strathclyde.

- Chapter 3 – **Nitinol Material Constitutive Modelling**: Description and implementation of a constitutive model for the specific grade of Nitinol used in the ring-stents of *Vascutek* devices.
- Chapter 4 – **Simulation Methodology Development and Validation**: Description and rationale of the methodologies developed to simulate Nitinol ring-stents, aortic artery, and their interaction.
- Chapter 5 – **Ring-Stent Mechanics**: Investigating the radial force and strain states of rings through parametric studies.
- Chapter 6 – **FEA for Ring Fatigue Testing**: Simulation and strain analysis of the ring component fatigue tests to define new strain-life fatigue limits.
- Chapter 7 – ***Anaconda* Ring-Stent in Langewouters' Artery Simulations**: Combining the ring-stent and artery modelling methodologies into an interactive system simulation to provide findings on the mechanical interaction and fatigue capability of the ring-stent in the aortic environment.
- Chapter 8 – **Investigating Compaction Strain**: A geometric analysis of ring-stent compaction feasibility and empirical analysis with Micro CT to investigate the true deformation and therefore strain levels in the compacted ring-stent devices.
- Chapter 9 – **Conclusions and Future Recommendations**

2
Technology Background and Literature Review

2.1 Foreword on *Vascutek-University of Strathclyde* Collaboration

The history of the *University of Strathclyde* collaborating with *Vascutek* goes back to the development of the initial enabling technology on which the company was formed: a bespoke knitted textile manufacturing method for medical graft products. The University has also been involved in developing the gelatin graft coatings in the late 80's.

Relevant to this thesis, the *Mechanical and Aerospace Department* have provided consultation and two previous PhD projects providing analysis on fatigue resistance, Nitinol wire characterisation, initial development of FEA methodology and a bespoke empirical approach to validate ring-artery interaction with cadaveric testing. These pieces of work will be reviewed at the end of this chapter (section 2.5), however findings from the literature review of the first PhD project of McCummiskey [6] will be included in the Nitinol literature review here in section 2.3.

2.2 Ring-Stent Technology

While *Vascutek* are the only company implementing ring-stent technology in the form of multiple-strand bundles of fine Nitinol wire (owning the intellectual property to do so), there are a number of competitors utilising Nitinol in a 'Z-stent' configuration. Of which the most prominent competitors to the Anaconda device are *Cook Medical's 'Zenith'* [8]*, GORE's 'Excluder'* [9] *and Medtronic's 'Endurant'* [10] devices.

The *Anaconda* product is a modular system comprising a main body device in a range of sizes and a range of leg devices which connect, or 'dock', with the main body. Each device is essentially comprised of the metal stent structure supporting a polyester woven graft. An

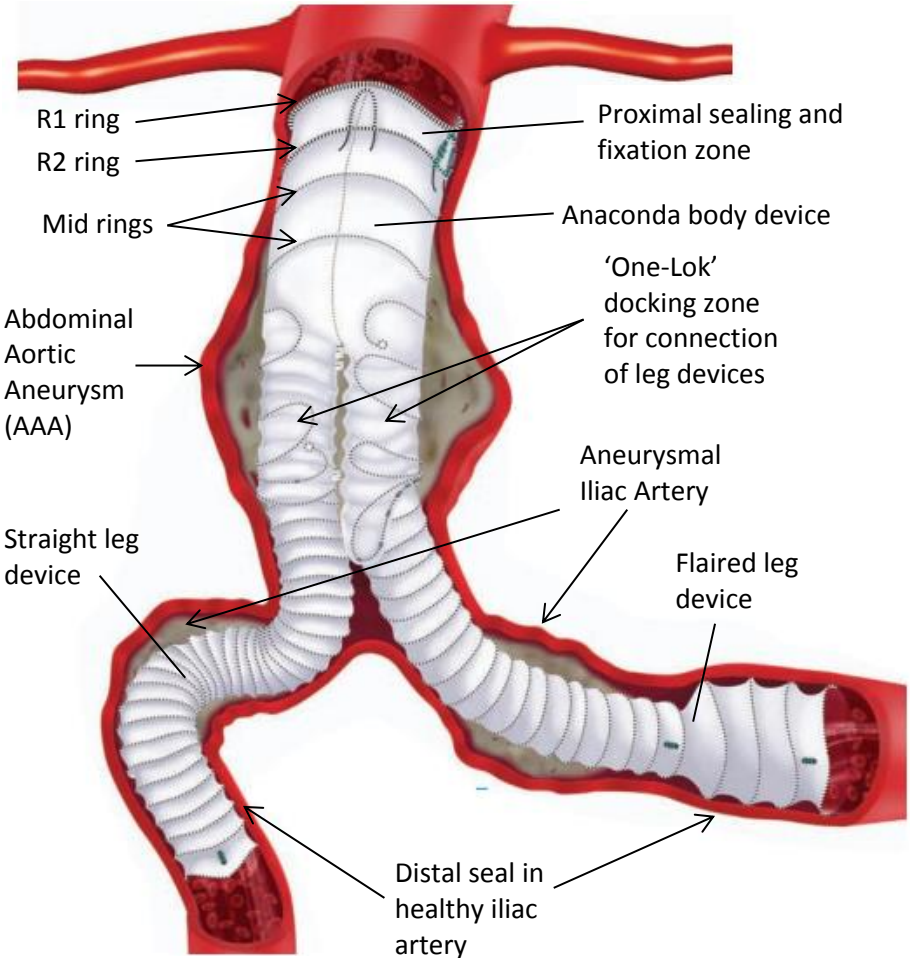

Figure 3 - A depiction of the Anaconda stent graft system treating aneurysmal abdominal aorta and iliac vessels. The left iliac (right on image) is treated with a so-called flared leg with larger rings distally.

example system is depicted in Figure 3 treating aneurysmal abdominal aorta and iliac arteries. The device is delivered by endovascular deployment: the stent-graft is compacted into the end of a flexible tubular delivery system (see Figure 4), which can be introduced into the femoral artery in the groin and guided through the arterial system to the section of aorta to be treated. The procedure initially requires temporary guidewires to be steered into the body, which can be 'tracked over' by the endovascular devices to the target site. In

Figure 4 – An *Anaconda* delivery system with an unsheathed *Anaconda* body device still connected to system.

the region of the device, the delivery system has a 'central core' which houses control wires and provides a central lumen for the passing of a guidewire. The introduction, deployment, positioning and monitoring of performance of such devices is all carried out by careful intermittent use of radiographic imaging.

The functional requirement of the *Anaconda* device is to provide a new sealed conduit for blood to flow from the healthy artery upstream (proximally) relative to the aneurysm, through the aneurysm sac, to the healthy artery downstream (distally). When the device is 'unsheathed' from the deployment system inside the artery the superelasticity in the Nitinol structure allows it to 'self-expand' towards its original shape; applying enough outward radial pressure to create a seal at the proximal and distal regions either end of the aneurysm. The outward radial load is also required for embedding the proximal hooks into the vessel wall, which are designed to prevent device 'migration' through the vessel.

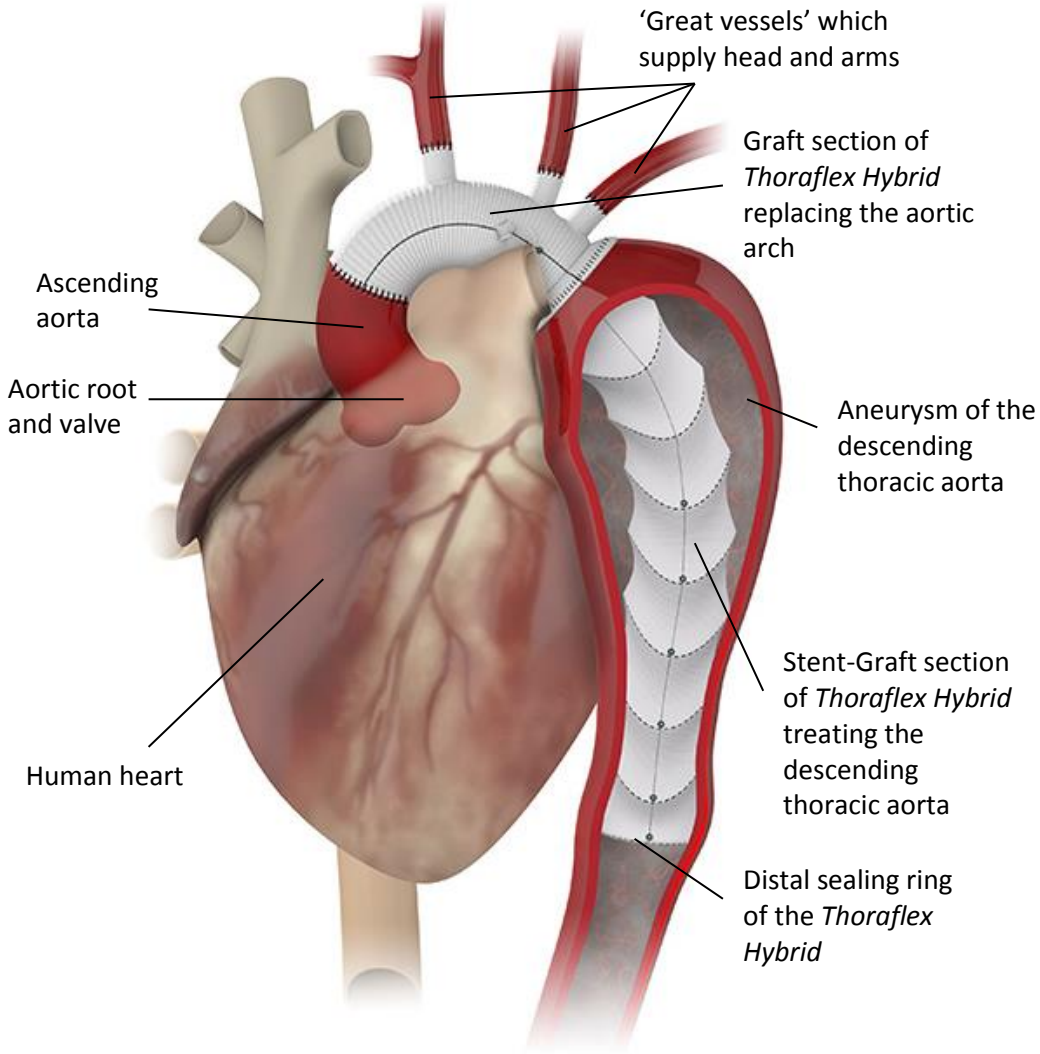

Figure 5 - Illustration of the *Thoraflex™ Hybrid* system treating the thoracic arch and descending aorta

Planning of the operation includes the clinical team assessing 3D X-Ray CT (Computed Tomography) scans, making key geometric measurements of the aorta, and 'oversizing' the device accordingly. The 'oversize' is the percentage by which the device is larger than the vessel lumen in terms of diameter. The *Anaconda* sizing chart (Appendix A) recommends minimum and maximum vessel sizes for each device size, which correspond to approximately oversizes of 20% and 10% respectively.

More recently the Ring-Stent technology has been applied to the *Thoraflex*™ *Hybrid* device which is an innovative product used to treat arterial disease in the thoracic aorta (illustrated in Figure 5). The product was termed 'hybrid' due to half of the device being a conventional graft, while the distal end is a stent-graft referred to in the industry as a 'frozen elephant trunk'. Open surgery is required to implant the device, however the stented section can be advanced into the descending aorta in an atraumatic manner, causing minimal tissue damage. The conventional graft part is then used to reconstruct the aortic arch and its connections to the 'great vessels' which supply blood to the head and arms. As well as the treatment of aneurysmal aorta in the Thoracic region, the *Thoraflex*™ *Hybrid* device is used to treat the condition known as 'dissection' in which the layers of the artery wall become separated.

The ring-stent components are manufactured from a single Nitinol wire, turned multiple times to create a 'bundle' of wires, with the two ends of the wire joined with a tantalum crimp. The wire diameters used range from 0.10 to 0.24mm across different devices. A manufactured ring-stent with four temporary suture ties is shown in Figure 6 (left) with a close-up (right) in which the individual strands in the bundle can be seen. The positioning

Figure 6 - A manufactured stent ring consisting of multiple turns of fine Nitinol wire as seen in close-up on right

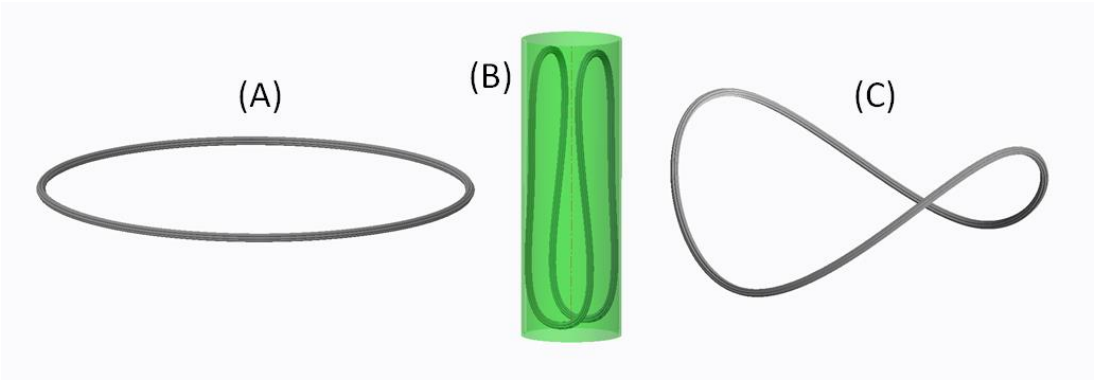

Figure 7 – A Computer generated graphic of a ring-stent in manufactured 'flat ring' position (A), compacted in a sheath (B) and a typical 'saddle shape' *in-vivo* deformation.

of the wires in the bundle cross-section is dependent on how they settle and are held by the temporary sutures when the ring is removed from the tooling used to wrap the turns (essentially two mandrels at a set separation dependent on desired ring diameter). By visual inspection, all turns appear to remain parallel with the general ring circumference, i.e. the bundle does not appear to twist in the fashion of a cable. The assumption on wire positioning in the bundle will be addressed in section 4.2.7.2.

The deformation life-cycle of a ring-stent includes the wire being formed into a ring, compaction into a delivery sheath once sewn onto a device, deployment to engage with artery, and pulsatile motion due to the cardiac cycle. Figure 7 depicts a ring-stent in its manufactured ('flat ring') position (A), compacted state approximation (B) and a typical *in-vivo* 'saddle shape' deformation (C)

The various diameters of the manufactured 'flat ring', which will be discussed in this work, are defined in the schematic image of a manufactured ring in Figure 8.

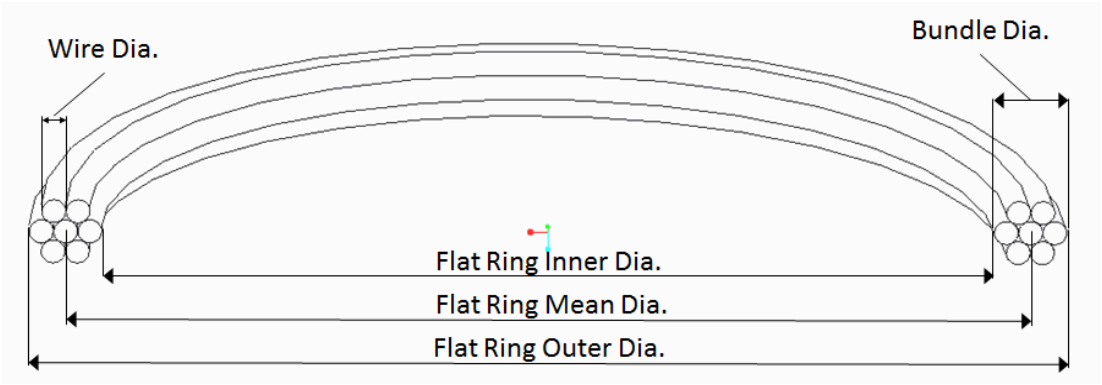

Figure 8 - Diagram of a manufactured flat ring-stent (not to typical scale), defining the diameters of interest

2.2.1 Finite Element Modelling of Ring-Stents

The most applicable preceding work on modelling the ring-stent technology is that of two previous PhDs carried out at the University of Strathclyde, as will be discussed in section 2.5. However, the recent work of Perrin *et al* [11] (at Ecole Nationale Supérieure des Mines, Saint-Etienne, France) has developed methodology, using *Abaqus*, to model full *Anaconda* devices with fabric represented but simplified linear-elastic, single-turn rings. The objective of the work of Perrin *et al* is to capture full device deformation, not to assess stress/strain or radial loading.

2.3 Nitinol

2.3.1 General Characteristics and Application to Stents

Nitinol is a Nickel-Titanium metal alloy. The Nickel (Ni) and Titanium (Ti) atoms are bound in a crystal lattice structure and represent approximately 55% to 45% atomic weight respectively (see Chapter 3 for more detail). A phase transformation of the molecular structure enables the superelasticity: Nitinol initially in an Austenite phase will 'dislocate' to a martensitic arrangement under a certain load. This is known as 'stress induced martensite', and allows the metal alloy to extend to levels of recoverable strain as high as 10% [12] through a non-linear stress-strain relation. The general form of this behaviour is shown in Figure 9 in which a sample is loaded to a strain of 8%, unloaded to zero stress and then reloaded to failure at approximately 17% in this case. The austenite and martensite

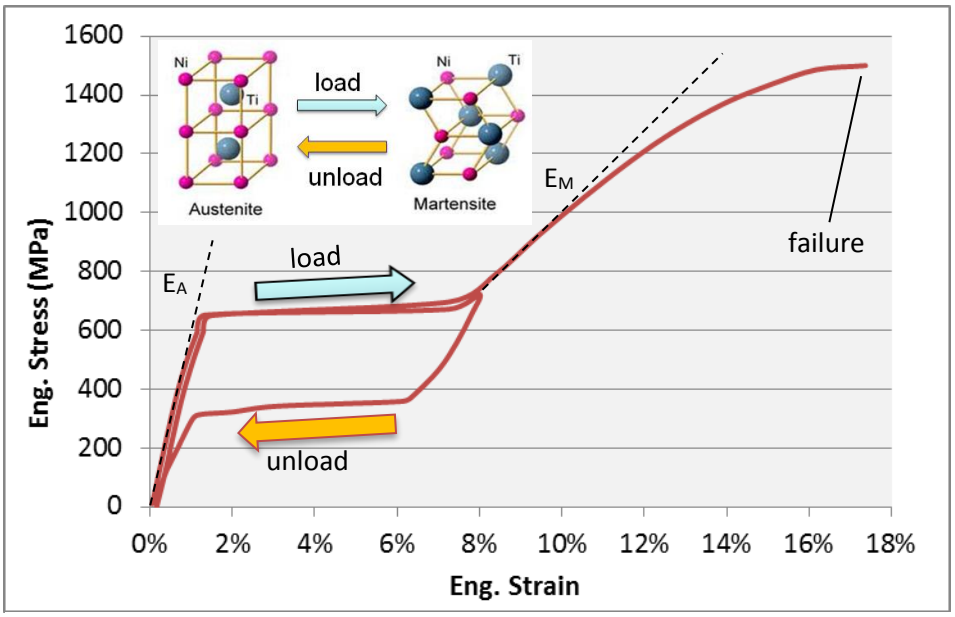

Figure 9 - A typical tensile stress-strain relation for superelastic Nitinol loaded to 8% nominal strain, unloaded to zero stress and then loaded to failure. The insert depicts the change in molecular lattice structure from austenite to martensite.

moduli are shown as E_A and E_M respectively and the inset in Figure 9 depicts the change in molecular lattice structure. Once the initiation of transformation from austenite to martensite has begun, it takes relatively little further load to progress the transformation, i.e. a plateau in the stress-strain relation occurs between the austenite and martensite moduli. If the stress is reduced, the strain will recover with the lattice structure returning to its Austenite phase. However, on recovery, the unloading plateau occurs at a lower level of stress: this is known as elastic hysteresis where some strain energy has been dissipated as heat. Comparatively, the recoverable strain levels are much greater than in other metals commonly used for structural purpose which are limited to around 1% [13].

As shown in Figure 10, there is asymmetry between tension and compression of the stress-strain curves. This is mainly observed in terms of the plateaus being shorter, not as flat and existing at higher magnitude stress levels for the compressive state [12], [14]–[16].

It is important to note that the described superelastic behaviour only exists within a certain temperature range, or 'superelastic window': at lower temperatures the material already exists as martensite in stress free condition, and at higher temperatures plastic

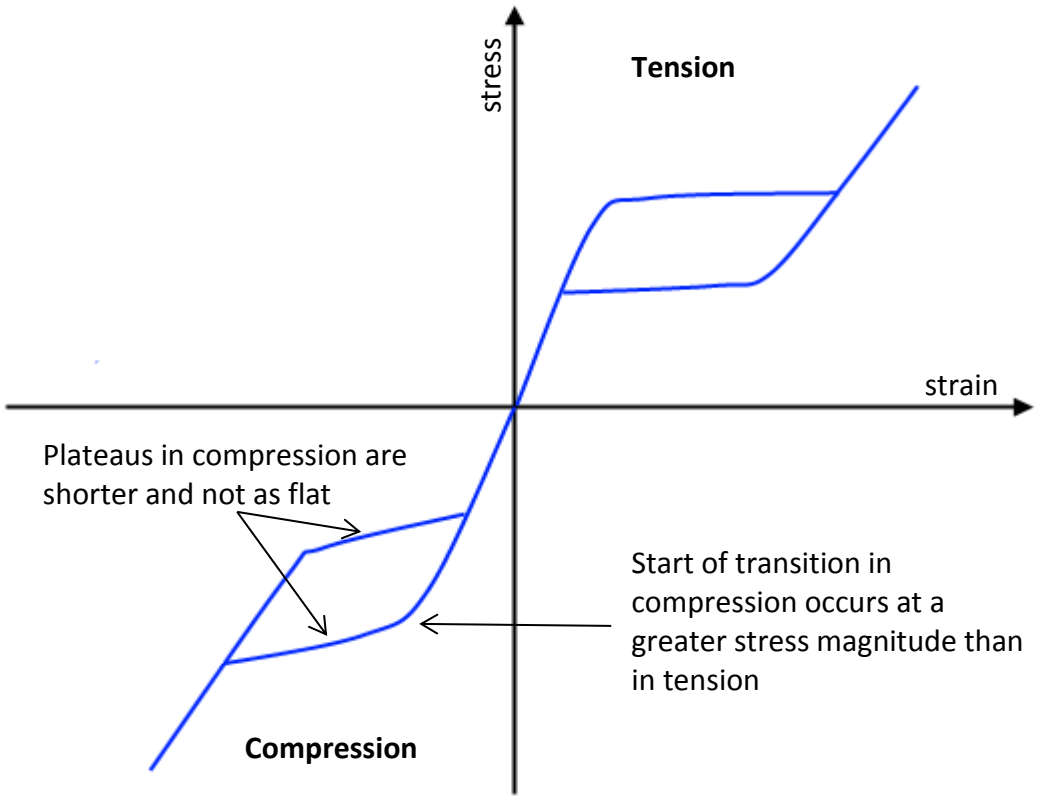

Figure 10 - Schematic of typical asymmetry of superelastic Nitinol stress-strain relation in tension and compression from uni-axial testing.

deformation of austenite occurs rather than transformation to martensite. The temperature above which the alloy remains Austenite in stress free condition and therefore has the potential to be superelastically loaded to a 'stress induced martensite' phase is the 'A_f (austenite finish) temperature'. The thermo-mechanical process of the alloy during manufacture determines the important A_f temperature. The 'superelastic window' is only available between the A_f and A_f+50˚C [6], and the stress-strain response is sensitive to temperature even within this range. To take advantage of the superelastic characteristic in medical implants the operating temperature, i.e. 37°C, must lie in the 'superelastic window'.

Nitinol is also well known for its 'shape-memory' behaviour which involves taking advantages of the described molecular structure changes through heating and cooling. Essentially if a Nitinol component in a stress-free martensitic state is then plastically deformed, the original undeformed shape can be recovered to by heating to Austenite, above the A_f temperature. However this phenomenon is not directly relevant to the ring-stents which are designed to operate within the 'superelastic window'.

The sensitivity of the plateau stress levels within the 'superelastic window' is shown in Figure 11, from the work of Pelton *et al.* [17], in which Nitinol wire with an A_f temperature of 11°C is strained to 6%, unloaded to zero stress, and subsequently loaded to failure at various temperatures. It is clearly important to understand the behaviour of the specific grade of Nitinol in question and the implications to the design application.

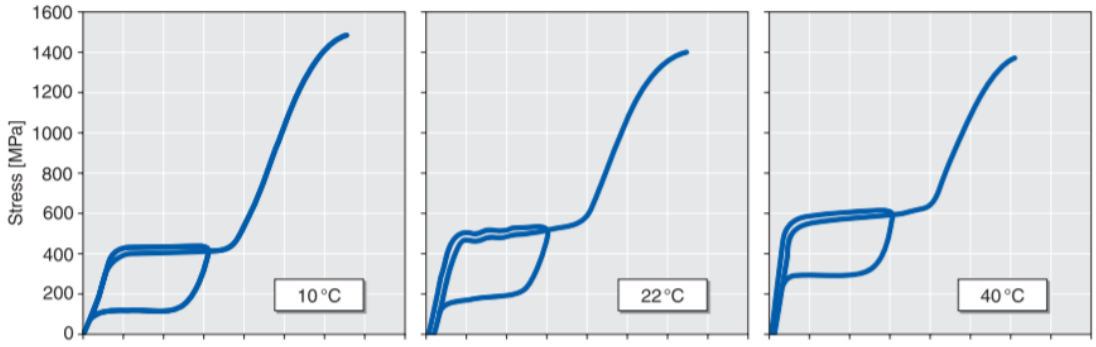

Figure 11 - Nitinol wire with an A_f temperature of 11°C loaded to 6%, unloaded to zero stress, and loaded then loaded to failure at 10°C, 22°C and 40°C

In the literature review of the work of McCummiskey [6], she identified this requirement to characterise the specific grade of wire being implemented before developing an FE

approach for analysis. McCummiskey identified the following factors which were subsequently addressed in testing as will be described in 2.5:

- The stress-strain response in bending does not correlate with the tensile stress-strain response, and that this was due to the asymmetry in tensile/compressive behaviour. [14], [18]–[21]
- The plateau levels reduce and the residual strain levels increase when subject to repeated cyclic loading [21]
- The sensitivity of the stress-strain curve to temperature with regards to both processing treatments and testing temperature [22]
- The strain rate dependency of the stress-strain behaviour in testing [23]–[25]

These findings and the testing carried out by McCummiskey (see 2.5) have provided experience to the recent efforts to fully characterise the current grade of Nitinol wire (*Vascutek* have changed supplier since the thesis of McCummiskey) by Brodie [26], which has run in parallel with the work of this thesis. The results of Brodie's work are used to define a material model for simulation as described in Chapter 3.

Regarding the deterioration of plateau levels and increased residual strain due to cyclic loading; this is representative of high strain range testing (0-6% was applied by McCummiskey and the testing of Siddons & Moon which she referenced [21]), however this

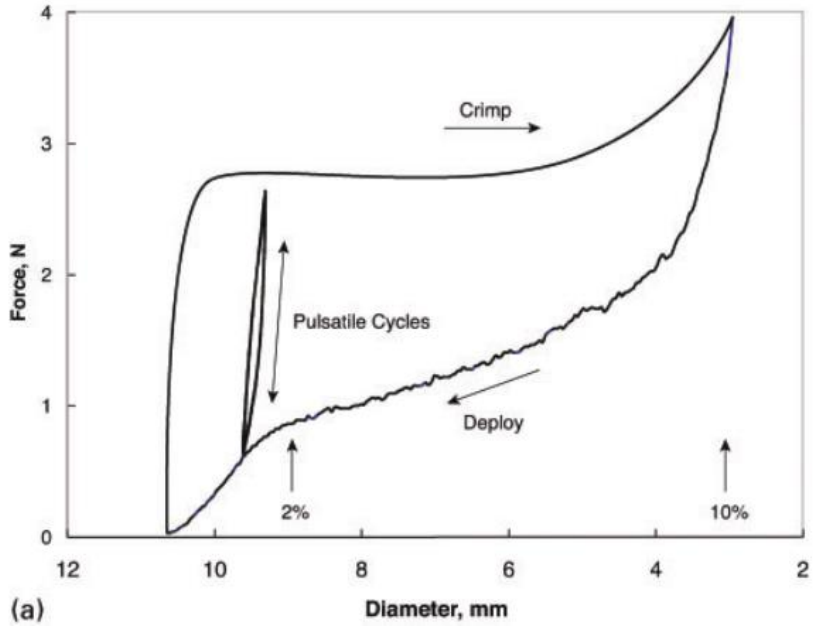

Figure 12 – A Force-Diameter plot for a Nitinol self-expanding stent subject to crimping, deployment and cyclic loading. Reproduced from Robertson *et al* [12]**.**

is not necessarily relevant to the mechanical life of a stent as will now be considered.

Nitinol stents are termed 'self-expanding' because they use the superelastic phenomenon to recover from the highly deformed compacted position. Significant recovery of the deformation occurs on deployment *in vivo*, with areas of the structure that underwent the superelastic transformation recovering strain to some point along the unload plateau [2], [13]. Indeed, the force-displacement relationship of a Nitinol stent being compacted (or 'crimped') and then deployed, is analogous to the uniaxial stress-strain behaviour of Nitinol, as shown in Figure 12 from Robertson *et al* [12], with an example Force-Diameter plot for a *Cordis SMART* stent. The '2%' and '10%' marked in Figure 12 are indicating the maximum strain levels in the device at ~9mm and ~3mm diameter respectively.

The gradient of Force to Diameter in Figure 12 during the pulsatile cycling stage is similar to the initial loading gradient, which is reflective of the uni-axial cyclic testing of Nitinol at low level strain amplitudes [12], [27] (0.25%, 0.20% strain amplitude respectively) as depicted in Figure 13. The literature [12], [27] and the parallel work of Brodie [26] have found that the stress-strain gradient through low level strain amplitude testing is stable but dependent on the mean-strain: the modulus reducing from the austenitic level to the martensitic as mean-strain is increased.

Gaining evidence of the percentage change in diameter of a stent, referred to as 'pulsatility' herein, in the *in-vivo* condition, is perhaps the most challenging aspect which is required to understand the relevant levels of strain amplitudes. A method which has been used by *Vascutek*, and is believed to be common to the industry, is to measure the pulsatility of

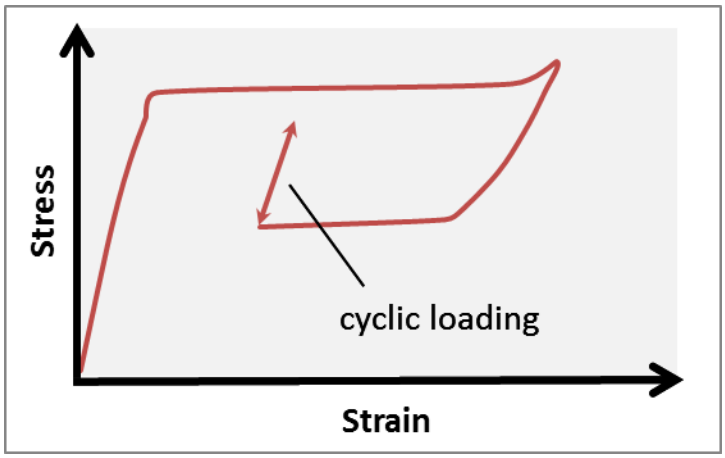

Figure 13 - Typical Stress-Strain behaviour of Nitinol loaded, unloaded to a strain level on lower plateau and subsequently loaded with 'low amplitude' cyclic strains.

devices deployed into a silicone tube of known compliance, loaded with a worst-case systolic-diastolic blood pressure range [28], [29]. Silicone tubes however, do not behave in the non-linear fashion of human artery, which is investigated and discussed in section 2.4.

2.3.2 Nitinol Fatigue Analysis

Any endovascular stent device designed to be used in the aorta will be subject to pulsatile loading from the cardiac cycle as blood pressure ranges from diastolic to systolic pressure with every beat.

Typically, the fatigue performance of an engineering alloy is assessed considering cyclic stress amplitudes and how it relates to number of cycles to failure (S-N graphs). Due to the very non-linear behaviour of Nitinol, 'strain-life' analysis, as opposed to 'stress-life', is the industry standard approach [12] constant amplitude strain cycles are used to define fatigue limits Nitinol material over a range of mean-strain levels.

As specified by international standards [3], [4]; endovascular stent-grafts are required to prove (through *in vitro* testing) fatigue resistance to survive at least 10 years of a heart beating, which is equated to approximately 380 million cycles. Cyclic durability testing of full devices must be carried out, but also there is a requirement to characterise the material fatigue performance through component level testing. The Nitinol wire used to construct the ring-stent has been subject to 'rotary bend fatigue' testing by the wire supplier, and recent individual ring fatigue testing at *Vascutek* in a manner which attempts to replicate the type of loading applied to the components *in vivo*.

Rotary bend fatigue testing involves the wire being spun on its own axis while bent to a measured curvature. This produces stress-strain amplitudes, highest at the surface, which oscillate about a zero mean-strain. The strain amplitude is dependent on the radius of curvature of the wire. This testing carried out by Vascutek was purely to compare wire from different manufacturers. The comparative benchmark which was used as a Pass/Fail criteria for wire samples was to survive 0.7% strain amplitude for 100M cycles [30]. The *Fort Wayne Metals* wire had the highest pass rate of samples, outperforming two alternatives.

The component level testing of ring-stents, addressed in Chapter 6 applies stress-strain amplitudes about a non-zero mean strain level. The magnitude of the mean strain depends

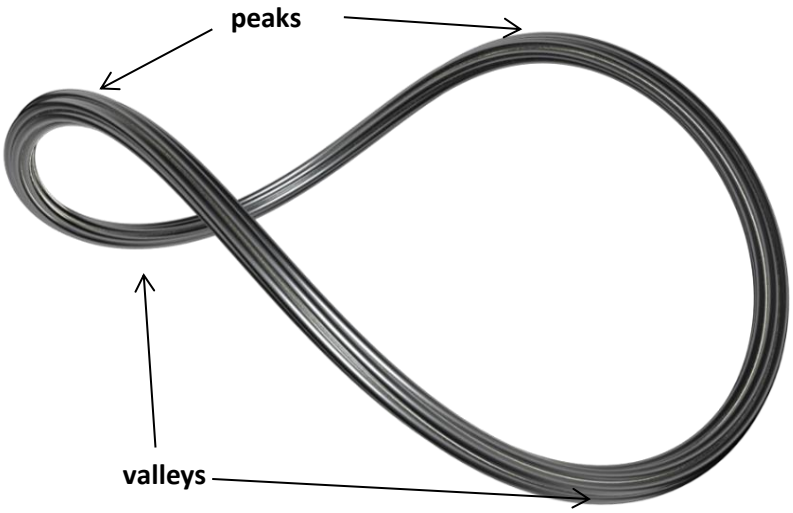

Figure 14 - A computer generated image of a multi strand ring-stent in the *in vivo* 'saddle shape' position with peaks and valleys annotated.

on the location on the ring, and the level of deformation. The strained shape which a ring-stent takes *in vivo*, when exerting an outward force against the vessel, depicted in Figure 14, will be referred to as a 'saddle shape'. The 'peaks' (most proximal) and 'valleys' (most distal) are of particular focus because they exhibit the highest mean-strain and delta-strain (2×strain amplitude) levels *in vivo* and are the point which deform the most during compaction, as will be discussed in Chapters 5-8.

The actual fatigue performance of a Nitinol wire is dependent on many factors: the precise chemical composition of the batch; the shape and size of microscopic inclusions; the transformation temperature of the melt ingot, the annealing temperature, the amount of cold work performed and the surface finish of the wire [31]–[35].

A thorough review of Nitinol fatigue studies was carried out in 2012 by Robertson *et al*. [12] (part of the 'Nitinol Devices and Components' group (now 'Confluent Inc.') [36] who have been the most prominent research group in the community). Their literature review on the strain-life approach provides the following notable conclusions:

- "*The overwhelming conclusion from these recent studies is that fatigue life for superelastic Nitinol is driven by strain amplitude rather than mean-strain or peak strain*"

However, they note that the mean-strain does still have a noticeable effect;

- *"Fatigue life is increased with increasing mean-strain up to the end of the phase transformation plateau"*

The latter conclusion could be attributed to a lower modulus due to a greater portion of martensite, which therefore results in lower cyclic stress amplitude for a given change in strain. However, a closer look at the data reviewed by Robertson *et al*. [12] show that this increase in fatigue life is only clear up to 3% mean-strain. Beyond which, one of the studies reviewed in the paper shows a reduction in delta-strain limit, and for another study there "*are insufficient data for a complete analysis*" between 3% and 7% mean-strain. What is clear from the review paper is that beyond the superelastic transformation, i.e. approximately >7% mean-strain, the delta-strain limit for fatigue reduces, presumably related to the higher stress levels in the fully transformed stress-induced martensite.

It has been identified in preceding work, and re-iterated in the above relatively recent review by Robertson et al. [12], the importance to carry out bespoke fatigue testing to determine a fatigue limit for the specific grade of Nitinol as well as the specific loading condition the component may be subject to.

The literature review undertaken by Robertson et al. [12] on the strain-life testing was mainly on 'diamond stent' sub components as opposed to wire. Regarding fatigue testing on Nitinol wire, there are published studies which use rotary bend testing [35], [37], [38], however this method implies a zero mean-strain condition which is not applicable to the ring-stent loading condition *in vivo*. There are no known publications on the fatigue testing of Nitinol wire at non-zero mean-strain levels.

2.4 Human Artery, Characterisation and Modelling

The aorta itself is naturally designed to have compliance which acts to dampen the pulsatile pressure wave from the heart [39]. Compliance is greatest in the thoracic region which is most proximal to the heart, and decreases distally through the arterial system.

Human artery is a complex bio-mechanical construct, with three main layers: the inner most *intima*; the middle *media* layer*;* and the outer most *adventitia* layer as shown in Figure 15. These key structural layers consist of vascular smooth muscle, elastin and helically arranged collagen fibres [40] which characterise the resulting non-linear anisotropic mechanical responses. Layers are separated by thin 'elastic lamina' and a single layer of endothelial cells line the innermost Intima layer.

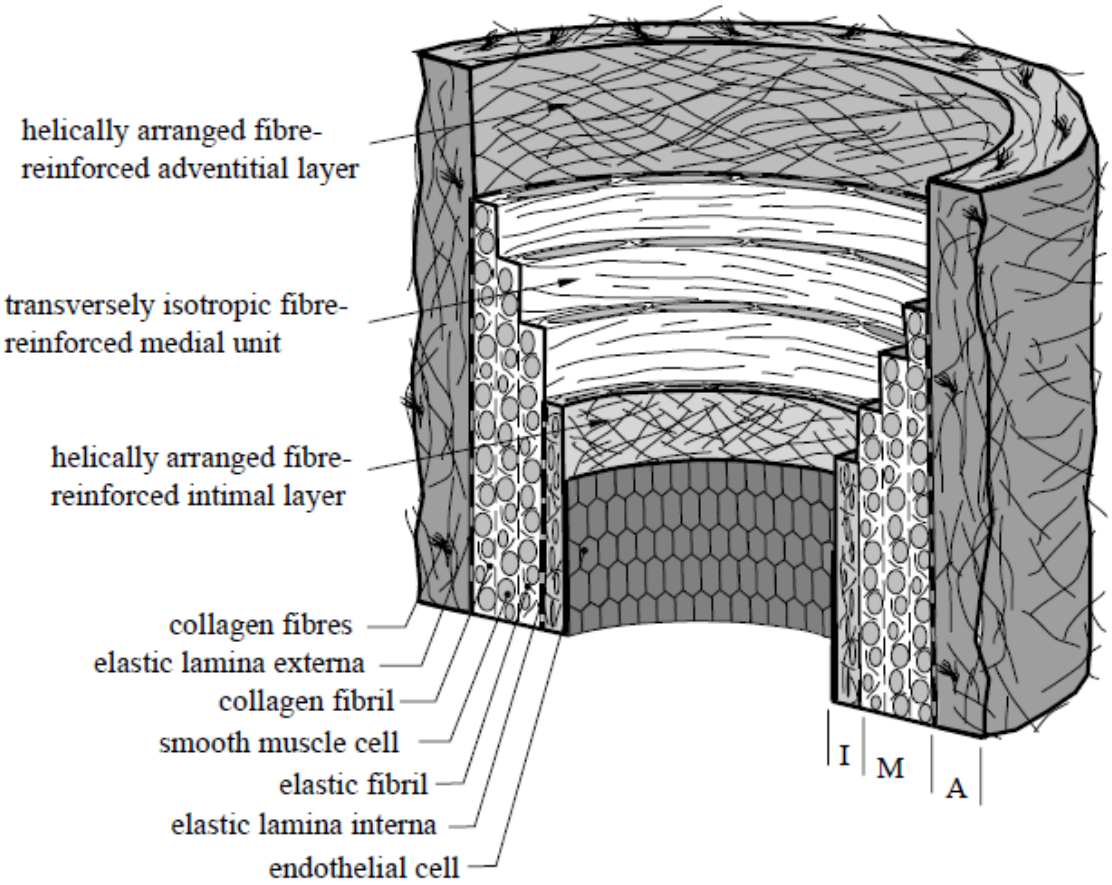

Figure 15 - A schematic of the construct of health human artery wall. The main structural layers are the Intima, Media and Adventitia. (Reproduced from [56]**, with permission from publisher *The Royal Society Interface*)**

There have been various attempts to characterise and mathematically define the mechanical response of arteries from animal tissue as well as human cadaveric samples. The level of characterisation has varied from purely capturing the change in vessel volume with pressure increase, to more recent histological examinations with efforts to phenomenologically capture the behaviour of each layer and their composite structures (i.e. smooth muscle, elastin and collagen fibres).

The non-linearity in the stiffness of arteries was first described by Roy in 1881 [41] with a series of pressurisation tests on animal and human arteries. This early historical experiment is depicted by the neat sketches reproduced in Figure 16. Roy found that arteries are '*most elastic at pressures corresponding, more or less exactly, to their normal blood pressure*' and that artery response is to stiffen at higher pressures. In the proceeding century a number of similar studies characterising the overall response of artery to

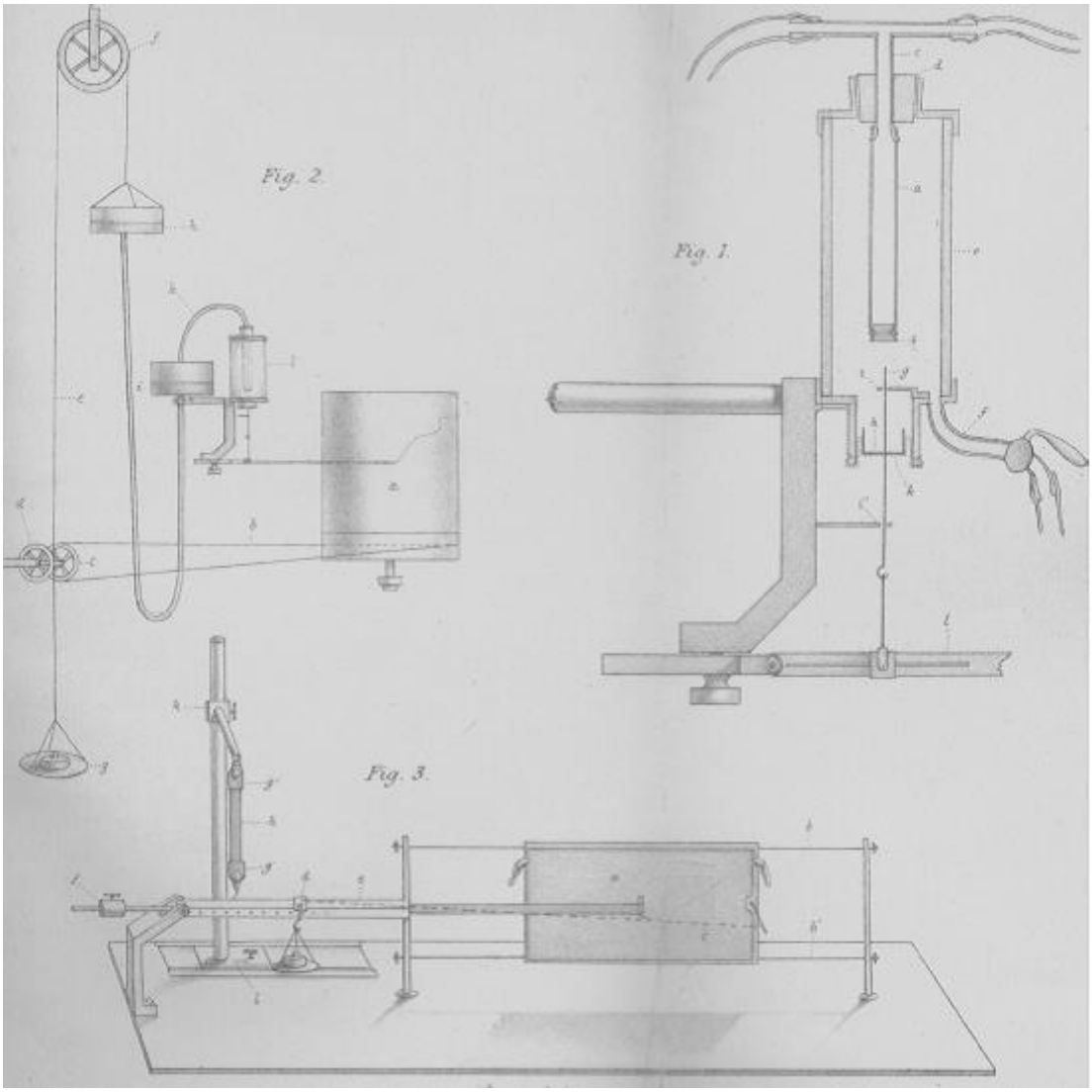

Figure 16 - A sketch of the experimental setup used by Roy in 1881 to investigate the loading response of artery (Reproduced with permission from publisher John Wiley and Sons)

pressure, as well as longitudinal stiffness, have been produced: Hallock and Benson in 1937 [42] and Hass in 1942 [43] studied 18 and 21 human aortas respectively of various ages for volume change with pressure; in 1961 the first use of 'photo-electric' micrometer type equipment was used for both static and dynamic vessel diametric response on extracted dog arteries by Bergel [44]; in 1966 Learoyd and Taylor [45] used a similar optical method to measure the outer diameter change of 59 segments (thoracic, abdominal, iliac, femoral, carotid) from 12 human cadavers ranging in age from 11 to 52 years; and in 1971 Nakashima and Taniwaka [46] reverted to measuring volume change to measure artery 'distensibility' of 114 human aortas.

The earlier papers (1961 and before) do not attempt to calculate elastic modulus values for arterial wall: reporting the general stiffening in terms of rate of change of volume with pressure, as well as focusing on calculating 'pulse wave velocities' related to the vessel viscosity. However Learoyd and Taylor [45] report incremental elastic modulus, for which it is necessary to make measurements or assumptions on the thickness of the artery wall, and collated the results into young (<35 year) and old (>35 year) data sets. For example, they calculate the elastic modulus from the 'old' abdominal aortic data to range on average from ~0.3MPa at 0mmHgh to ~3MPa at 160mmHg. Nakashima and Taniwaka [46], mentioned above, provided further segregation into numerous age ranges, indicating clearly that that arteries stiffen with age (see Figure 17).

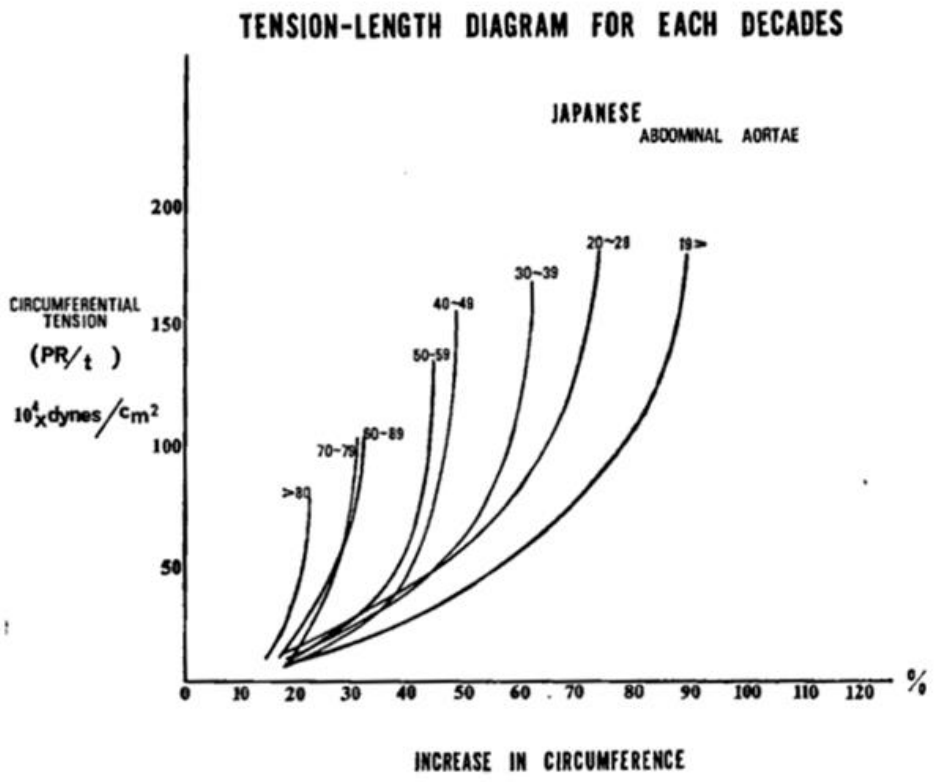

Figure 17 - Wall stress plotted against circumferential increase from empirical testing of aortic samples, showing variation in stiffness with age, as produced by Nakashima and Taniwaka [46] **(Reproduced with permission from publisher *SAGE Publications*)**

In 1984 another extensive pressure-diameter characterisation study on human aortic samples was carried out by Langewouters et al [47] in which 45 thoracic and 20 abdominal cadaveric samples with an age range of 30-88 years were analysed. Further to previous studies, a mathematical expression was introduced to describe the mechanical response;

relating pressure to the increase in vessel internal cross-sectional area with two parameters defined to accommodate variability (discussed further in 4.3.1).

Ultrasound has been used to assess aortic diameter and compliance within living patients by a group in Sweden; Lanne, Sonesson *et al* with publications from 1992 to 1994 [48], [49], [50]. As well as the stiffening with age relation described above, they show that the mean diameter of human abdominal aorta increases through adult life: a 30% increase in the average male aorta from age 25 to 71 years. The cardiac phased ultrasound method is consistent with previous testing in finding a stiffening Pressure-Diameter relationship; however this can only be extracted over the patient's operating blood pressure range of course – which is a limitation to characterising material stiffness for the purpose of modelling. This ultrasound work does however provide the first real proof of the reduction of aortic compliance with age, from live patients, which can be used to benchmark and compare against cadaver based testing. It is also the most complete source of data on *in-situ* 'diametric strain', ε_d for the abdominal aorta, defined as the fraction of change in vessel internal diameter (Eq. 2.1). This diametric strain data has been extracted from their initial study on 76 healthy males and plotted in Figure 18, which shows the significant decrease in diametric strain with age.

$$\varepsilon_d = \frac{D_{systolic} - D_{diastolic}}{D_{diastolic}} \qquad \textbf{(Eq. 2.1)}$$

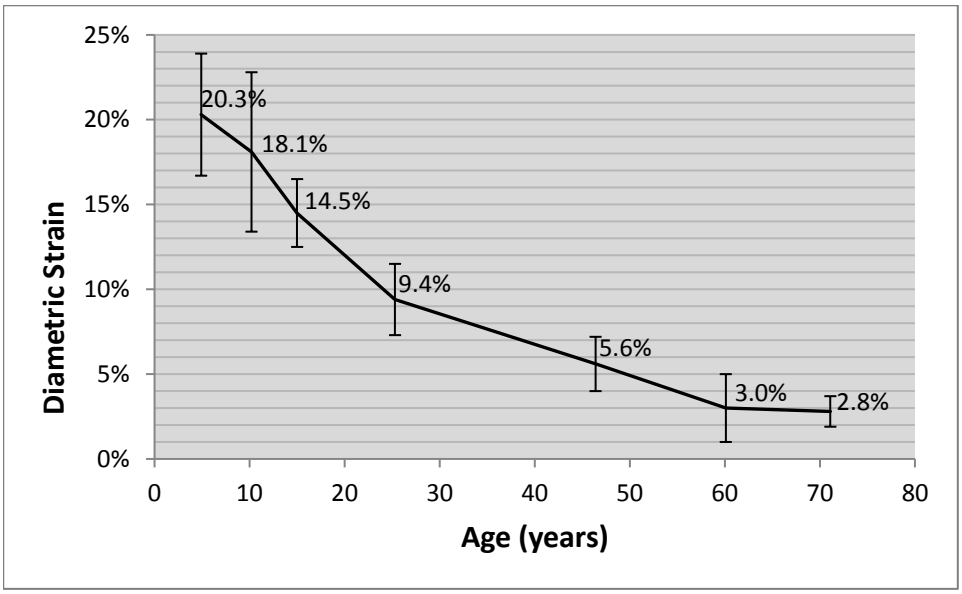

Figure 18 – Diametric strain of abdominal aorta for males of various age, assessed by ultrasound, data extracted from Lanne, Sonesson *et al* [48]. Error bars are showing ±S.D.=1

Many of the papers described do not reach the point of being able to provide measures of material stiffness for arterial wall because a measurement or assumption on wall thickness, which is required to deduce stress and therefore stiffness in the material, has not been acquired. An alternative 'pressure-strain elastic modulus', E_p was defined by Peterson [51] (another study on dog artery compliance in 1960) as (Eq. 2.2):

$$E_p = \frac{P_s - P_d}{(d_s - d_d)/d_d} \quad \textbf{(Eq. 2.2)}$$

where *P* is pressure, *d* is diameter and subscript *s* and *d* refer to systole and diastole. Care must be taken when papers are reporting this modulus which is a 'structural stiffness' as opposed to a material stiffness quantification, however it can be converted to material elastic modulus (*E*) if wall thickness (*h*) is assumed as described in *Biomechanics and Mechanobiology of Aneurysms* [1]:

$$E = \frac{d_d}{2h} E_p \quad \textbf{(Eq. 2.3)}$$

To gain an appreciation of the approximate levels of material stiffness which human aortic artery may experience, Table 1 compares such data which is collated from the Learoyd & Taylor [45] and Langewouters [47] papers.

Table 1 - Comparison of the elastic modulus of human aorta at 100mmHg reported in two separate publications

Publication	Elastic Modulus at 100mmHg	Comments
Learoyd & Taylor [45]	~2MPa for Upper Thoracic ~1.5MPa for Lower Thoracic ~1.2MPa for Abdominal	Read from graph value; average from cadaveric samples of age >35 (1 male, 5 female)
Langewouter [47]	Range of values: 0.36-4.09MPa for Thoracic 0.39-2.52MPa for Abdominal	Age range of 30-78 for Abdominal (n=20); 30-88 for Thoracic values (n=45). Male/Female ratio not specified.

It should be noted that the material stiffness decreasing distally in the Learoyd and Taylor results is misleading: the consensus of literature agrees that the compliance of artery decreases distally through the aorta, i.e. becoming stiffer from Thoracic to Abdominal. However, the above apparent contradiction can be explained by considering that Learoyd & Taylor also found that the wall thickness increases distally in the >35 cohort assessed: the

abdominal artery could have a lower material stiffness but a higher structural stiffness due to thicker wall layer when compared to thoracic.

More recently, in publications since 2000, perhaps the most active group researching the mechanical characteristics and mathematical modelling of aortic tissue has been the *Institute of Biomechanics* at the *Technische Universität Graz*, Austria which is headed by Gerhard A. Holzapfel [52]. The Holzapfel group collaborate with Raymond Ogden of *University of Glasgow*, who has an extensive publication history in the field of modelling the non-linear response of elastomers and rubbers [53], [54] as well as biomechanics applications. Both Ogden and Holzapfel have their names associated with two separate 'hyperelastic' constitutive material models which have been implemented within *Abaqus* software[1]. The Ogden model is a more generic isotropic hyperelastic model capable of curve-fitting various non-linear elastomer-like responses, while the Holzapfel model implementation in *Abaqus* is more specifically dedicated to representing arterial tissue.

The 'Holzapfel-Gasser-Ogden' (HGO) model embedded in the *Abaqus* software is based on an initial paper in 2000 [55], and enhanced by a follow-up paper in 2006 [56]. The first paper provides a "new constitutive framework for the description of the (passive) mechanical response of arterial tissue" which assumes that each artery layer is a composite reinforced by (collagen) fibres arranged in two symmetrically opposed helical directions, as depicted in Figure 19. The governing equation is a 'strain energy function' with two contributory terms: one representing the isotropic response associated with the elastin, and a second representing the anisotropic contribution from the collagen fibres. This model has four parameters which allow different artery types to be fitted to the constitutive equation. The helical angle of the collagen fibres is represented by one parameter, γ, however the latter paper [56] added to the description of orientation with a new 'dispersion' parameter which quantifies the distribution of fibre angles away from the mean helical angle. The main motivation being the relatively high levels of dispersion found in the adventitia and intima, and a finding that a continuum model without the ability to account for the dispersion (e.g. the earlier model) would not capture the stress-strain response accurately.

[1] There is a focus on the material models available in *Abaqus* FEA software since a decision was made early in the project to use *Abaqus* primarily because the work herein was adopting and building on methodologies already developed using the software by parallel work at the University of Strathclyde as described in [7].

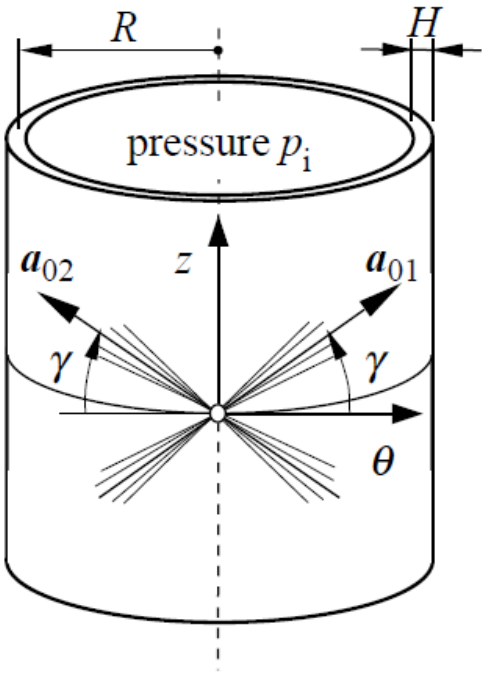

Figure 19 - Schematic from the Holzapfel-Gasser-Ogden model [55], [56] showing the mean fibre angle, from the circumferential axis, which collagen fibres are dispersed about. (Reproduced from Gasser *et al* [56])

Early artery mechanical characterisation work from this group focused on biaxial testing and histological studies of the anisotropic structure of tissue from iliac and coronary arteries [57], [58] as well as other tissue such as atherosclerotic plaque [59]. Since 2007 their vascular characterisation work has shifted towards the aorta, providing information on the fibre orientations (described above) as well as the pre-stressed states of the aortic wall layers *in situ* [60], [61]. The aorta is under permanent tension in the body, with an axial strain of 20% on average, while the layers (intima, media, adventitia) have significantly varying degrees of residual stress in the circumferential curvature. The media most so: cylindrical samples of media cut in the axial direction, would 'spring open' with the curvature actually inverting slightly [60]. These residual stresses clearly add an extra level of complexity to modelling the mechanical response of the aorta, and seem logically necessary if the effort to include the detailed 'composite structure' representation in the mathematical expression is to be worthwhile. A demonstration of modelling such phenomenon in FEA was provided [62]. The most comprehensive data set of constitutive model parameters provided by the Holzapfel group, for abdominal and thoracic aorta, is from testing of 16 cadaveric samples in 2012[63]. However, values for some of the

parameters vary significantly; by orders of magnitude, making it difficult to determine a representative model for a certain age for example.

Prof. J.D.Humphrey at the Department of Biomedical Engineering and Vascular Biology and Therapeutics Program, Yale University is another key publisher in the field of vascular mechanics. Publications which he has been involved in include investigating the origin of the residual stresses described above and their biological purpose [64], [65], but there is more so a focus on the mathematical modelling of the evolution of arterial tissue through aging, stress induced growth, and deterioration of an artery towards aneurysmal state [66]–[68]. Indeed, there exists significant effort in the literature from others to understand the mechanics of the Abdominal Aneurysm itself (e.g. [69]–[73]), however the application of this is beyond the aims of the work of this thesis.

Prior to the 'Holzapfel model' and also available within *Abaqus* is the 'Generalised Fung type' hyperelastic model based on the two-dimensional strain energy function provided by Fung et al [74], and 'generalised' to arbitrary three dimensional states from the proposal of Humphrey [75]. Other notable mathematical models providing hyperelastic strain energy functions for representing arterial tissue are that proposed by Raghavan & Vorp in 2000 [76], and Vande Geest et al in 2006 [77]. The latter also provides significant bi-axial testing data, and parameters to fit the provided equations, from 26 abdominal aortic aneurysms plus 8 non-aneurysmal tissue samples. However, these studies are also more focused on providing models to simulate the aneurysmal mechanical response, which as mentioned is not within the scope of the current work.

2.5 Preceding Work by the University of Strathclyde

The initial consultancy mentioned earlier provided an approach in 2001, implemented by Dempster and Forbes [78], to mathematically represent the ring-stent and artery interaction using classic structural mechanics and artery stiffness information from Langewouters [79]. A precursory task to this thesis was to assess the accuracy and limitations of this model. The approach considered the 'saddle shaped' ring to comprise of four identical arcs each on separate planes (see Figure 20 which highlights one of the mentioned arcs). The load-deflection behaviours of bending in the plane of the arc and bending perpendicular to the plane were modelled using formulae from *Roark's Formulas for Stress and Strain* [5] for curved beams. The main limitation identified was that the mechanical approximation of the ring-stent had not been validated in isolation, and the

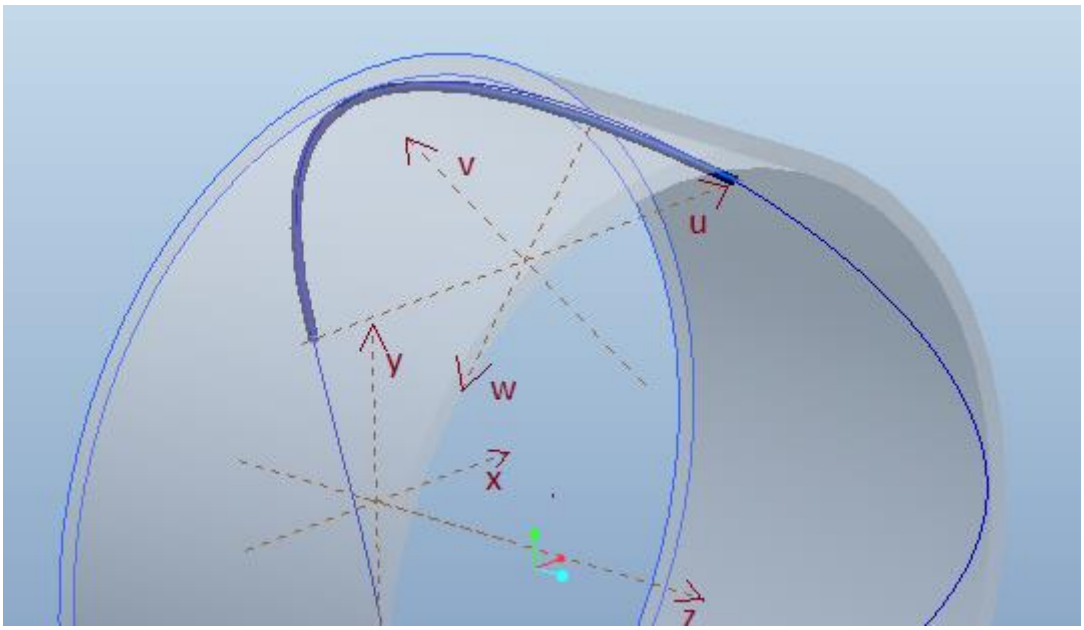

Figure 20 - The arc beam in bold blue, on local plane v-u, represents quarter of a saddle shaped ring-stent in the approach implemented by Dempster and Forbes [76].

load-deflection response was highly sensitive to key assumptions in the detail of the calculations. A comparison of the load-deflection response of a ring with early FEA results implemented here (Chapter 5) showed a complete contrast in the shape of the curve. Suggestions on how to improve the mathematical modelling of the ring-stent were identified [80], however it was decided to concentrate efforts on the FEA approach with the aim of achieving a better accuracy of the mechanical strength, compared to what would be achievable with structural mechanics calculations.

The PhD work of McCummiskey [6] in 2008 included a comprehensive literature review discussing the advantages and disadvantages of endovascular treatment compared with conventional 'open repair', a thorough review of Nitinol characterisation work at the time as well as a summary of FE methodologies employed to simulate other types of stent devices.

The initial work carried out by McCummiskey [6] involved sensitivity studies on the properties of the Nitinol wire followed by uniaxial characterisation of the wire used at the time. The sensitivity studies focused on assessing the influence of strain rate, temperature dependence, and low level cyclic effects on the stress-strain response of the Nitinol wire through a strain range of zero to approximately 6%:

- It was reported from testing on 2.4mm diameter Nitinol wire that even the lowest strain rates tested of 0.1mm/min caused sample temperatures to rise to 7˚C higher than ambient room temperature, while the highest rate of 50mm/min caused 22˚C rise over ambient. The actual effect on the stress-strain response was not as severe as the temperature variance, especially in loading. The resulting decision was to run further tests on fine wire (0.1-0.3mm diameter) at 5mm/min for single cycle tests and 50mm/min for multiple cycle tests, noting that the effect would be significantly less severe on fine wire diameter (greater ratio of surface are to volume). It was not possible to use fine wire for the strain rate test because of requirements to weld a thermocouple to a more significant diameter sample. The decision on strain rates made in units of mm/min would only be applicable to the specific sample lengths tested, which was not specified.
- Repetitive cyclic loading testing involving 100 tensile loading cycles from 0% to 6% showed significant reduction in stress-strain plateau levels and a development of residual strain to a maximum of approximately 1%. Considering device life, cycling Nitinol through the full phase transformation to 6% repeatedly is only relevant to the potential case of multiple compactions to a ring-stent; not the *in vivo* cyclic loading due to pulsatile blood pressure which will impose much smaller cyclic deformations.
- The effect of varying temperature, within the superelastic window, was investigated by tensile loading at 20˚C, 30˚C and 40˚C above the A_f point. Increased temperature had the effect of increasing the modulus and loading plateau levels, which highlighted the requirement for further testing to be tightly temperature controlled and the need for *Vascutek* to tighten the specification on the A_f temperature of supplied wire.

Subsequent to the above sensitivity studies, the wire was characterised in uniaxial tension and compression for the purpose of implementing within a material model for FEA. The compressive testing involved development of a bespoke jig for testing short samples (21.5-48.5mm) of Nitinol wire/rod of 1.0, 1.8 and 2.4mm diameter. The compressive testing indicated a 'start of transformation in loading' stress value of 853MPa, compared to 645MPa in tension.

The thesis of McCummiskey [6] also included work on developing an FE approach to model a Nitinol ring, focusing on the *Anaconda* device proximal ring, using the commercially available *ANSYS* package. A simulation methodology was achieved for a single turn, quarter ring model (symmetry can be used as will be discussed in Chapter 4) subject to the manufacture deformation, partial compaction and release into a linear elastic tube (the limitations of which are discussed in section 4.2.7.1). Progress was also made with a method to model a three-strand bundle, however it was not fully validated and issues with computational expense were mentioned in her conclusions. Strain analysis carried out on a number of single turn ring models provided data which was implemented to improve the mathematical model produced by Dempster and Forbes [81]. In addition to the modelling, McCummiskey also devised a ring fatigue test program that ran at *Vascutek* to determine a fatigue limit in terms of strain amplitude for the Nitinol wire in a loading representative of *in vivo*. Unfortunately, significant deviations exist in the maintenance of the testing, carried out by *Vascutek* personnel, resulting in incomplete data for defining a strain based fatigue limit reliably.

It was realised and noted in the recommendations of McCummiskey [6] that *ANSYS* had limitations compared to the FE package *ABAQUS* in terms of the implemented Nitinol model. The succeeding PhD work of van Zyl [7] developed a more computationally efficient method of modelling single strand Nitinol rings using *ABAQUS*, before proceeding to investigate the mechanical behaviour and constitutive modelling of human aorta. The initial FE work of van Zyl has been adopted and progressed in the work described in this thesis (see 4.2). In parallel to the development of the full-bundle model in the work of this thesis, van Zyl also proposed an alternative 'bi-element' method to capture the mechanical response of the ring-stent: overlaying a number of beam element strands, and joining them to one continuum element ring. The load-deflection response of this 'bi-element' approach was qualitatively compared to the empirical results of one ring configuration, showing an improvement over using a single turn of 'equivalent *'I'* value' (discussed later in 4.2.7.1).

The full-bundle ring-stent modelling methodology devised in this thesis will be quantitatively validated against various ring configurations in representative cyclic loading positions, in Chapter 4 of this thesis. Furthermore, the objectives of the ring simulations devised by both McCummiskey and van Zyl were focused on the stress/strain and

deformation analysis of the Nitinol wire; a method to assess the radial loading, between ring-stents and artery, had not been addressed.

2.6 Summary of Chapter Two

The ring-stent components of *Vascutek's* stent-grafts are required to 'self-expand' from the delivery sheath, provide sufficient radial force for hook engagement and sealing, and survive the cyclic loading of pulsatile blood pressure. The load-deflection response of Nitinol stent being compacted and deployed will display non-linearity and hysteresis analogous to the stress-strain relation of Nitinol. In cyclic loading, the Nitinol material will display a stable stiffness so-long as the strain amplitudes are considered low, which was defined as <0.25% by Robertson *et al*. [12].

The fatigue life of Nitinol is highly dependent on the manufacturing process, material composition and inclusion size of trace elements/residual contaminants. Such sensitivity leads to the necessity to carry out fatigue testing on any Nitinol components which have unique manufacture or application. *Vascutek* have changed grade of wire since the work of McCummiskey [6], and therefore the need is apparent to define a new fatigue limit based on the 'strain-life' approach, which is still considered most appropriate according to the review by Robertson *et al*. [12]. The work herein will inform the setup, and analyse the results of a new empirical fatigue test program to achieve a reliable strain-life fatigue characterisation of current wire, specifically for the ring-stent application (see Chapter 6).

Mechanical characterisation of the human aorta has sporadically progressed through various studies: from first identifying the 'stiffening' response, progressing to giving some estimates of the range of elastic modulus of the wall (see Table 1), to more recent detailed histological assessments into the composite structure including the influential collagen fibre distribution. Mathematical expressions have been provided in an attempt to phenomenologically capture the described behaviours at each stage of understanding. However, partly due to the difficulty in acquiring significant sample numbers of cadaveric tissue for testing, and also due to the natural variability from one person's aorta to the next, there is still no significantly comprehensive database which can easily provide mechanical parameters to represent a certain demographic.

Efforts towards this thesis assessed the feasibility of implementing the more complex Holzapfel constitutive model in detail, however a simpler method based on the work of

Langewouters [47], capturing the global pressure-diameter response of artery, has been proposed and implemented as will be detailed in section 4.3. In parallel to this, van Zyl worked to mechanically characterise the response of three cadaveric human aortas, acquiring parameters for the Holzapfel model.

The previous work of McCummiskey [6] has provided a clear insight into the behaviours of Nitinol which must be appreciated and accounted for in the characterisation and constitutive modelling of the superelastic material. Namely; how the strain rate, temperature dependence, and low-level cyclic fatigue influences the stress-strain behaviour. An important first attempt at quantifying the asymmetry of Nitinol's stress-strain response was also provided. The follow on and complimentary work of van Zyl [7] provides a neat and computationally efficient methodology to model the pre-strain and partial compaction of a single-turn quarter Nitinol ring-stent. This has been adopted and progressed herein to achieve and validate a more mechanically and geometrically accurate 'full-bundle' model of the Nitinol ring-stent, enabling the fatigue and radial force analysis objectives to be achieved.

3
Nitinol Material Constitutive Modelling

3.1 The Nitinol Wire Grade

The characteristics of Nitinol are significantly dependent on the material processing as discussed in 2.3. As such, in the parallel work of Brodie [26], a significant effort has been placed on characterising and modelling the current grade of Nitinol wire used in the manufacture of ring-stent grafts. The current wire used to manufacture the Nitinol rings is 'medical grade', supplied by *Fort Wayne Metals* and identified as 'Nitinol #1 Super-Elastic Straight Annealed'.

The wire undergoes a cold work and heat treatment process which may involve being drawn numerous times through a die to reduce diameter as depicted in Figure 21.

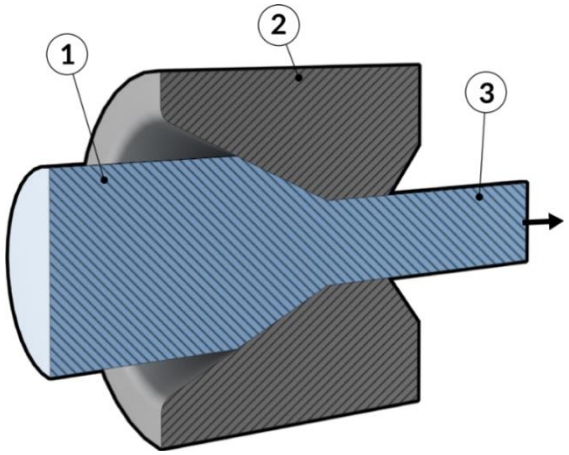

Figure 21 - Depiction of wire being drawn to a smaller diameter through a die. 1: wire pre-drawn, 2: the die workpiece, 3: the reduced diameter drawn wire (Image credit: www.manufacturingguide.com)

Annealing between draws and after final draw relieves the effect of cold work on the micro grain structure. The exact details of the cold working and heat treatment process are not disclosed by the wire supplier. A chemical etch finish is applied to remove any oxide layer and to leave a relatively smooth surface. The range of Nitinol wire currently used in devices, which are analysed herein, vary in diameter and specified tolerance as shown in Table 2.

Table 2 - Nitinol wire diameter and design specification tolerances as used by *Vascutek*

Wire diameter (mm)	0.12	0.13	0.14	0.15	0.16	0.18	0.20	0.22	0.24
Design specification tolerance (μm)	±2.5	±5.0	±5.0	±5.0	±5.0	±5.0	±5.0	±7.5	±7.5

The chemical composition of the wire is stated to meet or exceed that set out by ASTM F2063 [82] such that the percentage of Nickel in the alloy (per weight) is between 54.5% to 57.0%, other impurities are lower than stated in Table 3, while Titanium content comprises the remaining balance.

Table 3 - Chemical composition of Nitinol as per ASTM F2063

Element	weight %
Nickel	54.5 to 57.0 (Reference)
Titanium	Balance
Carbon	< 0.05
Cobalt	< 0.05
Copper	< 0.01
Chromium	< 0.01
Hydrogen	< 0.005
Iron	< 0.05
Niobium	< 0.025
Nitrogen plus Oxygen	< 0.05
Any Single Trace Element	< 0.1
Total Trace Elements	< 0.25

The Nitinol must be in the 'superelastic window' austenitic state, discussed in 2.3.1, at room temperature as well as at body temperature (37˚C). To ensure this the 'A_f (austenite finish) temperature' is specified to be slightly lower than the operating range: 12˚C < A_f < 18˚C.

A number of characteristics of the tensile stress-strain curve are specified as basic requirements by *Vascutek*: loading plateau >560MPa; unload plateau >250MPa; permanent set after 8% strain <0.5%; elongation to failure >10%; ultimate tensile strength >1300MPa. However, the behaviour needs to be assessed further to fully define the parameters for the

numerical constitutive model. A typical stress-strain plot of the above-mentioned grade of wire from *Fort Wayne Metals* is plotted in Figure 22 from data provided by the supplier. This sample was loaded to 8% nominal strain (7.70% true strain), unloaded to zero stress, and then loaded to failure which occurs beyond 16% true strain.

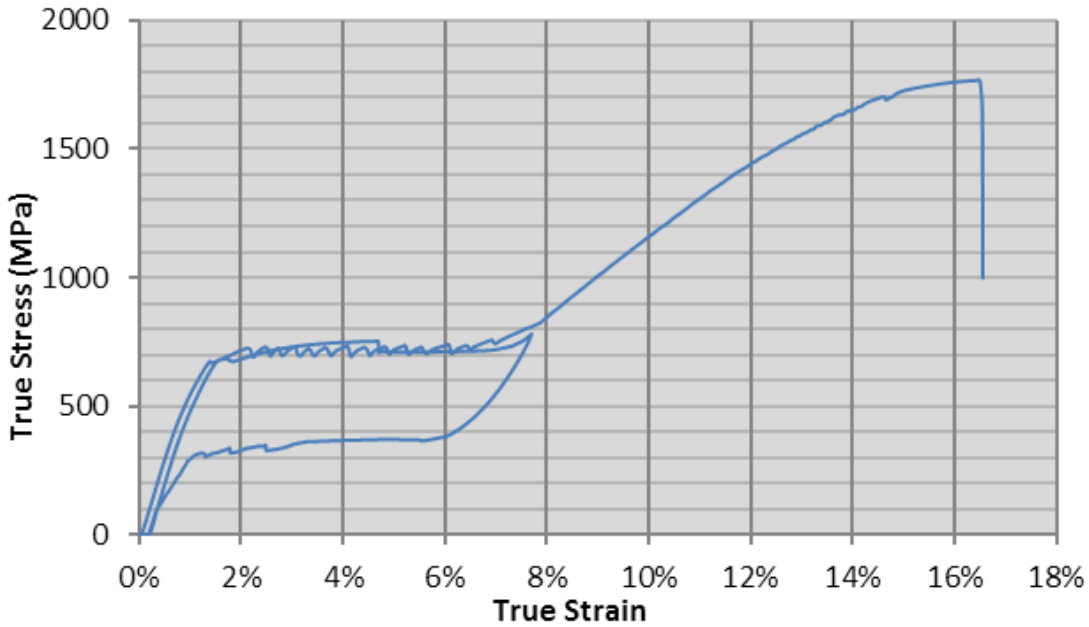

Figure 22 - Example Nitinol stress-strain plot from data provided by *Vascutek's* wire supplier *Fort Wayne Metals*. The wire was strained to 8% engineering strain, unloaded to zero stress, and then loaded to failure.

The unsmooth, jagged plateau paths (particularly in loading) observed in Figure 22 often occur in testing of Nitinol. It was suggested by McCummiskey that this "saw-tooth" effect is due to localised nucleations of martensite. However, more recent testing carried out at *Vascutek* [83], using different equipment, produces stress-strain responses with smooth plateaus in the transition zone, suggesting that the effect could be largely method dependent.

3.2 Constitutive Model

The constitutive model available in *Abaqus* for superelastic materials is described as 'phenomenological' meaning in this case that it mathematically describes the macro physical behaviour of a superelastic material observed empirically, but it does not achieve this by representing any crystallographic or molecular level structural phenomena. It is based on the work of Auricchio and Taylor [84], [85] who adopted the 'generalised plasticity' modelling approach of Lubliner [86] to develop a mathematical framework specific for superelastic-shapememory alloys. The model assumes isotropic and rate-

independent behaviour and it decomposes the calculation of recoverable strain into two separate parts: elastic strain and transformation strain. The transformation is modelled with a 'Drucker-Prager' type function which is a theory for calculating yield criterion which accounts for hydrostatic pressure stress in addition to the deviatoric part of the stress. This facilitates, to some degree, the modelling of asymmetric behaviour between tension and compression.

The mentioned constitutive model is implemented in *Abaqus* as a 'user material model', or 'UMAT', which is a type of sub-routine to the main software package, written in *FORTRAN* programming language. The basic information sheet for the model, provided by *Dassault Systèmes (Abaqus* provider), is attached as Appendix B. The basic 'UMAT for Superelasticity and Plasticity of Shape Memory Alloys' can model the observed uni-axial behaviour including: the separate austenite and martensite moduli, the superelastic transition, the stress variance in loading and unloading (hysteresis) and allows for some degree of asymmetry between tensile and compressive behaviour. It also provides for variance in stress levels due to temperature to be specified, however for the modelling herein, parameters will be kept constant, taken from characterisation tests performed at 37°C. The model also facilitates for a plasticity curve in the martensite phase to be defined by a number of coordinate sets, however this also will not be considered for the work herein as the ring-stents are designed to operate in the recoverable strain range.

A schematic from the information sheet (Appendix B) showing some of the 15 parameters which are required to define the superelastic stress-strain curve is shown in Figure 23. The austenite and martensite moduli are denoted by E_A and E_M respectively. The superelastic loading plateau is defined by stress point σ_{tL}^{S} and σ_{tL}^{E} at the start and end of the plateau respectively (superscript *S* and *E* refer to start and end, and subscript *tL* refers to transformation in loading). Likewise the unloading plateau is defined by stress points σ_{tU}^{S} and σ_{tU}^{E} (*tU* refers to transformation in unloading). The strains at which transformation in loading will complete is not defined directly: it is dependent on the transformation strain (ε^{L}), martensite modulus (E_M), and the end of transition in loading stress point (σ_{tL}^{E}). As depicted in Figure 23, the transformation strain (ε^{L}) is the point at which the martensite modulus crosses the strain axis. On the compressive side the 'start of transformation in loading stress' (σ_{cL}^{S}) can be defined if asymmetric response is desired and the data available. This stress point on the compressive side, along with a value entered for

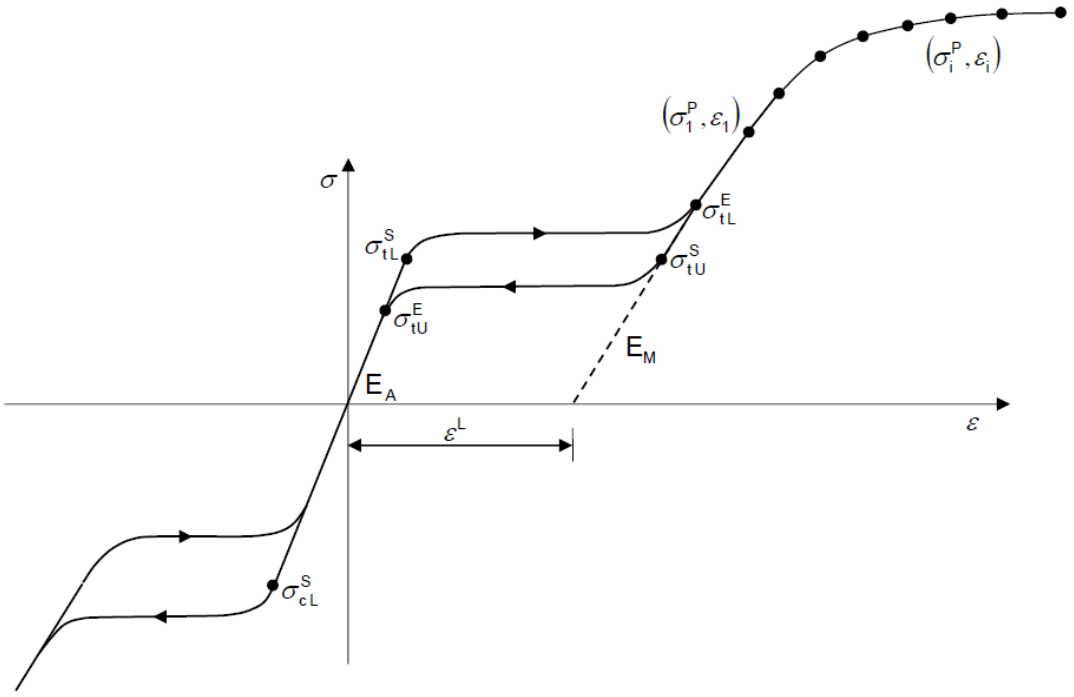

Figure 23 - The diagram from the information sheet (Appendix B) of the 'UMAT for Superelasticity and Plasticity of Shape Memory Alloys', annotating parameters associated with stress-strain relationship at a single temperature point.

'volumetric transformation strain' (ε_V^L) defines the full compressive behaviour of the model. Volumetric strain is the change in volume due to an applied hydrostatic pressure. As a volumetric strain over the transformation was not known, and not easily attainable, ε_V^L was set to a value equal to the transformation strain, ε^L, which instructs the sub-routine to re-calculate ε_V^L based on σ_L^S and σ_{CL}^S. This allows for some of the effect of asymmetry to be accounted for, meaning the overall model is more accurate in bending than if a symmetric model is assumed, however there is still susceptibility to inaccuracies in the slope and length of the compressive transformation plateaus in particular. The parallel work of Brodie [26] has justified the most appropriate parameters to use, taking account of the tensile, compressive and bending behaviour of the wire.

The coordinates $(\sigma_1^P, \varepsilon_1)$ and $(\sigma_i^P, \varepsilon_i)$ in Figure 23 are stress-strain points on the yield curve beyond the superelastic transition. As mentioned above, considering plastic deformation of Nitinol is out-with the scope of work covered herein. If no yield points are defined the model assumes the linear martensite modulus E_M beyond the transition in loading, and also in unloading until the 'start of transformation in unloading' stress level is met.

A Poisson's ratio for the austenite and martensite phases must also be specified, and two thermal parameters which dictate the change in both plateau levels per degree Celcius temperature change. All of the parameters discussed in this section are outlined in Table 4.

3.3 Model Parameters Implemented

Two different sets of Nitinol modelling parameters have been implemented in the simulations of the work herein. A provisional material model was used for the work in

Table 4 – The parameters of the 'UMAT for Superelasticity and Plasticity of Shape Memory Alloys'

Constitutive Model Parameter				Provisional Model Parameters	**Improved Model Parameters of** [26]
No.	Symbol	Description (from *Dassault Systemes*)	Units		
1	E_A	Austenite elasticity	MPa	64000	**61000**
2	υ_A	Austenite Poisson's ratio	N/A	0.435	**0.45**
3	E_M	Martensite elasticity	MPa	40000	**32500**
4	υ_M	Martensite Poisson's ratio	N/A	0.435	**0.45**
5	ε^L	Transformation strain	N/A	0.06	**0.05**
6	$\frac{\delta\sigma}{\delta T}$	$\frac{\delta\sigma}{\delta T}$ loading	MPa/ºC	4.30	**7.1**
7	σ_{tL}^S	Start of transformation loading	MPa	660	**680**
8	σ_{tL}^E	End of transformation loading	MPa	680	**710**
9	T_O	Reference temperature	ºC	0	**0**
10	$\left(\frac{\delta\sigma}{\delta T}\right)_U$	$\frac{\delta\sigma}{\delta T}$ unloading	MPa/ºC	5.03	**7.1**
11	σ_{tU}^S	Start of transformation unloading	MPa	400	**380**
12	σ_{tU}^E	End of transformation unloading	MPa	350	**350**
13	σ_{CL}^S	Start of transformation stress during loading in compression, as a positive value	MPa	1100	**965**
14	ε_V^L	Volumetric transformation strain. If $\varepsilon_V^L = \varepsilon^L$, an associated flow algorithm is used, with ε_V^L computed based on σ_L^S and σ_{CL}^S. For all other cases, a non-associated flow algorithm is used, which produces an unsymmetric Jacobian matrix. The USYMM parameter is thus required on the *USER MATERIAL keyword	N/A	0.06	**0.05**
15	N_A	Number of anneals to be performed during analysis	N/A	0	**0**

Chapter 5, which was derived from uniaxial testing data available early in the project, plus an initial attempt at compressive uni-axial testing. An improved, more accurate and thoroughly validated model was developed in the parallel work of Brodie [26]. This model was implemented in the component level validations described later in section 4.5, and was applied to all further analyses which are reported in Chapters 6-8. Both sets of parameters are shown and can be compared in Table 4.

The improved model of the work of Brodie [26] was derived from uni-axial tensile and compressive tests and validated with 'three point bend' load-deflection tests as well as Digital Image Correlation (DIC) verification of surface strain levels.

3.4 Summary of Chapter Three

Prior to the work of this thesis, sufficient characterisation had been accomplished at *Vascutek* and by McCummiskey to implement a provisional model of Nitinol in the 'user subroutine' constitutive model for superelastic materials within *Abaqus* with confidence that meaningful results will be produced. The investigations and work of Brodie [26] have significantly furthered the confidence in the ability to model the current grade of Nitinol wire now used by Vascutek to manufacture ring-stents. However, there are still limitations which bring sources of error to the accuracy of the material modelling, particularly with respect to modelling the asymmetry of compression versus tension, which can be partially taken account of but not defined with the fidelity of the options for the tensile side.

The constitutive model available in *Abaqus* based on Auricchio and Taylor [84], [85] certainly provides adequate flexibility to justify progressing with development of a methodology to simulate and analyse the ring-stents' mechanical performance. However, the limitations of the model will also be researched parallel to this work.

4

Simulation Methodology Development and Validation

The use of numerical modelling such as FEA is becoming more common in the development of medical devices [87]. The most relevant international standards to stent-graft design are ISO 25539 part 1 and 2 [3], [4], which recommends using tools such as FEA for stress/strain analysis of implants.

The problem presented - of analysing the structural state of a ring-stent through its typical lifecycle - is highly non-linear. As discussed in Chapter 2, the constitutive material models themselves have non-linear stress-strain relationships. The 'large deflections' of the ring-stents also contribute to non-linear effects in terms of the load-displacement response. The complexity of modelling contact between stent and artery is a 'boundary non-linearity' which adds to the mathematical complexity required within the FE solver.

Commercially established FEA packages are available with 'tried-and-tested' solving methods with non-linear capabilities for common industrial applications. Constitutive material models are included in many of these software packages, providing a flexible mathematical construct which can be adapted, to some degree, to represent the non-linear response of specific materials such as Nitinol as has been described in Chapter 3.

The *Abaqus* documentation provides example models which validate the accuracy of the solvers against industry standard 'benchmark' problems. However, it is an important practice to validate as far as possible the specific scenario and methodology which has been developed, in this case bespoke modelling of ring-stents and aortic artery.

This chapter will present the general mathematical theory of the relevant *Abaqus* solvers, the modelling methodologies developed to represent the ring-stent and stiffness of artery, and the validation work carried out.

4.1 Software, Governing Equations, Solution and Control

4.1.1 Chosen Software Package

Abaqus FEA software (versions 6.11 – 6.14) has been used for all the simulation work described herein. This program was selected primarily because of the initial methodology which was adopted from the preceding work of van Zyl as will be described in 4.2.1, but also it is noted that *Abaqus* provides some dedicated 'add-ons' for stent simulation and is used widely by the stent simulation community.

'*Abaqus Standard*' which is the conventional implicit FEA solver has been used with 'general static' simulation steps for the simulations described herein, unless otherwise stated. The 'general static' solver breaks highly non-linear simulation steps into smaller increments which are solved to approximate static-equilibrium using the Newton-Raphson method. The scenario of a stent pulsating in an aorta is indeed not static, but quite a dynamic problem in which the inertia and interaction of stent, artery and blood will, together, influence the deflections involved. To include the mass and haemodynamics of blood in a simulation would require the investment in a computational fluid dynamics (CFD) approach coupled with the FEA (recently known as Fluid-Structure Interaction (FSI)), however the current body of work is focused purely on the initial challenge: being able to simulate the superelastic ring-stent and its interaction in an aorta under pulsatile internal pressure, approximating static equilibrium at any solution point, to provide validated input for fatigue resistant design.

4.1.2 Governing Equations

In the following explanation, the key mathematical principals and equations are outlined but are not fully derived. Derivation is lengthy, usually described with the use of examples, and can be found in literature on the Finite Element Method [88]–[90]. *Abaqus* standard uses the common approach of the 'virtual work principle' and 'minimum total potential energy principle' as a basis from which to formulate the system of equations which relate a finite element body's deformation to the applied loads and boundary conditions. The

principle of virtual work (Eq. 4.1) essentially states that the total work done by external forces on a body (left side of equation) is equal to the increase in internal elastic strain energy in the volume of the body (right side of the equation) for some infinitesimally small 'virtual displacement':

$$\sum_{i=1}^{n}\{P_i\}^T\{\delta s_i\} = \int_{Vol}\{\sigma\}^T\{\delta\varepsilon\}dVol \qquad \textbf{(Eq. 4.1)}$$

where $\{P_i\}$ and $\{\delta s_i\}$ are vectors of force and 'virtual displacement' respectively for node i. On the right-hand side of the equation, the 'virtual work' done, $\{\sigma\}^T\{\delta\varepsilon\}$ is integrated over the volume where σ and $\delta\varepsilon$ are stress and virtual strain components respectively.

The 'minimum total potential energy principle' builds on the above by stating that if Π is the total potential energy of the system, then for a stable equilibrium state, the change in that energy, $d\Pi$ over a 'virtual displacement' is a minimum as mathematically implied by (Eq. 4.2):

$$d\Pi = \int_{Vol}\{\sigma\}^T\{\delta\varepsilon\}dVol - \sum_{i=1}^{n}\{P_i\}^T\{\delta s_i\} = 0 \qquad \textbf{(Eq. 4.2)}$$

The principle of 'minimum total potential energy' allows the 'element stiffness matrix', $[K]^e$ to be derived in terms of the strain displacement matrix, $[B]$ and the elasticity matrix $[D]$ as an integral over the volume (Eq. 4.3). Again, derivation of these new terms will not be provided here, but can be found with examples in Finite Element Method texts such as [88]–[90]. However; in short these matrices represent the following:

- $[B]$ is the strain displacement matrix which relates strain to displacement for each element such that $\{\varepsilon\} = [B]\{\delta\}^e$, where $\{\varepsilon\}$ is the strain vector, and $\{\delta\}^e$ is the nodal displacement vector for an element, *e*.
- $[D]$ is the elasticity matrix which relates an element's strain vector to stress vector via Young's modulus and Poisson's ratio (for a linear elastic material).
- $[K]^e$ is the element stiffness matrix, which relates the nodal displacements to the applied loads: $\{F\}^e = [K]^e\{\delta\}$, where $\{F\}^e$ is the vector of force on an element's nodes.

$$[K]^e = \int_{Vol} [B]^T [D][B]\, dVol \qquad \textbf{(Eq. 4.3)}$$

To be able to incorporate mathematically the rotation of a body relative to the global coordinate system the 'Jacobian' matrix is introduced which relates the transformed local coordinate axes to the global coordinate axis through the use of 'shape functions'.

$$dVol = dxdydz = |J| d\xi d\eta d\varsigma \qquad \textbf{(Eq. 4.4)}$$

where ξ, η, ς are the local Cartesian axes and $|J|$is the determinate of the Jacobian. The stiffness matrix including the Jacobian:

$$[K]^e = \int_{-1}^{1}\int_{-1}^{1}\int_{-1}^{1} [B]^T [D][B]\, |J|\, d\xi d\eta d\varsigma \qquad \textbf{(Eq. 4.5)}$$

The stiffness matrices for every element in the system are combined to create the global stiffness matrix $[K]^G$, which along with the global force vector, $\{f\}^G$ and global nodal displacement vector, $\{u\}^G$ define the system of non-linear differential equations to be solved. The number of equations to be solved in each increment of a solution is equal to the number of nodal degrees of freedom in the system.

$$\{f\}^G = [K]^G \{u\}^G \qquad \textbf{(Eq. 4.6)}$$

4.1.3 Solution

The ring-stent simulations required are highly non-linear in terms of the structure's deformation; let-alone non-linear material response and contact complexities once artery interactions are introduced. Any highly non-linear 'step' of the simulation requires to be split into smaller increments which may require several iterations to solve to sufficient accuracy. The Newton-Raphson method is the iterative procedure which is applied with an aim to converge a solution for each increment. Reviewing the method briefly; suppose that a non-linear simulation step applying a final loading of, P is attempting an increment in which a portion of the loading, ΔP is applied. The stiffness of the system first assumed, K_0 is the stiffness instantaneously at the start of the increment, or otherwise known as the 'tangent stiffness' (see Figure 24) at u_0. The principle of minimum total potential energy

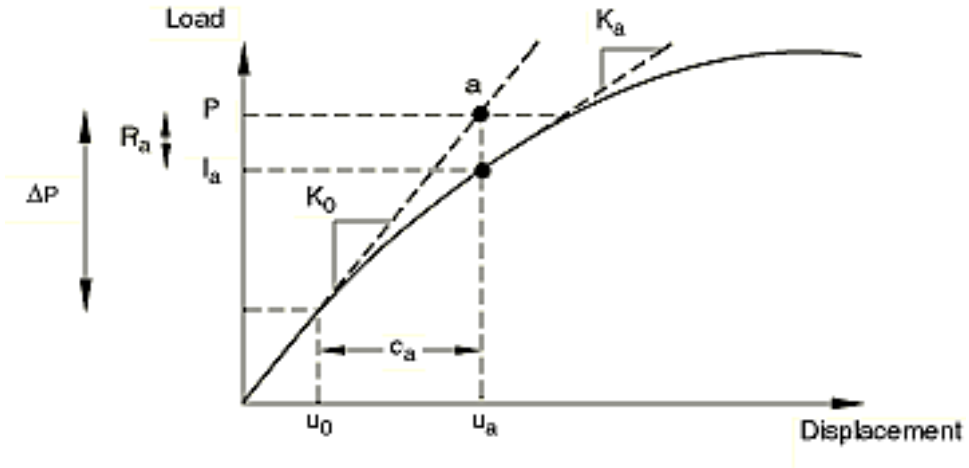

Figure 24 - Graphical explanation of the first increment of the Newton-Raphson method (Reproduced from *Abaqus* Documentation [91])

essentially stated that the external loading P, must equal the internal loading, I for equilibrium as per (Eq. 4.7).

$$P - I = 0 \qquad \textbf{(Eq. 4.7)}$$

An initial displacement correction c_a is calculated and subsequently the associated internal forces I_a in the 'updated configuration' of the system. The residual forces, R_a for every node can then be calculated which are used as a convergence check. The default criteria is that every residual force is less than 0.5% of an average nodal force in the structure. A second convergence check is that c_a is less than a fraction, 1% by default, of the total incremental displacement, u_a. If both convergence checks are satisfied, the system is

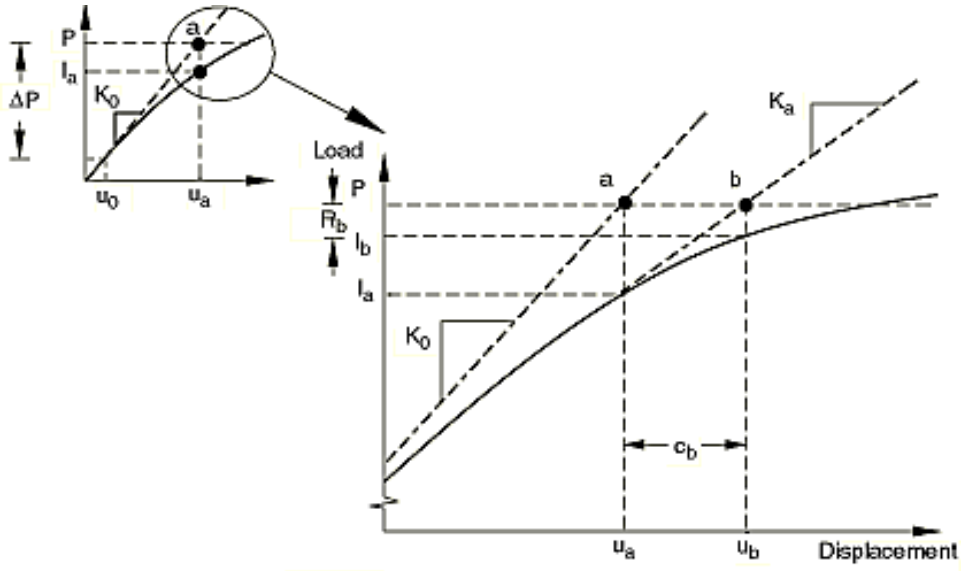

Figure 25 - Graphical explanation of the second increment of the Newton-Raphson method (Reproduced from Abaqus Documentation)

considered in approximate equilibrium, and the next increment of loading can be commenced.

If however, the iteration described above has not converged to acceptable tolerances, then a new increment is started in which first a new stiffness matrix, K_1 is computed from the most recent displacement position, u_a (see Figure 25). If the solution is converging, then the new residual force, R_b and the new displacement correction, c_b will have reduced, and if they are now within the acceptance criteria then the increment is assumed converged.

4.1.4 Automatic Incrementation Control

The size of increments in any given step can either be fixed, or varied automatically as the solution requires: smaller increments if the solution becomes more non-linear, and vice-versa. In cases in which the non-linearity of a problem is expected to vary throughout the step, it is usually most efficient to allow automatic control of the increment size, rather than fixed. Controls for the initial, minimum and maximum increment size can still be specified as guidance.

The ring-stent simulation steps can have sudden changes in linearity mainly due to the stiffness of the material, and therefore the structure, changing dramatically, or the initiation or changing of a contact interaction status when surfaces meet, come apart or move relative to one another. The former can be dealt with automatically as 'equilibrium iterations' and the latter as a 'severe discontinuity iterations' which will be outlined in the following (4.1.4.1 and 4.1.4.2).

4.1.4.1 Equilibrium Iterations

For the convergence of the 'static general' solution described in 4.1.3, the default rules applied by *Abaqus* governing the automatic increase or decrease of increment size throughout a step are as follows:

An increment is abandoned, and re-attempted at 25% of the size if any of the following criteria are triggered during equilibrium iterations:

- After the first four iterations of an increment a check begins to ensure that the largest residuals are decreasing. If they fail to decrease over two consecutive iterations, the increment is abandoned, deemed as diverging.

- After eight iterations of an increment, a check is introduced to ensure that the rate of convergence is following a logarithmic trend. If not, the increment is abandoned.
- After 16 equilibrium iterations have taken place and the residuals are still not within the tolerances, the increment is abandoned.
- If *Abaqus* has trouble with calculations because of excessive distortion in any element, the increment is abandoned. (This could be caused by non-linear material elements transitioning to a significantly different stiffness over the period of an increment.)

If a successful increment required more than 10 iterations to converge, the next increment size will be reduced to 75% of the previous.

The increment size is increased by 50% if two consecutive increments converge in less than five iterations.

4.1.4.2 Severe Discontinuity Iterations

If contact interactions are being used, the solver also needs to run severe discontinuity iterations to deal with abrupt changes in the stiffness due to slave surface nodes either coming into contact (closing), or separating (opening) from the master surface. If a severe discontinuity is detected, an iteration is forced in which loads representing contact pressures will either be applied, according to the specified pressure-overclosure relationship, or removed if the overclosure becomes negative (a clearance). Severe discontinuity iterations will continue until discontinuities are sufficiently small, or do not exist. Overclosure discontinuities are judged sufficiently small by assessing the 'penetration error' and 'estimated contact force error'. The penetration error is defined as the difference between the initial overclosure and the overclosure once the contact pressure-overclose load has been applied. The 'estimated contact force error' is obtained by multiplying the initial overclosure by the effective contact stiffness.

To be deemed sufficiently small, the 'penetration error' must be smaller than the 'contact and slip compatibility tolerance', T_{cont}, multiplied by the nodal incremental displacement. By default T_{cont} is 0.005. Likewise, the 'estimated contact force error' must be less than the 'contact force error tolerance', T_{cfe}, multiplied by the average nodal force. By default T_{cfe} is 1.

In cases where 'soft contact' is used, the 'contact and slip compatibility tolerance', T_{cont} is replaced by 'soft contact compatibility tolerance', T_{soft} which by default is 0.1.

In the case of a contact opening, when a contact force is removed from a node, this force discontinuity will cause force residuals which are checked to be sufficiently small relative to the average nodal force, in the same manner as described in 4.1.3.

4.1.5 Automatic Damping Stabilisation

Abaqus has 'automatic stabilisation' capability for the 'static general' solver, which is suitable for solving local instabilities in static problems. Damping forces, proportional to the local nodal velocities and a damping factor, are added to the global equilibrium equations. The damping factor can be applied as a constant value or it can be varied 'adaptively'; specified by algorithm based on the complexity of convergence of a previous increment. The automatic stabilisation is detailed further in section 7.1.1 of *Abaqus* Analysis User's Manual [91]. If stabilisation is used in any step of an analysis it is recommended to check that the energy dissipated against viscous damping forces is relatively small compared to the internal strain energy: a ratio of 0.05 is suggested and this was adopted as a check in simulations in this work.

Automatic Stabilisation has only been used in steps of analysis which were proving to have local instabilities. For the analyses presented later in this thesis, it has been specified when it was necessary to apply stabilisation.

4.1.6 Summary of Numerical Implementation

The decision to use the *Abaqus* software package is justifiable not only because of the preceding methodology development by van Zyl, but it also has: a proven robust numerical approach, based on the commonly used Newton-Raphson method, suitable for the solution of non-linear problems; some stent specific add-on tools; and is known to be widely used in the medical device industry.

The flexibility of the automatic incrementation control allows different steps in the ring-stent simulations to be configured individually to optimise the cost of analysis.

4.2 Ring Modelling Methodology

This section describes the single-turn ring model method which was adopted from the previous work of van Zyl [7], how it has been progressed, the methods added to radially

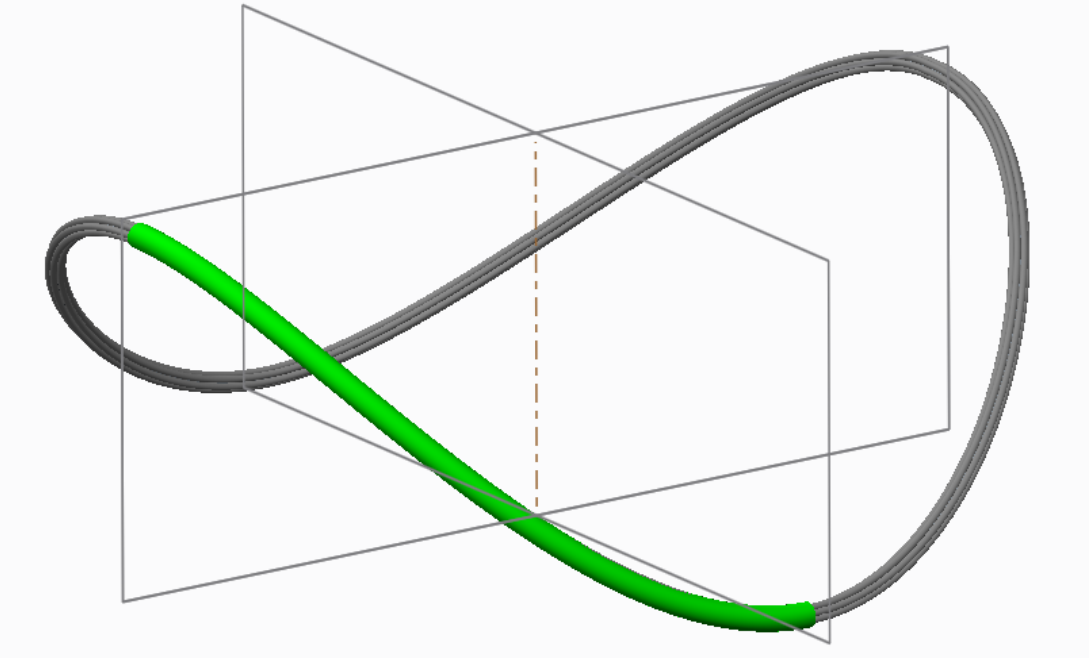

Figure 26 – A computationally generated graphic of a ring-stent depicted with the symmetry planes assumed and a quarter ring between peak and valley highlighted

load rings, and the justification on mesh structure and element choice. Subsequently the approach to model multiple turn 'full bundle' rings is covered.

For both the single-turn and 'full bundle' methods, the approach to simulate only a quarter of a ring, taking advantage of symmetry, has been implemented to reduce computational expense. This is valid for the case that a ring-stent is aligned perfectly (as opposed to rings being lopsided) and in idealised straight vessel. The symmetry planes of this approach are shown in Figure 26 with one quarter of a ring highlighted.

The validation of the ring modelling methods is covered later in section 4.5.

4.2.1 Adopted Quarter Turn Method

As discussed in 2.5, the preceding work at the University of Strathclyde on the modelling of Nitinol rings was most recently progressed as part of the work by van Zyl [7]. As was recommended by the earlier work of McCummiskey [6], van Zyl decided to use the *Abaqus* FE package to develop a methodology of modelling the ring-stent, as well as assess the capability of in-built arterial tissue constitutive models. An efficient method of simulating the initial bending (during manufacture) and semi-compaction of a single strand, quarter

Nitinol ring was developed by van Zyl and adopted as a fundamental method to be built upon for the work herein.

The method was developed using *Python* scripting to instruct the *Abaqus CAE* pre-processing interface. This allows a user to rapidly generate any model configuration by altering the key geometric parameters in the script, e.g. ring diameter and wire diameter, prior to the script being read by *Abaqus CAE*. The modelling method, implemented through the *Python* script includes the following features:

- Creating a quarter-circumference length of wire and partitioning the cross-section through the whole length to enforce an axially symmetrical mesh of continuum 'brick' elements.
- Generation of a structured hexahedral mesh with control over the number of elements in the cross section, and longitudinal direction.
- The simulation was implemented using 'static general' steps which use the governing equations and solution method described above in 4.1.
- C3D20R (20 node quadratic elements with reduced integration) were used to model the wire.

The first step, in which the straight wire is formed into a quarter ring, is achieved by applying a unique linear displacement condition for every node on the end faces of the quarter wire. These boundary conditions force the faces to displace and rotate onto the

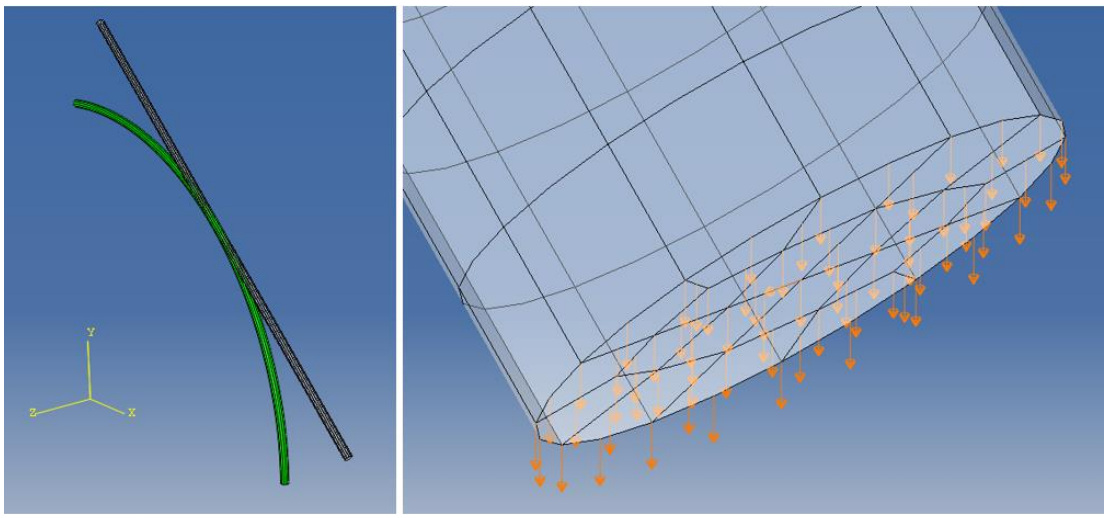

Figure 27 - LEFT: The undeformed (transparent) and deformed (green) position of a quarter turn wire after initial ring forming simulation step. RIGHT: Close-up of the wire end face (undeformed position) with unique linear displacements applied to each node.

global Y-Z and X-Z planes respectively as depicted in Figure 27. The wire's initial position is at 45° from the planes stated, with the central mid-point node of the wire located at a distance equal to the ring radius from the global origin. The unique displacement condition for each node on the end faces was achieved by scripting a loop in *Python* which, for each of these nodes, first of all queries its position relative to the Y-Z or X-Z plane and subsequently applies the necessary displacement required to move the node to the plane. This initial step is defined to complete in twenty increments of the 'static-general' solver with 'large displacement formulation' active to account for non-linearities. The displacement boundary conditions applied to each node on the end faces are propagated for all subsequent steps.

The linear displacement boundary conditions which are applied to the nodes are clearly sufficient to enforce the desired angular displacement of the faces, however there is potential for a slight inaccuracy of local strain levels due to being unable to apply rotational constraints to the individual nodes. Ideal symmetry modelling would constrain the rotation of nodes about the axes which lie on the plane of symmetry, however the *Abaqus* formulation does not allow rotational boundary conditions at nodes of continuum element

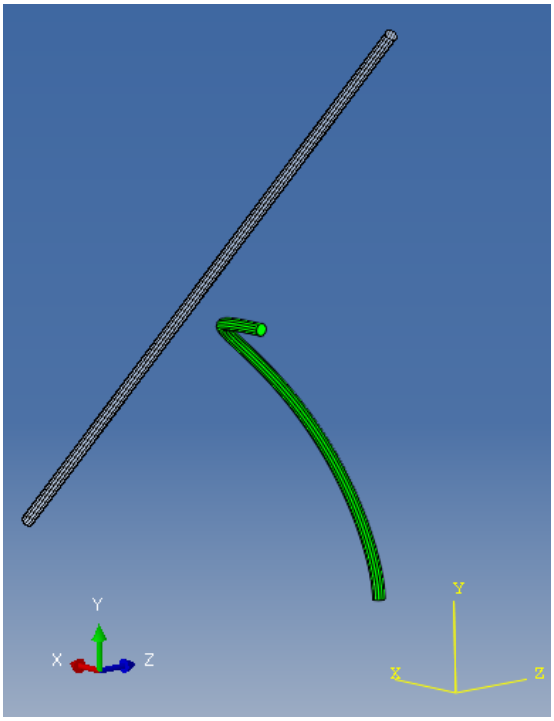

Figure 28 - The undeformed (translucent) and deformed (green) position of a quarter turn wire after a second step to simply load the ring into a 'saddle shape'.

models. This potential inaccuracy was investigated and negated, in the work of this thesis, by comparison with a half ring model (see sections 4.2.5 and 4.2.6).

The second step which loads a ring into some level of 'saddle shape' is enforced by simply applying user specified displacement boundary conditions to the central node on each end face in opposing directions along the Z-axis. The resulting deformation of a quarter turn after this second step is shown in Figure 28.

The capability to deploy the ring from a semi-compacted 'saddle shape' position into a vessel was demonstrated using default 'hard contact' interaction definition between the wire and relatively rigid tube (compared to modulus of artery).

The modelling methodology was adopted at the stage of development described here, and progressed further as will be described in 4.2.2-4.2.7. In the additional work of van Zyl, which focused on empirical testing and simulation of artery tissue modelling, the ring-stent methodology was also developed further in-parallel to the work herein, but with slightly different approaches.

Beam elements to represent the wire was an approach also investigated by van Zyl, however, for the work herein it was decided to focus on the continuum element approach described above because the continuum elements provide greater fidelity in analysing the state of the material through the cross section of the wire, and there were concerns over the accuracy of beam elements in high bending.

4.2.2 Fundamental Advancements to the Quarter Turn Method

The adopted quarter ring model was first improved by resolving an instability issue, adding new loading methods and running a mesh convergence study to define a suitable choice of element and mesh density.

In terms of stability, it was realised that the quarter turn model was essentially torsionally unrestricted causing what could perhaps be called a rotational 'chattering' in which the wire was displacing about its axis back-and-forth by some angle every increment. This artificial movement in the static-solver model was causing the automatic incrementation to reduce to extremely small levels, and sometimes requiring automatic damping stabilisation (see 4.1.5) to solve. Resolving this, by adding an equation constraint at two axially-opposed nodes at the longitudinal mid-point of the wire, essentially restricted free rotation at that

point, stabilises the model, and vastly reduces computational expense: an example single-turn ring model being formed and pulled into an arbitrary saddle-shape showed a 77% reduction in processing time, and the saddle loading step solution required 49 increments without damping stabilisation, compared to 280 increments with damping stabilisation.

Regarding the basic loading of a ring into a 'saddle shape', it is more convenient to be able to apply concentrated force rather than displacement boundary conditions to the quarter wire ends. To stop rigid body motion along the same axis as the loading, partitioning was changed to allow a central node to be selected and pinned in that direction.

4.2.3 Radial Compression Methods

Three different methods of radial loading have been implemented in order to analyse Nitinol rings at various levels of loading or to approximate the deformation which compaction enforces. The methods are listed below in chronological order of implementation (4.2.3.1-4.2.3.3):

4.2.3.1 Uniform Radial Force Application

A script was developed in *Python* (Appendix C) which distributes a desired radial force over all the nodes which lie on the central axis of the single turn quarter ring. The script uses 'for loops' to query the position of nodes longitudinally on the wire and subsequently applies a radial load to each node (except the central nodes on the end faces) in the form of appropriate Cartesian components. Figure 29 shows a ring loaded with the uniform radial force (depicted by the red force vector arrows from every central node) along a quarter

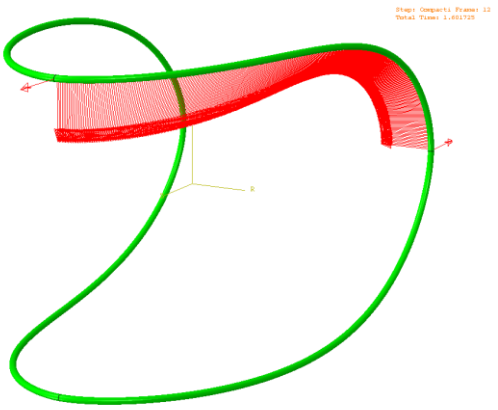

Figure 29 - A single turn quarter ring model loaded with the 'uniform radial force' and a small axial loading. The geometry only, not the loading, is mirrored to show the full ring being represented.

length of the ring. The geometry is mirrored on the assumed planes of symmetry to show a representation of a full ring. A small axial load has also been applied in this case which is necessary to initiate the bending of a flat ring.

This application of a 'uniform radial force' was used as an early method of investigating the radial force-displacement characteristic of a ring-stent, as well as used in combination with axial loads to enforce a deformation similar to that in compaction, prior to being unloaded into a vessel (section 5.4).

4.2.3.2 Adjustable Rigid Torus (ART) *Abaqus* Extension

The ART Extension in *Abaqus* is a stent simulation dedicated plug-in for the *Abaqus* graphical user interface (*Abaqus/CAE*), which drives a user-subroutine called '*RSURFU*', to define a rigid contact surface in the shape of a torus or cylinder. The implementation of this '*RSURFU*' user-subroutine, is essentially a bespoke definition of an 'analytical contact surface' in *Abaqus*. 'Analytical contact surfaces' define surfaces mathematically by straight and curved lines and do not need to be discretised into elements. An advantage is that the geometry of curved surfaces are represented exactly, which is not achieved in the case of a contact surface being defined by linear elements.

The ART plug-in automatically creates a contact behaviour assuming an exponential pressure-overclosure relationship to be applied between the contact surface and stent. However, this interaction rule was found to be not as robust, causing convergence issues, so a simpler 'hard contact' definition using the penalty method with default parameters was implemented.

NOTE: To be compatible with the ART extension, the adopted quarter turn method (4.2.1) had to be re-orientated to take account of the orientation of the 'adjustable rigid torus'.

4.2.3.3 Rigid Cylinder with Variable Diameter

A simpler method of creating a variable diameter cylindrical contact surface (only a quarter cylinder is required if the quarter ring model is implemented), without the need of the ART extension, is to define a cylindrical '3D deformable' shell part, and discretise it into surface elements. Surface elements have no inherent stiffness but one of their uses is in defining rigid contact surfaces either by fully controlling their position with boundary conditions or embedding them in a host element. In this case the former: using a cylindrical coordinate system the quarter cylindrical surface is fully fixed in the angular and axial directions, and

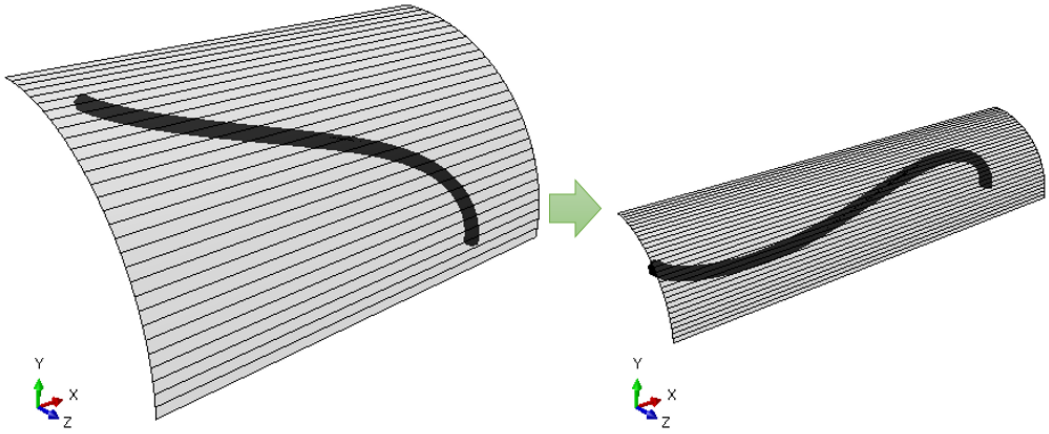

Figure 30 - An image from Abaqus showing the cylinder of surface elements reducing in diameter to compact a ring-stent.

varied in the radial direction to force the diameter change during a step, as shown in Figure 30. These boundary conditions can be applied either as displacement or velocity conditions. Regarding the element choice, 8-node quadratic elements were used in order to capture the curvature of the geometry.

4.2.4 Radial Force from Circumferential Force

In some early studies contributing to Chapter 5, an approximation of radial force was extracted by applying a factor of 2π to the circumferential compression load experienced by the ring. This is equal and opposite to the circumferential tensile load which a ring exerts on a vessel. This approach is derived from thin walled vessel theory which states that the stress in the wall of an open ended cylindrical vessel is given by:

$$\sigma_{circ} = \frac{Pd}{2t} \qquad \textbf{(Eq. 4.8)}$$

The circumferential wall stress can be considered as the circumferential force, F_{circ} over the wall cross section area (thickness, t × length, L):

$$\sigma_{circ} = \frac{F_{circ}}{Lt} \qquad \textbf{(Eq. 4.9)}$$

and the internal pressure can be considered as the total outward radial force over the internal surface area ($\pi d \times L$):

$$P = \frac{F_{radial}}{\pi dL} \qquad \textbf{(Eq. 4.10)}$$

Substituting (Eq. 4.9) and (Eq. 4.10) into (Eq. 4.8) gives:

$$\frac{F_{circ}}{Lt} = \frac{F_{radial}}{\pi dL} \cdot \frac{d}{2t} \quad \textbf{(Eq. 4.11)}$$

which simplifies to:

$$F_{radial} = 2\pi \times F_{circ} \quad \textbf{(Eq. 4.12)}$$

The radial force from a ring-stent is not a uniformly distributed load (i.e. an internal pressure), however it still ultimately results in circumferential load in the vessel wall, and therefore the radial force from a ring can be calculated using (Eq. 4.12), if the internal tensile circumferential force is known. This was taken a step further to consider that the internal compressive circumferential force through a loaded ring-stent would give the same value. The internal compressive load in a ring was verified to be equal to the internal tensile load it exerts on a vessel in a test simulation with no friction. The method as a whole was also compared to the later analysis method of directly calculating the radial force by totalling all nodal contact forces in the radial direction, which was developed for post processing of full ring-artery simulations (see 7.2.1). The 'radial force from circumferential force' was 3.09% greater than that summed from radial contact forces for a OLB28 R1 ring.

During the work of this thesis, a similar calculation to acquire the radial force from the measured force from a 'sling type' radial force tester, (see Figure 31) was published in ASTM (American Society for Testing and Materials) standard F3067-14 [92]. The 'sling type' apparatus implements a flexible sheet material to wrap around a stent and tightens by being pulled through a restriction which is connected to a tensile tester. As per the standard, the radial force is calculated by $\pi F_{L,}$ where F_L is the linear force measured by tensile tester machine which is attached to the tester apparatus. This differs from (Eq. 4.12) by a factor of 2 because the circumferential force is being applied to the tensile tester from both ends of the sling material. This physical method of measuring radial force of stents is being implemented and refined at *Vascutek* at the time of writing but was not used for the work herein.

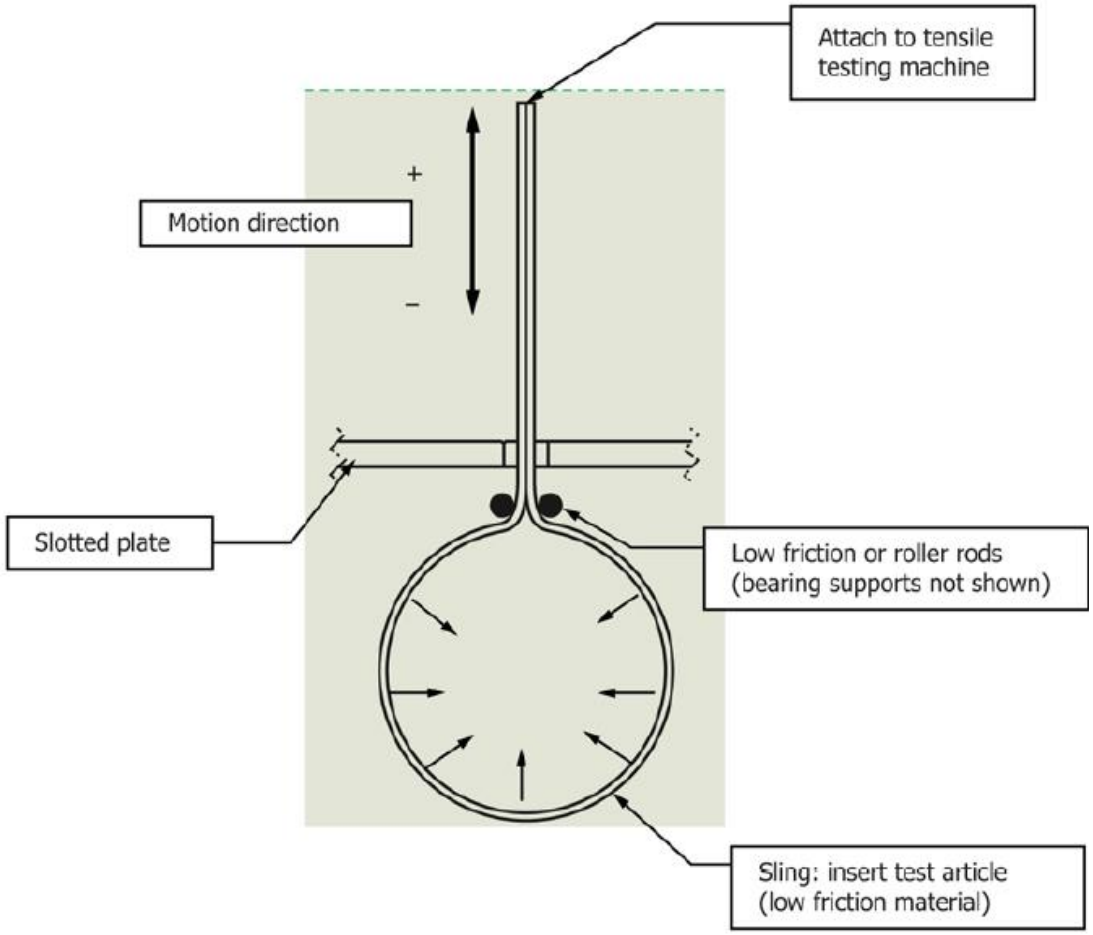

Figure 31 - Diagram of the 'sling type' radial force tester apparatus from ASTM F3067-14[92]

4.2.5 Half Ring Model

A half-ring model was developed firstly to probe the accuracy of the symmetry approximation applied to the quarter model (discussed in 4.2.1), and secondly to provide the ability to simulate rings deployed in a tilted orientation relative to a vessel axis. The general approach is the same as the quarter ring method above; in that a *Python* script is used to apply unique displacement boundary conditions to the end face nodes to enforce the initial ring formation step. An example *Python* script is found in Appendix D. In this case however, the straight wire is initially orientated parallel to the Z axis, the central node pinned at a radius distance from the origin, and the unique nodal displacement conditions force the end faces onto the X-Z plane, forming the half ring, as depicted in Figure 32.

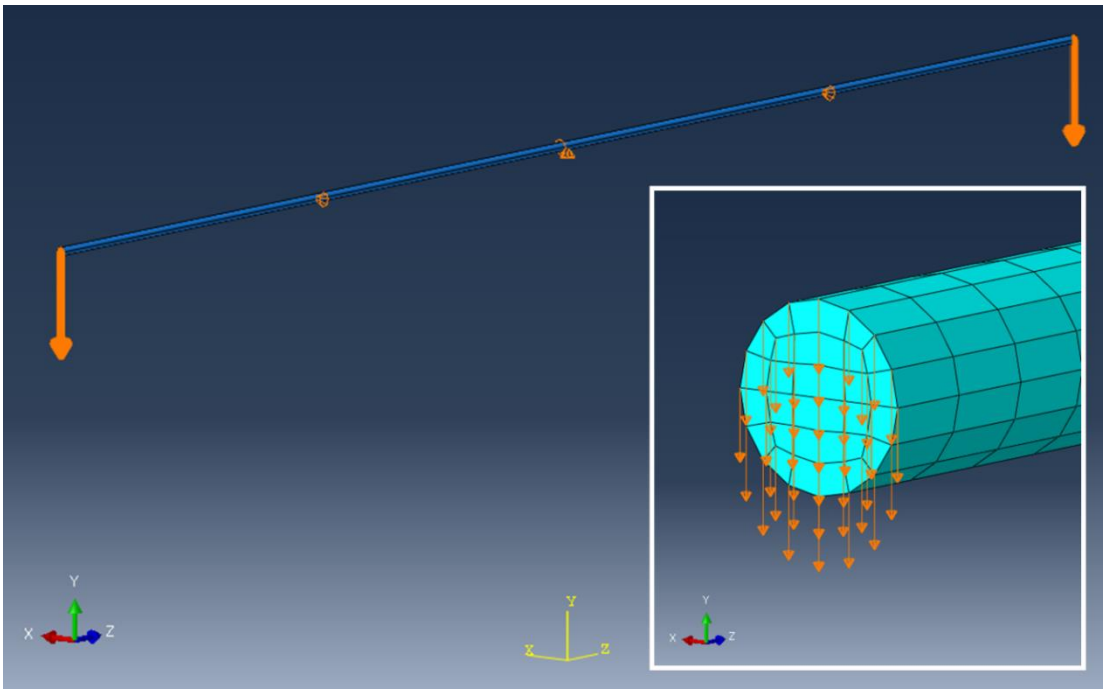

Figure 32 - The initial state of a half turn wire, with displacement boundary conditions indicated. INSET: Detail of the wire end with individual boundary conditions applied to each node.

4.2.6 Ring Mesh Convergence Study

A mesh convergence study was undertaken to assess the influence of mesh density and element type on the resulting radial strength and strain amplitudes of the ring subject to cyclic loading in a typical 'saddle shape'. The study involved both the quarter-ring and half-ring single strand models to represent an average turn from the proximal ring of a 28mm *Anaconda ONE-LOK* device. The central core of the delivery system was included as a rigid contact surface, because it has an effect on the resulting deformed position of the compacted ring. The simulation steps in the study include: the appropriate initial ring forming; a step to pull the ring into an arbitrary initial saddle shape; a compaction approximation using the ART extension to radially compress the ring to a diameter of 6mm; an expansion of the rigid cylinder to a position typical of deployment and subsequent radial cyclic loading using the ART extension. The initial steps, prior to cycling, for a half-ring simulation are shown in Figure 33. During the cycling, the cylinder diameter was varied by 5% and ten cycles were applied to converge any initial variance in results due to the material model hysteresis (discussed further in 4.5.3). A 'hard' contact pressure-overclosure relationship was applied using the default 'penalty enforcement method' settings.

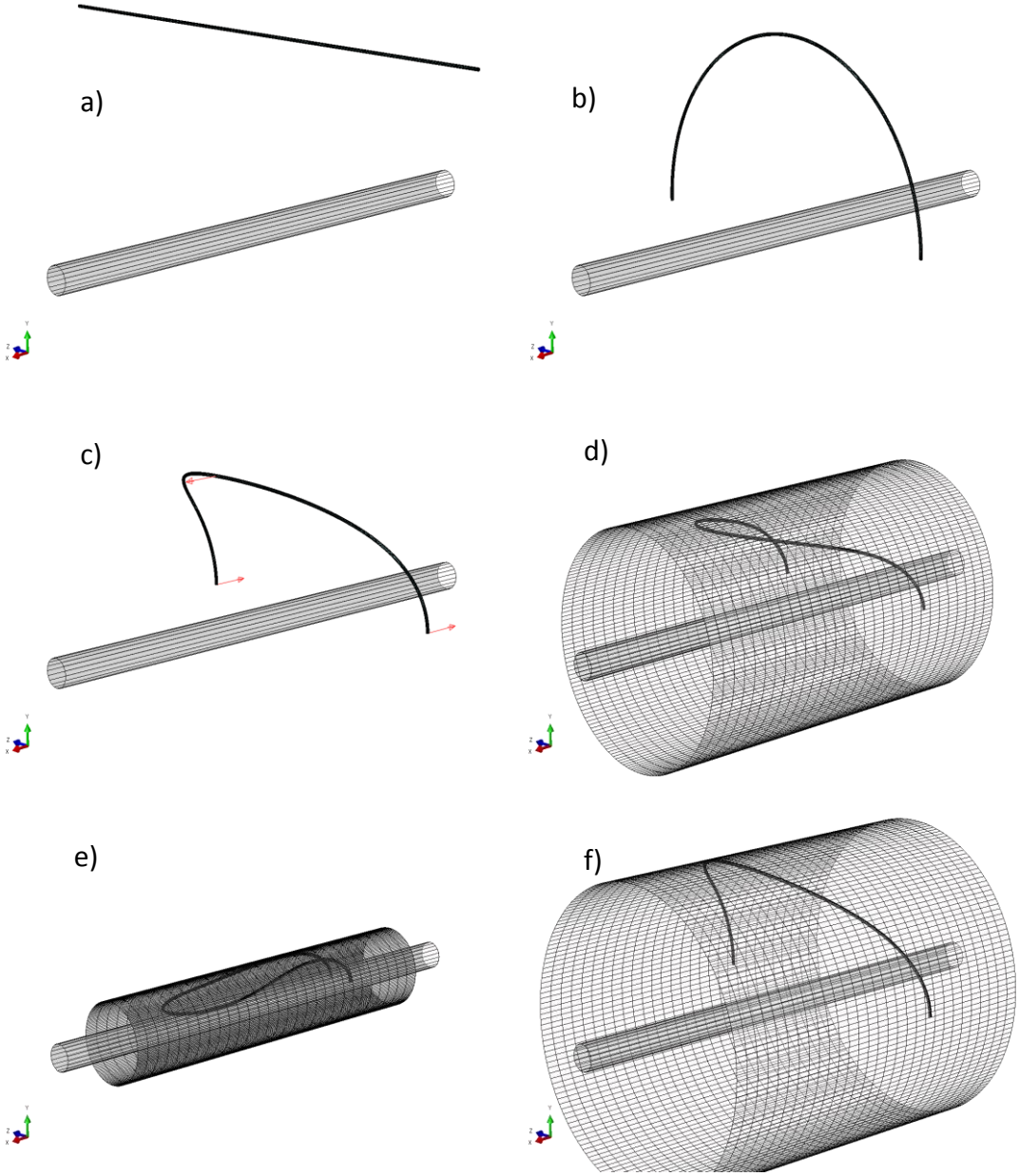

Figure 33 –*Abaqus* images from a half-ring mesh convergence simulation: a) initial position of straight wire and central core; b) formed half-ring; c) forces at peak and valley pull ring into a saddle shape; d) initial compaction using the ART extension; e) final compaction state; f) unloading to the diameter at which cyclic loading will commence in further steps.

4.2.6.1 Elements

Fully integrated, second-order (quadratic), quadrilateral elements (C3D20) were used as the datum to which to compare, with a goal to find an acceptably accurate, less computationally expensive solution with linear elements. Fully integrated linear elements (C3D8) and their slightly enhanced 'incompatible modes' version (C3D8I) were compared

with the datum case. The least expensive, linear reduced integration elements (C3D8R) were rejected because they are inconvenient to use with the superelastic material model as it does not automatically calculate the required 'hourglass control parameters'.

'Incompatible mode' elements in *Abaqus* have an addition to the formulation which enhances the elements' degrees of freedom, allowing the 'deformation gradient' to be linearly variable rather than constant. This is an enhancement which overcomes the 'shear locking' limitation of fully integrated, first order elements and provides an option to simulate bending more accurately with a small cost to computational time. (Discussed in more detail in the following sections of [91]: Getting Started with *Abaqus*: Interactive Edition 4.1.3 and *Abaqus* Analysis User's Guide 28.1.1)

4.2.6.2 Mesh Structure

The applied methodology partitions the wire such that there are four quarters in the circular cross section which are sufficient to enforce a structured, symmetrical mesh of hexahedral elements. The number of elements in the cross-section can be varied by changing the seeding size along the cross-section partition edges. The element length (in the wire longitudinal direction) can be separately controlled with seed sizing along edges in that direction. Three different cross-section mesh densities with a count of 20,32 and 60 were applied as can be seen in Figure 34.

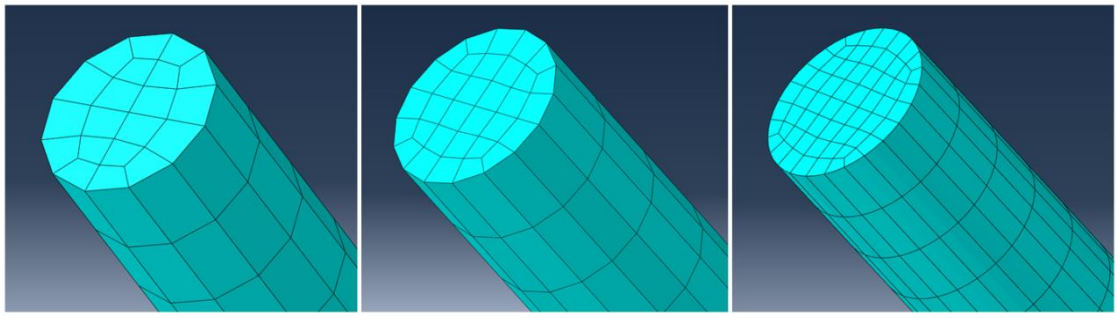

Figure 34 - From left to right: a 20, 32 and 60 element cross-section mesh of hexahedral elements applied to the wire.

In the case of the 32 and 60 element version, the longitudinal seeding was applied such that the element length to width ratio would be approximately 3:1. In the case of the 20 element version the element length was defined as half the wire diameter.

4.2.6.1 Mesh Study Results

The details of the six configurations studied, as well as the strain and force results are shown in Table 5 in order of computational expense (highest at top). In the case of the half model, strain results were extracted from the peak/valley at the middle of the wire length, i.e. negating the potential effect of imperfect symmetry boundary conditions discussed above.

Table 5 - Ring mesh study details and results

Model No.	Quarter model OR Half model	No. of elements in cross-section	No. of elements in wire	Element Type	Delta-strain % variance from datum	Radial Force % variance from datum	Percent reduction in computation cost relative to datum
1 (datum)	Half	60	30,720	C3D20	0%	0%	0.0%
2	Half	32	12,288	C3D8I	2.50%	-4.12%	93.2%
3	Quarter	32	6,144	C3D8I	2.47%	-4.22%	93.8%
4	Quarter	32	6,144	C3D8	4.88%	8.09%	96.7%
5	Quarter	20	3,840	C3D8I	1.78%	-7.29%	97.6%
6	Quarter	20	3,840	C3D8	7.76%	5.56%	97.9%

The percentage variance in radial force and delta-strain results are also plotted in Figure 35 (all shown as positive in magnitude). It was decided to proceed with the quarter model, 32 element cross-section, linear 'incompatible mode' C3D8I elements version (model no. 3)

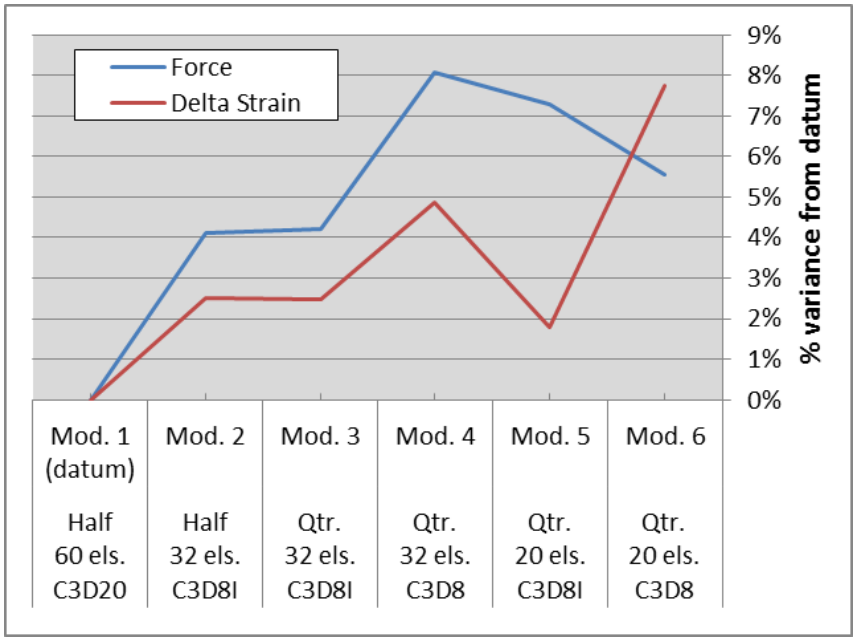

Figure 35 - Mesh convergence study: radial force and delta-strain results for a single strand model

which shows acceptably low variance of 2.47% and -4.22% for delta-strain and radial force respectively. The negligibly small difference in results between the half model and quarter model with the same mesh specification (model no. 2 and 3 respectively) is also a reassuring result giving confidence in using the quarter model.

The chosen configuration (model no. 3) provides a 94% improvement on computational cost relative to the datum model. The datum model took 95.6 hours to solve on a single 3.47GHz processing core, with sufficient RAM (random access memory) available. The lack of computational difference between the quarter and half model for the same mesh specification was due to the quarter model having more instability in torsion, which had not been resolved at the time of this study (see 4.2.2 for discussion on the torsional instability). Automatic stabilisation with a specified damping factor of 0.0002 was used to stabilise all the above mesh study models. Although this has been resolved and stabilisation is not required in further modelling, the strain and force results from this study were still regarded as a valid justification of the model no. 3 mesh configuration to be applied to further ring modelling.

4.2.7 Full Bundle Modelling

In reality, each individual ring-stent is a multiple winding of a single strand of Nitinol wire, the ends connected with a tantalum crimp at a position between peak and valley position. The turns of the ring are also held together temporarily with four simple thread ties when manufactured, before being sewn onto the fabric of the full stent device with threading spacing of approximately 1mm. Other than the crimp and suturing the turns are not bonded or connected further. Collectively the multiple strands held together will be referred to as the 'bundle'. The manufactured rings have minimal twisting of the bundle along its axis, i.e. they could not be classified as a cable structure in which there is some twisting, braiding and/or bonding of strands. Therefore, for modelling purpose it has been assumed that the strands of the bundle run relatively parallel to each other as well as the axis of the bundle as a whole. Longitudinal sliding of one turn relative to another during large deflection of the ring is possible with the main resistance being friction which is likely to be dependent on tightness of suturing.

4.2.7.1 Considering the 'Equivalent I value' method

In the preceding work of McCummiskey [6] a model of three interconnected strands was demonstrated, however the methodology was not developed further to simulate the greater number of strands existing in the physical rings. Prior to this demonstration, structural approximations had been suggested based on assuming an 'equivalent *'I'* value' of the bundle of strands. Symbol *'I'* being the 'second moment of area' of a beam cross-section. There are two theoretical options on how to apply this assumption:

1) The '*I*' value of individual strands are simply added to give a total *'I'* value. A single 'equivalent' diameter for this total *'I'* value is modelled.
2) The strands are assumed bonded longitudinally and therefore the *'I'* value of the more complex bundle shape is calculated with a reference to one neutral axis. This greater second moment of area is then assumed to calculate an 'equivalent' single strand diameter as above.

The former could provide an equivalent stiffness of the structure for low-deflection applications in which the material behaves within a linear elastic range. Indeed, McCummiskey did show reasonable accuracy (maximum variation of 13% between FE and empirical) in validation of a ring being loaded in moderate bending (for comparison: the saddle height was extended to 25% of ring ID). The validation work herein (4.5.1) is more thorough in that various rings are tested and loaded to a 'high', semi-compacted, saddle state (55%-62% saddle height relative to ring ID) and then unloaded and cycled at saddle shapes deemed to be representative of *in-vivo* deformation (averaging between 37% and 42% saddle height relative to ring ID). Irrespectively, the major drawbacks of this equivalent 'I' approach are:

- Firstly; the strain levels in an equivalent (larger diameter) strand in bending are false: exaggerated to a level proportional to the difference in diameters (between equivalent single strand and real strand diameter).
- Subsequently; an equivalent diameter ring would start transition to a martensitic state earlier than the real strands in loading because of the higher strain levels explained in the previous point. This leads to underestimation of the structural stiffness.

McCummiskey overcame the first of these limitations by an additional step in her simulation methodology; deploying a ring of the true wire diameter into the exported geometry of a vessel which had been deformed by the 'equivalent' ring. However the methodology was not extended to enable the true wire diameter ring model to follow the deformation of the equivalent diameter ring through the simulation, which would enable the stress and strains during cyclic motion to be analysed.

To generate a methodology which can provide accurate strain assessment for fatigue analysis as well as a sound structural representation it was deemed not an option to use an 'equivalent *'I'* approach'.

4.2.7.2 Bundle Configuration

As per the visual observation mentioned in 2.2, it is assumed that in the flat ring position, there is no twisting of the bundle. In the quarter model methodology developed the strands are modelled as separate parts with slightly varying ring radii.

When a ring is in place, connected to a full device, the bundle is generally held together with polyester fabric and suture. It is assumed that the flexible nature of these materials allow the bundle to settle into an arrangement which is fairly circular, since a circular shape is optimal in terms of increased area for a given perimeter. For the purpose of practicality the turns are assumed to fall into a triangular lattice, keeping the same relative distances from the centre of one turn to an adjacent. These two assumptions have been used to create the arrangements shown in Figure 36 for strand counts of 3 to 14, where the centreline shown represents the ring's mean radius. The strands have been distributed in

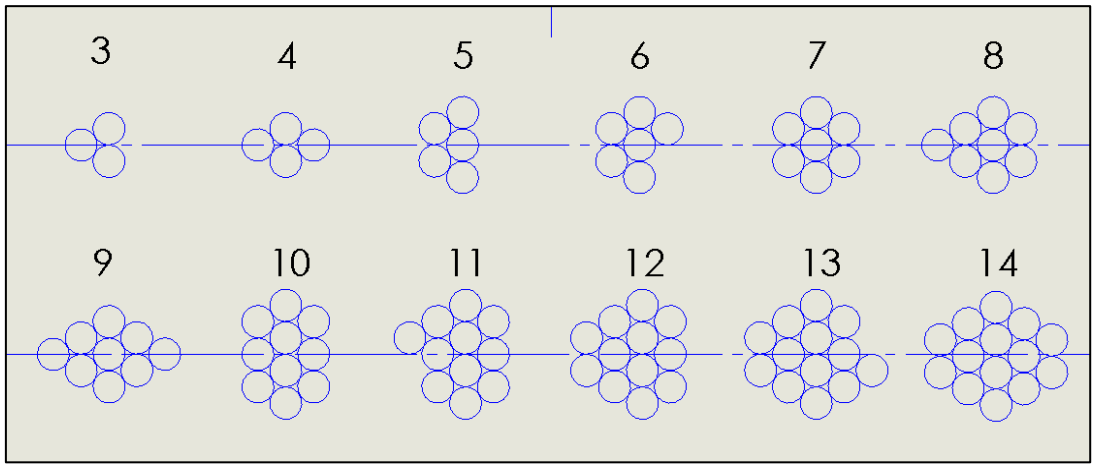

Figure 36 - Assumed bundle configurations for multiple turn modelling. The centrelines represent the mean radius of the ring.

as circular a layout as possible while using the hexagonal lattice pattern, with distribution symmetrical about the mean radius line for all cases except n=6,11,13 where this was not possible. These inaccuracies are deemed acceptable because moving the position of a single turn, from the inner side of a bundle to outer say, would have negligible effect on the mean diameter of the ring, and therefore negligible impact on radial strength or reported strain levels.

4.2.7.3 Turn to Turn Connectivity

Adjacent turns are connected to each other at multiple points along their axes using 'wire features' in *Abaqus*, which are assigned specific properties through defining and assigning them a 'connector section'. These wire features are essentially linear elements which can be given a range of mechanical characteristics. The connector elements at the end of an undeformed (straight wire) quarter *Anaconda* OLB32 R1 ring are shown in Figure 37, in which the differing strand lengths can also be observed. The intent has been to avoid using a contact interaction which could add considerable expense to the simulation and possibly cause instabilities. However, a 'soft contact' interaction was found to be necessary during compaction to avoid wires becoming tangled for some ring configurations – see 4.2.7.5.

The connectivity approach was iteratively refined during repeated sensitivity studies carried out to assess the dependence of results on methodology options in general. It was found that nine connectors were required down the length of the quarter ring in order to avoid some artificially induced strains around the connector locations. Regarding the properties

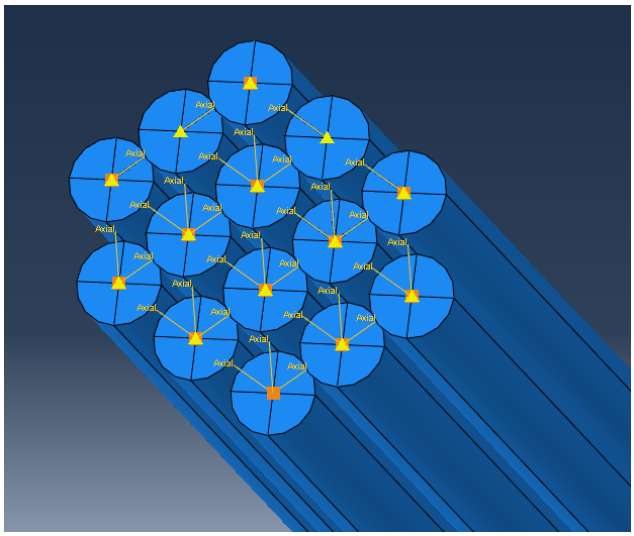

Figure 37 - The end of an OLB32 R1 wire bundle in initial undeformed condition. Connector elements are shown in yellow.

of the ‘connector section’ which was applied to the wire features, the following approach was finalised on:

- The connector section type was assigned as ‘axial’, which means that it will simply act as a linear spring with pin-joint like connections to nodes on either end, i.e. no moments are transferred.
- A ‘reference length’ equal to one wire diameter was applied. This is the natural unstrained length of the connector.
- A minimum ‘stop’ length condition of 99% of one wire diameter was applied at which point the connectors become completely resistant to further compression. This length is slightly different to the ‘reference length’ to avoid discontinuity instabilities
- Regarding the stiffness of the connector elements, which is defined in terms of force per unit extension, a specific sensitivity study was run to investigate the influence on mechanical behaviour (see ‘Connector Stiffness Assessment’ below).
- A small damping coefficient, specified to be equal in value to the applied stiffness, was assigned in the connector property. The purpose of this is to reduce potential severe discontinuities in the solution caused by connectors switching suddenly between a compressive state, to tensile.

4.2.7.4 Connector Stiffness Assessment

Firstly, and perhaps counter intuitively, it was found that connector stiffness had a negligible influence on the stiffness of the ring when pulled and cycled in the saddle shape as per the validation tests which are outlined in 4.5. This stands even when the connectors were defined to be completely rigid in linear stiffness. This case can be explained by considering that although points on the axes of the turns are held firmly at a ‘reference length’ apart, the connectors can still pivot away from the wire axis perpendicular, allowing the turns to slide relative to each other and overlap somewhat in space. This can be appreciated in Figure 38 in which the HY28-01 (HY denotes Thoraflex Hybrid device) ring model is fully extended in the validation test.

Satisfied that the choice of connector stiffness does not influence the structural strength of the ring, the influence on fatigue strain analysis had to be assessed. The connector stiffness was normalised in the *Python* script to be proportional to the strength of a turn on the ring it would be applied to. This is based on the 'ring strength' theory derived later in section 5.4.2.1, such that the connectors are specified a stiffness (in N per mm extension) according to (Eq. 4.13):

$$Connector\ Stiffness = C \times 847870 \times \frac{d^4}{D^2} \qquad \textbf{(Eq. 4.13)}$$

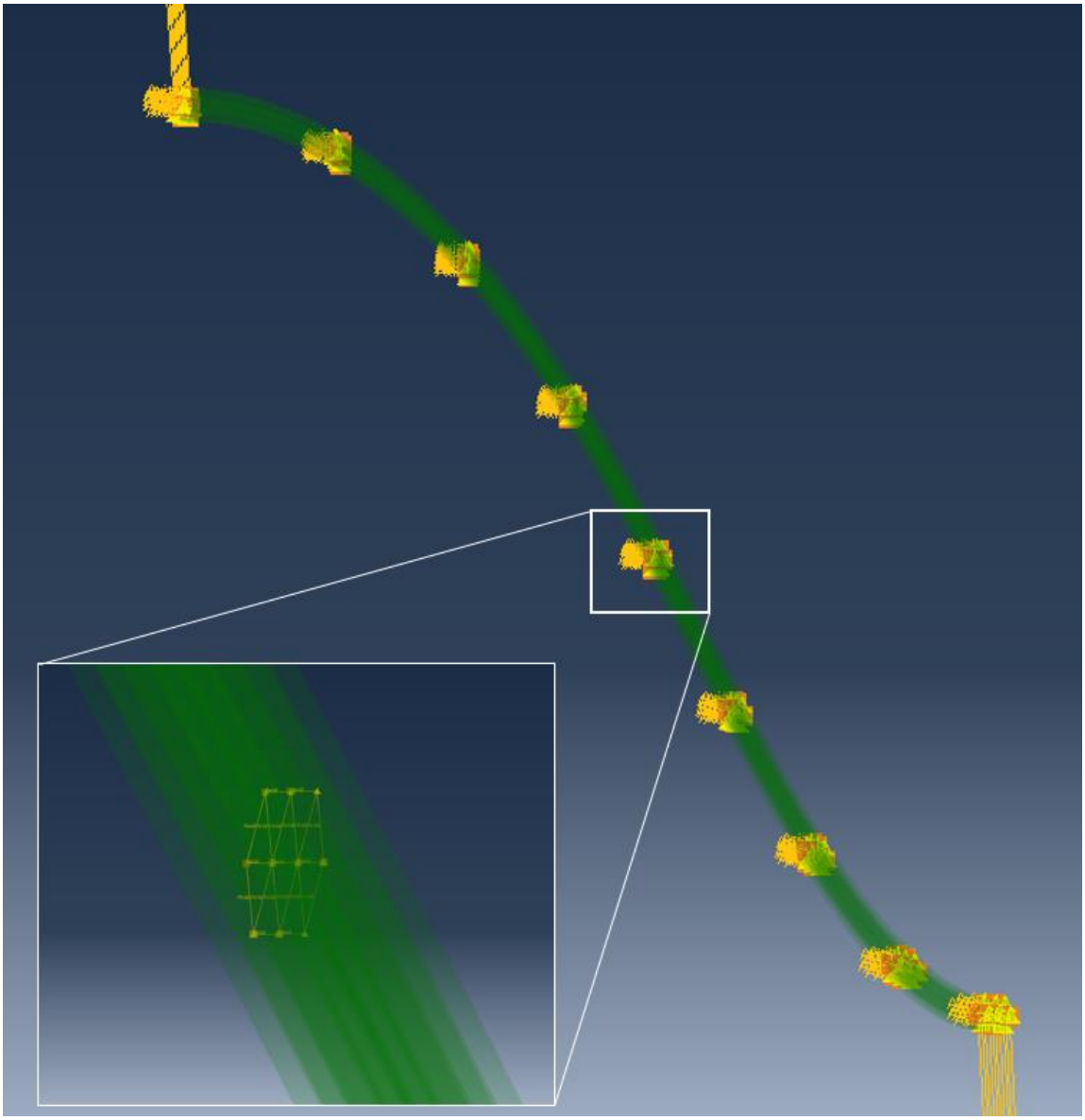

Figure 38 - Quarter ring bundle model pulled into a high saddle shape during a validation test. Turns are shown with translucency. The non-perpendicular connector elements are due to turns moving longitudinally (relative to each other) and overlapping somewhat

where *C* was introduced as a coefficient to probe the effect of changing the relative stiffness. The initial stiffness, when *C*=1.0, refers to 2.5N/mm on an experimental ring (approximately the OLB30 R1) which was used to probe the stiffness at which bundles are held in their cross-section geometric arrangement without splaying apart when contacting a vessel model (as per methodology described which will be described in section 4.4). This was used as an arbitrary point from which to probe the sensitivity of delta strain to connector stiffness as described below.

The connector stiffness coefficient, *C*, was probed over a range: from a low value at which the turns of the bundle splay apart excessively, to a high value at which they are held at the 'reference length' firmly. Referring to Figure 39, it was found that the stiffness did not have a considerable effect on the resulting delta-strain except over a small range of values, peaking at *C*=0.1, at which the delta-strain results were artificially raised due to some adjacent turns rolling or pivoting about each other, in a manner judged to be unrealistic. This motion is depicted for one turn in particular in the red bordered inset of Figure 39. The same relative motion was observed on other rings tested with the same relative connector stiffness.

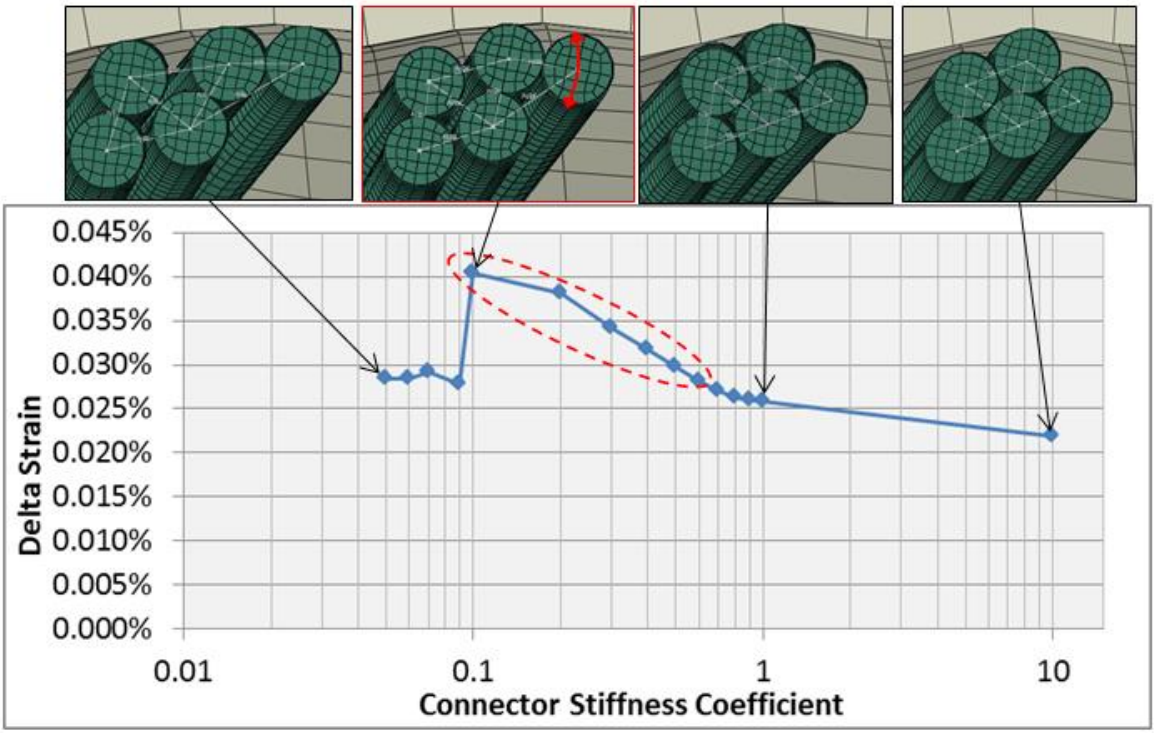

Figure 39 - Investigating the sensitivity of delta-strain to connector stiffness. The relatively elevated results were due to a turn having exaggerated movement, pivoting relative to adjacent turns. This was not observed at lower or higher connection stiffness.

The values probed below *C*=0.1 were ruled out because the bundles are not held together tightly as is observed in reality. The coefficient was chosen to be kept as 1.0, which is high enough to stop the artificial relative motion and is conservative considering that raising the stiffness reduces delta strain results slightly.

4.2.7.5 Additional Turn to Turn Interaction

It was found that during simulation of full compaction some ring models had turns which were tangled within the bundle and on release from compaction they would exist in an artificially twisted position, penetrating other turns completely. A 'soft contact' interaction was created to restrict adjacent turns from being able to fully penetrate each other in the highly deformed compacted state. A 'tabular' pressure-overclosure relation was specified to have zero pressure until an overclosure of 5% of the wire diameter, increasing to a pressure of 10N/mm^2 at an overclosure of half the wire diameter. To aid stability, an arbitrary tangential resistance of 0.1 friction coefficient was assumed. This soft contact definition was found sufficient to stop wires completely passing through each other during compaction, for a range of ring configurations. The interaction is deactivated once the deployment into an artery is achieved to avoid any potential effects on results.

4.2.8 A Method to Estimate Bundle Diameter

A method to approximate the bundle diameter is required to calculate the mean flat ring diameter of a ring-stent, given the manufactured inner diameter; which is what the rings are specified to for production. The mean ring diameter information has been applied, for example, as follows:

- To single turn FE models to represent a turn in the centre of the bundle
- As the datum point from which to configure the bundle in as circular an arrangement as possible (see 4.2.7.2)
- To calculate a 'ring strength coefficient' as will be described in 5.4.2.1.
- In geometric compaction calculations which will be described in Chapter 8

Coefficients from 'Circle Packing Theory' have been used to approximate the bundle diameters, based on assuming the bundles of strands arrange in as circular a fashion as possible. 'Circle Packing Theory' is a branch of maths which deals with optimally arranging a maximum number of circles in various shapes. The detailed 'optimal arrangements' are

not important here, but the data from 'circles in circles' analysis can be used as a valid estimate of bundle diameter.

Bundle diameter, D_{bundle} can be calculated given the number of turns, n and the wire diameter d_{wire} reference of a circle-packing coefficient, c which simply represents the ratio of bundle diameter to wire diameter ($c = D_{bundle} / d_{wire}$,) - see Figure 40.

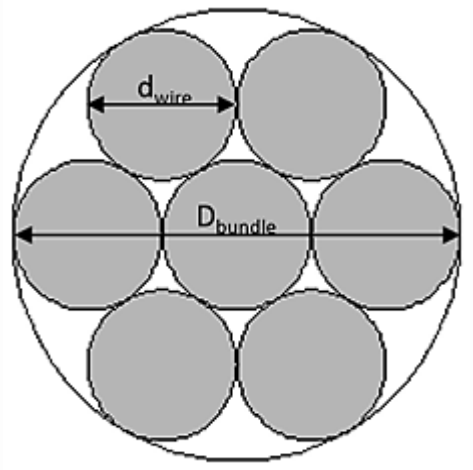

$c = D_{bundle} / d_{wire}$

Figure 40 – Circle packing theory provides coefficients which have been used to estimate the bundle diameter, given the number for turns and wire diameter. (Un-annotated image from Graham *et al*. [93])

The coefficient values up to *n=40* have been extracted from the work of Graham *et al*. [93], which is the most thorough summary publication found on the matter. There are also a number of preceding publications [94]–[96] which contributed to the data presented by Graham *et al* [93]. The values of *c* are not tabulated by Graham *et al*., however they are easily calculated from an alternative optimisation parameter, using an equation provided in the paper. The packing arrangements and respective coefficients are shown in Figure 41 for integer values up to *n*=20.

As an example, to calculate the bundle diameter of 12 turns of 0.22mm wire, the coefficient *c*=4.030 is relevant, and the bundle diameter would be calculated to be 0.89mm (4.030 × 0.22mm).

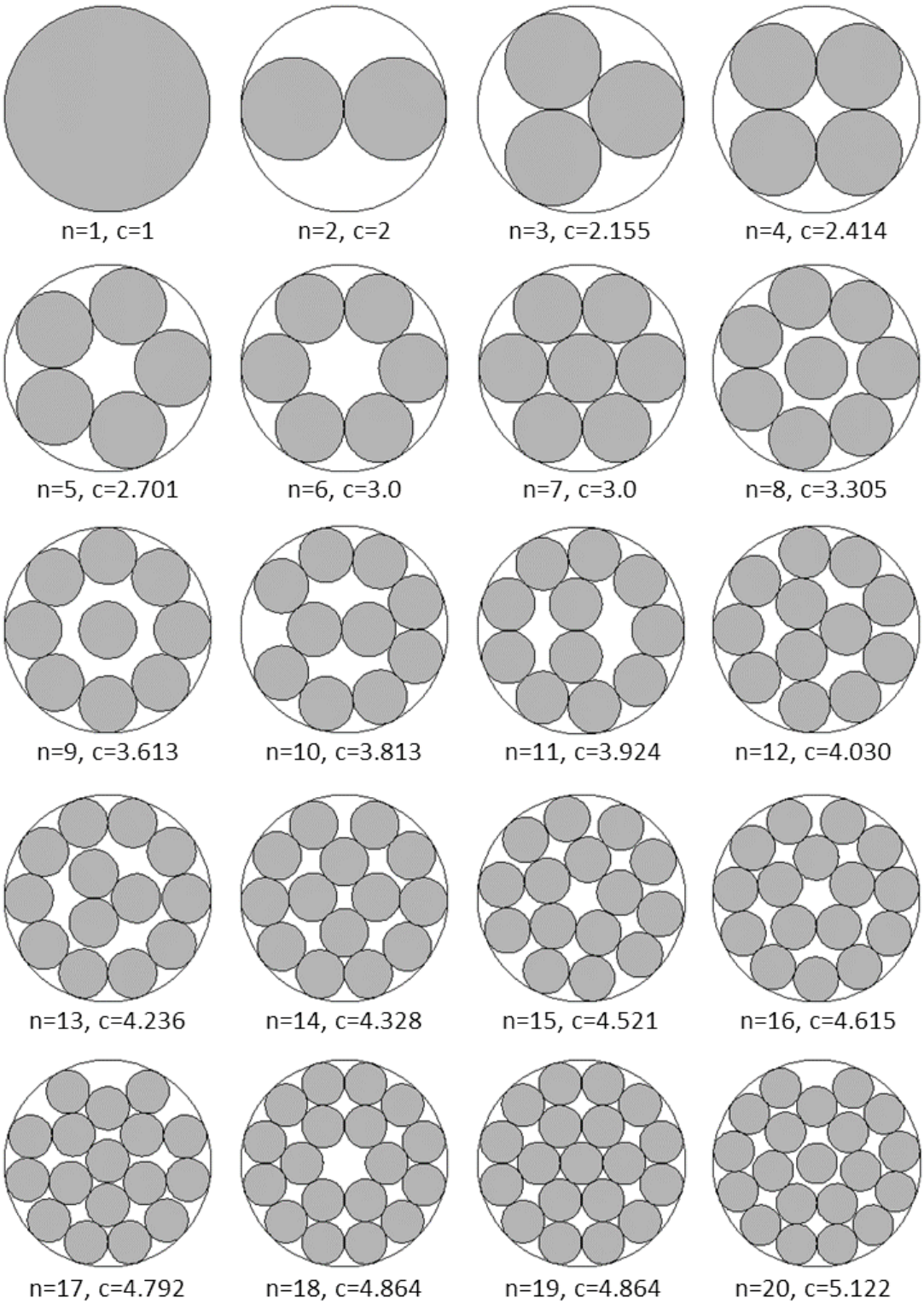

Figure 41 - Circle packing theory optimal arrangements for up to n=20, with respective coefficients for the ratio of bundle diameter to wire diameter. (Images from Graham *et al*. [93])

4.2.9 Summary of Ring Modelling Methodology

A single-turn modelling approach has been adopted and advanced, and will be used in Chapter 5, with the methods of applying a uniform radial force as well as the ART user subroutine, to investigate the load-deflection response and strain state of a Nitinol ring acting as a radial spring. Analysis using single-turn simulations are also implemented for Chapters 6 & 8: on ring fatigue test analysis and compaction strain analysis respectively. The full bundle modelling method does not account for contact between wires, but implements a simplified interaction with connector elements. This is a bespoke solution which captures the geometry of the bundle as well as the mechanical stiffness of a full ring. The accuracy of the structural representation is assessed in 4.5.

4.3 Artery Model Implementation

The aim of the work herein is to produce a representative and effective method to simulate the basic mechanical response of healthy aortic tissue, as opposed to diseased tissue.

Human artery is a complex bio-mechanical construct, primarily composed of three layers each containing different proportions of vascular smooth muscle, elastin and collagen fibres as discussed in 2.4.

The literature studies on mathematically capturing the mechanics of human aorta were discussed in detail section 2.4, but will be briefly revisited here, from a perspective of availability of use within *Abaqus*. The elastic response of human aorta is known to generally increase in stiffness with pressure, as well as significantly reduce in elasticity with age [45]–[48]. Section 2.4 also covered the numerous studies aimed at capturing the stiffening 'pressure-diameter' behaviour from cadaveric samples [42], [43], [45]–[47], the use of ultrasound to assess the compliance within living patients [48]–[50] and the more recent work at the *Institute of Biomechanics*, *Technische Universität Graz* (Austria) which is headed by Gerhard A. Holzapfel [52]. Holzapfel has worked with Raymond Ogden of *Glasgow University*, who has an extensive publication history in the field of modelling the non-linear response of elastomers and rubbers [53], [54] as well as biomechanics. Both Ogden and Holzapfel have their names associated with 'hyperelastic' constitutive material models available within *Abaqus* software. The former being a more generic isotropic hyperelastic model capable of curve-fitting various non-linear elastomer-like responses,

while the 'Holzapfel' model in *Abaqus* is specifically designed to represent arterial tissue at a more detailed level (See papers [55], [56]).

The experimental work on tissue carried out by the Holzapfel group aims to capture the detailed mechanical behaviour through bi-axial testing and histological examination of the anisotropic tissue composition [60], [61]. The most comprehensive data set of constitutive model parameters provided by the Holzapfel group, for abdominal and thoracic aorta, is from testing of 16 cadaveric samples in 2012 [63]. However, the range of values provided for certain parameters have very high variation, making it impossible to determine a representative model with statistical confidence.

Prior to the 'Holzapfel model' and also available within *Abaqus* is the 'Generalised Fung type' hyperelastic model based on the two-dimensional strain energy function provided by Fung et al [74], and 'generalised' to arbitrary three dimensional states from the proposal of Humphrey [75]. Other notable mathematical models providing hyperelastic strain energy function for representing arterial tissue are that proposed by Raghavan & Vorp in 2000 [76], and Vande Geest et al in 2006 [77]. The latter also provides significant bi-axial testing data, and parameters to fit the provided equations, from 26 abdominal aortic aneurysms plus 8 non-aneurysmal tissue samples. However, these channels of work are more focused on providing models to simulate the aneurysmal mechanical response, which is not within the scope of the work described here.

Although there are the mentioned dedicated constitutive models for mathematically representing artery tissue, the data required to inform the choice of parameters for the models is not substantial enough to be able to determine representative models for specific age groups. Therefore, a simpler method is proposed here in which the more basic 'pressure-diameter' response from the characterisation work of Langewouters [47] is modelled. The Langewouters' paper provides the most extensive dataset for this purpose (45 thoracic and 20 abdominal samples) found, and a proposed 2-parameter mathematical expression which can be used to create age-representative curves.

4.3.1 The Langewouters' Equation

The aortic characterisation work of Langewouters *et al*. [47] has been selected as the most appropriate data from which to develop an isotropic artery material model due to its adequacy in terms of: sample size; age range; availability of raw data in the publication; and

the fact that all of the data has been correlated to a mathematical expression which can be easily adopted.

The work of Langewouters involves pressure-diameter testing of human aorta segments stretched longitudinally to a level of pre-strain measured *in-situ* (at autopsy). Measurements were taken from zero pressure to 180mmHg, at 20mmHg intervals. It was stated that all of the sample measurements can be mathematically described by the following formula to an accuracy value of >99% (based on the coefficient of determination, r^2 being >0.991 when comparing with linear regression of the calculated maximal area to the measured maximal area).

$$A(p) = A_m(\frac{1}{2} + \tan^{-1}(\frac{(p - p_0)p_1}{\pi})) \qquad \textbf{(Eq. 4.14)}$$

where *A(p)*, the cross-sectional area of the artery is a function of pressure, *p* in mmHg. Parameter A_m is the theoretical 'maximal area' of the artery lumen cross-section which *A(p)* tends towards with increasing pressure, *p*. Parameters p_0 and p_1 are pressure unit constants which are calculated specifically for each sample tested.

Parameter p_0 is described as the pressure at which artery compliance is maximal, however for many test results in the Langewouter paper the value is mathematically determined to be beyond the pressure range tested. Parameter p_1 is related to the 'steepness of rise of the curve', or can be described as the difference in pressure (from p_0) at which the compliance has reduced to half its maximum value.

The p_0 and p_1 are the only parameters required to define a curve of pressure against diameter change for each case, as will be described in the following. Assessing the trend of p_0 and p_1 against the age of samples allows an averagely representative pressure-diameter curve to be produced for any specific age. The values reported in the paper of p_0 and p_1 and age are provided in Appendix E for both abdominal and thoracic cases.

The following is a mathematical explanation of how a pressure vs. diameter change curve can be determined using only p_0 and p_1. The diameter change will be provided in terms of percentage increase in diameter, $d_{\%increase}$.

First, (Eq. 4.14) is arranged as a ratio of Area, *A(p)* to Maximal Area, A_m:

$$\frac{A(p)}{A_m} = (\frac{1}{2} + \tan^{-1}(\frac{(p - p_0)p_1}{\pi})) \quad \textbf{(Eq. 4.15)}$$

Area, *A(p)* and Maximal Area, A_m relate to diameter, *d(p)* and maximal diameter d_m as per (Eq. 4.16) and (Eq. 4.17):

$$A(p) = \frac{\pi[d(p)]^2}{4} \quad \textbf{(Eq. 4.16)}$$

$$A_m = \frac{\pi {d_m}^2}{4} \quad \textbf{(Eq. 4.17)}$$

where *d(p)* and d_m are 'diameter (as a function of *p*)' and 'maximal diameter' respectively

Rearranging (Eq. 4.16) and (Eq. 4.17):

$$\frac{d(p)}{d_m} = \sqrt{\frac{A(p)}{A_m}} \quad \textbf{(Eq. 4.18)}$$

Therefore:

$$\frac{d(p)}{d_m} = \sqrt{(\frac{1}{2} + \tan^{-1}(\frac{(p - p_0)p_1}{\pi}))} \quad \textbf{(Eq. 4.19)}$$

When *p* = 0mmHg the ratio of unpressurised vessel diameter to maximal pressure diameter is given by:

$$\frac{d(0)}{d_m} = \sqrt{(\frac{1}{2} + \tan^{-1}(\frac{(-p_0)p_1}{\pi}))} \quad \textbf{(Eq. 4.20)}$$

In order to define the vessel response in terms of the percentage increase ($d_{\%increase}$) relative to the zero pressure state, then for some pressure, *p*:

$$d_{\%increase}(p) = \frac{d(p) - d(0)}{d(0)} \times 100\% \quad \textbf{(Eq. 4.21)}$$

Therefore:

$$d_{\%increase}(p) = \frac{\frac{d(p)}{d_m} - \frac{d(0)}{d_m}}{\frac{d(0)}{d_m}} \times 100\% \quad \textbf{(Eq. 4.22)}$$

This allows (Eq. 4.19) and (Eq. 4.20) to be used to relate $d_{\%increase}$ to pressure, given the two constants p_0 and p_1:

$$d_{\%increase}(p) = \frac{\sqrt{\left(\frac{1}{2} + \tan^{-1}\left(\frac{(p - p_0)p_1}{\pi}\right)\right)} - \sqrt{\left(\frac{1}{2} + \tan^{-1}\left(\frac{(-p_0)p_1}{\pi}\right)\right)}}{\sqrt{\left(\frac{1}{2} + \tan^{-1}\left(\frac{(-p_0)p_1}{\pi}\right)\right)}} \times 100\% \quad \textbf{(Eq. 4.23)}$$

4.3.2 Abdominal Aortic Data

Taking the values of p_0 and p_1 derived for each abdominal sample during the work of Langewouters (provided in Appendix E) and implementing (Eq. 4.23) results in the pressure-diameter relationships plotted in Figure 42 (age indicated by colour assignment). The general trend of stiffening with age can be appreciated, however the natural scatter of this relationship is also evident (for example the oldest sample is not the most rigid, but third most). It is also observed that samples which have very similar overall deformation values (at 200mmHg) can have variation in linearity.

The definition of each unique curve in Figure 42 is purely dependent on the parameters p_0 and p_1. The spread of these parameters as well as correlation with age can be assessed in order to define most representative, or worst-case curves for a specific age value of

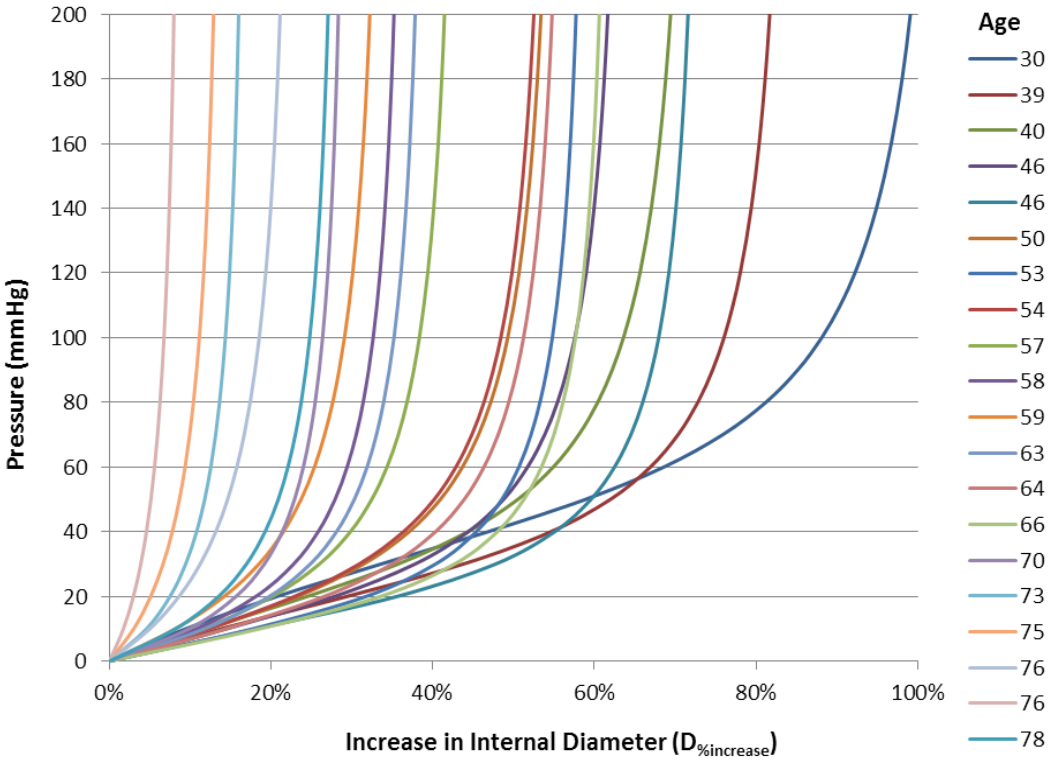

Figure 42 - Pressure-Diameter relationships of individual abdominal aortic samples from Langewouters, using the specific parameters for each case with the mathematical relation presented in the paper.

interest. All values of p_0 and p_1 have been plotted in Figure 43 for the abdominal cases. There is a clear trend of p_0 decreasing with age, therefore the equation of the linear approximation shown in Figure 43 has been used to define the most representative p_0 value for any given age. No trend appears to exist for p_1 values relative to age. Excluding the youngest age point of 30 (because it is much lower than the age range considered for endovascular treatment of abdominal aneurysms) p_1 values range from 20mmHg to 34mmHg, with a mean of 26.3mmHg.

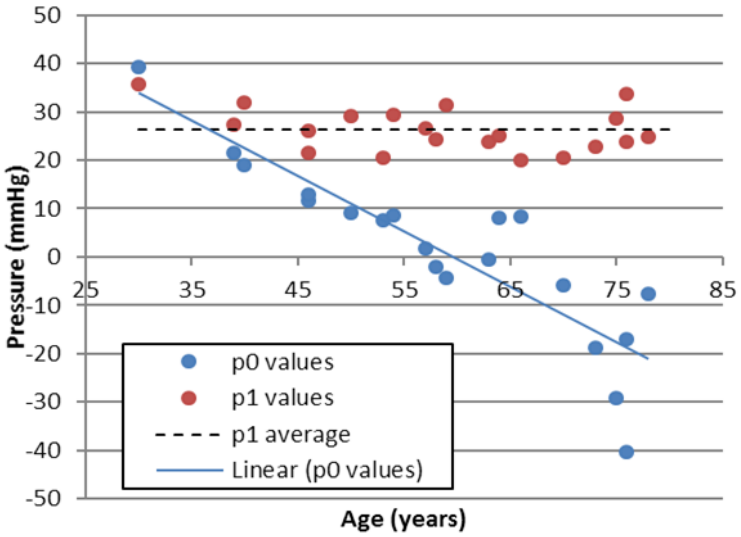

Figure 43 - The Langewouters parameters of p0 and p1 from abdominal cases, plotted against age.

Age-independent variability has been removed by assuming the linear approximation for p_0 values plus for p_1 either:

1) a mean value of 26.3mmHg for p_1, or;
2) a worst-case value chosen to be 35mmHg

According to the relevant post-market registry [97], the average age of patients treated with the *Anaconda* device is 76 years, with a standard deviation of 8 years. The resulting 'age representative' curves for 76, 68, 60 and 52 years have been plotted in Figure 44 representing a range from average (76 years) to -3 standard deviations (52 years). The consistent and most significant effect of raising p_1 to a worst-case value is the increased linearity of the overall curve, which leads to greater diametric strain over typical diastolic-systolic blood pressure ranges. This is reflected in the diametric strain results shown in

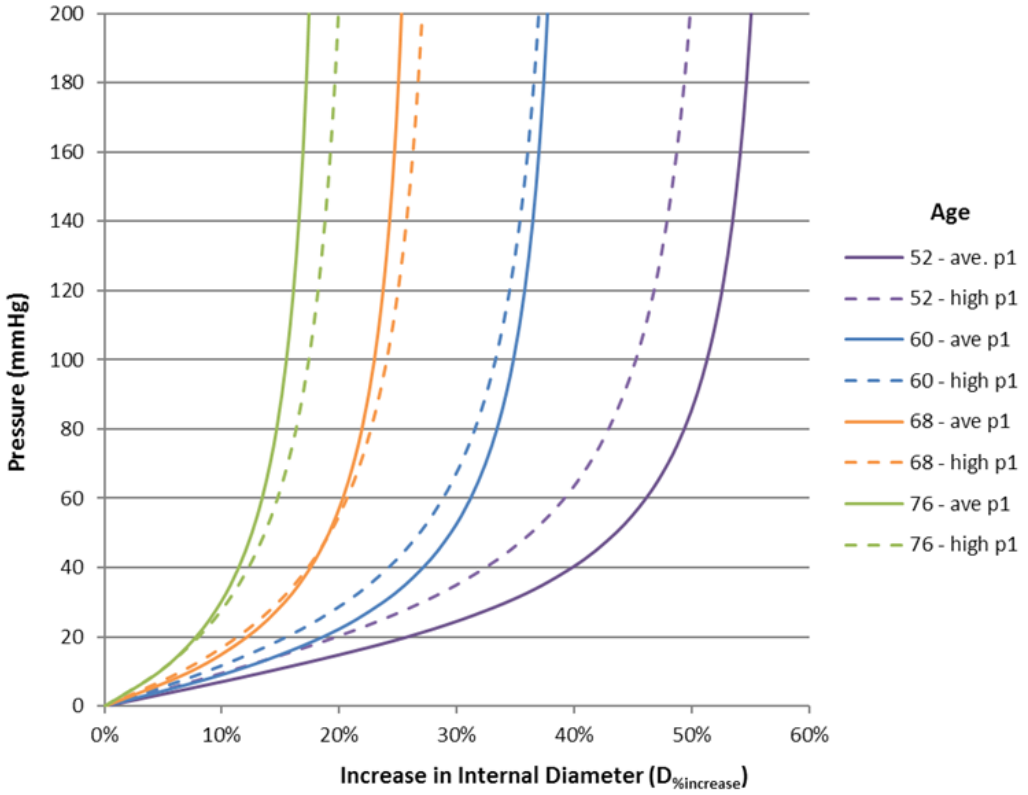

Figure 44 - Age representative 'Pressure-Diameter Change' curves produced from Langewouters' data for the Abdominal Aorta using a linear correlation for p0 parameter and either an average (solid lines) or worst case (dashed lines) for p1 parameter.

Table 6 for two hypothetical cases: a 'healthy' blood pressure range of 80-120mmHg and a hypertensive blood pressure range of 80-160mmHg.

Assuming the higher value for p_1 parameter causes an increase in diametric strain of 31%±2% for all the age and pressure scenarios outlined in Table 6.

Table 6 – Calculated abdominal aortic diametric strains for Langewouters' based 'Pressure-Diameter Change' curves, assuming example blood pressure ranges of 80-120mmHg and 80-160mmHg

Age	Vessel Diametric Strain for 80-120mmHg		Vessel Diametric Strain for 80-160mmHg	
	Assuming average p_1 value	Assuming high p_1 value	Assuming average p_1 value	Assuming high p_1 value
52	2.16%	2.79%	3.20%	4.18%
60	1.77%	2.31%	2.68%	3.52%
68	1.48%	1.94%	2.28%	3.00%
76	1.26%	1.65%	1.98%	2.59%

4.3.3 Thoracic Aortic Data

Repeating the above process for the thoracic data provided in the Langewouters paper, the values of p_0 and p_1 are plotted in Figure 45. The magnitudes of both parameters are shown to decrease with age for the thoracic data. Therefore, the linear approximations of these trends (shown in Figure 45) have been assumed for extracting age specific values to construct the 'age representative' pressure vs diameter-change curves.

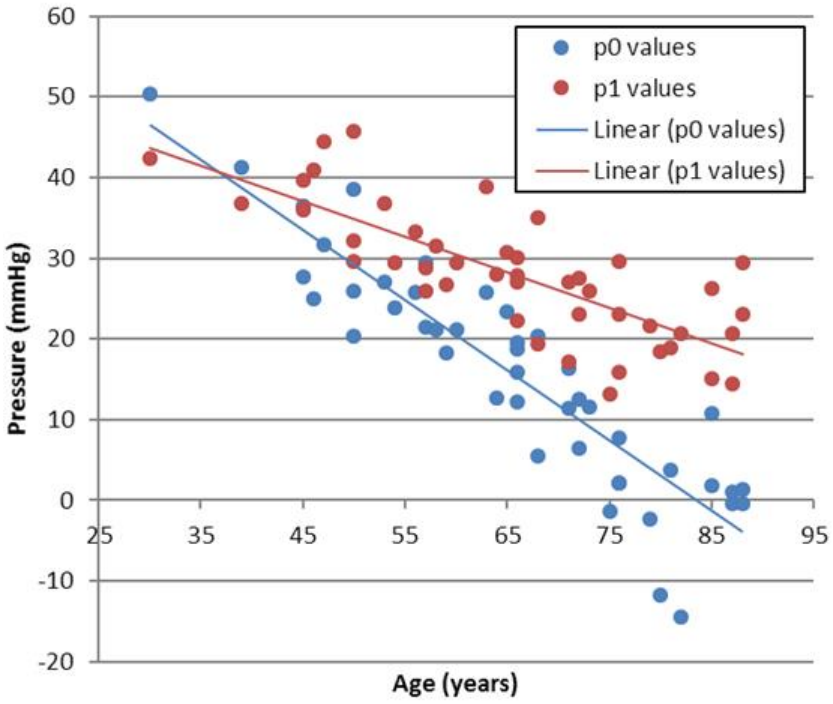

Figure 45 - The Langewouters parameters of p0 and p1 from thoracic cases, plotted against age.

The resulting 'age representative' curves for ages 30 through 80 years (increments of 10 years) are plotted in Figure 46. This larger age range represents the relatively broad demographics of patients implanted with *Vascutek's Thoraflex Hybrid* device: mean age of 61 years with a standard deviation of 12 years (from 152 patients in the study)[98].

The extracted vessel diametric strain values from curves in Figure 46 are shown in Table 7 for the hypothetical healthy and hypertensive blood pressure ranges of 80-120mmHg and 80-160mmHg.

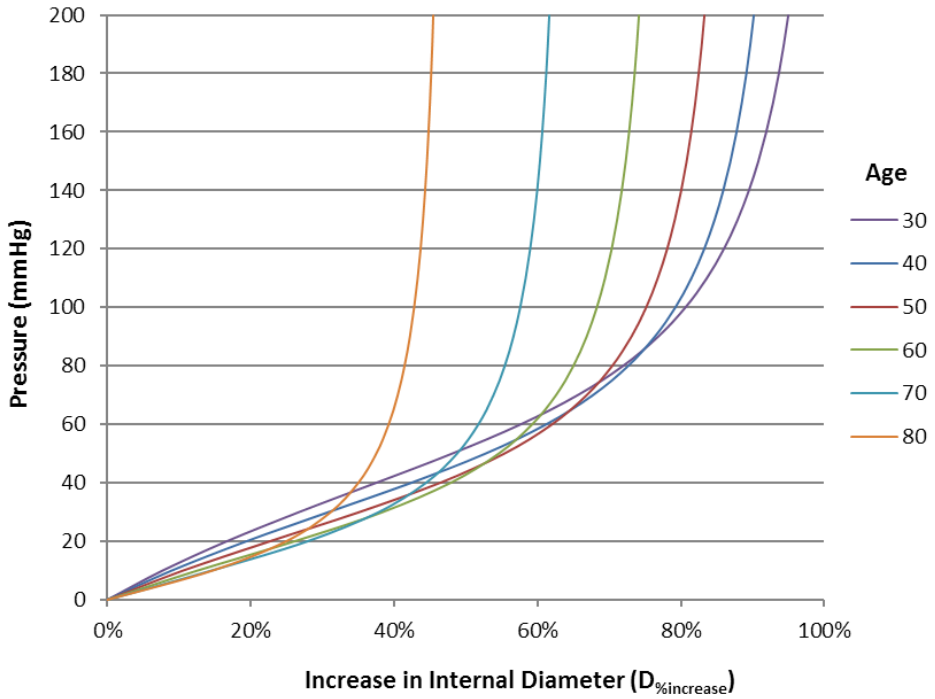

Figure 46 - Age representative 'Pressure-Diameter Change' curves produced from Langewouters' data for the Thoracic Aorta using a linear correlation for p0 and p1 parameters.

Table 7 - Calculated thoracic aortic diametric strains for Langewouters' based 'Pressure-Diameter Change' curves, assuming example blood pressure ranges of 80-120mmHg and 80-160mmHg

Age	Vessel Diametric Strain for 80-120mmHg	Vessel Diametric Strain for 80-160mmHg
30	8.21%	11.65%
40	6.15%	8.77%
50	4.50%	6.48%
60	3.24%	4.71%
70	2.28%	3.37%
80	1.58%	2.37%

4.3.4 Modelling the 'Pressure-Diameter' Curves

To simulate the aorta's non-linear response to pressure which has been defined above, 'hyperelastic' material models have been utilised: converting the 'pressure-diameter' behaviour to the fundamental uni-axial stress-strain material response. A single layer isotropic material has therefore been assumed with an objective of simply capturing the global arterial pressure-diameter curve.

4.3.4.1 Choice of Hyperelastic Model

Hyperelastic material models are designed to provide the ability to simulate rubber-like materials which have non-linear elastic properties over a large strain range. These models use 'strain energy potentials' rather than Young's modulus and Poisson's ratio to relate stress to strain. Of the various 'strain energy potentials' available within *Abaqus*, the *Marlow* model [99] was used because it is recommended for cases in which only one set of test data, such as uni-axial, can be provided. The *Marlow* strain energy per unit volume is split into a 'deviatoric' part and a volumetric part. The former must be defined by uni-axial, or biaxial data and the latter using volumetric test data or simply a Poisson's ratio value if compressibility is deemed to be significant.

The 'deviatoric' part of the *Marlow* model will be defined using stress and strain points of the incrementally increasing modulus, derived from the pressure vs diameter-change curves, of abdominal aorta, which have been produced in section 4.3.2.

4.3.4.2 Defining the Uni-Axial Data

The 'Pressure-Diameter' responses defined in 4.3.2 are here related to the material stress-strain state through thin walled cylinder mechanical theory. Stress-strain transformation equations analogous to those describing planar behaviour are assumed for the circumferential and longitudinal cylindrical directions.

Thin walled cylinder theory is proven to be accurate for vessels with a wall thickness less than $1/10^{th}$ of the vessel radius [100], beyond this, accuracy depreciates. In the current application the vessel wall thickness implemented is slightly thicker than $1/10^{th}$ (see below 1.4mm for 12mm radius), however this is not of concern because the equations are only used as a method to develop a structural response which is ultimately verified for accuracy at the end of the process anyway. To allow the use of the same material model across various vessel sizes, a constant 'wall thickness' to 'inner vessel diameter' ratio was assumed for all abdominal aortic models. The average vessel thickness found by measurement of cadaveric tissue samples by Schriefl et al was 1.39mm [61] for both Abdominal and Thoracic. (Other studies have returned similar results with average thicknesses ranging from 1.25mm to 1.63mm [60], [101], [102]). The abdominal ratio was based on assuming an initial average vessel thickness of 1.4mm (rounded from Schriefl et al [61]) to a vessel with inner diameter of 24mm at 100mmHg which is approximately mid—range of treatable aortic 'landing-zone' diameters for the *Anaconda ONE-LOK* device (the recommended range

being 17.5 - 31.0mm according to the sizing chart (Appendix A)). This ratio (1.4:24) is maintained for models by varying the wall thickness dependent on the specified inner vessel diameter at 100mmHg (assumed to be mid systolic-diastolic pressure). The vessel thickness, and therefore choice of discussed ratio, was proven through a sensitivity study to not affect the final strain amplitude results of the ring-artery simulations and is therefore relatively arbitrary. Using this approach, the initial diameter *d(0)* of the vessel must be calculated by first gaining the theoretical maximal diameter d_m: by rearranging (Eq. 4.19) and entering d(100) = 24mm:

$$d_m = {d(100)} \Big/ \sqrt{\frac{1}{2} + \frac{1}{\pi}\tan^{-1}\left(\frac{p - p_0}{p_1}\right)} \qquad \textbf{(Eq. 4.24)}$$

Subsequently the initial diameter, *d(0)* can be calculated through (Eq. 4.20).

While *in vivo* human aorta is under some longitudinal strain [60], the relevant influence of this is highly dependent on the anisotropic mechanical characteristics of the tissue. Since this is not being modelled (isotropy assumed), it is unnecessary to axially 'pre-strain' the artery. However, it was deemed that fixing the axial displacement of the vessel model ends is more realistic than allowing contraction due to Poisson's ratio upon pressurisation. In the literature, it is widely assumed that arterial tissue is nearly incompressible [56], [103]. However, on applying a nearly incompressible material (Poisson's ratio near 0.5) in the method described here, modelling stability issues were experienced. Considering that the key aim of this isotropic implementation was to purely replicate the pressure-diameter curve, an arbitrary Poisson's ratio of 0.3 was applied to the method described in the following. It was also found that using such a ratio resulted in a closer match of pressure-diameter, than compared to using a near incompressible case.

Stress-strain transformation equations for planar bi-axial loading (i.e. in *x* and *y* Cartesian directions) can be applied analogously to the circumferential and axial directions of thin walled cylindrical vessels, loaded with uniform internal pressure, such that for the case of axial strain being zero, the modulus, *E* can be shown to be:

$$E = \frac{\sigma_{circ}}{\varepsilon_{circ}}(1 - \nu^2) \qquad \textbf{(Eq. 4.25)}$$

where σ_{circ} and ε_{circ} are the stress and strain in the circumferential direction respectively.

For Hyperelastic materials the uni-axial data must be entered in *Abaqus* in nominal stress and nominal strain form, as opposed to true stress and strain. The nominal stress in the circumferential direction, σ_{circ} of a thin walled cylinder of wall thickness t and inner diameter *d,* due to internal pressure *p,* is given by:

$$\sigma_{circ}(p) = \frac{p \times d(p)}{2t} \quad \textbf{(Eq. 4.26)}$$

Nominal circumferential stress values have been calculated at increments of 10mmHg (1.333×10^{-3} MPa) in pressure, assuming the initial thickness value of t=1.4mm. The varying value of inner diameter, d must be taken account of here, even for nominal stress, because the circumferential load increases due to the pressure acting on an increasing internal area. Therefore; at each pressure increment the inner diameter, d is calculated using (Eq. 4.27) (where $d_{\%increase}$ was derived in (Eq. 4.23) in section 4.3.1:

$$d(p) = d(0) \times (1 + d_{\%increase}(p)) \quad \textbf{(Eq. 4.27)}$$

The strain in the circumferential direction of a thin walled cylinder is assumed equal to the percentage change in the mid-plane diameter (between inner and outer diameter) of the vessel. While the pressure-diameter curves are describing the change in inner diameter of the vessel, the mid-plane diameter has been calculated at each pressure increment by adding the wall thickness to the inner diameter. The change in thickness due to Poisson's effect for the case that the vessel ends are fixed can be shown, through transformation equations, to be:

$$t(p) = t_0 - \left(\frac{\nu \times d_{\%increase}(p) \times (1-\nu)}{(1-\nu^2)}\right) \quad \textbf{(Eq. 4.28)}$$

Where t_0 is the initial thickness and ν is Poisson's ratio. The mid-plane diameter can therefore be calculated for any pressure:

$$d_{mid-plane}(p) = d(p) + t(p) \quad \textbf{(Eq. 4.29)}$$

Subsequently the circumferential strain as calculated from the mid-plane diameter is provided by:

$$\varepsilon_{circ}(p) = \frac{d_{mid-plane}(p) - d_{mid-plane}(0)}{d_{mid-plane}(0)} \quad \textbf{(Eq. 4.30)}$$

The nominal stress and strain in the circumferential direction are therefore obtainable using (Eq. 4.26) and (Eq. 4.30) respectively. Now; referring to (Eq. 4.25), rather than defining the Hyperelastic Marlow model with nominal stress and strain points from a uniaxial scenario, the points have been input as σ_{circ} and $\varepsilon_{circ}/(1-\nu^2)$ which are a ratio equal to Young's modulus, *E*.

This method has been used to define the material for multiple artery pressure-diameter curves, for example those shown in Figure 44. Every curve has been defined at increments of 10mmHg up to a pressure of 250mmHg, after which the Marlow model assumes a linear response equal to that of the last portion of the curve defined (240-250mmHg). This was considered a conservative method, from a fatigue point of view, as the alternative of using the Langewouters' equation to define the pressure-diameter curve at higher pressures (beyond those tested) results in continuously increasing artery stiffness.

The abdominal aorta is the focus of the current work, with the multiple age-representative samples modelled, calibrated and verified in section 4.3.4.3.

4.3.4.3 Application to FE Model with Calibration and Verification

To verify that the method of modelling a specific pressure-diameter curve has acceptable accuracy, simple 10mm length quarter vessel sections were modelled with 20 elements in the axial direction, 50 in the circumferential and 4 through the thickness. The vessel end faces were constrained from motion in the axial direction and the symmetry faces were fixed from motion in their respective normal direction, as depicted in Figure 47.

As discussed in 4.3.4.2, for abdominal aorta, an initial wall thickness of 1.4mm has been assumed for a vessel of 24mm diameter at 100mmHg. The verification model has a thickness of 1.4mm, and the initial diameter (at 0mmHg) was calculated for each curve as described in 4.3.4.2. Stress-strain points defining the *Marlow* Hyperelastic material model were specified as described in 4.3.4.2.

For each abdominal case, an initial model and a calibrated model has been produced. The calibrated model simply has a ratio applied to change the initial internal diameter, such that the target diameter at 100mmHg is matched. The material parameters and the thickness to diameter ratio are kept the same as the initial model so that the percentage change in diameter with pressure increase is not altered.

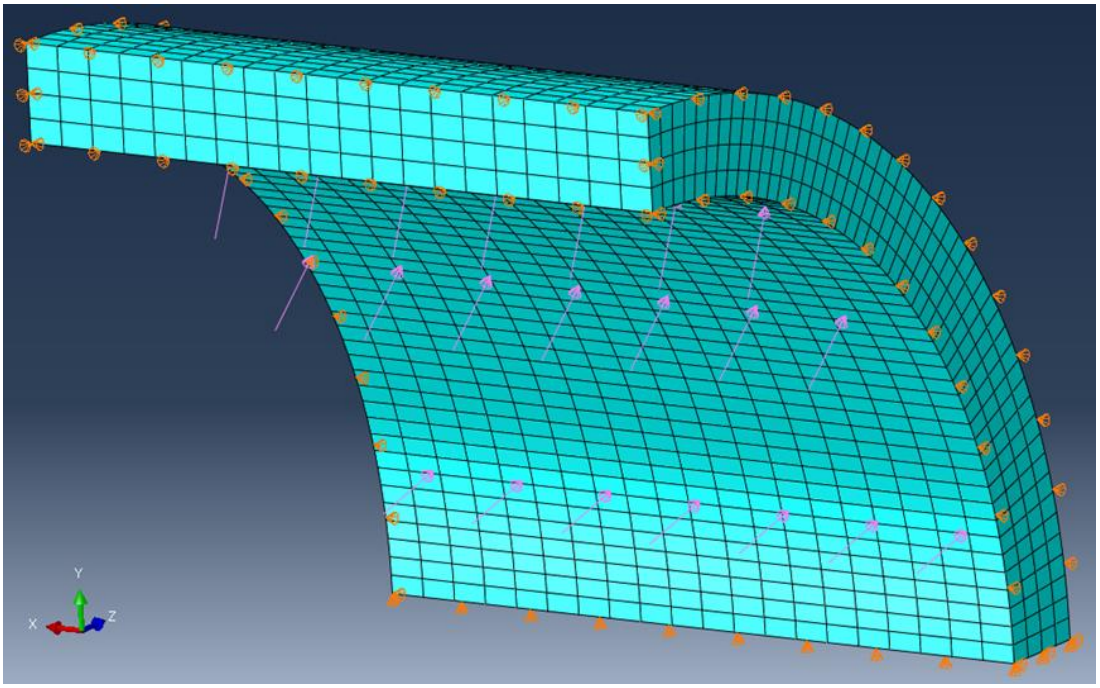

Figure 47 - Simple vessel quarter model used to verify the application of pressure-diameter responses. Boundary conditions and pressure load depicted by the orange and pink arrows respectively.

The target and modelled behaviour in terms of percentage diameter change are plotted in Figure 48. The general shape of the curves match well, with slightly increased strain observed with the FEA modelled cases. The calibrated models are created by reducing the initial internal diameter by a ratio determined by the discrepancy of the initial model

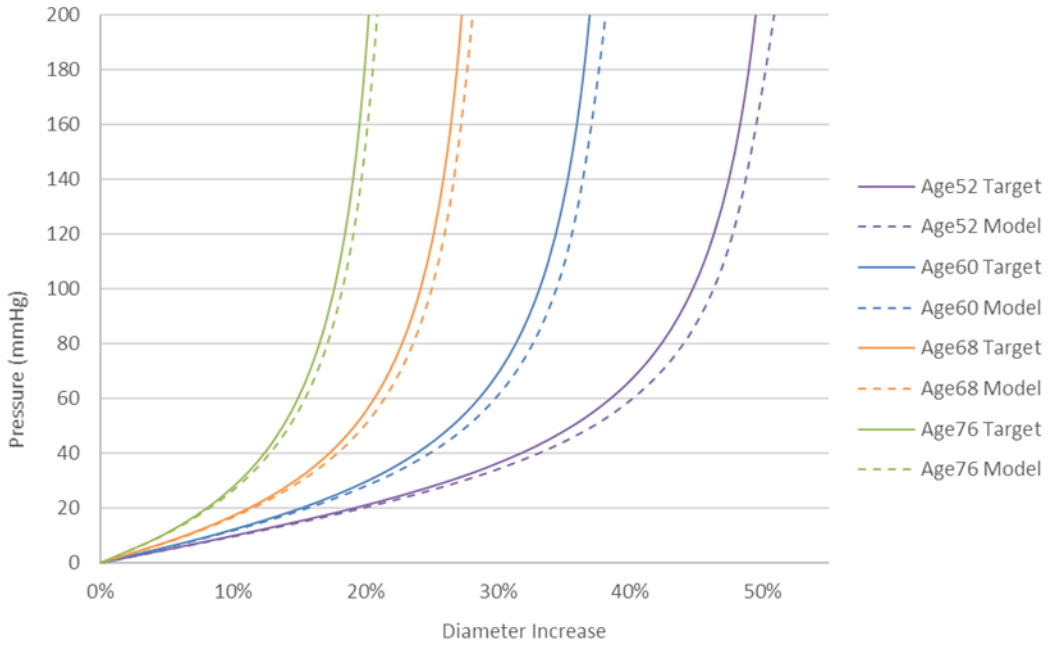

Figure 48 - Comparing the Target Langewouters and Modelled P-D curves for chosen abdominal ages.

diameter at 100mmHg. The result of the calibrated 52-year-old vessel is shown in Figure 49, in terms of actual diameter change, to demonstrate the ability to match diameter at 100mmHg.

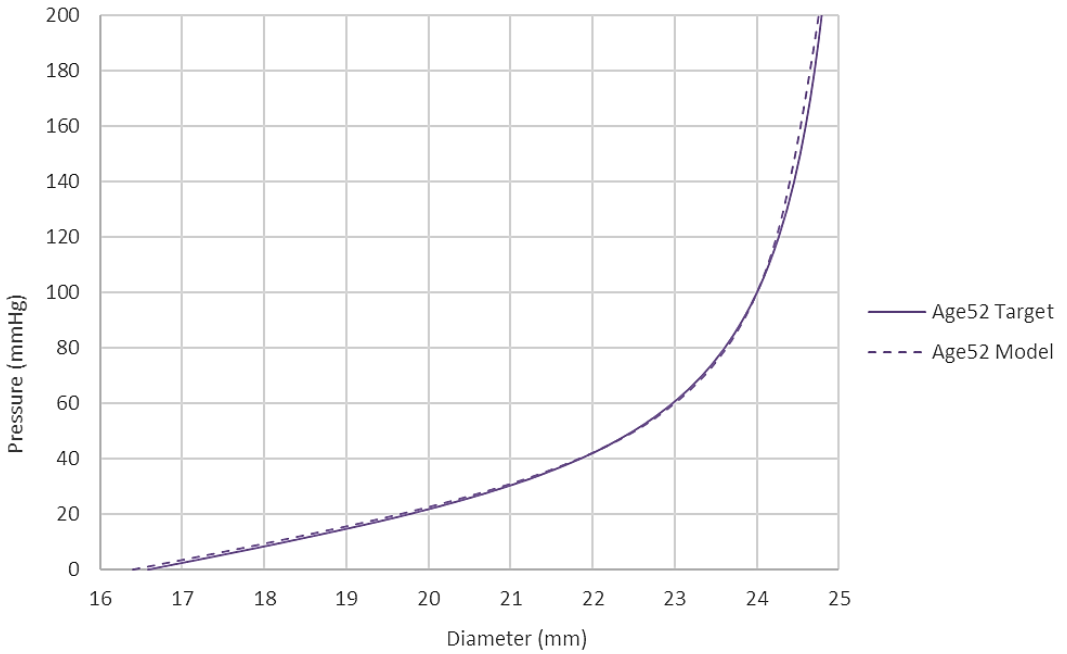

Figure 49 - Target and Modelled Pressure - Diameter curve for the 52 year old abdominal case, with initial diameter corrected to ensure the target diameter at 100mmHg is matched

The accuracy of the calibrated models has been assessed in terms of actual inner diameter as well as the diametric strain over ranges of 80-120mmHg and 80-160mmHg. The inner diameters of the modelled vessels have a worst-case discrepancy of 0.26% which was on the 52-year-old case. This was assessed over the exaggerated operating range of 60-250mmHg. The discrepancy in diametric strain for blood pressure ranges 80-120mmHg and 80-160mmHg are summarised in Table 8, showing the highest error for the 52-year-old case: the model resulting in 2.58% compared to the 2.79% targeted.

The overall characteristic of the pressure diameter curves has been well matched, however the discrepancy in diametric strain over specific ranges will require to be considered if targeting specific vessel motions for ring-in-artery studies. A specific diametric strain can be matched by altering the diastolic-systolic pressure range.

Table 8 - Target and resulting diametric strain values for modelled abdominal vessels over the blood pressure ranges of 80-120mmHg and 80-160mmHg

Age	Vessel Diametric Strain for 80-120mmHg			Vessel Diametric Strain for 80-160mmHg		
	Langewouters derived (assuming high p_1 value)	Model result	**Error**	Langewouters derived (assuming high p_1 value)	Model result	**Error**
52	2.79%	2.58%	**-7.45%**	4.18%	4.07%	**-2.74%**
60	2.31%	2.23%	**-3.61%**	3.52%	3.55%	**0.98%**
68	1.94%	1.93%	**-0.73%**	3.00%	3.13%	**4.19%**
76	1.65%	1.66%	**1.16%**	2.59%	2.77%	**6.67%**

The same method as described above has been demonstrated for the 30-year-old thoracic curve displayed in Figure 46, which results in a maximum error of 0.74% on diameter over the 60-250mmHg range and variance of -5.02% and -3.70% to the diametric strain for 80-120mmHg and 80-160mmHg ranges respectively.

4.3.5 Summary of Artery Model Implementation

A novel method of averaging data from the Langewouters study to create age-averaged Pressure-Diameter curves has been shown for both Abdominal and Thoracic aortic artery. Subsequently these Pressure-Diameter responses have been implemented into a quarter vessel model and verified to have reasonable accuracy. The age specific diametric strain values are an addition to knowledge which is sparse in the literature, and the above provides a comparison between abdominal and thoracic vessel elasticity. The abdominal vessel models will be implemented in Chapter 7.

4.4 Implementing 'Ring in Artery' Simulation

The methodologies developed and described in the sections above for finite element mechanical simulation of a ring-stent (section 4.2) and aortic artery (section 4.3) have been combined such that the interaction of a ring-stent in an artery can be analysed. The simulation steps, boundary conditions and interaction properties implemented to achieve the ring-in-artery simulation are described in this section. Studies on the *Anaconda* proximal rings, using the methodology described here are documented in Chapter 7.

4.4.1 Purpose and Rational

The methodology was developed for two main purposes:

1) Strain based fatigue analysis of the Nitinol ring-stents in the non-linear vessel under pulsatile cardiac pressure loading. This provides a more advanced assessment than using a simple linear elastic vessel with the same diametric strain because the 'damping' effect of the ring's radial force on the overall motion will be included. The resulting ring motion and 'damping' phenomenon can be quantified. It should be noted that the true dynamic motion of the interacting ring and artery due to the haemodynamic blood pressure wave is dependent on: the wave profile of the cardiac cycle; the active viscoelastic response of artery wall, and the inertia associated with the mass of the blood, stent, artery and other perivascular tissue. As these factors cannot be modelled in this level of simulation, attempting a dynamic solution would be irrelevant, and therefore the general-static solver is assumed.
2) The radial force applied by the ring on the vessel will be quantified in terms of total magnitude as well as distribution. This can be carried out at diastolic, systolic or any incremental solution time point at which the simulation successfully solved.

4.4.2 Components of the model

Each ring-in-artery model is generated in *Abaqus CAE* via a *Python* script according to the user specified parameters in the script. The top-level structure of this script is provided in flow-chart form in Appendix F. Each model consists of the ring, a length of vessel, an inner cylinder representing the delivery system central core and a movable quarter cylindrical surface for compacting the ring, as shown in Figure 50. The multi-turn ring is constructed exactly as described in section 4.2.

The artery length modelled is programmed to be 1.9 times the length of the ring diameter. This was justified from a brief study to assess the proximity at which the radial strength of the ring has negligible effect on the dilation of the vessel. A worst-case ring in terms of high relative strength was used for this assessment. The script includes various artery definitions which have been defined from Langewouters' data as described in section 4.3. The meshing approach applies 5 elements through the wall thickness, a concentration centrally with near equilateral cuboids, and longer elements at the vessel ends where ring

interaction will not occur (see Figure 50). All elements in the vessel are specified to be linear with the 'incompatible modes' enhancement which improves prediction of bending behaviour.

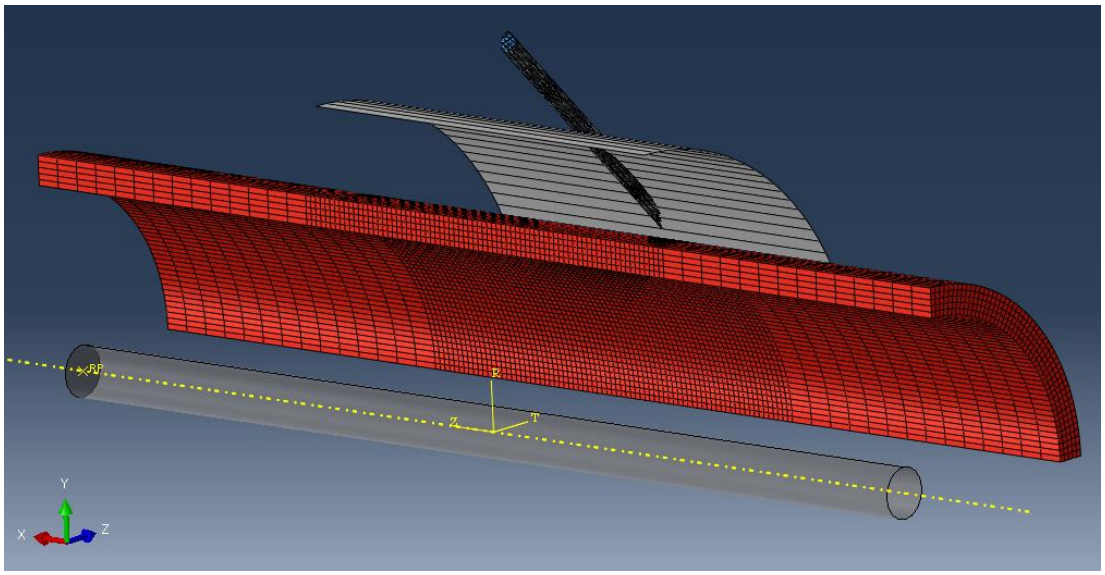

Figure 50 - Example ring-in-artery model generated in *Abaqus* CAE, consisting of the quarter ring, vessel, compaction surface and a central core.

The inner cylinder is modelled as an 'analytical rigid surface' which does not require to be meshed.

The quarter-cylinder compaction surface is a shell part discretised into 30 quadrilateral surface elements (SFM3D8R) in the circumferential direction. This structure has no modelled stiffness, and its diameter can be varied throughout the simulation.

The various loads and boundary conditions throughout the simulation on each component of the model are described in the following section (4.4.3).

4.4.3 Simulation Steps and Boundary Conditions

The simulation steps are outlined, with a summary of the applied boundary conditions and interaction states, in Table 9. See Figure 51 for images of the first 8 steps. All steps are 'Static, General' and use an arbitrary step time of one second. A description of the governing equations for this simulation type, as well as the settings chosen for solution and incrementation control were outlined in section 4.1. The first cyclic systolic and diastolic steps are notated S1 and D1 with subsequent *n*th cycles defined S*n* and D*n*. The purpose of repeating the systolic and diastolic steps is to ensure that the ring-artery interaction has settled to a repeatable motion. Small variation in the first few cycles can be observed as

the global stress-strain field of the simulated ring-stent settles. The default number of cycles performed has been set to 10, which was found to reduce variance to negligible levels.

Table 9 - Summary of ring-vessel simulation steps and the associated boundary conditions and loads

Step	Boundary Conditions and Interactions Summary
Initial State	**Vessel** – the vessel's end faces are constrained in the axial direction and symmetry faces constrained in their respective normal directions. These constraints are maintained through all steps. **Ring** – The node at the mid-point of 'Turn2' is held in the axial direction to prevent rigid body motion. This is maintained until the 'S1' step. **Compaction Surface** – whole surface fully fixed in the radial, theta and axial cylindrical directions. Initial diameter is equal to the ring's flat mean diameter.
Ring	Forming of the ring from straight wire **Ring** – displacement conditions are applied to each node on the end surfaces of the wires to form the quarter ring, as described in 4.2.1.
Pull	Ring pulled into a saddle shape **Ring –** opposing loads are applied to central nodes of each wire end in order to pull the quarter ring into the 'saddle shape'. The magnitude of the force has been normalised to pull every ring to approximately the same level of saddle shape. The loads are maintained until 'Compact2' step. **Interactions –** The turn-to-turn contact interaction is activated
Compact1	Initial Compaction **Compaction Surface –** the radial position of the compaction surface is reduced such that the compaction is 90% complete **Interactions –** the contact interactions are activated between: 1) ring and compaction surface; 2) ring and internal central core
Compact2	Final Compaction **Compaction Surface -** the radial position of the compaction surface is further reduced such that the specified inner sheath diameter has been reached. **Ring –** the loads applied to pull the ring into a saddle shape are deactivated over the course of this step.
Pressure	Initial diastolic pressure applied to the internal surface **Vessel –** the specified diastolic pressure is applied to the internal surface of the vessel
Release	Ring is deployed into the vessel **Compaction Surface –** the radial position of the compaction surface is increased to diameter larger than that of the ring in its flat position. **Interactions –** the contact interaction between ring and vessel is activated.
Steps S1…S*n*	Systolic blood pressure step **Vessel** – the specified systolic pressure is applied to the internal surface of the vessel **Ring –** the node at the mid-point of 'Turn2' which was preventing rigid body motion in the axial direction is released. **Interactions –** the contact interactions are deactivated between: 1) ring and compaction surface; 2) ring and internal central core; and 3) ring turn-to-turn
D1…D*n*	Diastolic blood pressure step **Vessel** – the specified diastolic pressure is applied to the internal surface of the vessel

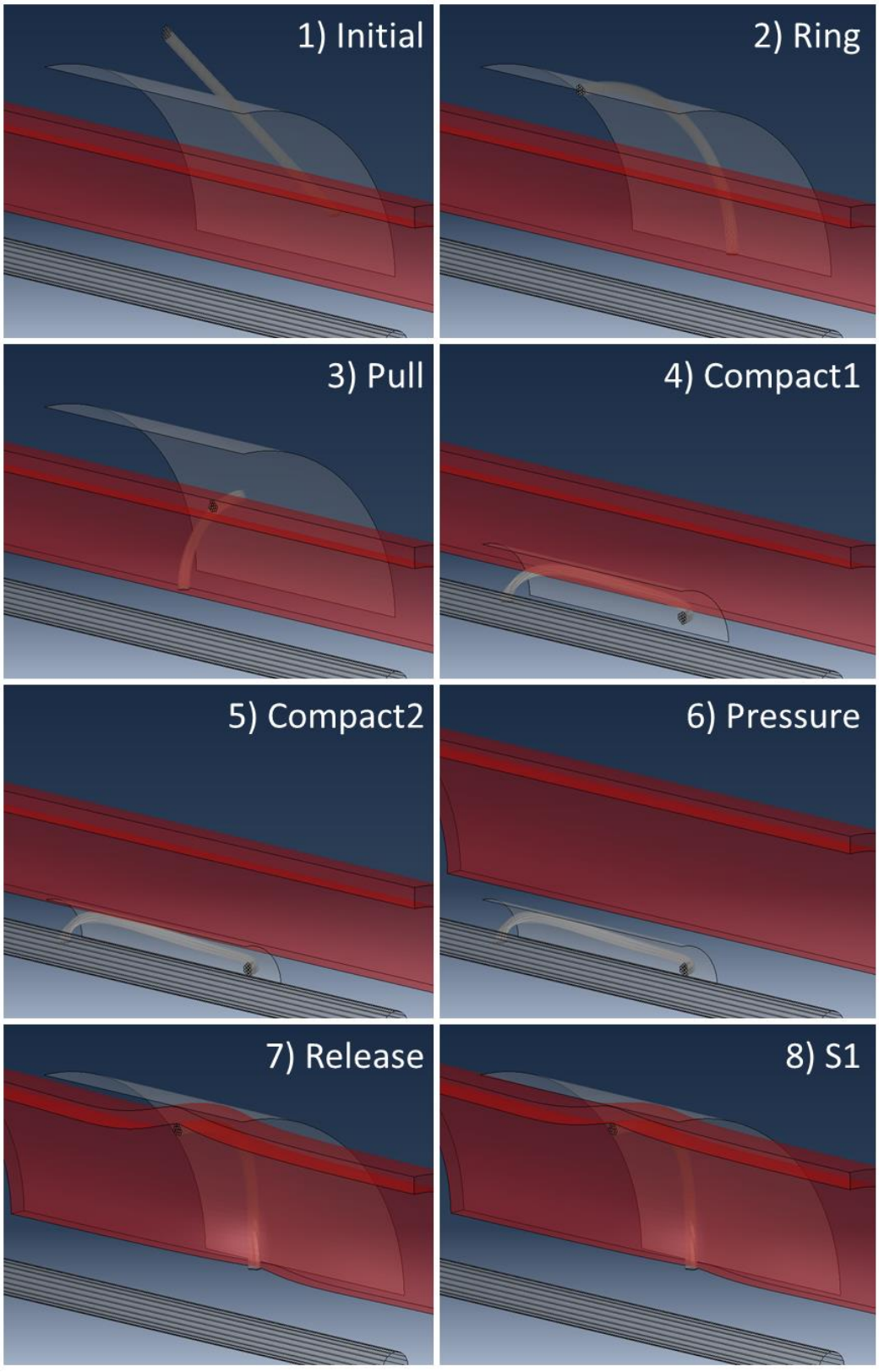

Figure 51 - Depicting the first 8 steps of a ring-artery interaction simulation

Simulating the compaction of the ring-stent is not intended to provide accurate stress-strain estimations of the compacted ring, but is more intended to approximate the superelastic strain levels at this stage prior to ring deployment. This is necessary because the final stress-strain field of a Nitinol structure is dependent on the 'strain history'. This is an effect of hysteresis.

As an example of the computational cost of these 'ring in Langewouters artery' models, the OLB28 R1 and R2 rings simulated separately, with twenty systolic to diastolic cycles, took 26.9 and 14.4 hours respectively on a 6-core *Intel® Xeon®* 3.47GHz processor with 24 GB of RAM (random access memory) available.

4.4.4 Interactions, Constraints and Cardiac Cycle Application

4.4.4.1 Interactions

There are four distinct contact interactions defined in the model which are summarised below:

Ring – Compaction Surface

A linear contact 'pressure-overclosure' relationship has been defined which initiates interaction at 0.03mm clearance and applies an increasing pressure to 25MPa at zero clearance. The default constraint enforcement method is used. An arbitrary friction coefficient of 0.1 is applied in the tangential direction.

Ring – Central Core

The same interaction definition as above (Ring -Compaction Surface) is implemented.

Ring – Vessel

A basic 'hard contact' pressure-overclosure using the 'Penalty method' for constraint enforcement has been applied. This allows *Abaqus* to determine a highly stiff linear contact condition based on the stiffness of the materials. A very low friction coefficient of 0.01 is applied in the tangential direction as the result of a sensitivity study which indicated higher strain amplitudes with lower friction values.

The maximum degree of master surface smoothing (of *a:l* = 0.5, see Figure 52) is applied to the vessel. This ensures that turns of the ring do not embed within artificial channels caused by discontinuous transitions of surface angle at the nodes between linear elements.

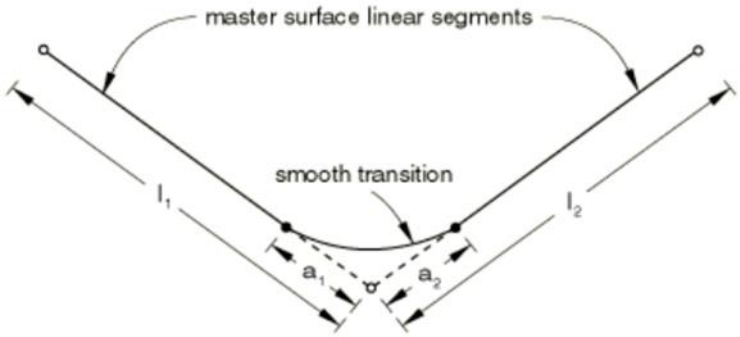

Figure 52 - Illustration from Abaqus documentation [91] explaining the degree of master surface smoothing for linear elements.

Ring Turn-to-Turn Contact (during compaction)

A 'soft' contact between adjacent turns was introduced as an additional modelling requirement due to what can be described as an unrealistic tangling of wires during compaction when only the turn-to-turn connecters were used. As mentioned in 4.4.3 the simulation of the compaction is acknowledged to be very approximate. A linear pressure-overclosure relationship which prevents the tangling mechanism and does not cause solution issues was arrived upon which initiates the contact at an overclosure of 5% the wire thickness, and increases to a pressure of 10MPa at overclosure of 50% wire diameter. This allows adjacent turns to overlap, however with a repelling pressure which increases with level of overlap. An arbitrary friction coefficient of 0.1 is applied.

4.4.4.2 Constraints

The centre of each turn is constrained from freely rotating by apply an 'equation constraint', relating motion of two opposing nodes on the surface. This is the same method as described in 4.2.2, and does not add stiffness to the structure.

4.5 Validation of Models

4.5.1 Physical Load-Deflection Testing

Empirical load-deflection testing of various Nitinol multi-strand rings was carried out at *Vascutek* using a Tinius Olsen tensile tester (*Vascutek* machine ID 293) with a 50N load cell and heated chamber at 37˚C. This setup is calibrated in the range of 0.5-50N and had a resolution of 0.002N. The rings were loaded into a 'saddle shape' position, as depicted in Figure 53, pulled to a maximum deflection before being partially unloaded to an *in-vivo* representative saddle shape position from which they are cycled 100 times over a relatively large deflection (more than would be seen *in-vivo*). The connections between ring and the

fixation points on the tensile tester were provided by single large loops of high stiffness polyethylene braided fibre strings (designed for fishing).

The five different ring designs (4 from the Thoraflex Hybrid device denoted HY, and one from the Anaconda denoted OLB) which have been tested in the manner described are outlined below in Table 10, along with the deflections applied. The deflection levels vary due to the rings being different diameters. Three samples were tested for each case.

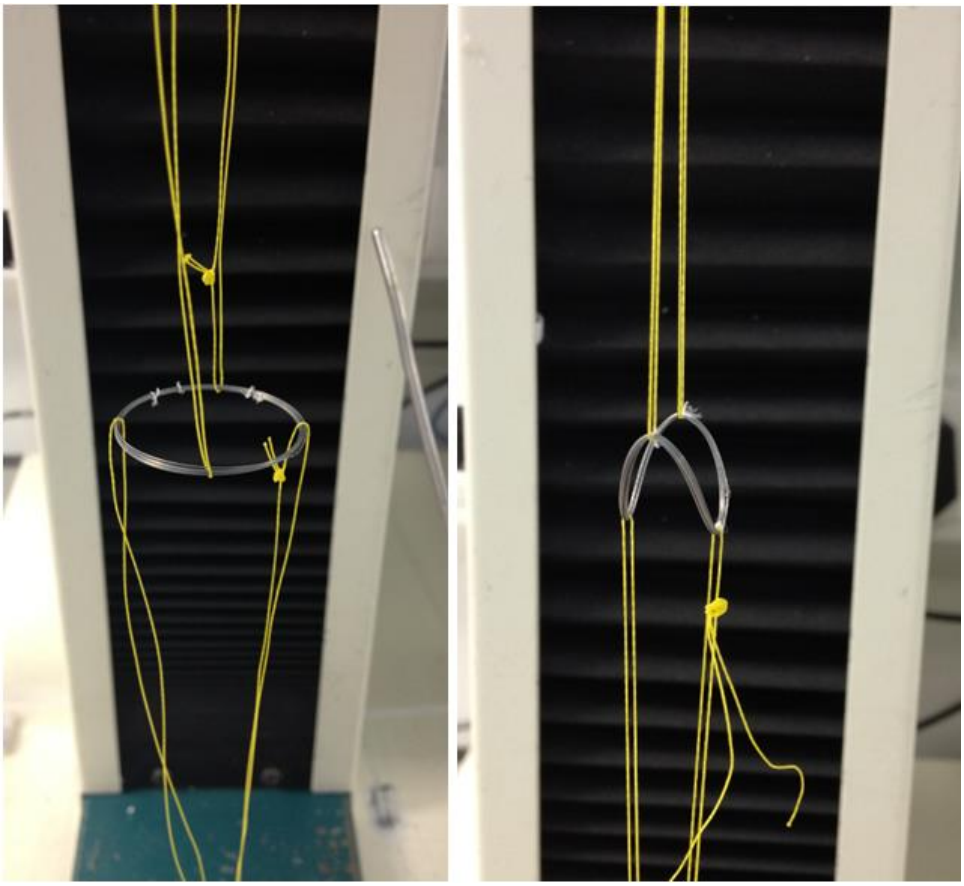

Figure 53 - A Nitinol ring load-deflection test showing unloaded and fully loaded positions

Table 10 - Overview of Nitinol rings in load-deflection empirical testing

Ring	Flat Ring Mean Diameter (mm)	Wire Diameter (mm) × No. turns	Maximum Displacement (mm)	Cycling Displacement Range (mm)
HY28-01	27.09	0.18 × 10	16.0	10.0-11.5
HY28-02	33.43	0.16 × 8	18.0	12.0-13.0
HY40-01	39.35	0.22 × 14	21.0	13.75-17.0
HY40-02	48.32	0.20 × 9	26.0	19.5-21.0
OLB28-R1	26.56	0.22 × 11	16.0	8.5-12.0

Three 100mm samples of the polyethylene connection lines were tensile tested at 37˚C to establish a stiffness which could be applied to the FEA model (see Appendix G). The stiffness of the lines is fairly constant after initial stiffening which is believed to be associated with taking slack out of the twisted braid pattern. It was therefore this 'settled' stiffness value of 0.395N/mm which was assumed for modelling (further discussed in Appendix H).

An example plot of load-deflection for the HY28-01 samples is provided Figure 54 in which it can be see that there is some variation in force levels between the three samples. Some hysteresis is observed in each sample: slightly lower unloading load level due to some material being strained into Nitinol's superelastic transformation zone.

Each empirical data set of three samples has been averaged to provide a single curve for comparison with FEA, however the deviation of the physical data will be considered in the comparison.

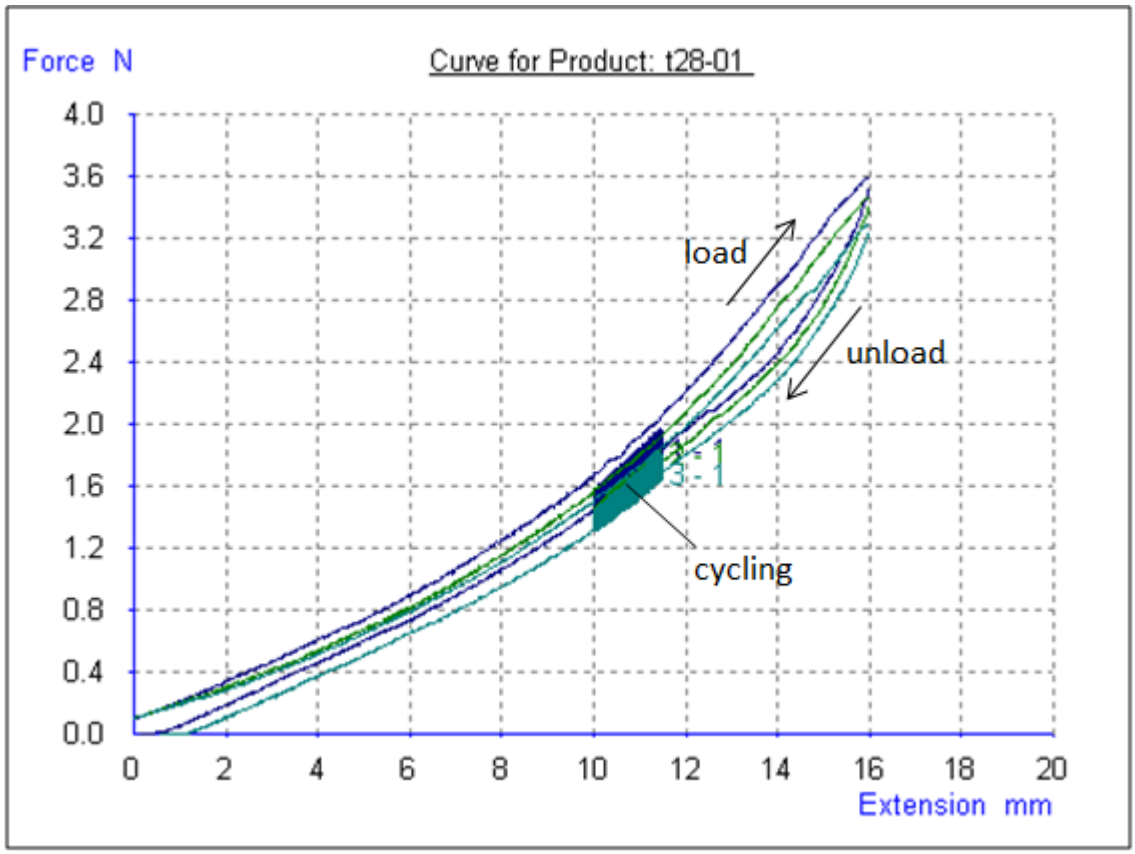

Figure 54 – Load-Deflection raw data plots for three T28-01 rings

4.5.2 Considering the Connection Friction

The setup described above (4.5.1) is relatively simple, however the detail of the interaction between the connector lines and the ring requires some consideration because the way in which it can be modelled has a considerable effect on the overall stiffness of the system. The connector lines are simply looped around the ring bundle as can be seen in Figure 53. Considering that the load in the system increases with increased extension, any friction between the connection loop and the bundle will also increase. The rotation of a connector line (in a global sense) is negligible compared to the tendency of the peaks/valley cross-section to rotate (about an axis normal to the cross-section) as the ring is pulled into a 'saddle shape'. Therefore, the increasing friction will cause some level of varying resistance to the rotation of the bundle at the connection points.

Quantifying the described resistance and replicating it within the model would be challenging, therefore it was decided to take the approach of modelling both extremes: allowing free rotation or constraining rotation completely at the peak and valleys. Both extremes have been modelled and are assessed for both a single ring and full bundle models below (4.5.3 - 4.5.4).

4.5.3 Single Turn Ring Model Validation Results

A single-strand quarter model was used, as described in 4.2, with linear stiffness connectors between the mid-node on each end face to the lower fixed point and upper loading point respectively (see Figure 55). The results here are specific for the 'improved' material model described in section 3.3. The connectors were applied a stiffness of 0.395N/mm as defined in 4.5.1. Velocity/displacement boundary conditions were applied to the load point to replicate the relevant load, unload and cyclic loading applied in empirical testing as outlined in Table 10. After load, and unload steps the simulation model was cycled only 10 times (as opposed to 99 of the empirical) because the load-displacement output had settled to negligible variation. From a modelling theoretical point of view: there exists some initial 'settling' or converging of force values in the first few cycles of the simulation due to the global stress-strain state in the ring varying slightly in these cycles, which is directly related to the hysteresis behaviour defined in the material model. If the whole model was linear elastic there would be no gap between load and unload, no variation in the first few cycles, and the cyclic load-deflection response would lie on the initial load-unload stiffness line.

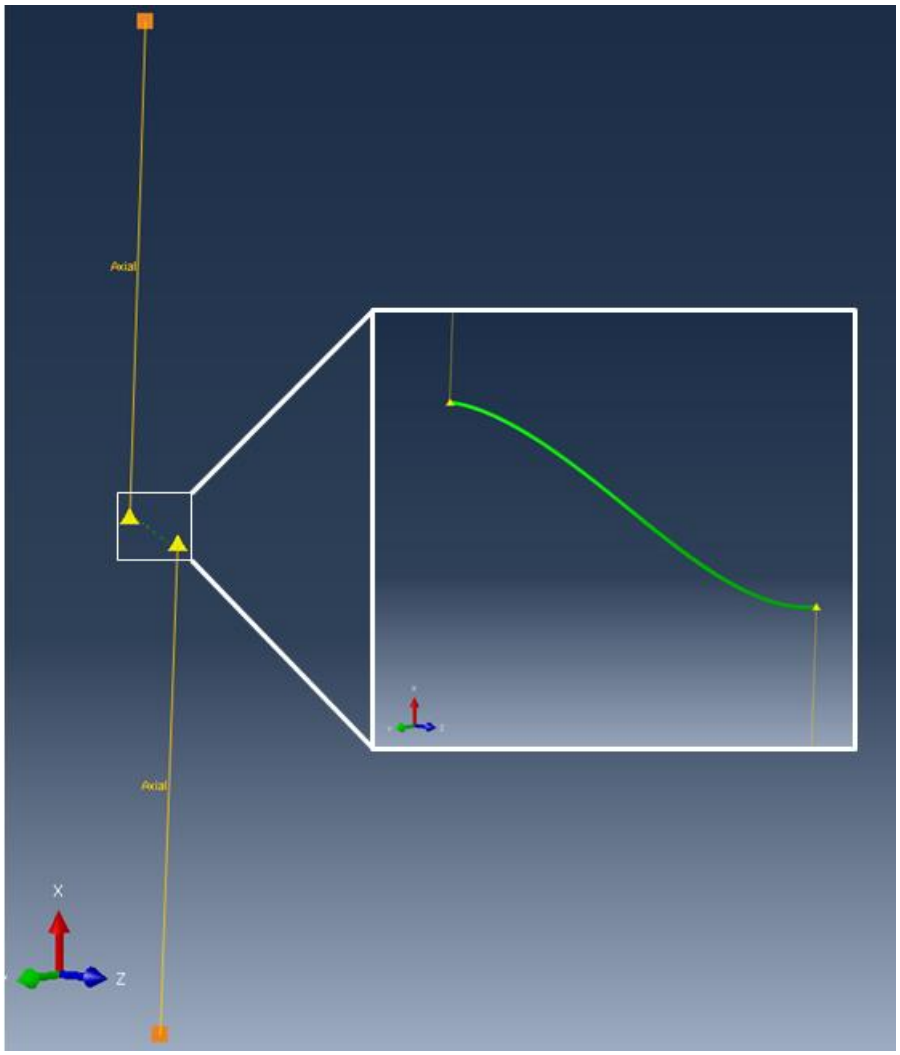

Figure 55 - Single-turn quarter ring model of HY28-01 in cyclic position of validation load-deflection test

Furthermore, the constitutive superelastic model does not simulate any type of 'low-cycle fatigue', i.e. a change in properties during cyclic loading.

As discussed in 4.5.2, two modelling options will be compared to empirical results for each ring configuration:

- Case A - allowing free rotation of the wire at the peak and valley and;
- Case B -constraining rotation completely at the peak and valley

Each load-displacement response is extracted from the upper loading point of the simulation, and the load values are multiplied by 4×*number of turns* (by 4 because it is only a quarter model and by the number of turns based on the assumption that turns are working primarily as individual entities).

The full load-deflection response for simulation Case A and Case B are plotted along with empirical data for comparison in Figure 56 and Figure 57 respectively. These plots include data from the load, unload, first cycle and 99th cycle from the physical test, while all steps from the simulation are plotted as one continuous line. To quantify the validation, forces from the 99th cycle of empirical data will be used to compare with simulation results later.

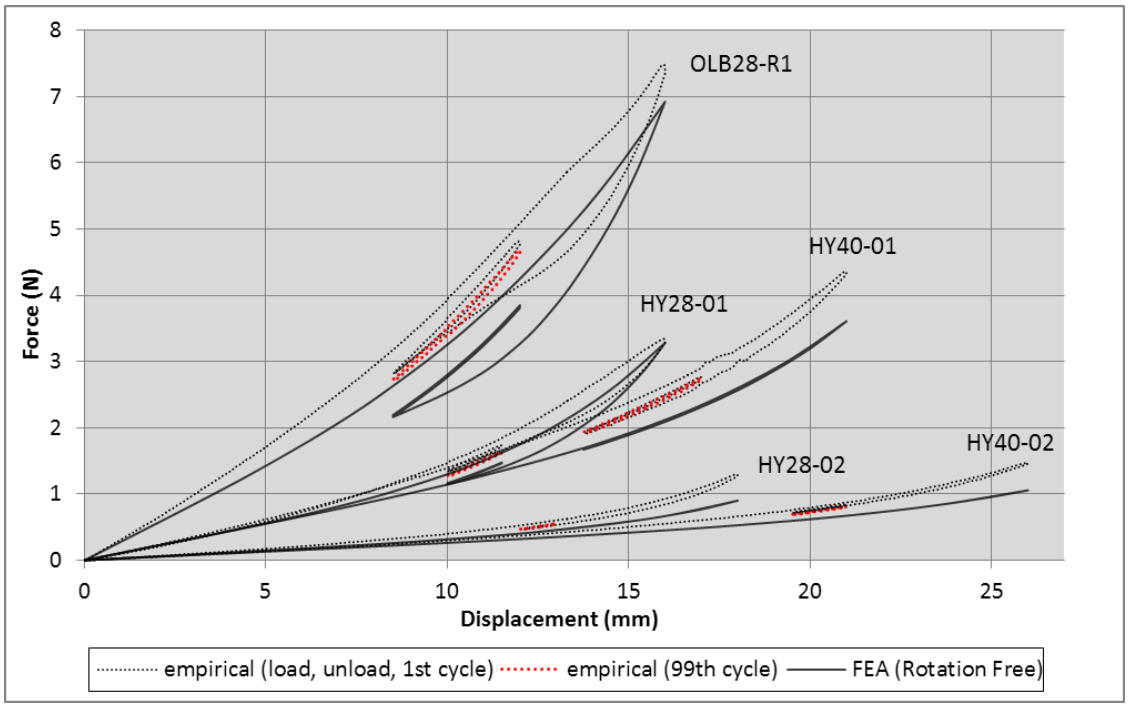

Figure 56 - Single-turn quarter model load deflection validation for 'Case A: rotation at peak and valley allowed'

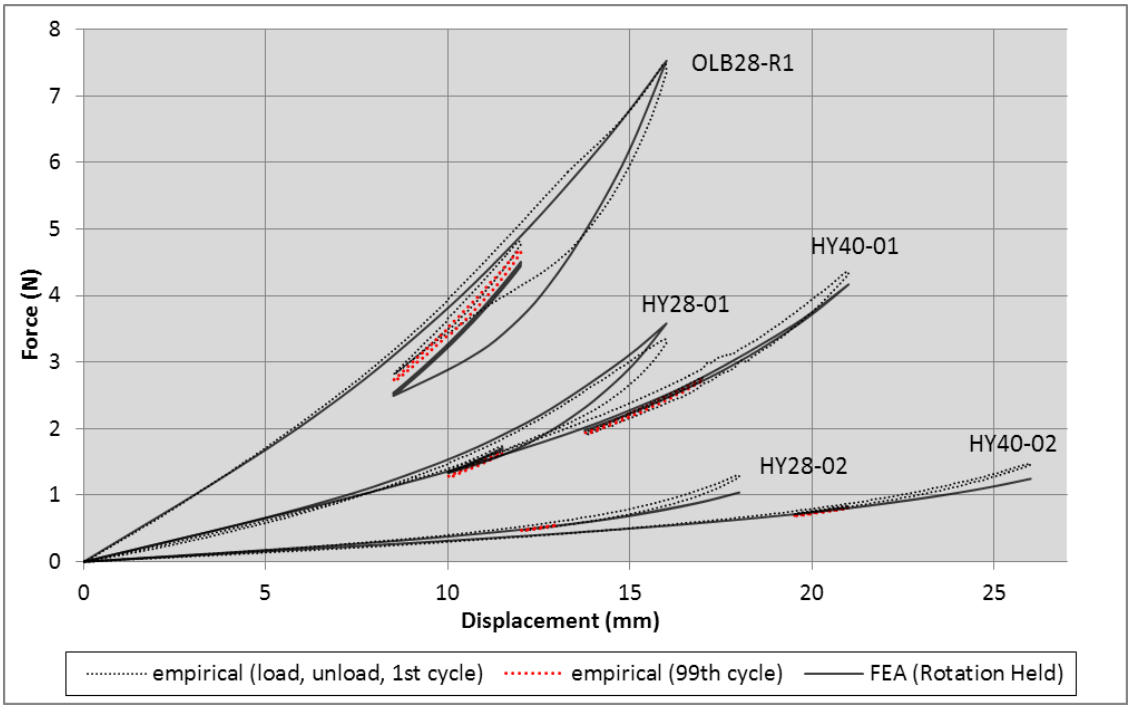

Figure 57 - Single-turn quarter model load deflection validation for 'Case B: rotation at peak and valley constrained'

Briefly first considering the averaged empirical data plots (dotted lines) repeated in Figure 56 & Figure 57; the difference between load and unload force levels in the system, or 'global hysteresis', is more evident the stiffer the ring. This can be explained considering that the stronger rings, which are composed of thicker wire, have more material being loaded to a superelastic plateau level, i.e. in the hysteresis zone of the material. The constitutive model used (detailed in 0) has start of transformation strain of 1.11%. The simulations showing no hysteresis; HY28-02 and HY40-02, have not exceeded this strain level in the initial loading step at any node (0.97% and 0.87% maximum respectively for 'Case B' which has slightly higher max strain values than 'Case A'). HY40-01 fractionally exceeds the start of transformation for the 'Case B' but not for 'Case A' (1.16% and 1.08% respectively) which explains the slight hysteresis seen in Figure 57 for this ring. The OLB28-R1 and HY28-01 simulations, which show considerable hysteresis in the structural load-deflection response had maximum strains of 2.98% and 2.25% respectively ('case B'): some significant transformation occurring in the initial load step.

A slight drop in load levels is observed for the empirical results between 1st and 99th cycles, again more apparent for the stronger rings. This does not occur in simulation: in fact a very slight increase in the cyclic force values occurs during the settling. The slight decrease in reality could be due to a slackening in the system occurring over cycling which is not captured in simulation.

All 'Case A' (rotation allowed) simulations (Figure 56) under-predict force levels and stiffness. The 'Case B' (rotation constrained) simulations (Figure 57) appear to provide a much-improved overall agreement relative to 'Case A' for the load-unload as well as cyclic steps. The most significant discrepancy for 'Case B' appears to be the unloading of OLB28-R1, however the cyclic load levels are in reasonable agreement.

In order to quantify the comparison, the 'low force' and 'high force' values have been extracted from the respective final cycles of both the empirical averaged results as well as the simulations ('case A' and 'case B'). The cyclic loading steps have been used as they were intended to be representative of a ring's final deployed position; considered the most important from an analysis point of view. These force values are provided in Table 11 along with the standard deviation of empirical results and the discrepancy of the simulated results relative to the empirical. A colour scale has been used to visually emphasise the

discrepancy results: from red for the highest value tending to green as discrepancy results approach zero.

Table 11 - Single Turn Ring Model Validation Accuracy Assessment: comparison of low and high force values from the final cycle. Colour scale indicates severity of discrepancy in the simulation results (red=highest; green=lowest). S.D. = Standard Deviation.

Ring	Empirical				Simulation - Single Turn							
					Case A - rotation allowed				Case B - rotation constrained			
	final cycle low		final cycle high		final cycle low		final cycle high		final cycle low		final cycle high	
	Force (N)	S.D. (%)	Force (N)	S.D. (%)	Force (N)	% disc.	Force (N)	% disc.	Force (N)	% disc.	Force (N)	% disc.
HY28-01	1.27	4.61%	1.62	3.51%	1.16	-8.5%	1.47	-9.2%	1.34	5.7%	1.71	5.1%
HY28-02	0.47	2.50%	0.55	2.71%	0.40	-13.6%	0.45	-16.9%	0.48	2.4%	0.54	-1.6%
HY40-01	1.92	3.14%	2.72	2.68%	1.67	-12.7%	2.32	-14.9%	1.97	2.9%	2.73	0.1%
HY40-02	0.69	3.15%	0.80	3.63%	0.60	-13.7%	0.67	-16.1%	0.71	3.2%	0.80	0.3%
OLB28-R1	2.71	5.06%	4.64	4.28%	2.19	-19.2%	3.85	-17.0%	2.54	-6.4%	4.51	-2.8%

It is immediately clear from Table 11 that simulation 'Case B' has lower discrepancy relative to the empirical data. 'Case A', applying no rotational constraint, under-predicts force levels in every ring, while in 'Case B' the majority show a slight over-prediction of force values, with the exception of the OLB28-R1 ring and the high value for HY28-02 having slight under-predictions. In light of this result and for the purpose of quantifying the validation it has been assumed that the empirical setup behaves more closely to that of simulation 'Case B'. It should be noted that most of the discrepancy values for 'Case B' are actually less than the respective standard deviation associated with the empirical results. However ultimately from this study, it can be stated that the structural strength of a ring in a typical *in-situ* position (extrapolated by multiplication of a result from a single turn simulation model) has an accuracy range of ±6.4%.

4.5.4 Full Bundle Model Validation

The full bundle model to be validated is as described in 4.2.7 in which there are multiple turns with axial connectors joining nodes at the wire centreline at nine equally spaced intervals along the length of the quarter ring. For the purpose of the validation, linear-stiffness axial elements were connected from the mid node at the end of each turn to the loading points (see Figure 58). The connectors were applied a stiffness of 0.395N/mm as defined in 4.5.1. The boundary conditions to load the quarter ring model were applied to

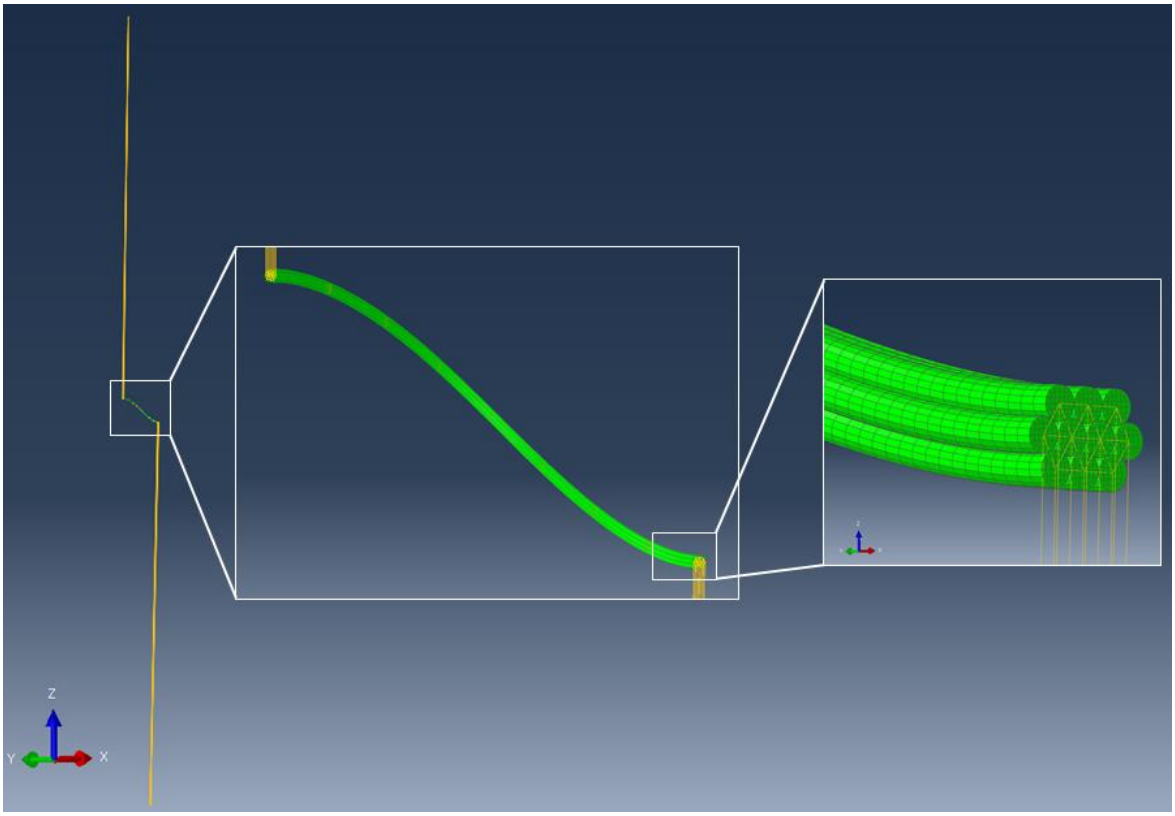

Figure 58 - Full-bundle quarter ring model of HY28-01 in cyclic position of validation load-deflection test

the top loading point in exactly the same manner as was described for the single ring validation in 4.5.3.

As with the validation study of the single ring, and discussed in 4.5.2, the same two constraint configurations have been investigated:

- Case A - allowing free rotation of the wire at the peak and valley and;
- Case B -constraining rotation completely at the peak and valley

The results of the simulated 'Case A' and 'Case B' are plotted with the empirical average data in Figure 59 and Figure 60. The general analysis of the empirical force-displacement trends was discussed in the section above (4.5.3).

In general, the results are very similar to the single ring validation, and the discussion in 4.5.3 is relevant for the full bundle validation. The simulation of 'Case A', in which no rotational constraint is applied, the force levels are under-predicted as with the single turn study. Again 'Case B', with rotation constrained, provided a much-improved overall agreement with the key discrepancy again being the unload curve of OLB28-R1.

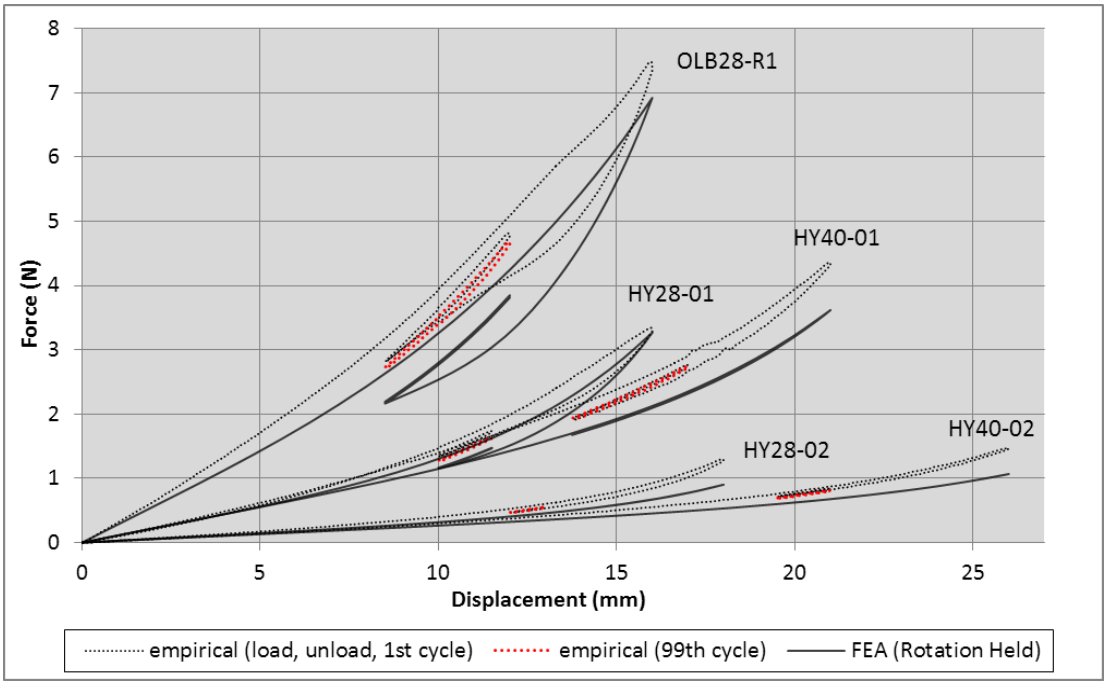

Figure 59 - Full-bundle quarter model load deflection validation for 'Case A: rotation at peak and valley free'

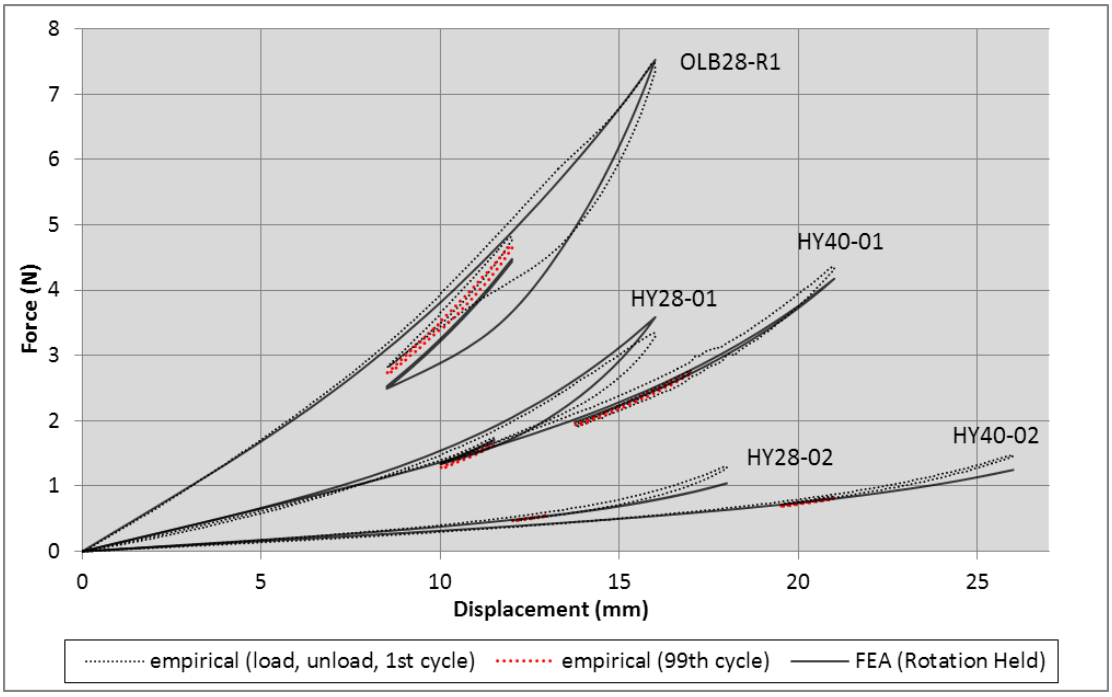

Figure 60 - Full-bundle quarter model load deflection validation for 'Case B: rotation at peak and valley constrained'

The low force value and high force value from the final cyclic step have been tabulated for comparison in Table 12 with the same colour scale for clarity as described in 4.5.3. As is expected from analysing the load-deflection plots, the results again are much better

agreement with empirical testing for 'Case B'. The discrepancy values are very similar to those for the single ring analysis in Table 11. However, there is slight increase in the highest discrepancies meaning that for the full-bundle modelling approach it can be stated that the structural strength of a ring in a typical *in-situ* position has an accuracy range of ±6.9%.

Table 12 - Full Bundle Ring Model Validation Accuracy Assessment: comparison of low and high force values from the final cycle. Colour scale indicates severity of discrepancy in the simulation results (red=highest; green=lowest). S.D. = Standard Deviation.

Ring	Empirical				Simulation - Full Bundle							
					Case A - rotation allowed				Case B - rotation constrained			
	final cycle low		final cycle high		final cycle low		final cycle high		final cycle low		final cycle high	
	Force (N)	S.D. (%)	Force (N)	S.D. (%)	Force (N)	% disc.	Force (N)	% disc.	Force (N)	% disc.	Force (N)	% disc.
HY28-01	1.27	4.61%	1.62	3.51%	1.16	-8.4%	1.48	-9.1%	1.34	5.8%	1.71	5.3%
HY28-02	0.47	2.50%	0.55	2.71%	0.40	-13.4%	0.46	-16.7%	0.48	2.6%	0.54	-1.4%
HY40-01	1.92	3.14%	2.72	2.68%	1.68	-12.5%	2.32	-14.7%	1.98	3.2%	2.73	0.3%
HY40-02	0.69	3.15%	0.80	3.63%	0.60	-13.3%	0.68	-15.6%	0.71	3.4%	0.81	0.4%
OLB28-R1	2.71	5.06%	4.64	4.28%	2.19	-19.2%	3.85	-17.0%	2.52	-6.9%	4.48	-3.5%

4.6 Summary of Chapter 4

Bespoke FEA methodologies have been developed to mechanically simulate ring-stents being subject to the high deformations which are part of their life-cycle. A new method to capture the stiffening pressure-diameter response of human aortic artery has been devised based on one of the most thorough cadaveric tests available from the literature (Langewouters *et al* [47]). The methods have been scripted in *Python* language so that any ring configuration and vessel size can be rapidly modelled with desired loading applied.

The ring methodology has been validated against 'saddle pull tests' as described in the section 4.5 and the artery models' pressure-diameter response has been verified as described in 4.3.4.3. The structural representation of both entities is unchanged when they are combined as described in section 4.4, however ideally a validation of the full system would be carried out. This would aim to confirm the deformed geometry of ring-in-artery and the combined pulsatile motion for fatigue analysis. In the absence of this full system validation, efforts have been made to ensure that the worst-case assumptions are specified for parameters such as friction.

5
Ring-Stent Mechanics

This chapter details the early studies aimed at gaining a fundamental understanding of how the Nitinol ring acts as a radial spring structure and gives insights to the general strain state of the wire through a ring-stent's life-cycle. The studies described in this chapter implement the initial basic single-strand quarter ring methodology described in 4.2.1-4.2.2.

5.1 Definitions

For the purpose of the studies in this chapter, the deformation of a ring in isolation will be defined as per (Eq. 5.1) where D_0 is the mean (centreline) diameter of the flat ring and D is the diameter of the deformed ring in a 'saddle shape' position.

$$ring\ deformation = \frac{D_0 - D}{D_0} \times 100\% \qquad \textbf{(Eq. 5.1)}$$

In the studies which deploy a single strand into a simple elastic tube the diameter of the ring measured at the peaks is slightly less than measured at the mid-point (between peak and valley), therefore the measurement of D is taken as an average of the peak and mid-point positions.

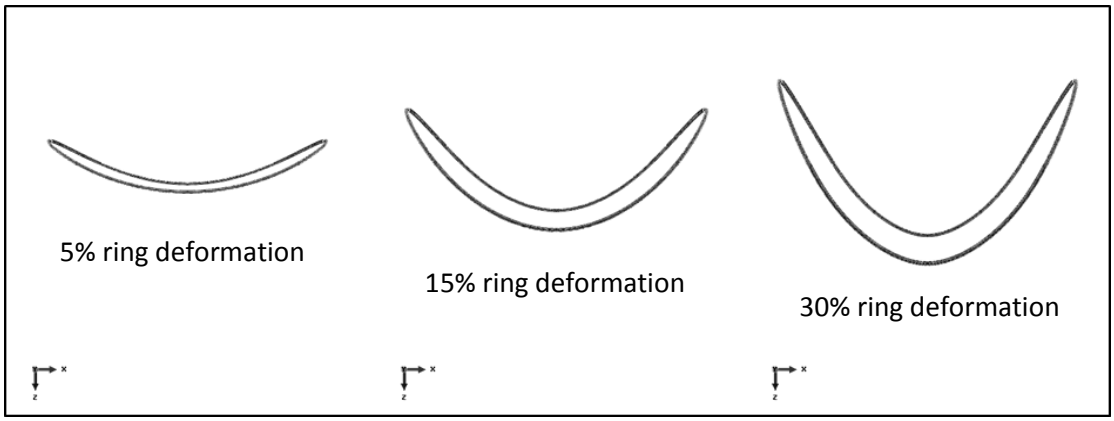

Figure 61 - Ring deformation of 5%,15% and 30%

To give a visual indication of the level of deformation being referred to, the ring deformations of 5%, 15% and 30% are shown in Figure 61.

The cyclic deflection of a ring will also be referred to in this study, where 'pulsatility' is the magnitude change in diameter between an upper and lower measurement, (i.e. D_{upper} – D_{lower}), and the 'percentage pulsatility' will be defined as the change in magnitude relative to the smaller diameter measurement, D_{lower}:

$$\%\_Pulsatility = \frac{D_{upper} - D_{lower}}{D_{lower}} \qquad \textbf{(Eq. 5.2)}$$

In vivo the D_{upper} would typically occur at systolic pressure and D_{lower} typically at diastolic, assuming the ring is following the compliant movement of the vessel responding to blood pressure (this is not always observed as will be discussed in Chapter 7). It is useful to understand the relationship between 'Pulsatility' and 'Delta-strain' for fatigue analysis purposes which will be addressed in 5.4.1.

5.2 Nitinol Ring as a Radial Spring

A fine wire Nitinol ring deformed to a sufficient 'saddle' position is predominantly experiencing bending deformation; shear loading from torsion and direct tension/compression loading are less significant in magnitude. However, a ring at a low enough 'saddle shape', practically flat, will experience mainly direct compressive force when radially loaded. For the purpose of this study, it is assumed that the rings are in a saddle shape in which bending is the main mode of mechanical deformation.

A 'saddle shape' deformed ring within a cylindrical vessel will inherently be applying an outward force on the vessel, which the vessel opposes with an equal inward force. Considering the simplified case in which 1) the cylindrical vessel remains perfectly cylindrical; 2) the ring is in contact with the cylinder along its full length; 3) there is no friction - then the normal force between ring and vessel will always be in the radial direction along the length of the ring.

Of course, in reality there is friction involved and a flexible vessel wall into which ring-stents may imbed to some degree. These factors will allow some component of the overall force transferred between ring and vessel to be non-radial: in the axial and circumferential direction when considering a cylindrical coordinate system.

It should also be noted that the force exerted between ring and vessel will not be totally uniform along the length of the ring. The radial force distribution along the length has been analysed in Chapter 7.

For the purpose of the studies herein, the assumption is made that the problem is dominated by radial force and the overall force measured via the total hoop force (as described in 4.2.4) is purely radial.

The radial stiffness of a Nitinol ring is not constant. That is to say: as a ring is compressed radially, the force required to progressively deform it does not keep increasing linearly with radial deflection. In fact, for some rings the load required to compact it further may even decrease after some point– i.e. a negative stiffness.

The *Adjustable Rigid Torus (ART)* extension tool for *Abaqus*, described in 4.2.3.2, has been used to apply a radial loading and unloading of a turn of an *Anaconda* OLB28 R1 ring for both the true Nitinol material, and of a hypothetical linear elastic material for comparison. The hypothetical linear elastic material has the same modulus as that of the initial austenite modulus of the Nitinol model used. The load-deflection in terms of Radial Force vs. Ring Deformation for both cases are plotted in Figure 62. The simulation investigates the radial loading over a ring-deformation of approximately 2% - 50%. At some point below 2%

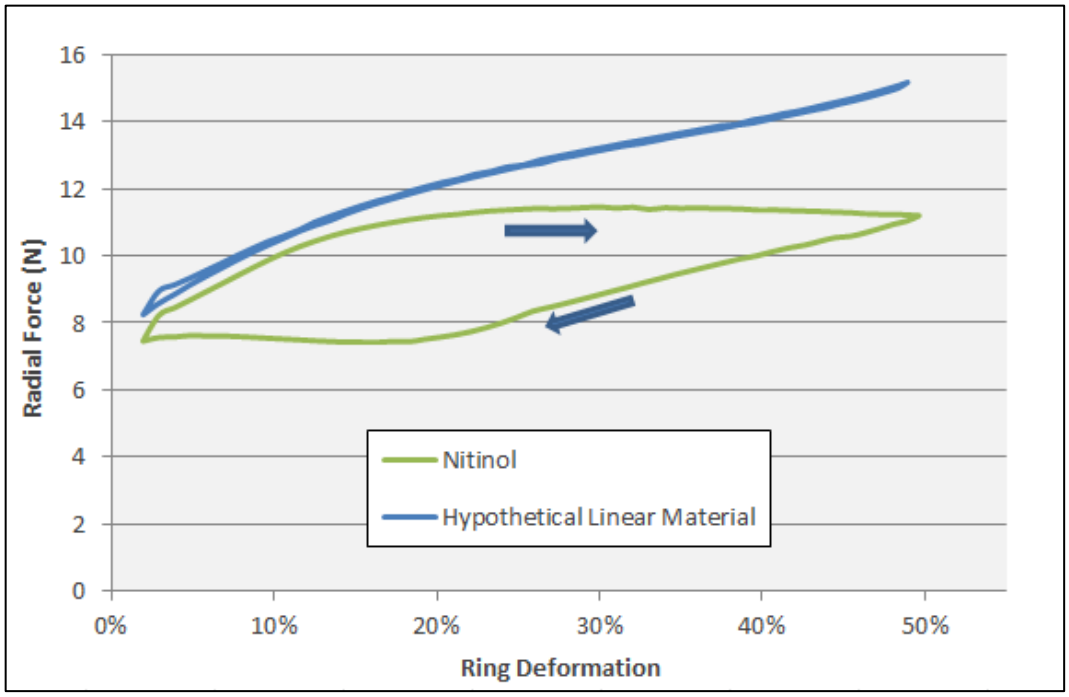

Figure 62 - Comparing radial force from Nitinol and linear elastic rings deformed to a compacted state and then unloaded

deformation, the problem would become a compression problem rather than bending dominated problem.

It can be seen that for both cases, even at the low ring deformation of around 2%, there is a significant load required to hold a ring in a saddle shape. For the case displayed, it can be seen that a hypothetical linear elastic ring maintains a positive stiffness through the range investigated. However, the Nitinol case appears to plateau in terms of load value which is partly synonymous with Nitinol's uniaxial stress-strain behaviour plateauing as phase change occurs, although only a small region of material in the ring in this case is at a level of strain which would exhibit phase change. As would be expected with a Nitinol structure reaching some superelastic level, there is a degree of hysteresis in the global response for loading and unloading.

5.3 Global Hysteresis

Nitinol exhibits hysteresis in simple uniaxial tensile testing, in the form of higher stress values in loading than in unloading as some of the energy input is lost to heat dissipation. Any Nitinol structure being loaded which has part of its material reach superelastic (phase change) state will also exhibit hysteresis when unloaded. The Nitinol rings being deformed into a 'saddle shape' have varying strain states throughout the length of the wire, with

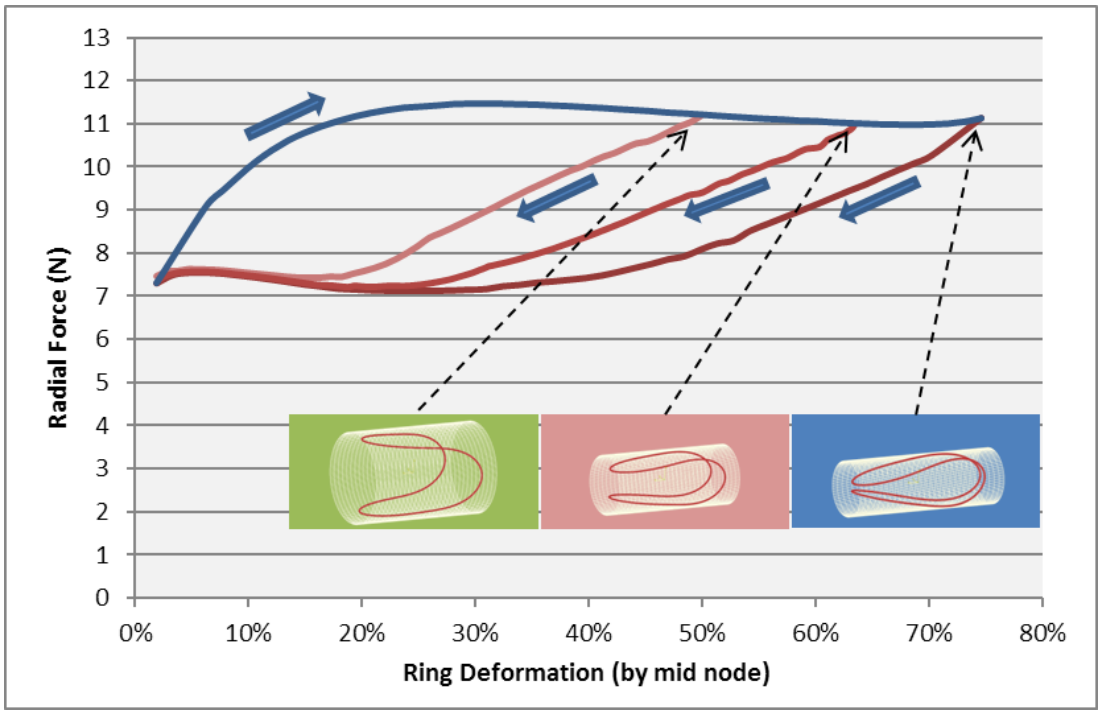

Figure 63 - Load-Deflection plot for a Nitinol ring in saddle shape loaded to various levels of deformation

significant levels of both compression and tension because of the dominant loading behaviour being bending. The 'peaks' and 'valleys' are the areas which first reach superelastic levels of strain at ~1.03% (for the constitutive model with the 'provisional model parameters' defined in 3.3) and not much of the wire between peak and valley will reach superelastic state even when a ring is compacted down to a level representative of a compacted device.

The described 'global hysteresis' of a Nitinol structure is the behaviour responsible for 'load history dependency': the reaction force of a component at some level of deformation is dependent on what deformation it has been through to get there. In this case the unloading force-deflection path depends on how far the structure was deformed. This is shown for the Nitinol ring application in Figure 63, where the different unload paths are shown for a ring which has been loaded to different levels of deformation.

As mentioned above only part of the volume of material of a deformed Nitinol ring's wire is actually in a superelastic state. To appreciate this, a significantly deformed Nitinol ring model is displayed in Figure 64 with a contour plot of 'fraction of martensite', which is an output provided as part of the superelastic material constitutive model in *Abaqus*. Fully transformed martensite is represented by the red end of the scale, while material remaining purely austenitic (<~1.03% strain) is at the blue end of the colour contour scale (misleadingly the scale in the figure suggests some material has a fraction greater than 1; this is due to values being exaggerated when the visualisation algorithm extrapolates this

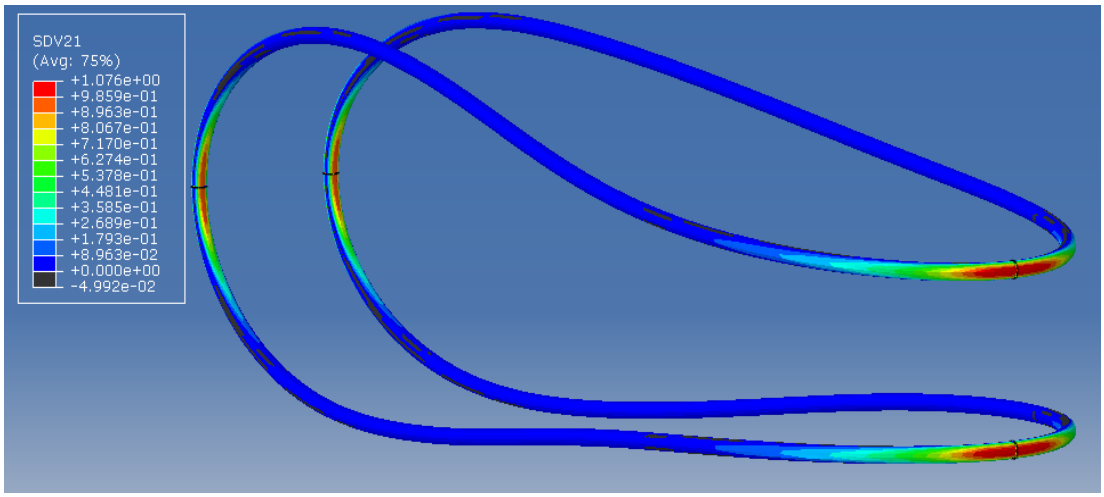

Figure 64 - A highly deformed ring with a contour plot of 'fraction of martensite'. Fully austenitic material is represented by the blue end of the scale and full martensitic by the red.

output from integration point values to nodal values on the surface. The values calculated at the integration points do not exceed 1). Only the areas near the peaks and valleys of the Nitinol are actually experiencing superelastic strain levels. Most of the length of wire between peak and valley is still linear elastic austenite.

5.4 Single Turn Parametric Study

Parametric studies have been carried out using the single turn modelling methodology to investigate strain and radial force levels experienced in a Nitinol ring at levels of ring deformation which would be typically experienced *in-vivo*. A turn from the proximal R1 ring of the OLB28 device has been simulated through ring forming and a compaction approximation before deployment into a simple linear elastic tube model with one element through the wall thickness. The resulting position of the single-strand model in a thin tube model (at ~15% device oversize) is shown in Figure 65. Various elastic tube diameters were simulated (separate simulations) to provide comparison at a range of ring deformation levels from 7.8%-21.9% which correspond to device oversize levels of approximately 10%-30% for this case (*Anaconda* 28mm device). Each of these simulations loads a ring through an approximate compaction deformation by the combined uniform radial loading and axial loading technique as described in 4.2.3.1. This is to approximate the true load history, the importance of which was described in section 5.3.

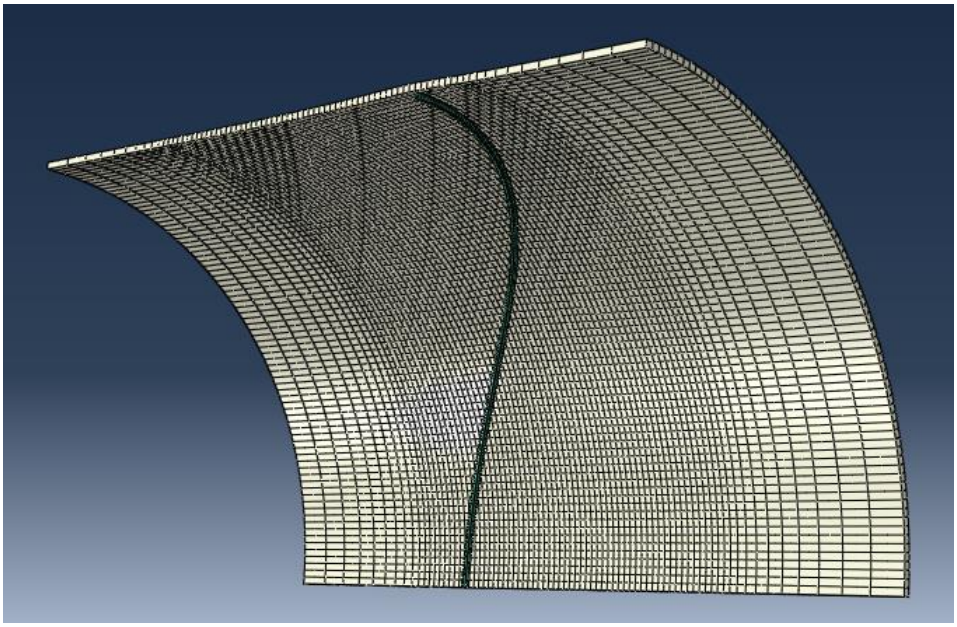

Figure 65 - Simple single-strand model in linear elastic tube used to probe the mechanical characteristics of the ring-stent.

The thin walled linear elastic tube models were cyclically loaded with internal pressures to enforce a diametric strain and therefore a pulsatility on the ring. For the case of approximately 14% device oversize, the effect of varying the magnitude of pulsatility has been investigated in separate models.

A further two studies using single turn modelling were carried out: investigating correlation with wire diameter and ring diameter on the strain levels and radial force independently. The methodology here was slightly different in that the ART add-on (4.2.3.2) was used to load the rings through compaction approximation, unloading and cyclic loading – no linear elastic simple tube model was implemented.

The strain levels analysed in the following results are always the maximum strains in the single turn ring. The maximum strain result in these simulations is always at some point on the outer surface at the peak/valley position.

5.4.1 Strain Analysis

The plot in Figure 66 shows the simulated maximum strain levels for a turn of an OLB28 R1 ring going through typical lifecycle stages of: forming in manufacture, compaction, deployment and cycling *in vivo* at four different levels of resulting pulsatility. Through the manufacture step the maximum strain increases to the ring's 'pre-strain' state as the wire is formed into a circle. The 'pre-strain', ε_0 in a flat ring can be calculated accurately from simple beam bending theory as long as Nitinol material is still in initial linear-elastic Austenite phase (a very thick wire/small ring diameter ring would be highly strained in manufacture). Simple theory of elastic bending states (Eq. 5.3):

$$\frac{\sigma}{y} = \frac{E}{R} \qquad \textbf{(Eq. 5.3)}$$

Where *E* is Young's modulus, *R* is radius of curvature of the beam's neutral axis, and σ is the stress at a distance *y* from the neutral axis. Rearranging and substituting σ/E for strain, then the strain at the outer surface (*y* = wire radius) of a formed wire ring is given by (Eq. 5.4):

$$\varepsilon_0 = \frac{y}{R} = \frac{d}{D} \qquad \textbf{(Eq. 5.4)}$$

where *d* is the wire diameter and *D* is the flat ring mean diameter.

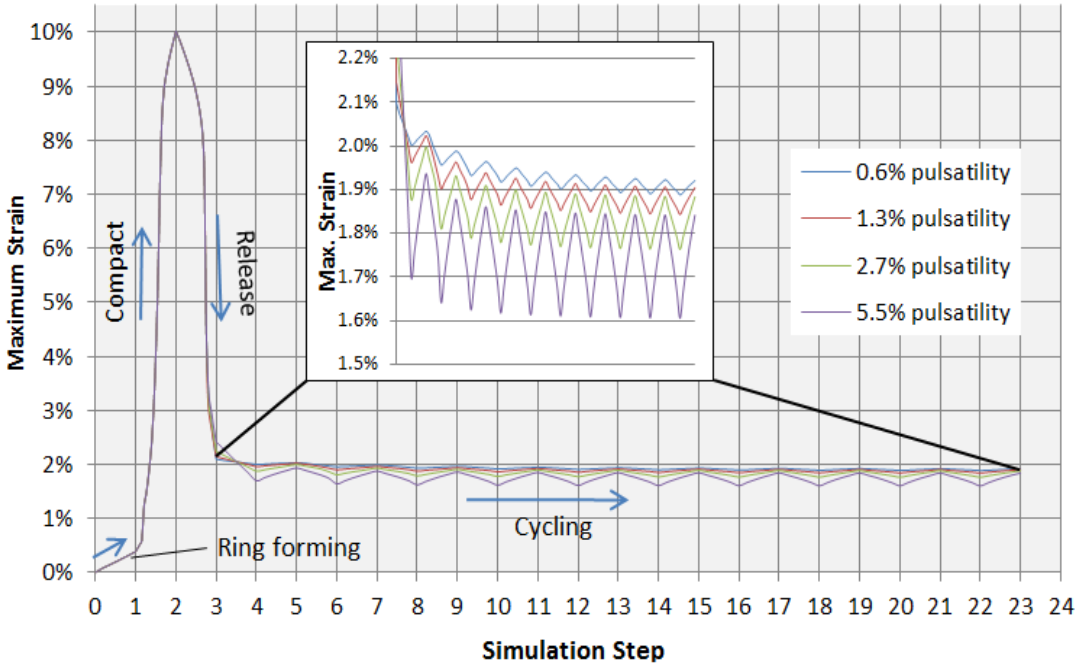

Figure 66 - A plot of typical maximum strain through a ring's lifecycle: ring forming, compaction, release to a deployed position and ten pulsatile loading cycles. Various levels of pulsatility show the effect on strain amplitudes.

As the ring is compacted from a flat ring position to the approximate shape within the diameter of a sheath, the strain concentrations appear at the peaks and valleys, where the highest level of bending occurs. The exact location of maximum strain on the outer surface of the cross section will not remain constant: to some degree this point moves around the circumference of the wire as the ring is deformed. As expected, Figure 66 shows the maximum strain level reducing significantly in deployment as the ring is expanded.

The cycling phase of the simulation displays some settling effect over the ten cycles which were applied in this case. The settling in these FEA simulations is due to the hysteresis incorporated in the material model as the global stress-strain state narrows to a cyclic routine. The constitutive material model does not incorporate 'low cycle fatigue' effects such as the modulus changing over a relatively low level of cycles.

It is observed from the inset plot in Figure 66 that the mean-strain in cycling reduces slightly from 1.9% to 1.72% with increased pulsatility. This does make logical sense when considering that the initial unload from compaction is reducing in strain rapidly along the unload plateau before cycling occurs on a modulus closer to that of the Austenite state – the higher pulsatility cases drop slightly further down the unload plateau, because of the

specified higher amplitude, before cycling which leads to the slightly lower mean-strain. The mean-strains at various levels of oversize are considered below.

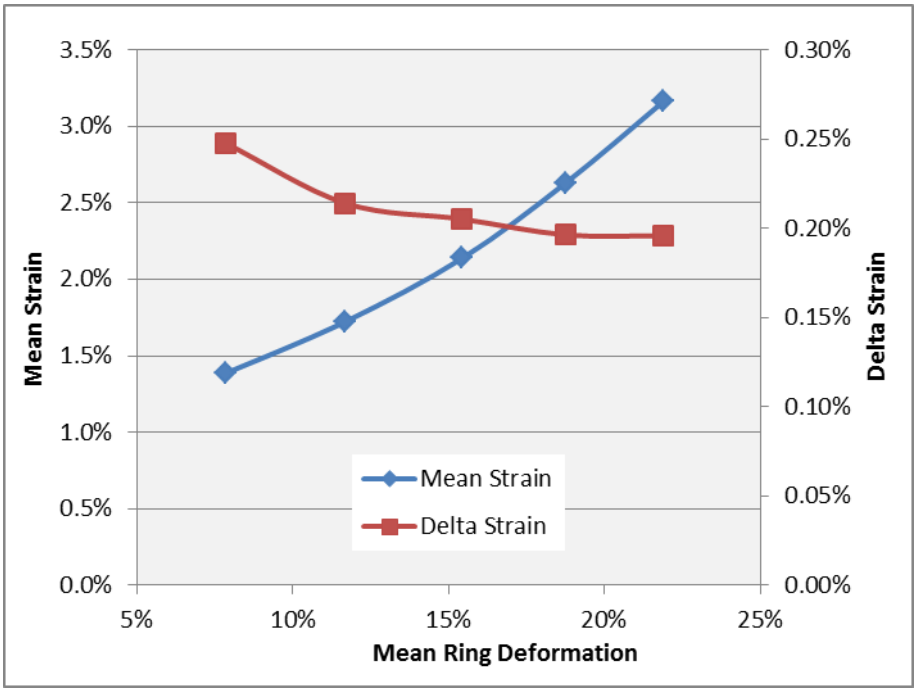

Figure 67 - Mean-Strain and Delta-Strain relation with the ring deformation level for a OLB28 R1 ring.

Analysis from the parametric studies on the OLB28 R1 strand shows the relation of both mean-strain and delta-strain with ring deformation in Figure 67 for a ring percentage pulsatility of 5%. As mentioned above; this range of ring deformation relates to approximately 10%-30% oversize for the device. (*Anaconda* devices are recommended to be implanted at 10%-20% oversize, and 15%-25% for fenestrated cases.) The mean-strain relates fairly linearly with the ring deformation however the delta-strain drops slightly with increased deformation. This is consistent with that found in Chapters 6 and 7, where it is discussed further.

The simulations varying ring pulsatility (at the same level of average deformation of ~12%), introduced in Figure 66, confirm that there is a linear relationship between percentage pulsatility and delta-strain as plotted in Figure 68.

The further studies which investigate the influence of wire diameter and ring diameter in isolation provide the results which are plotted in Figure 69.

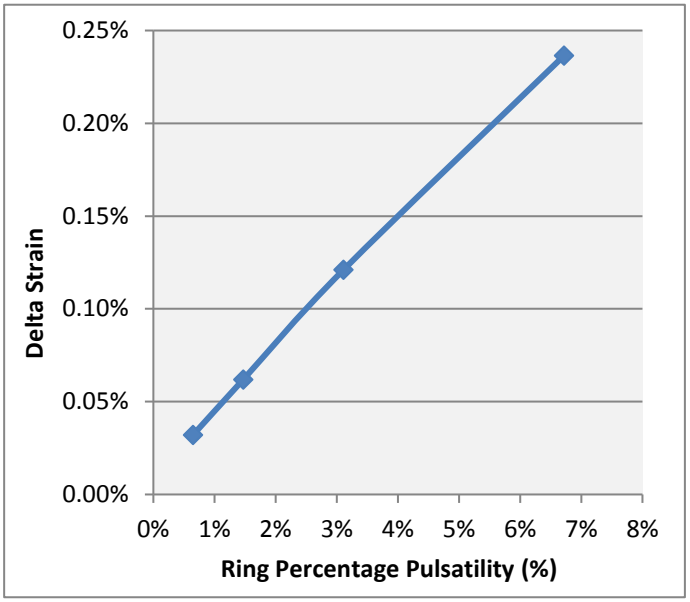

Figure 68 - The linear relationship between delta-strain and ring percentage pulsatility according to the simulation results of single strand OLB28 R1

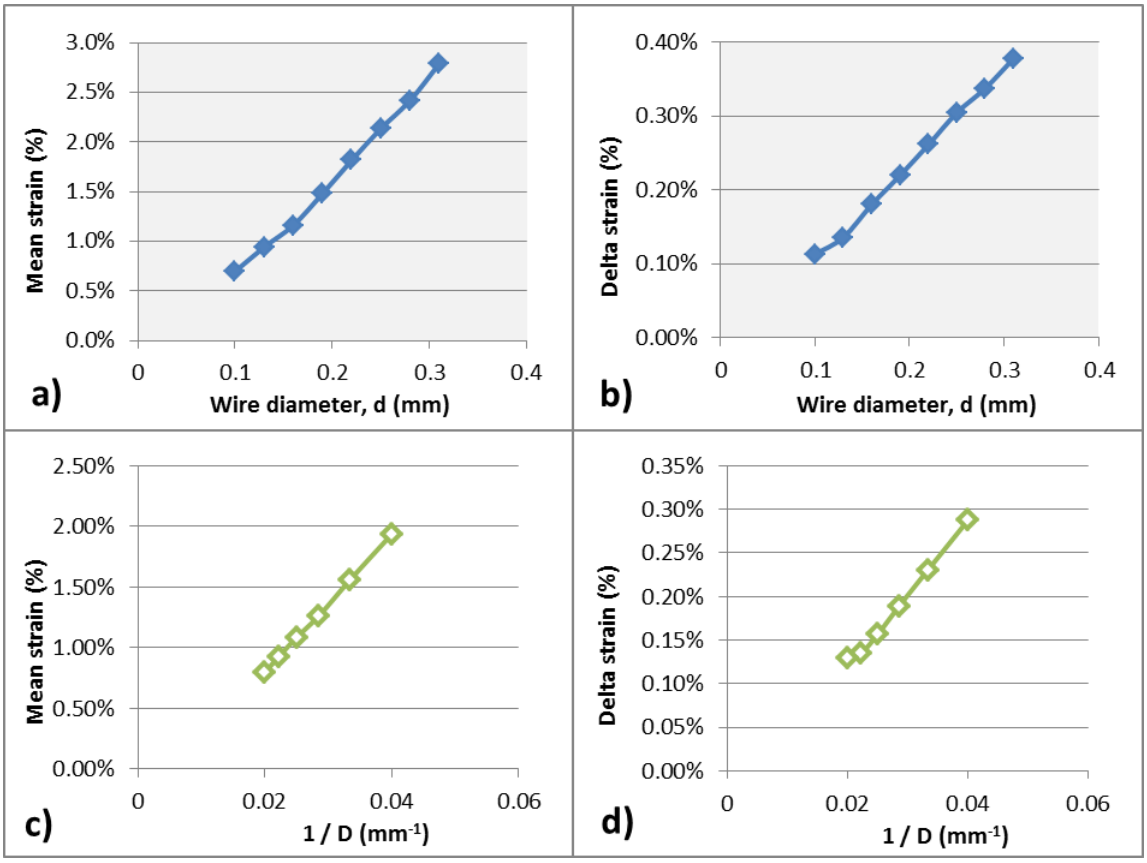

Figure 69 - Results from parametric study showing strain relations: a) mean-strain vs wire diameter; b) delta-strain vs wire diameter; c) mean-strain vs 1/D; d) delta-strain vs 1/D, where D is flat ring mean diameter.

For clarity: during the parametric study in which the ring diameter was increased, the other parameters of wire diameter, ring deformation and pulsatility were all kept constant as normal. Keeping ring deformation constant actually requires the vessel size to increase proportionally with ring diameter.

Considering fundamental beam bending theory the mean-strain levels are expected to be proportional to wire diameter and inversely proportional to the diameter of curvature. Since the latter is proportional to the ring diameter being modelled, then mean-strain is expected to be inversely proportional to ring diameter. The simulation results in Figure 69 are consistent with this for mean-strain and this is also reflected for delta-strain.

5.4.2 Radial Strength Analysis

Radial force is a quantification of the load applied by a stent on a vessel in the outward radial direction. It is an important indication of the 'strength' of a stent device and there are efforts in the industry to standardise the way in which it can be measured empirically [92]. In the case of linear springs, the force exerted is proportional to the deflection the spring is loaded to, and the 'spring stiffness'. However as shown in 5.2, the Nitinol ring-stent does not behave like a linear spring and has varying stiffness depending not only on deflection, but the loading history. The term 'strength' will be used herein primarily to mean the radial force which a ring-stent exerts on a vessel, when loaded to a degree of 'saddle shape' position, however stiffness will also be considered.

Vascutek have historically used a formula to comparatively assess the radial strength of their ring-stents (Eq. 5.5) based on number of turns, *n*, wire diameter, *d*, and ring diameter, *D*. Referred to in the previous work as the 'Lutz Strength' (after the inventor of the ring-stent), this formula provides a comparative coefficient, however the workings behind the derivation of the formula were not fully explained.

$$Lutz\ Ring\ Strength\ Coefficient = n \times \frac{d^4}{D^3} \times 10^6 \qquad \textbf{(Eq. 5.5)}$$

As part of the work herein, a proposed derivation of the coefficient is provided from beam bending theory in the following section (5.4.2.1). This will be compared for validity with the Finite Element parametric study on the effect of wire diameter and ring diameter in 5.4.2.4.

The radial force has been measured from the same set of parametric studies used to produce the results investigating strain above (5.4.1), using the method of measuring radial force described in 4.2.4. The radial force values from the single turn analyses are multiplied by 11, the number of turns in a OLB28 R1 ring, to give approximate total force of the bundle. (This approach has been validated in 4.5)

5.4.2.1 A Derivation of the 'Lutz Ring Strength Coefficient'

Beam bending theory is used to estimate the static behaviour of many applications which can be approximated as simple beam structures. The theory is accurate for linear problems: low deflections with linear elastic materials. The case of a Nitinol ring deformed to a 'saddle shape' is far from this linear assumption, however the fundamental relationships which beam theory is based on may still be the best way to swiftly estimate the strength of a Nitinol ring.

The aim is to relate 'Ring Strength' (the loading applied by a ring upon a vessel) to ring diameter, *D* and wire diameter, *d*.

Consider the ring-stent approximated as a simply supported circular beam with an evenly distributed load, *W*, as depicted in Figure 70. Where *D* is the length of the beam (or diameter of the ring), *d* is the cross-section diameter and *δ* is the linear deflection at the beam centre.

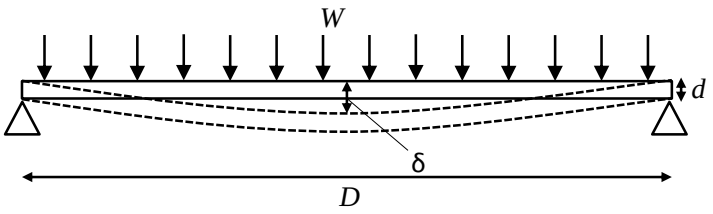

Figure 70 - A simply supported beam of length *D*, cross-section dimension *d* and distributed load *W*. The deflected position is shown by the dashed line. δ represents the linear deflection.

From beam bending theory [104], the deflection of the beam in Figure 70 is given by (Eq. 5.6):

$$\delta = \frac{5WD^3}{384EI} \qquad \textbf{(Eq. 5.6)}$$

where *E* = Young's Modulus of Elasticity
I = Second Moment of Area

Therefore, allowing the modulus to be assumed constant, the deflection is related to load, diameter and second moment of area as per (Eq. 5.7):

$$\delta \propto \frac{WD^3}{I} \quad \textbf{(Eq. 5.7)}$$

The above relation (Eq. 5.7) actually stands for all the loading and support configurations for a beam in bending given in [104], meaning that the specific configuration chosen to best approximate the ring (Eq. 5.6) is not important.

For a circular cross-section of diameter, *d*:

$$I = \frac{\pi d^4}{64} \quad \textbf{(Eq. 5.8)}$$

Therefore:

$$\delta \propto \frac{WD^3}{d^4} \quad \textbf{(Eq. 5.9)}$$

To consider how the 'ring strength' varies with ring diameter and wire diameter, a constant level of ring deformation should be considered, i.e. the same level of saddle shape. Let ring deformation be defined as:

$$\beta = \frac{\delta}{D} \quad \textbf{(Eq. 5.10)}$$

Now considering 'ring strength' as that resisting the total applied load, *W* and rearranging (Eq. 5.9) with (Eq. 5.10) for *W*:

$$\beta \propto \frac{WD^2}{d^4} \quad \textbf{(Eq. 5.11)}$$

$$W \propto \frac{\beta d^4}{D^2} \quad \textbf{(Eq. 5.12)}$$

Considering a constant arbitrary saddle height (β=const.), the absolute force applied by a ring of *n* turns can be theoretically related to ring diameter, *D* and wire diameter, *d* as:

$$\boldsymbol{F_{absolute} \propto \frac{d^4}{D^2} \times n} \quad \textbf{(Eq. 5.13)}$$

However, if we assume that larger ring-stents are to treat larger vessels, and that larger vessels will require a greater absolute force, proportional to their diameter, then the force of a ring relative to its own diameter would be an appropriate way to standardise 'ring strength' independent of size (Eq. 5.14):

$$\boldsymbol{F_{relative} \propto \frac{d^4}{D^3} \times n} \qquad \textbf{(Eq. 5.14)}$$

The relation for a relative radial force given in (Eq. 5.14) is used in the 'Lutz Ring Strength Coefficient' (Eq. 5.5). It is the relative force rather than the absolute force which is most useful for comparing the strength of stent-graft devices of various designed diameters.

5.4.2.2 Considering the Ring Strength Calculation for Stiffness

Aiming for a constant 'relative radial force', $F_{relative}$ to design ring-stents for a product range with various sizes implies that the force required to load a ring to a certain ring deformation (Eq. 5.1), or 'saddle shape', is proportional to the ring's flat diameter, and that the radial force applied to the vessel should be proportional to the vessel diameter. However, if the 'stiffness' of such ring-stents is defined as the force applied per unit change of diameter (i.e. N/mm), then rings designed with this theory will have a constant ring stiffness because the change in diameter for the given 'saddle shape' is also proportional to the ring's flat diameter. In other words; the absolute stiffness, $k_{absolute}$ is proportional to $F_{relative}$ and therefore d^4 and $1/D^3$:

$$\boldsymbol{k_{absolute} \propto F_{relative} \propto \frac{d^4}{D^3} \times n} \qquad \textbf{(Eq. 5.15)}$$

This has been verified against FEA results in section 5.4.2.5.

Considering the structure of artery subject to an internal pressure; if proportions of wall thickness to diameter are assumed constant, then larger arteries will be stiffer than smaller arteries. They will result in the same diametric strain because they are exerted to greater haemodynamic loading due to greater inner surface area, but the larger arteries are fundamentally greater in stiffness under the assumption of geometric proportionality. This raises the question: should ring-stents be designed for their radial stiffness, rather than radial force, to be proportional to their size? This will be considered with the findings in section 7.4.

5.4.2.3 Radial Force vs Oversize

As a Nitinol ring is cycled in a calibrated elastic vessel with pressures representing diastolic-systolic loading, the force exerted on the vessel by the ring varies. Figure 71 shows radial force vs time plots for the cycling phase of the parametric study with various device oversize levels (approximately 10% to 30%). The variance in radial force amplitude in cycling from a low oversize to a high oversize is observed, however interestingly the mean radial force for the individual tests does not significantly vary. There is a slight settling effect over the ten simulated cycles, comparable to the settling strains seen in 5.4.1 due to the global hysteresis.

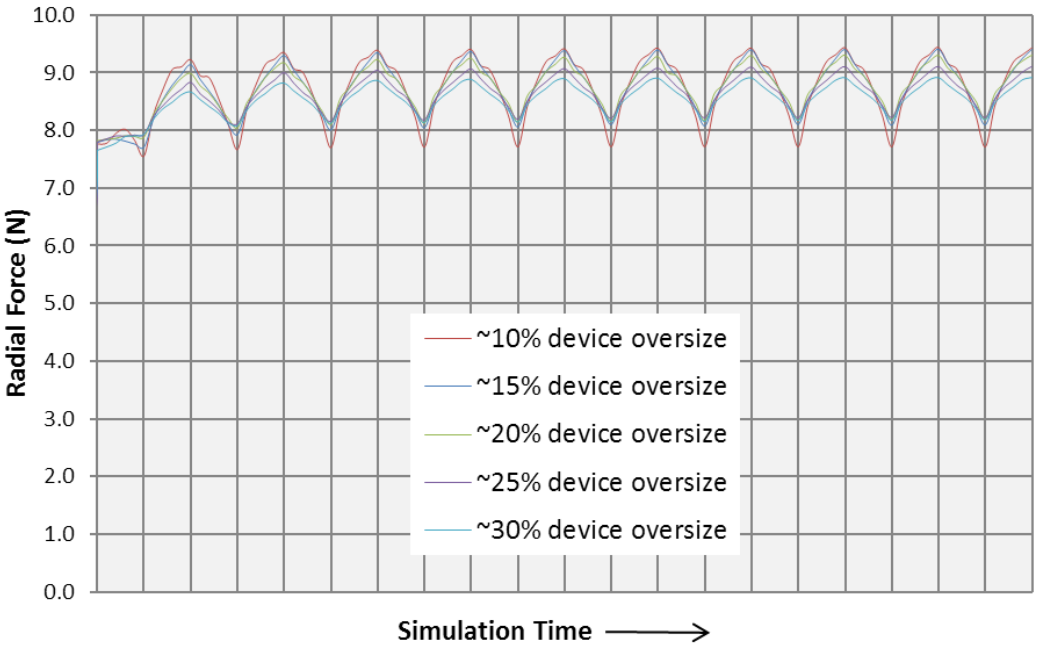

Figure 71 - Radial Force vs Time from the single turn OLB28 R1 simulations at various oversize. (The force values are representative of the full ring's 11 turns).

As with the strain levels analysis, it is more convenient to consider the radial force plotted against the ring deformation, which is related to device oversize as discussed previously. The radial force variance in cycling an OLB28 R1 ring at five different levels of device oversize, can be seen in Figure 72. As the pressure increases from diastolic to systolic the vessel size increases, ring deformation decreases and the force during this phase is considered the 'chronic outward force'. As the pressure decreases from systolic to diastolic, the vessel size decreases, ring oversize increases and the force is considered the 'radial resistive force'. The modelling technique for the parametric studies investigating

varying oversize and pulsatility used simple elastic compliant vessels as part of the modelling method. An arbitrary low friction coefficient of 0.01 was used for this study.

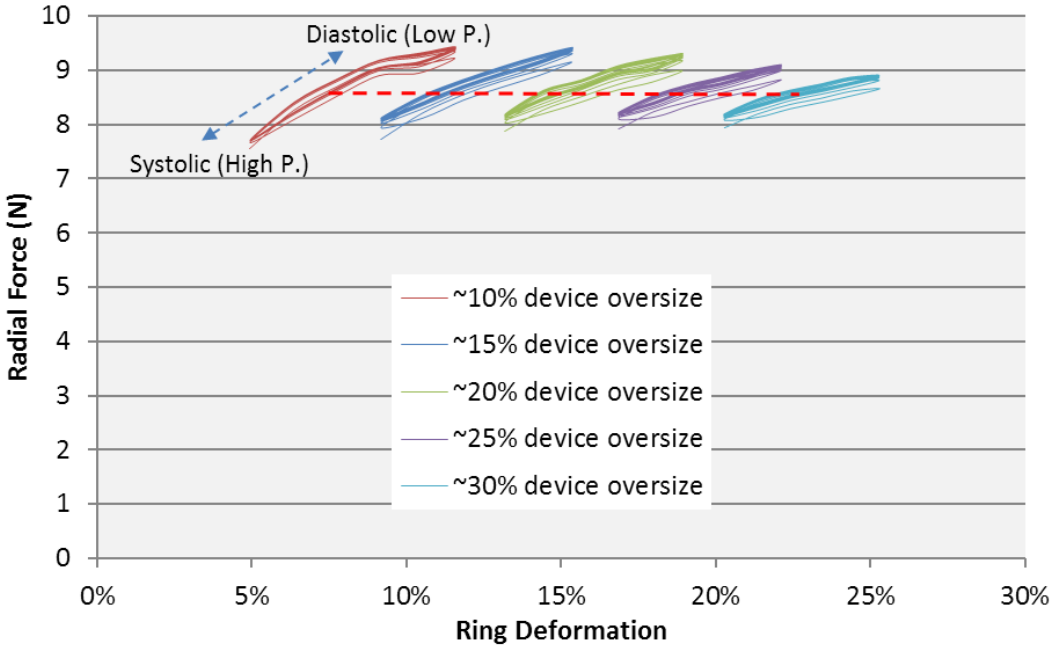

Figure 72 - Radial Force vs Ring Deformation from single turn analysis at various levels of mean deformation/oversize. (The force values are representative of the full ring's 11 turns).

Referring again to Figure 72 the mean of systolic and diastolic radial force, annotated by the red broken line, is almost constant for all levels of ring deformation, decreasing slightly from 8.57N to 8.55N as ring deformation is increased. Using the methodology described, only the OLB28 R1 ring was investigated in this way, and other ring configurations could behave differently. However, the simpler 'uniform radial loading' technique described in 4.2.3.1 was used as an early attempt to assess the loading curve of single turns of various wire diameter. The results of using this 'uniform radial loading' to investigate the radial force-oversize relation are plotted in Figure 73. A very small 'pull force' (1/1000th of the total radial force) was applied to ensure the problem being modelled was not a buckling scenario. Using this method, there is a very clear minimum force value needed before any significant increase in deformation from the flat ring position. All of the rings of various wire diameters show a relatively flat force level thereafter, with the thicker rings actually tending to reduce in force (negative stiffness). Although it is unclear from the plot, the rings of wire diameter <0.20mm have slight continuous increasing level of force as oversize is increased for the range investigated. However, the significance of this test is that over a range of 'wire diameter' to 'ring diameter' ratios which covers the range in use, the general

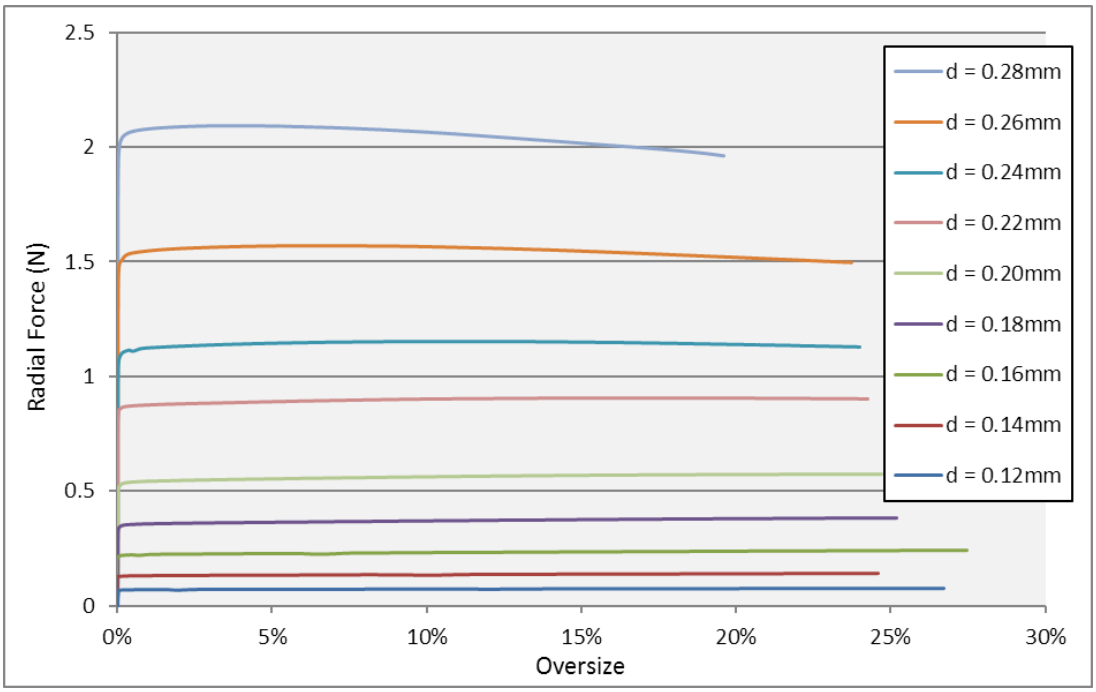

Figure 73 - Results from early simulations using the 'uniform radial loading' method to investigate radial force of single turn rings at various oversize levels across a range of wire diameters.

trend of radial force vs oversize is relatively flat, when a ring is initially compacted with the method described. This method does not represent the force levels of full bundle rings in deployed positions.

5.4.2.4 Radial Force vs Wire Diameter or Ring Diameter

Parametric study simulations varying wire diameter and ring diameter separately were used to investigate the effect on strain in 5.4.1. Data extracted from the same single-strand simulations are used here to assess the relationship of these parameters on the absolute radial force.

As was described in 5.4.2.1, simple beam bending theory suggests that the absolute radial force of a turn would be proportional to d^4 and inversely proportional to D^2 (see (Eq. 5.13)). The simplification of using beam bending equations assumes that the beam is only subject to small deflections and that the material is linear elastic – both not true for the case of the superelastic ring-stent. Therefore, the accuracy of these relations will be assessed here against the FE calculations which do take account of the non-linear effects. In all simulations in this study the rings were cyclically loaded to approximately 6% pulsatility, all at the same level of average ring deflection of ~12%.

The radial force from the single turn parametric study simulations are plotted against d^4 and $1/D^2$ in Figure 74 a) and b) respectively and compared with a linear trend line. For the study on wire diameter the OLB28 R1 ring diameter was applied while d was varied from 0.1mm to 0.31mm. The results in Figure 74 a) show that the linear approximation over this range is reasonable (coefficient of determination, r^2 = 0.976), however there is a slight decreasing gradient which would apparently become lower with increased d.

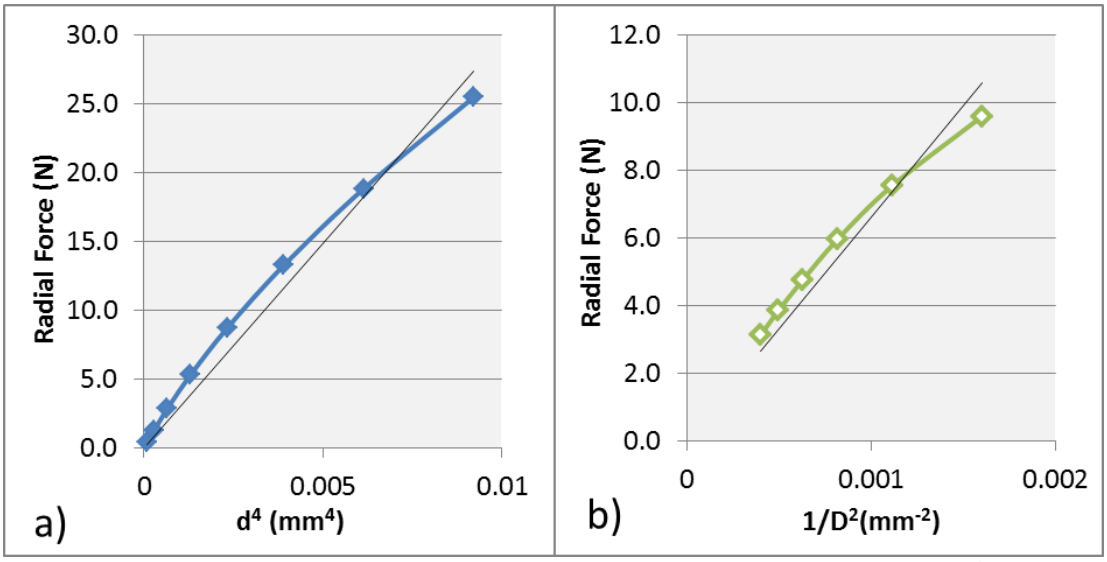

Figure 74 – Absolute Radial Force from FE parametric studies plotted against d^4 and $1/D^2$, where d is wire diameter and D is ring diameter.

The study on ring diameter used a constant wire diameter (0.22mm) and varied the flat ring mean diameter from 25mm to 50mm. The results in Figure 74 b) also show a reasonable correlation with the linear approximation (r^2 = 0.921), again however there is a slight reducing in gradient as $1/D^2$ increases. As with the wire diameter study this suggests that using the simple beam bending theory may become inaccurate outside the range tested. Using the beam bending theory will over-predict radial force for small rings of relatively thick wire diameter.

5.4.2.5 Radial Stiffness vs Wire Diameter or Ring Diameter

As discussed in section 5.4.2.2, the 'absolute radial stiffness', $k_{absolute}$ is theoretically proportional to the 'relative radial force', $F_{relative}$ and therefore proportional to d^4 and $1/D^3$ (Eq. 5.15). In the same manner as above for radial force, the FE simulation data will be used to verify these relations for $k_{absolute}$. As defined in 5.4.2.2, stiffness is considered the 'force applied per unit change of diameter' (i.e. N/mm), therefore this was extracted from the simulation as:

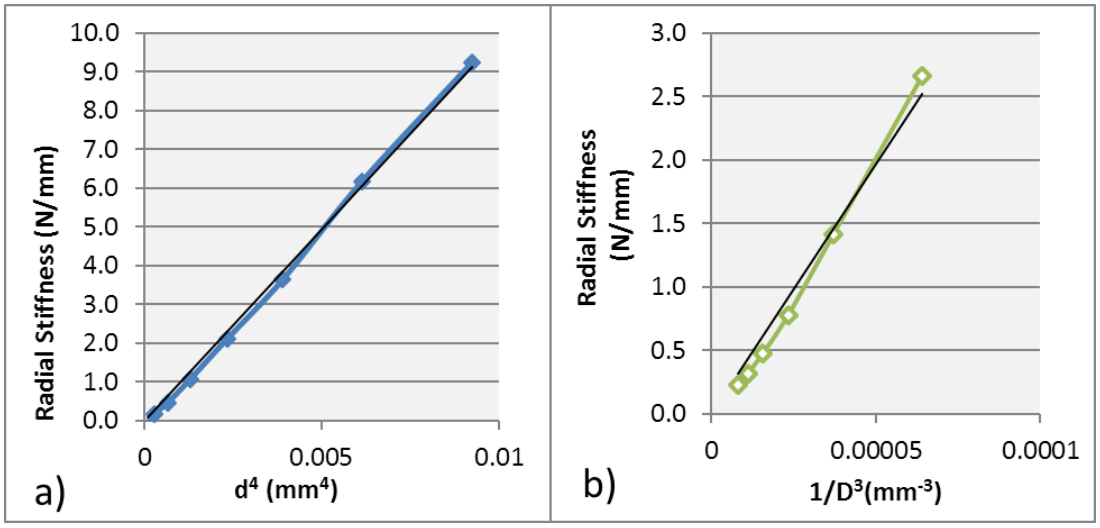

Figure 75 – Radial Stiffness from FE parametric studies plotted against d^4 and $1/D^3$, where d is wire diameter and D is ring diameter.

$$k_{absolute} = \frac{F_{dia} - F_{sys}}{\Delta D} \qquad \textbf{(Eq. 5.16)}$$

Where F_{dia} and F_{sys} are the absolute radial forces measured at diastolic and systolic position respectively, and ΔD is the change in diameter of the ring. The relation of $k_{absolute}$ to d^4 and $1/D^3$ is confirmed in Figure 75 to be linear, with coefficient of determination values r^2=0.997 and r^2=0.982 respectively. The variance of these stiffness results is lower than that of the absolute radial force (Figure 74), because the results are extracted from the difference in state from diastolic to systolic, which is much less non-linear than the full deformation of the ring from the flat position.

5.5 Summary of Chapter 5

Nitinol rings experience high levels of strain, and exhibit superelasticity at the peaks and valleys of the ring when radially deformed into a saddle shape. Much of the wire between peak and valley remains at low strains, in the Austenite phase. The use of the superelasticity to allow high deformation inherently means that a 'global hysteresis' is observed in terms of radial force and strain levels, and it is therefore important to consider the full load history which a Nitinol ring experiences to some degree of accuracy.

The investigations into the radial force vs oversize relationship of a Nitinol ring being initially deformed radially suggests that the radial force which a ring will exert is relatively

constant once in a saddle shape. The study on cycling a OLB28 R1 ring at different levels of oversize after compaction agreed with this.

The 'Lutz' ring strength coefficient based on simple beam bending theory has been verified to be in reasonable agreement with FEA simulations as an effective method of comparatively estimating the 'relative radial strength' of rings, for the ring proportions simulated. The 'absolute radial stiffness' of a ring has been shown to be directly proportional to the 'relative radial force'.

In terms of maximum material strain levels imposed on the rings in cycling, the following trends have been found from the FEA analysis:

- The mean-strain at the peak of a wire tends to increase linearly from pre-strain value as oversize is increased.
- The delta-strain is linearly related to the pulsatility of the ring.
- As the ratio of 'wire diameter' to 'ring diameter' is increased, mean-strains and delta-strains in cycling increase proportionally.

While the work of this Chapter provides some insight into the general behaviour of a ring-stent, and some strain relevant trends which are useful to know from a design perspective, the more advanced modelling of Chapter 7 is required to assess the true loading applied to artery and the magnitudes of cyclic motion experienced by rings.

6
FEA for Ring Fatigue Testing

The purpose of physical fatigue testing on Nitinol ring components is to characterise the fatigue resistance of Nitinol wire specifically under the type of loading experienced *in situ*, so the data can therefore be used in predictive design to develop fatigue resistant devices. The nature of response of a ring whilst in the deployed 'saddle shape' in a vessel is primarily bending as opposed to uniaxial or shearing for example. As well as other factors discussed in section 2.3, the high cycle fatigue life of a material is dependent on the surface finish of the material because imperfections local to the surface are a primary source of fatigue crack nucleation. A chemically etched surface finish on the current ring wire has been found through rotary bend testing [31] to provide the superior fatigue life capability in comparison to other treatments. The limitation of rotary bend fatigue testing is that the applied strain amplitudes oscillate about a zero mean-strain, i.e. a point on the surface of the wire from which a fatigue crack may develop is cycling between tension and compression. In contrast, the most fatigue susceptible zones of the Nitinol rings (peaks and valleys) are at significant levels of mean-strain, often in the superelastic region (>~1.1% for the constitutive model with 'improved parameters' specified in 3.3), as has been found in section 5.4.1. It is therefore necessary to carry out cyclic fatigue testing on rings in a representative loading which implies non-zero mean-strain levels to the ring. A range of mean-strain and delta-strains should be investigated, aiming to find the limits at which the Nitinol wire will survive the cyclic loading. It is also important that the typical stent ring history is considered and applied to the empirical test ring, most notably: the high compaction strains and any heat cycles in manufacture.

A finite element simulation allows accurate assessment of the material strain condition, and will be used to determine the mean-strain levels and delta-strain levels of rings being fatigue tested at various level of 'saddle shape' deformation and pulsatile motion.

The physical ring fatigue test programme, described in 6.1, was run at *Vascutek* in 2015. The study design, protocol development and results analysis were overseen by R.Brodie and are documented internally at the company [105], [106]. The output from the finite element analysis, described in 6.2 and 6.3, was used to define the rings' target levels of 'saddle shape' and cyclic deformations, and then to assess the strains as a result of the actual levels (deviation from target specifications could occur during running of the tests). The ultimate output from the combined physical testing and FEA was a fatigue limit defined in terms of a 'constant-life' diagram as discussed later in 6.4, fully reported at *Vascutek* [106].

6.1 The Nitinol Ring Physical Fatigue Test

The method used by *Vascutek* to fatigue test a ring involves deploying from a compacted state (see Figure 76) to a 'saddle shape' held by polyethylene fibre lines, connected to an electromagnetically driven vibrator head at the top and a fixed connection at the bottom (see Figure 77). It is acknowledged that this setup does not apply a predominantly radial

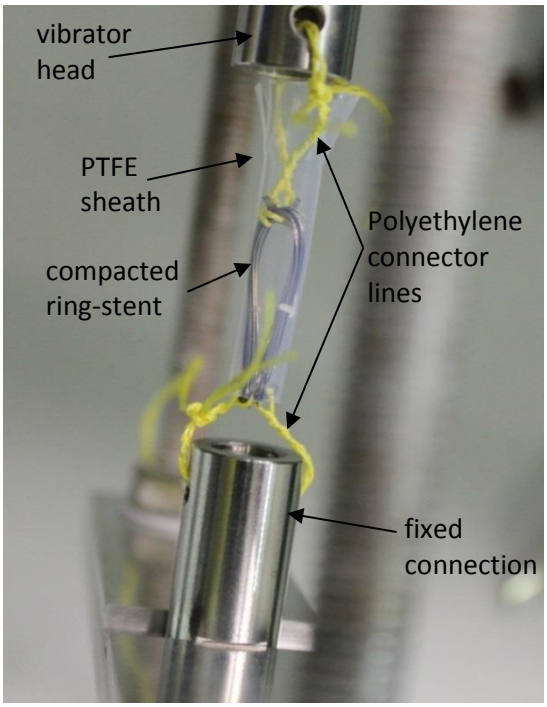

Figure 76 - Fatigue sample in compacted state prior to deployment

loading to the ring, as experienced from the interaction with the vessel *in situ*, however as explained above it is deemed appropriate as the geometric position and the predominant loading mechanism are consistent.

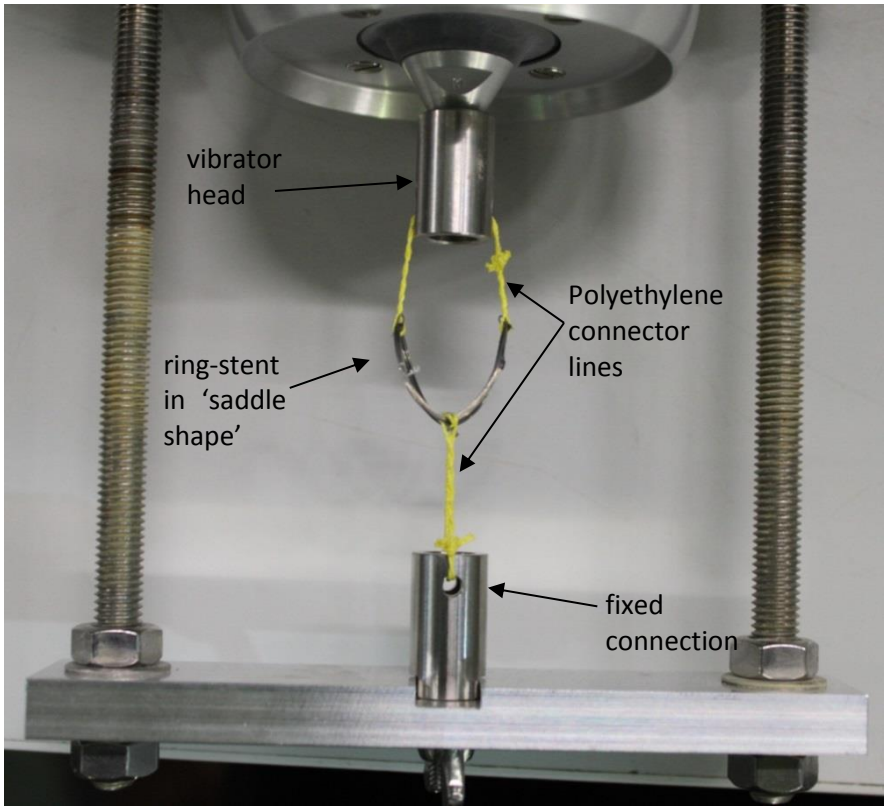

Figure 77 - A Nitinol ring in a saddle shape in fatigue test rig

The test method for each test sample, fully described by protocol [105], involves the following aspects:

- Compaction of the ring into a PTFE clear sheath three times to represent the worst-case number of compactions which can be applied to a device during manufacture.
- Subjecting the compacted ring to three thermal cycles from room temperature to 55˚C to replicate worst case sterilisation heat cycles.
- A fatigue ring sample is attached to the vibrator setup in the sheathed position, released from the sheath and adjusted to the desired 'saddle height' for targeting a specific mean-strain level.
- The vibrator heads' frequency is dictated by the mains supply frequency which is maintained to a long-term nominal value of 50Hz [107]. Variable transformers

control the input voltage load which subsequently governs the amplitude of the displacement on the suspended ring.

- The vibrating rings are submerged in water throughout for the main purpose of controlling temperature to be 37˚C.
- The motion of the ring is measured using a high-speed camera, running at 500 FPS. The most practical measurement with the equipment is the determination of the change in diameter of the ring from peak to peak, and valley to valley. The delta diameter is related to the delta-strain levels by assessing the FE data.
- Scheduled monitoring was carried out and failures (individual strand or full bundle) were recorded.
- Tests which successfully withstood the target 400 million cycles were stopped, and deemed as a 'pass'.

The inherent variability of fatigue life under constant conditions requires multiple samples per strain condition. The strain condition is composed of the 'mean-strain' and 'delta-strain' as described above. Numerous levels of both mean and delta-strain are required to properly characterise the strain based fatigue life of Nitinol wire in the described loading condition.

The particular ring which has been used by *Vascutek* for physical fatigue test is the OLB30 R1 ring: a twelve turn, 0.22mm wire manufactured to an inner diameter of 27.7mm.

The deformation and motion of a fatigue test is measured from individual frames captured on a high speed camera (approx. 500 FPS) using the appropriate software which can make a linear measurement calibrated against a pin gauge which is placed in the central axis of the test [105] (see Figure 78). The key measurements recorded are the diameters from peak-to-peak, and valley-to-valley. The protocol specifies capturing the minimum and maximum diameters from 5 consecutive cycles captured by the high speed camera. During setup and checking of samples, the minimum and maximum diameters could be specified to a tolerance of ±0.1mm. A test method validation, including a repeatability and reproducibility was carried out on the first 20 samples.

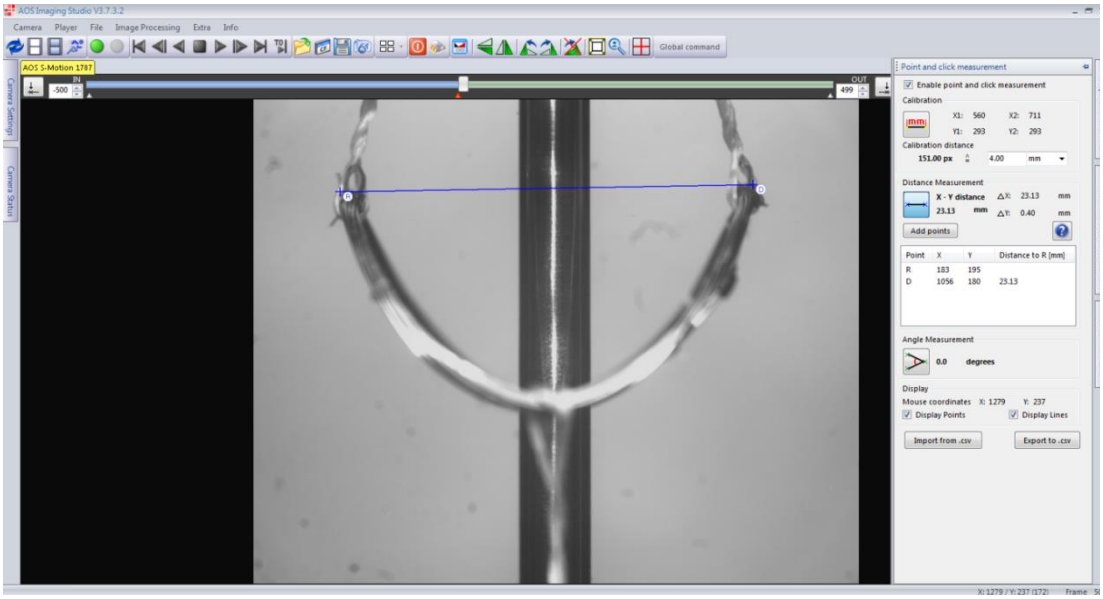

Figure 78 - The outer diameter, peak to peak, being measured with image measuring software. The image was captured as a single frame from high speed camera.

6.2 Simulation Method

The same type of static Newton-Raphson-method solver within '*Abaqus* Standard' as described in section 4.1.3, was used to simulate the motion of a single turn of the ring through the compaction and ten fatigue test cycles. As described previously, using a static analysis method assumes that the motion due to inertia can be ignored and the state of the structure is solved to be in approximate equilibrium at every incremental solution point. The stress-strain cyclic state (in simulation) due to global hysteresis is shown to have sufficiently converged from the effect of compaction after ten cycles so that subsequent cycles are not necessary. The convergence is demonstrated in Figure 79 which shows the strain at maximum extension of each cycle, from the node which is showing highest delta-strain, on a simulation from the study. The calculated delta-strain output converges to a negligible variance from previous cycle.

A sensitivity study was conducted to understand the effect of variations in both the physical setup, and simulation strategies. Subsequently, after deciding the most appropriate modelling strategy, numerous simulations of the OLB30 proximal ring were run to capture the range of possible setup configurations in terms of saddle height (analogous to mean-strain).

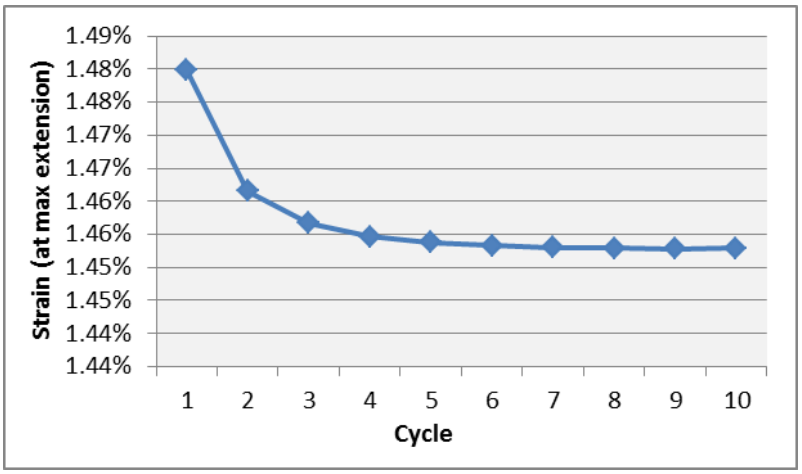

Figure 79 - Strain level convergence for the node with highest delta strain, from one fatigue simulation. Strain values are from maximum extension on each cycle.

The following are key assumptions for modelling of the ring fatigue test:

- Simulations have been run with a single strand of wire rather than the whole bundle because the single strand will still deform to the desired saddle shape and the effect of strand position in the bundle has been determined from a sensitivity study described in 6.3.3.
- The dynamic inertia effects of the oscillating system will have a negligible effect on the resulting delta-strains. Therefore, the deformation steps have been simulated using static analysis steps, approximating equilibrium at solution points.
- The long-term material cyclic state is assumed constant, i.e. there is no 'functional fatigue', and it is therefore valid to use the constitutive model for Nitinol which does not vary with the number of cycles. (Variation in global response is seen over a small number of initial cycles due to the hysteresis behaviour.)
- The polyethylene fibre lines are approximated as simple rigid connector elements only translating forces in the axial direction of the connection.

The details of the analysis are outlined in the following sections (6.2.1-6.2.6):

6.2.1 Model Configuration and Steps

The quarter turn method described in 4.2 for a single turn of Nitinol wire has been utilised to represent a single turn of the OLB30 R1. As with the previously described methodology the first step is to form the ring from straight wire. The central node of the wire model is pinned in the X-direction to prevent rigid body motion during this initial step. The

polyethylene lines connecting the ring to the vibrator are modelled as two connector elements with negligible axial flexibility: the first between the quarter turn valley and a fixed point representing the bottom attachment point (see 'Fixed Point' in Figure 80) and the second between the quarter ring peak and the vibrator head connection point (see 'Pull Point' in Figure 80). The displacement during cycling has been enforced to the top 'Pull Point'. The 'Fixed Point' and 'Pull Point' are at a distance of 6.25mm from the X-axis in the Z and Y directions respectively, which represents the radius of the vibrator head cylinder which the connector lines are threaded through.

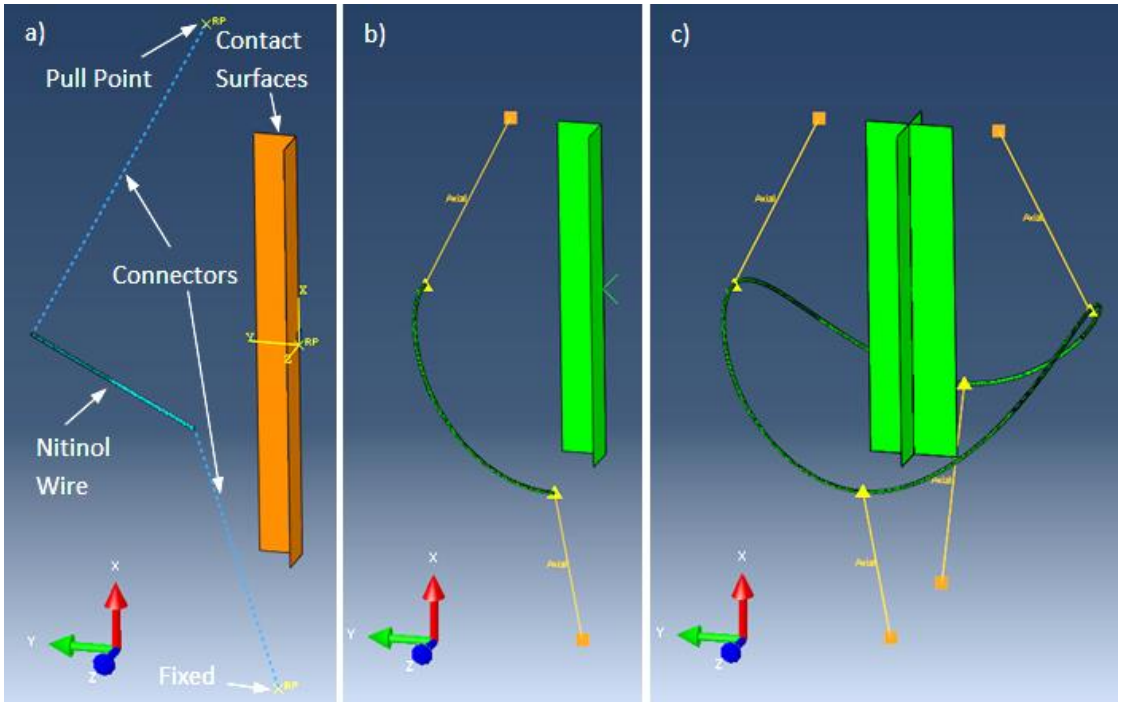

Figure 80 - a) Fatigue model quarter turn setup including wire, pull points, connectors and contact surfaces b) A deformed position of quarter turn c) Visualisation mirrors enabled to view full turn

Prior to the cycling steps, an approximation of the compaction state is applied to the single turn ring using the 'Adjustable Rigid Torus' (ART) add-on described in 4.2.3. To ensure that the compacted state of the quarter turn model is resembled properly; two artificial contact surfaces require to be employed to act as the plane at which the two peaks or two valleys would contact each other (had a full ring been modelled). The connector lines in the model are only activated at the end of the compaction step.

The steps of the simulation are summarised in the following:

- Step 1: The quarter ring model is formed from straight Nitinol wire

- Step 2: Opposing forces at peak and valley are applied (X-axis direction) to pull the ring into a saddle shape
- Step 3: Compaction step with 'ART' Add-on
- Step 4: Release compaction and activate connector elements to hold ring between the 'pull point' and the 'fixed point'
- Step 5: Move the 'Pull-Point' to initial cycling position
- Step 6-15: Cyclic steps: the pull point is controlled to oscillate over a 3mm range which would capture a large enough delta-strain value for each configuration

The application and status of boundary conditions throughout the above steps are described in 6.2.3.

6.2.2 Material Properties

The Nitinol ring wire properties were modelled using the UMAT constitutive model with the model parameters of the 'improved model' as specified in 3.3.

6.2.3 Loads and Boundary Conditions (initial and through each step)

The status of loads, boundary conditions and the 'ART' add-on, throughout the simulation steps, are provided in Table 13.

6.2.4 Discretization (meshing)

Initially the same 32 element cross-section mesh was used as described in 4.2.2. However, a slightly finer mesh (in cross-section) was applied later, increasing the number of cross-sectional elements from 32 to 60. This was deemed necessary after full analysis of various configurations with the 32 element model revealed that while the mesh is refined enough for delta-strains, the mean-strain value at the node with highest delta-strain may not be accurate with a less refined mesh (the change in delta-strain from the node of focus to adjacent was small, however the mean-strain change was significant). The sensitivity study was carried out with the 32 element version.

6.2.5 Numerical Implementation (Solution Technique and Controls)

A multistep, incremental 'static general' structural analysis in *Abaqus* Standard (6.13-4) was implemented with 'large displacement formulation' active to account for non-linearities. The 'ART' subroutine was used to provide the cylindrical, variable diameter, contact surface

Table 13 - A summary of the status of each boundary condition through the ring fatigue simulation

Step	Boundary Condition Status				
	-Central node of the Nitinol wire pinned in X-direction	-'Pull point' is held in Y and Z directions. -The 'Fixed Point' is held in all directions	-Displacement conditions applied to the wire end faces' nodes to form quarter ring	-'Pull Point' displacement/ velocity boundary condition in X direction	The 'ART' add-on is used to compact the ring
Initial State	**Applied**	**Applied**	Inactive	**Fixed**	Inactive
Step1: Form Ring	**Propagated**	**Propagated**	**Applied**	**Propagated**	Inactive
Step2: Pull ring into 'saddle shape'	**Propagated**	**Propagated**	**Propagated**	**Propagated**	Inactive
Step3: Compaction	Inactive	**Propagated**	**Propagated**	**Propagated**	**Applied**
Step4: Release to hold rings with 'Pull Point' and 'Fixed Point'	Inactive	**Propagated**	**Propagated**	**Propagated**	**Released**
Step5: Move 'Pull Point' to initial position	Inactive	**Propagated**	**Propagated**	**Displaced to initial cyclic position**	Inactive
Step6-15: Cyclic motion	Inactive	**Propagated**	**Propagated**	**Displacement cycled**	Inactive

for the compaction simulation. Solution was achieved using the direct Newton-Raphson method for each increment, with unsymmetrical matrix storage to accommodate the asymmetry of Nitinol's stiffness. The default arbitrary step time of one second was applied for each step, during which loads are applied linearly. Automatic incrementation was applied with controls on the initial, minimum and maximum increment size tailored for each step.

The convergence criteria for each equilibrium iteration are kept to the default as follows:

- the residual force at all nodes must be less than 0.005 of the time-average nodal force in the model
- each nodal displacement correction of an iteration must be <1% of the incremental displacement, except in the case that the increment has been linear (defined by the residual force < 10^{-8} of the time-averaged nodal force)

6.2.6 Validation

The validation of modelling Nitinol wire in bending is covered in the parallel work of Brodie [26] in which the load-displacement response as well as surface strain levels are validated. At the higher 'full system' level of validation: the cyclic loading of a single turn Nitinol ring into a saddle shape has been covered in 4.5.3.

6.3 FE Simulation Results

6.3.1 General Strain Location Analysis

When loaded as described into the 'saddle shape' the areas of the ring with highest strain are at the 'peaks' and 'valleys'. These zones of highest strains may not necessarily correspond to the highest delta-strains when subject to the cyclic loading. Therefore, it was necessary to conduct an initial analysis in order to understand where delta-strain results should be extracted from for all fatigue simulation cases. The variation of delta-strain in the proximity of the peak/valley was assessed in both the circumferential direction as well as along the wire surface longitudinally. The mean-strain and corresponding delta-strain results are assessed at individual nodal positions along a circumferential 'path' at the peak/valley as well as a longitudinal path which originated at the node with highest mean-strain: shown in Figure 81.

This initial analysis was carried out for three different fatigue test configurations: from a flat ring with low maximum mean-strain of ~1% to a high saddle shape ring with a maximum

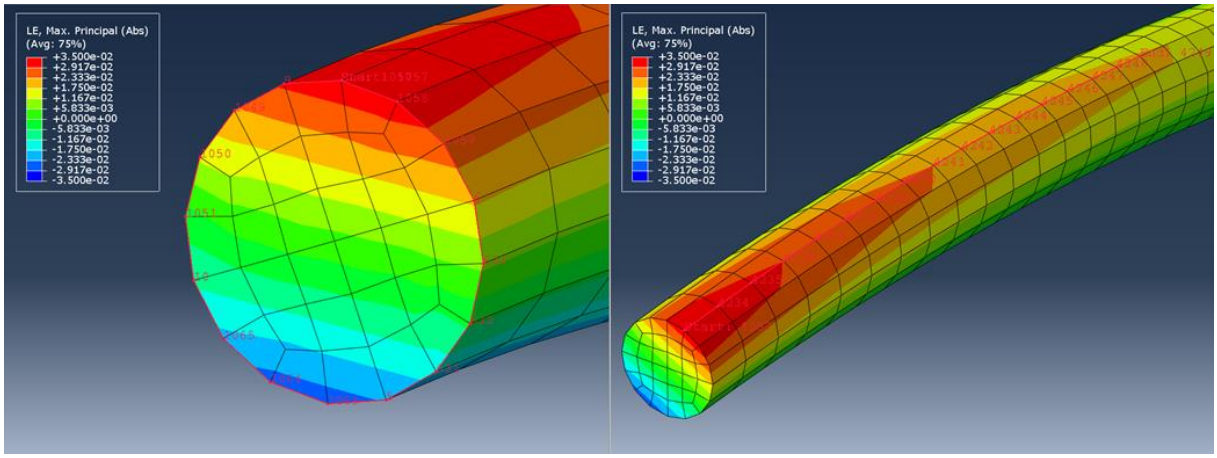

Figure 81 - Left: Peak/valley of fatigue ring with circumferential node path assessed for strain analysis. Right: peak/valley of fatigue ring with the longitudinal node path highlighted, which originates at the highest mean-strain.

mean-strain of ~6% and an average configuration with a maximum mean-strain of ~3.4%, as shown in Figure 82.

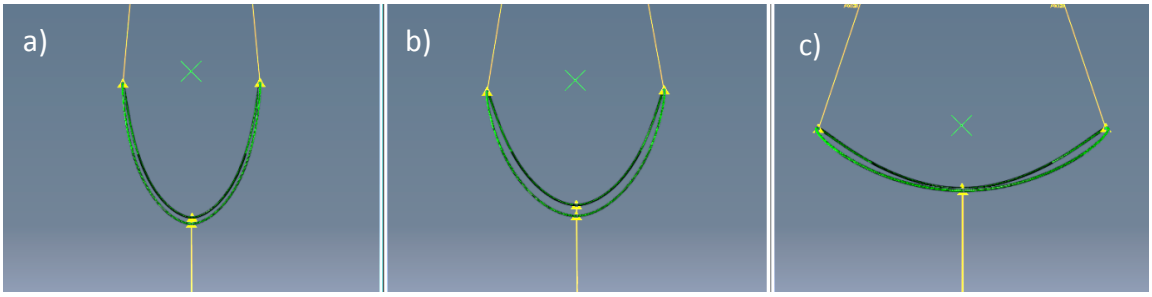

Figure 82 - Single strand ring fatigue models at various level of saddle height, mid-cycle. The highest strain levels at the positions shown are approximately: 6%, 3.4% and 1% for a), b) and c) respectively.

For the average case (mean-strain of ~3.4%), the mean-strain and delta-strain values for individual nodes have been co-plotted against circumferential position and longitudinal position in Figure 83 and Figure 84 respectively. Both plots suggest that the nodes with the highest mean-strain also experience the highest delta-strain. This result was also observed for the 'high saddle-shape' case (~6% mean-strain).

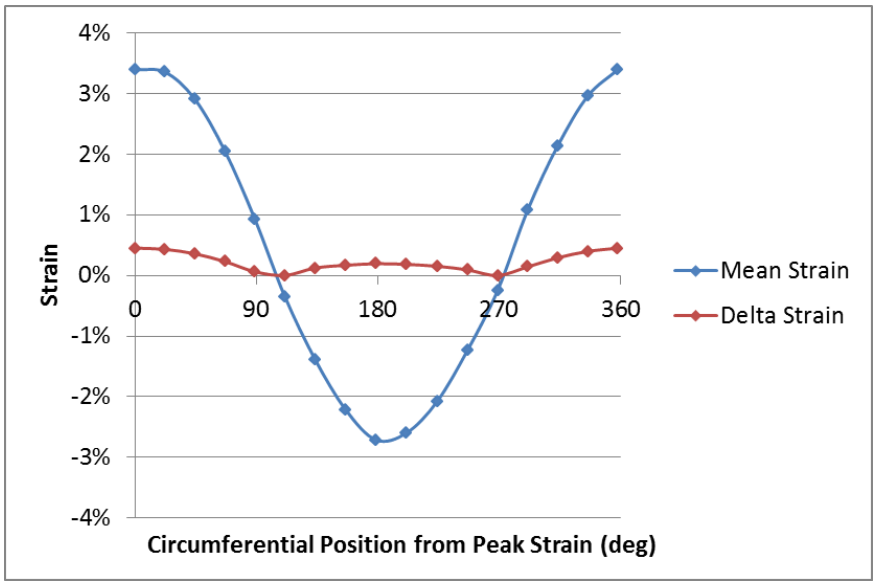

Figure 83 - Plot of mean-strain and delta-strain levels against the circumferential position around wire at peak/valley - ~3.4% mean-strain position

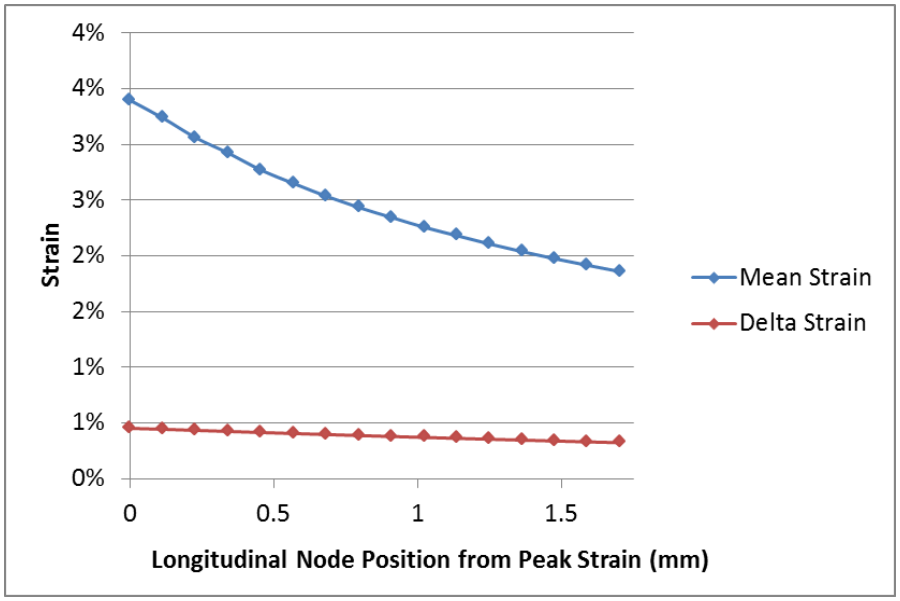

Figure 84 - Plot of mean-strain and delta-strain at peak/valley circumferential nodes for the low saddle-shape (~1% mean-strain) configuration. Delta-strain can be seen to be 'out-of-phase' with mean-strain.

However, for the low saddle-shape ring (~1% mean-strain) the above simple relationship only stood in the longitudinal plot: the circumferential results for the low saddle-shape show that the highest mean-strain and delta-strain do not occur at the same nodal position as displayed in Figure 85. This result differing from the higher saddle-shape configurations is logically acceptable: in the low saddle-shape, the plane on which the peak/valley has experienced the most bending resulting in the highest mean-strain is not the same plane at

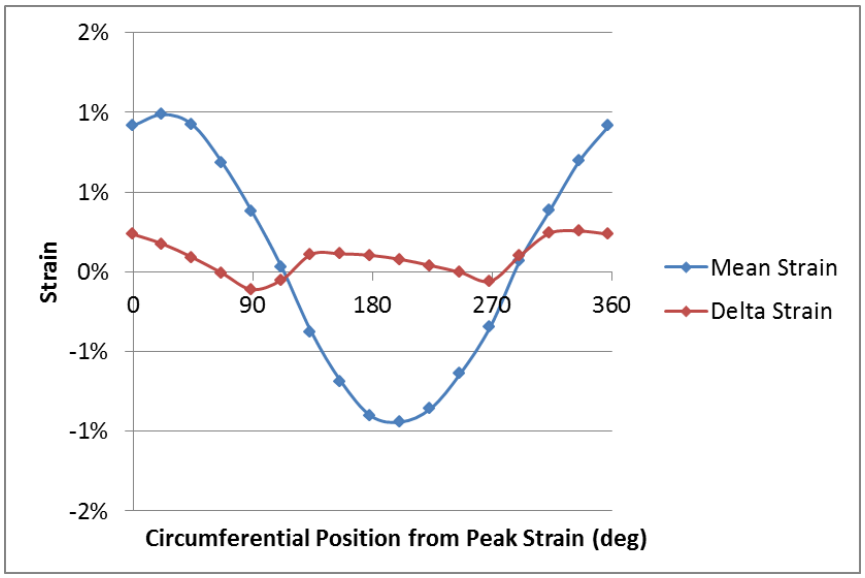

Figure 85 - Plot of mean-strain and delta-strain at peak/valley circumferential nodes for the low saddle-shape (~1% mean-strain) configuration. Delta-strain can be seen to be 'out-of-phase' with mean-strain

which bending due to cyclic loading from the connector strings occurs. Essentially; for low saddle-shape fatigue simulations it cannot be assumed that the highest delta-strain due to cyclic loading occurs at the node with the highest mean-strain. The results have suggested that delta-strain levels do reduce with distance from peak/valley in the longitudinal direction. For the final fatigue simulations, described in 6.3.4, a *Python* script was developed to assess the mean-strain and delta-strains at all nodes on the surface of the ring model.

6.3.2 Initial Analysis of Strain through the Simulation

Due to the fatigue ring being loaded essentially in the 'axial direction', which is the axis on which 'ring saddle height' would be measured; it is logical to initially consider the component strain levels against this dimension. The maximum strain in the ring is plotted against ring height for the loading, compaction, release and unloading steps in Figure 86 (black line/black dashed line). The maximum delta-strains are also plotted (red lines) from the cyclic loading at various saddle heights. The cyclic loading results were extracted from separate simulations which were all commenced from the same compacted state. As depicted by the separation between black and red lines: it is only at low levels of mean-strain (low saddle-shape) that the high delta-strains occur below the maximum strain in the model (as was found in section 6.3.1).

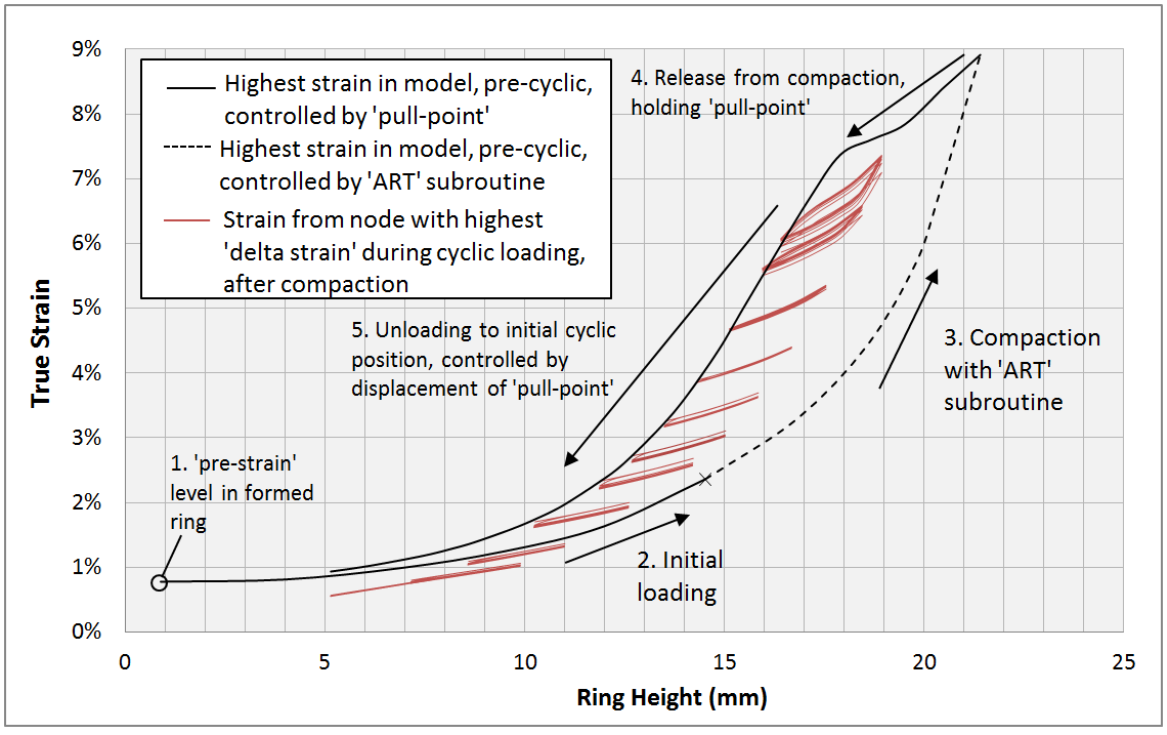

Figure 86 – Plot of strain varying with the position of the 'pull point' from FE simulation of ring fatigue test carried out at numerous levels of mean-strain

There is a significant level of hysteresis in the system; due not only to the stress-strain behaviour of Nitinol, but also the difference in the loading and unloading method: unload from compaction was not simply a reversal of the loading method.

Concentrating on the various cyclic loading simulations it can be seen that the gradient of strain-to-displacement varies slightly; tending to increase with higher ring saddle height. With the exception of the cyclic simulations at the highest mean-strain, the strain-displacement relation for each individual simulation is relatively linear without hysteresis. The reason for hysteresis occurring at the highest mean-strain levels can be explained by considering the fundamental stress-strain relation of Nitinol: the change in strain is large enough to span from lower plateau to upper plateau, at which point subsequent straining will initiate a hysteresis material response at that position as well as a global load-deflection hysteresis in the model. The level of delta-strain which would cause hysteresis in the material model varies from 0.54% assuming the austenite modulus, to 1.02% assuming the Martensite modulus. The lower mean-strain cyclic simulations do not span a large enough strain to initiate a hysteretic response. It should be noted however, that the levels of deflection applied to the ring in these simulations induce higher than required delta-strains. The final simulation (section 6.3.4), post sensitivity study (section 6.3.3), for determining fatigue life does not show hysteresis in the cyclic phases as the study was limited to a more representative range of mean-strains (<4%).

6.3.3 Sensitivity Studies

Variations in the physical setup as well as in the modelling assumptions were reason enough to warrant a sensitivity study to assess the potential effect on the results. The sole output from the modelling which will be used is the maximum rate of change of strain with respect to the diameter of the ring measured peak-to-peak as described in 6.1. This rate of change will be referred to as the 'strain gradient' in the following, and is the key measure of variability in the sensitivity studies.

6.3.3.1 Rotational Constraint Sensitivity

The combination of tension in the connection lines with a level of friction between line and ring will provide some level of constraint on the rotation of the bundle in these zones. The two extremes have been probed: no torsional constraint and full torsional constraint (at the peak and valley of the quarter wire strand) have been modelled. Constraining torsion at

the peak and valley of quarter wire induces significantly greater delta-strains or 'strain gradient' (40% greater). The torsional constraint will not be used: wire ends will be free to rotate as this is the conservative approach for developing a delta-strain limit from this perspective.

6.3.3.2 Connector Line Length Sensitivity

The connector lengths are variable on the physical samples due to the intricacy of manually tying the rings to the vibrator head cylinders, resulting in differing levels of slack when the compacted ring is connected. Once the sheath is removed the separation of the top and bottom vibrator heads are adjusted to attain the desired initial ring diameter. This 'cylinder spacing' between top and bottom has been measured from the initial round of testing to vary by 31-66mm for low saddle shape tests, 37-66mm for intermediate saddle shape tests and 42-67mm for high saddle shape tests.

The above extremes of connector line length, simulated for three saddle shape heights, to investigate the effect on strain gradient, resulted in higher values for the longer connector lines in all cases by 2.6%, 4.4% and 17.8% (low to high saddle respectively).

Modelling the shorter line length extreme will be conservative in this case because it will result in: lower strain gradients; therefore lower delta-strains for a given movement; and subsequently a lower determined delta-strain limit from the fatigue testing.

6.3.3.3 Connector Line Asymmetry Sensitivity

For the same reason as given in 6.3.3.2 the length of connector lines can vary above and below the ring. Analysing line length measurements of 48 samples found a maximum discrepancy of 58% between top and bottom connector. This ratio of asymmetry was applied to simulations at a low, medium and high saddle shapes to assess the potential effect on predicting delta-strain levels from change in diameter. It should be noted that the overall distance between the bottom and top connection point was constant: defined to be equal to the worst case 'shorter length' found in 6.3.3.2.

The asymmetric connector lines have the following affects:

- A difference in the angle of the resulting load applied to the peaks/valleys
- Asymmetrical ring in terms of average peak-peak and average valley-valley distances

- Asymmetry in terms of the diameter change in a cycle measured at peak-peak or valley-valley
- Slight asymmetry in delta-strain from peak to valley

For each of these asymmetric cases, two 'strain gradients' must be considered: one derived from the diameter measures at peak and one from measures at valley. The delta-strain is taken from the single node with the highest result in the whole quarter model, as with previous studies. The resulting strain gradients are compared in Table 14.

Table 14 - Sensitivity results from asymmetric connector line study

Saddle Height	Symmetrical S.Grad	Asymmetrical S.Grad valleys | % var. from Symm	Asymmetrical S.Grad peaks| % var. from Symm
Low	0.172	0.178 | +3.8%	0.162 | -5.6%
Medium	0.110	0.115 | +4.6%	0.122 | +10.7%
High	0.112	0.107 | -4.5%	0.121 | +7.5%

Considering that using the lowest strain gradient is the 'worst case' for defining a delta-strain limit – the above results suggest that at worst the low saddle height case with extreme asymmetry would result in a lower delta-strain by -5.6%. As this will only be for a few extremely asymmetric cases at low saddle shape, it was decided to assume symmetrical line lengths for the further fatigue test simulations. The measured outer diameters covered by this specific sensitivity study range from 16.34 – 28.46mm. Extreme cases which fall out with this category can be assessed on an individual basis if necessary.

6.3.3.4 Inner-Outer Strand Sensitivity and Effect of Manufacturing Tolerance

The design specification inner diameter, which is the key manufacturing parameter, for the OLB30 ring is 27.7mm. Using the 'circle packing' assumption a bundle diameter of 0.89mm is approximated, which subsequently results in a mean ring diameter of 28.59mm and outer diameter of 29.48mm. The diameter of the Nitinol wire used in the subject rings is 0.22mm which means an inner, mean or outer turn in the bundle would have a centre line at 27.92mm, 28.59 and 29.26mm respectively (which assumes no twist in the bundle through the circumferential length). Simulations with these three centreline diameters lead to strain gradients of: 0.1202%/mm, 0.1123%/mm and 0.1053%/mm respectively and mean-strain varies from 1.53%, 1.56% to 1.58% respectively.

The manufacturing tolerance on the ID of the ring bundle is defined as +/-0.3mm. The effect of this tolerance was simulated by applying the extremes to the mean strand in the bundle; i.e. 28.29mm and 28.89mm which yield delta-strain gradient results of 0.1157%/mm and 0.1090%/mm respectively. This represents a variation of +/-3.0% to delta-strain gradient and therefore delta-strain result.

As expected, a turn simulated at inner diameter yields higher delta-strain, however whether these delta-strains occur in the physical sample depends on the assumption that there is no twist within the bundle, i.e. turns moving from inner to outer position along the quarter length. On the contrary, using the OD strand to extract results was judged as too conservative because it is a certainty that there are wire strands in the bundle which do not occur at the outer extreme. It was therefore decided to simulate the full range of fatigue testing using a strand at mean diameter.

6.3.3.5 Location of Tie Connection to Ring

The polyethylene connector lines are wrapped around the 'eyelet' components at the peak/valley of the ring in a manner which results in the loading points being located slightly off-set from the apex of the peak/valley. This off-set was measured from 4 peak / valley samples to be approximately 0.85mm. Simulating a ring using these off-set positions as connector points (see Figure 87) decreases the delta-strain gradient from 0.1194%/mm to 0.1097%/mm: a relative decrease of 8.07%. As a result the methodology using an 'off-set' connection point will be used as it is the conservative approach from this perspective as well as considered to be a better assumption of the true loading.

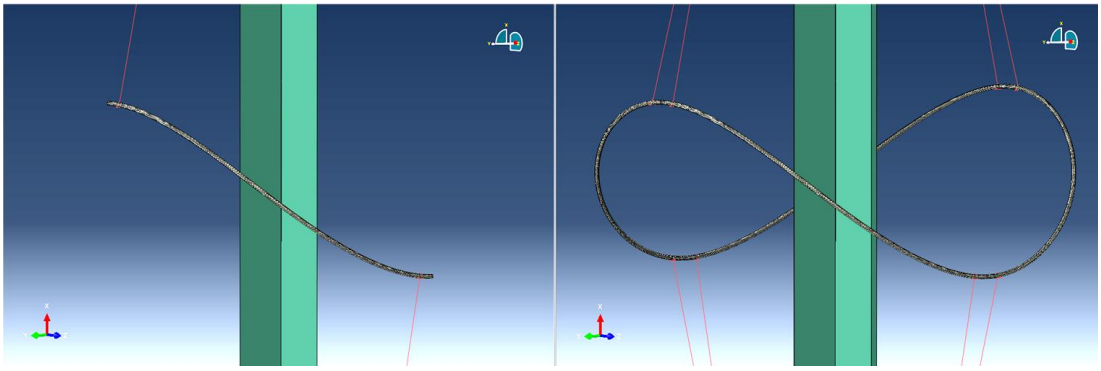

Figure 87 - Imaging showing the offset connection point of line to ring: a) the simulated quarter b) visualisation mirrors enabled to show full turn

6.3.3.6 Compaction Level Sensitivity

The diameter of sheath used empirically was 14Fr ('French, Fr' is a unit of length used in medicine. 1mm = 3Fr) which equates to 4.67mm. Considering the ring bundle in this compacted diameter; some turns will essentially be compacted to a smaller diameter. Diameters of 3.34mm and 4.00mm respectively represent a theoretical worst-case and an intermediate compaction which could be considered representative for the 'mean strand' in the bundle.

Despite the variation in maximum compaction strain simulated (8.22%, 8.71% and 9.40%), the effect on 'strain gradient' is small: 0.1206%/mm, 0.1194%/mm, 0.1184%/mm. This represents a percentage variance on final delta-strain values of +/- <1% from the mean case of compacting to 4.00mm diameter. Interestingly the final mean-strain value is affected considerably by the compaction level simulated; smaller compaction diameter results in higher mean-strain. The mean-strain levels from completion of the final cycle were 1.86%, 1.95% and 2.07% from high compaction diameter to low.

The average 4.00mm compaction diameter will be used in further studies as it is delta-strain which is of main focus, as opposed to mean-strain.

A further sensitivity on the compaction simulation method was carried out to assess the impact of the level of 'saddle pull' applied to the ring prior to full compaction. The process of compaction is substantially approximated in simulation such that; rather than the ring being pulled into a tube, the ring is initially folded to an arbitrary level of saddle shape before being compacted using the 'ART' user subroutine rigid surface. The sensitivity of strain results to the initial arbitrary level of saddle shape was probed by comparing results from two cases of initial (pre-compaction) saddle heights of 10mm and 15mm. The effect on 'strain gradient' was negligible: 0.2% variance.

6.3.3.7 Summary of Sensitivity Studies

As a result of the above sensitivity studies (6.3.3.1-6.3.3.6) the main fatigue simulations at various levels of saddle shape will use the following approach:

- A torsional constraint on quarter turn ends will not be used.
- Modelling connection lines at the short extreme was shown to be conservative, and is directly related to the measured 'cylinder spacing'. The shortest cylinder spacing

measured varied from 31mm to 42mm for low to high saddle shapes respectively. The value assumed will be calculated by linear interpolation between these values.

- Line lengths will be assumed symmetrical above and below the ring (same length).
- The bundle mean diameter strand will be simulated.
- The connection lines simulated will connect with the ring at 0.85mm from the peak/valley apex.
- The average compaction diameter (on a strand in the bundle) of 4.00mm will be used, as the variance was negligible.
- Initial saddle pull of 15mm will be used as this reduced the number of analysis increments slightly compared to 10mm, while having no significant impact on results.

6.3.4 Final Delta-Strain vs Ring Diameter Analysis

As described in 6.1 the most practical method of measuring the deformation of the ring in the empirical fatigue test is to measure the peak-to-peak diameter using a digital high-speed camera linked to a computer with imaging measurement software. The ultimate purpose of this fatigue simulation is to provide the relation between the peak-peak diameter measurements and the delta-strain state in the ring. Thus, the cyclic strain values will now be plotted against the outer ring diameter. As the FE model only represents a mean turn in the ring bundle, for the purpose of measuring the empirical test, the outer diameter is estimated by adding the value of the theoretical bundle diameter (a radius on each side).

It was found in 6.3.1 that the delta-strains tend to a higher value towards the peaks and the valleys but do not necessarily occur at the node with the highest mean-strain value. Also, from the sensitivity study investigating the point of connection to the ring (6.3.3.5) it was decided to simulate tests with the connection lines joining the ring turn at slight offset distance from the apex; this can shift the location of highest delta-strain to a node offset from the apex as well. For both reasons mentioned it was required to assess all surface nodes in the peak/valley region to identify the highest delta-strain. A *Python* script was created for post-processing which would calculate the delta-strain and mean-strain for every node and report the highest of both cases – not necessarily the same node.

The resulting strain vs diameter information, extracted from cyclic simulations at various mean-strains is plotted in Figure 88. Strain values are plotted from two nodes for each cyclic simulation: the node experiencing the highest delta-strain and the node experiencing the highest mean-strain. For most cases the strain gradient is very similar for both nodes, however at the low 'saddle shape' the node with highest mean-strain clearly has a lower gradient.

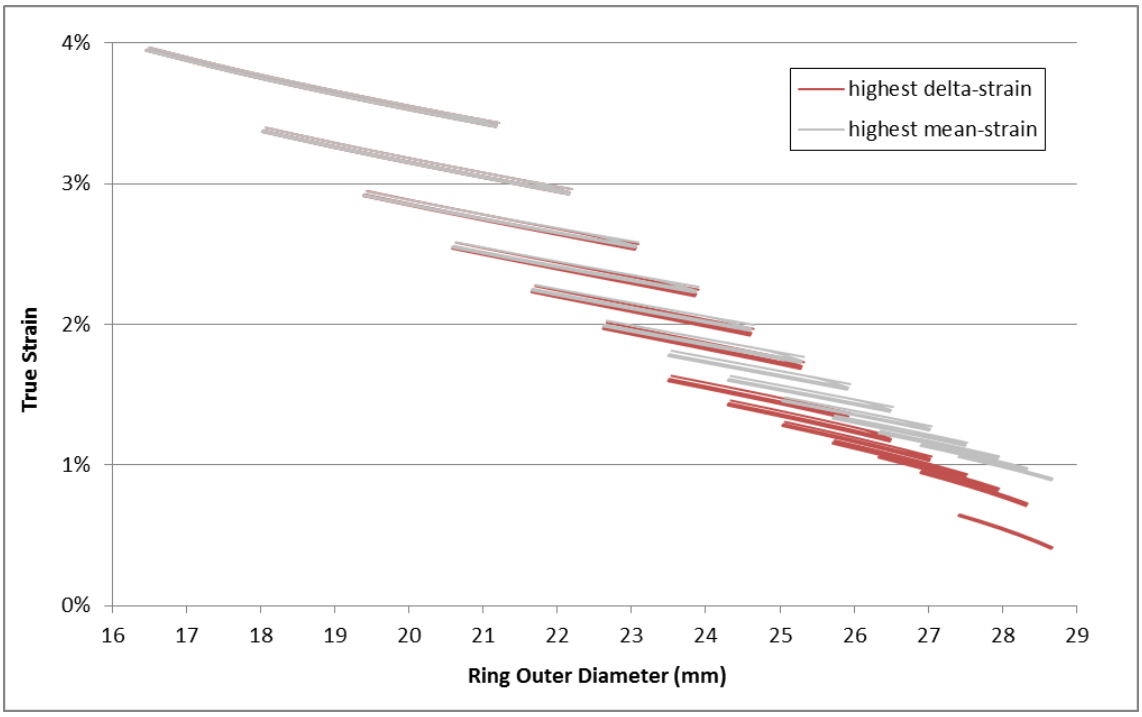

Figure 88 - Final Strain vs Diameter plot relating the delta-strain to change in diameter for various mean-strain levels for the 'B30R1' fatigue test ring

The linear gradients (change in strain relative to diameter) which best represent the data plotted have been extracted from the raw data and are used to relate ring movement to delta-strain. These gradients are only valid for changes in ring diameter equal or smaller than those simulated. However, the simulations covered a range adequate for the ring fatigue test plan.

Associating these 'strain-gradients' with the ring's initial, or 'open', outer diameter (before it is contracted in the first cycle) allows the strain state of any physical fatigue configuration to be calculated within the ranges analysed. This fundamentally required data has been extracted and is illustrated in the form of 'strain-gradient' against 'Initial/Open OD' in Figure 89. Noting that the 'strain-gradient' data values are negative, the plot reveals that the delta-strain per millimetre change in ring diameter is greatest for the flattest ring (high

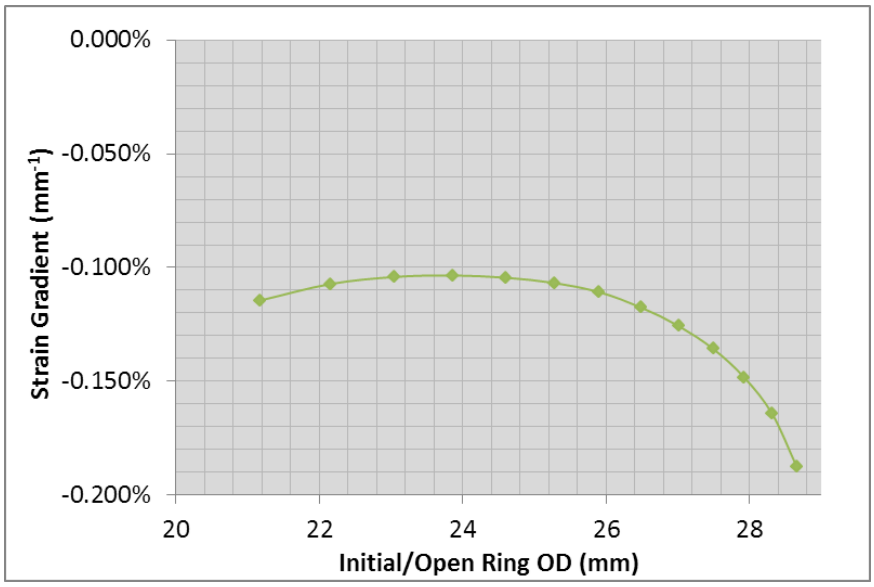

Figure 89 - Plot showing the variation of 'Strain Gradient' with initial ring outer diameter. 'Strain Gradient' can be used to calculate the maximum strain amplitudes in the empirical ring fatigue testing.

OD), and will be minimal at OD value of approximately 21mm, before increasing again slightly for higher saddle shape (low OD) configurations.

For a given initial ring OD, a specific 'strain-gradient' can be interpolated from the data acquired and multiplied by the cyclic change in diameter to estimate the strain amplitude or 'delta-strain' at the peak/valley. A spreadsheet based calculation tool has been produced which can give the strain state of a ring given the upper and lower diameters, or *vice versa*: to provide the diameters for the desired strain state.

As an example: the diameters defining the pulsatile motion of the ring required for specific mean-strains of 1%,2%,3% and delta-strains of 0.1%,0.2%,0.3% have been calculated using the spreadsheet tool and are shown in Table 15.

Table 15 - Diameters defining the pulsatile motion required for a range of strain conditions for fatigue testing of an OLB30 R1 ring, calculated using a numerical tool based on FEA analysis of a range of setup conditions

	Diameter Range (Peak-Peak/Valley-Valley) for various strain states for OLB30 R1 fatigue ring (mm)		
	$\Delta\varepsilon = 0.1\%$	$\Delta\varepsilon = 0.2\%$	$\Delta\varepsilon = 0.3\%$
mean $\varepsilon = 1\%$	26.61 – 27.37	26.12 – 27.57	25.69 – 27.78
mean $\varepsilon = 2\%$	23.50 – 24.46	22.68 – 24.60	21.88 – 24.75
mean $\varepsilon = 3\%$	20.89 – 21.81	20.08 – 21.94	19.25 – 22.06

The FE analysis described here was used to provide target ring deflections to the empirical testing [105]. The ring motions during the testing were monitored on regular basis, as they were prone to gradually acquiring some difference from the target. Hence, the FE analysis and spreadsheet tool mentioned was also used post-testing to calculate the average delta-strains of each ring sample during the tests. The resulting delta-strain fatigue limit results reported (in [106]) are shown below (section 6.4).

6.4 The 'Strain-Life' Fatigue Limit

The number of cycles defined as a fatigue limit 'pass' in the physical testing was 400M, which is slightly more than the 380M defined in standards as discussed in 2.3.2. The ring fatigue tests carried out at *Vascutek* by Brodie [105], [106] were setup at three levels of mean-strain and six levels of delta-strain, as shown in Figure 90. The number of repeat samples per strain condition varied because it was dependent on the progress of the testing, with the aim to focus on the delta-strain levels around the failure limit. (Once a high delta-strain sample had failed before reaching the target number of cycles, there would be no purpose in repeating it.) The protocol involved attaining a sample size of 5 for the delta-strain levels focused on the fatigue failure limit, at each mean-strain level. The number of test samples achieved per mean-strain exceeded the minimum requirement for

Target Strain		Wire Batch			No. of ring samples		
Mean ε range	Δε (%)	GRN 33024	GRN 42969	GRN 19123	Original plan	Updated plan	Actual Completed
Low (0.772 – 0.852%)	0.125	1	1	1	3	3	3
	0.191	1	2	2	5	5	5
	0.223	2	1	2	0	5	5
	0.258	1	1	1	5	3	3
	0.326	1	1	1	5	3	3
	0.404	0	0	1	3	0	1
Medium (1.841 – 1.867%)	0.103	1	1	1	3	3	3
	0.152	2	2	1	5	5	5
	0.179	2	1	2	0	5	5
	0.205	1	2	2	5	5	5
	0.256	0	1	2	5	3	3
	0.308	1	1	1	3	3	3
High (3.202 – 3.237%)	0.093	1	1	1	3	3	3
	0.140	2	1	2	5	5	5
	0.165	2	1	2	0	5	5
	0.188	2	1	1	5	4	4
	0.234	1	1	1	5	3	3
	0.281	1	1	1	3	3	3
				Total	63	66	67

Figure 90 - Sample plan from Vascutek Report: RD 1601R Nitinol Ring Fatigue Material Characterisation Testing Report [106]**.**

'exploratory research' of 15, based on a statistical justification following guidelines of BS ISO 12107 [108]. Ring samples were constructed from three different batches of wire, indicated by the 'GRN number' in Figure 90, and it was an aim that all the key strain configurations had at least one sample from each wire batch.

The 'pass' and 'fail' results of individual ring fatigue tests are depicted in Figure 91 by square and cross symbols respectively. The dashed line represents the constant amplitude 'strain-life' fatigue limit: all ring fatigue tests on and below this line passed the 400M cycles target. Linear interpolation was assumed for the limit between the 'low', 'medium' and 'high' mean-strain levels. This fatigue limit can be used with FEA to assess the safety of ring-stents under *in-vivo* cyclic motion by comparing the output delta-strains from such simulations with the delta-strain limit defined in Figure 91.

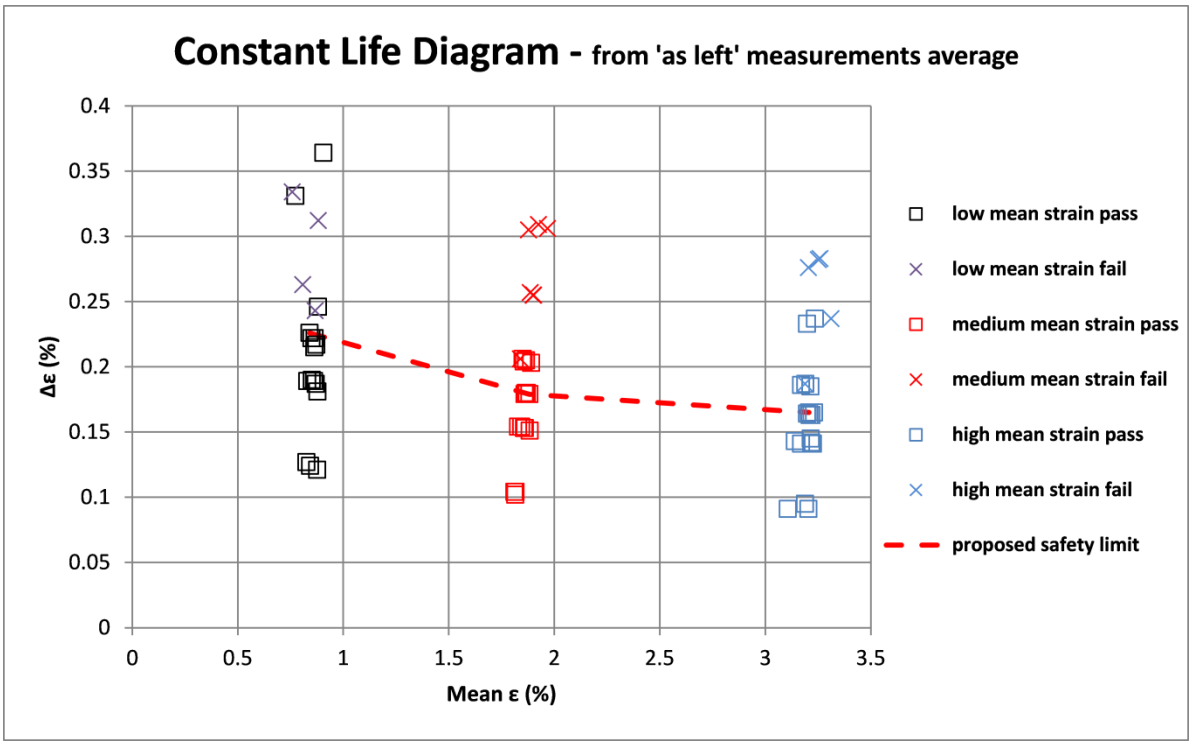

Figure 91 - The 'Constant-Life' fatigue limit diagram defined from a programme of physical ring-fatigue testing with FEA of strain levels, reproduced from [106]**.**

6.5 Summary of Chapter 6

The current ring fatigue test, used to define 'strain-life' based fatigue limits, has been modelled using the single-turn approach. A thorough sensitivity study was conducted to assess the influence of the following modelling assumptions on the levels of delta-strain:

rotational constraints, connector line length, asymmetry in connector lines, position of the strand in bundle and ring diameter tolerance, location of tie connectors and level of compaction. However, the overall result of applying the worst-case scenario for most of these options could be an overly conservative result, i.e. the delta-strain limits could perhaps be increased with more detailed modelling. Nevertheless, the above simulation strategy has been successfully applied to the physical ring fatigue testing to define the strain-life limit presented in Figure 91, which can be used to assess the fatigue safety of ring-stent devices under cyclic motion in vessel.

7

Anaconda Ring-Stent in Langewouters' Artery Simulations

The work in this chapter applies the methodology described in 4.4 to study the 'full bundle' ring-stent interacting with the non-linear aortic vessel model under pulsatile pressure for the *Anaconda* proximal rings (R1 and R2) from all device sizes. The purpose is to assess the cyclic ring motion and delta-strains for fatigue assessment, the magnitudes and distribution of the radial loading applied to the vessel, and how these factors vary with device oversize. Prior to this work, the strengths of ring-stents were not quantified in terms of units of force in the radial direction. Quantifying the radial force of *Anaconda* rings will allow comparison with some competitor devices and set a benchmark for future development. The non-linear mechanical response of aortic tissue has been modelled using data from Langewouters [47], as described in 4.3, which leads to levels of motion 'damping' as the load from the ring shifts the vessel to a stiffer zone of its pressure-diameter response curve. A comparison with a linear vessel is made to confirm that the damping is due to the non-linearity of the vessel's stiffness.

A sensitivity study on the assumptions associated with the modelling methodology has been carried out on the OLB25 R2 ring specification (section 7.3). The main study has been conducted at three oversize levels and three blood pressure ranges for each ring, and assuming a worst-case 52 year old abdominal aortic vessel model. The details of the main study design are described in 7.4.

Further parametric studies have been carried out on the mid-sized OLB28 rings to confirm the effect of artery age and also to probe the variation of delta-strains and radial force at

device oversize levels exaggerated beyond those recommended in *Anaconda* sizing chart (Appendix A), because it is known that this happens in practice [109].

7.1 Methodology and Model Definitions

The modelling methodology employed is exactly as described in section 4.4 with the addition of further cyclic loading steps to allow different blood pressure ranges, representing different classifications of hypertension, to be probed. The first blood pressure range is repeated for 10 cycles, as discussed in 4.4.3, with two subsequent pressure ranges repeated for 5 cycles each to ensure a settled result.

Automatic stabilisation has been implemented in the compaction steps, the release step, and the first systolic and diastolic steps with a specified stabilisation damping factor of 0.0001 (see 4.1.5) because the first two of these steps can exhibit local instabilities, generally due to change in contact statuses, for which the solver may not converge on a solution. If the damping forces were significant in the solution of the last increment of the release step, the subsequent step (first systolic) could be initially unstable if the stabilisation was turned off abruptly, and therefore the stabilisation was continued for the first systolic and diastolic step, after which the solution is stable and linear enough to turn damping off.

The ring specifications used to define each model (wire diameter, mean ring diameter and number of turns) are listed in Appendix I. For each ring, three separate models were created with different nominal vessel diameters representing the lower, upper and the mean of the recommended vessel sizes per the sizing guide (Appendix A). This was to probe the behaviour over the said recommended range. The vessel models are designed to be at the nominally specified inner diameters at 100mmHg pressure. The OLB21 and OLB23 models are compacted to an inner sheath diameter of 6.2mm while the rest are 6.7mm.

7.2 Post Processing Methodology

The post-processing capabilities inbuilt within *Abaqus* include the ability to view deformed geometry at any simulation time point at which data was written to the ODB (output database) file, and contour plotting of requested measurables such as stress or strain. However *Python* scripts have been developed in order to analyse the multiple simulations, and the ring-stent specific measurables, in a quick and consistent manner. The scripts are executed through *Abaqus* to open and read the ODB files, however output data can be

written to spreadsheet files (or other standard information formats). For clarity of how the output measurables have been defined, the methodology of each post-processing script is described in the following:

7.2.1 Radial Force Output

For the relevant frame of the step at which radial force is to be calculated, the 'contact normal force' (CNORMF) field is extracted from the vessel nodes only. The Cartesian results of this output parameter are converted to cylindrical system components (R,θ,Z), and all results in the radial direction are summed. A post-processing script which executes this is provided in Appendix J.

7.2.2 Ring Deformation and Pulsatility

Cylindrical coordinates for every turn in a ring are extracted from the last frame of the relevant diastolic and systolic loading steps for peak, valley and mid-point of the quarter ring bundle (see Figure 92), by post processing *Python* script (Appendix K). The ODB displacement data needs to be converted from Cartesian to cylindrical as above.

Firstly, the 'flat ring' mean diameter of the ring is calculated by averaging flat ring mean diameter of all turns (refer to Figure 8). The calculated flat ring mean diameter can be slightly different to the input mean diameter for the bundle with a turn count which could not be arranged perfectly symmetrically about that input mean diameter. It was necessary

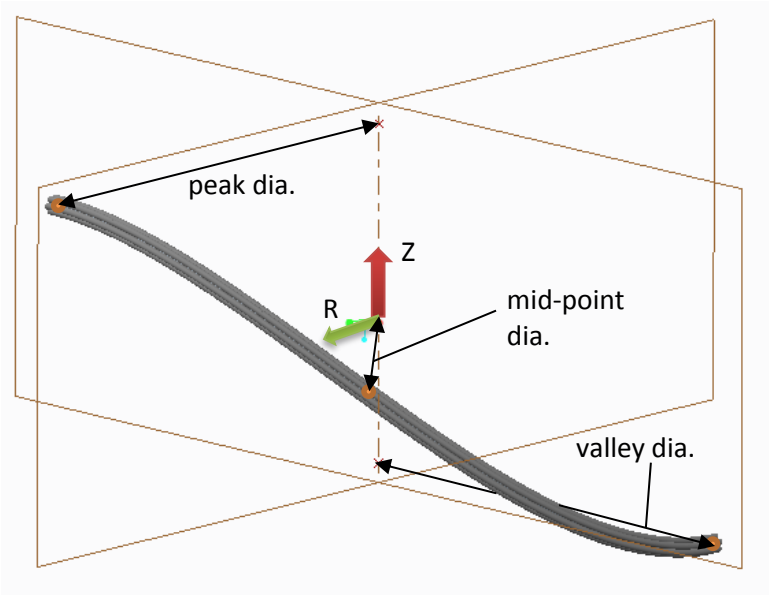

Figure 92 - Depiction of a quarter ring model in deformed saddle shape position, showing peak, mid-point and valley diameters.

to calculate the exact flat ring mean diameter for comparison with deformed (saddle-shape) diameters.

At the end of systolic and diastolic steps of interest, nodes on the centreline of each turn at the peak and valley positions were queried for Z and R axis coordinates. The mid-points of each turn were queried for R axis coordinate only. At each of the quarter ring positions (peak, valley and mid-point) the nodal coordinates of the individual strands are averaged to give the full ring coordinates. The average ring radius in the saddle-shape is collected for the peak, valley and mid-point. The ring height (by centre of bundle) is calculated by subtracting the Z position of the valley from that of the peak. The results from systolic and diastolic steps of interest are then used to calculate pulsatility.

7.2.3 Delta-Strain Calculation

As per fundamental Finite Element methodology; the strains in an element are calculated at the 'integration points', not at the surface or nodes. Interpolation is used by *Abaqus* post-processing to estimate strains at the nodes, however when calculating the principal strains a choice is presented in the order of calculation which can have small implication on the result of subsequent delta-strain calculation. The approach implemented here was to extrapolate the strain data in vector form from the integration points to the nodes before calculating the maximum principal strain invariant from the three Cartesian components. The delta-strain state of a node was then calculated by subtracting the defined maximum principal strain at systolic from that at diastolic. The 'mean-strain' was calculated by averaging these values. This calculation was carried out on the full field of results (every node in each turn). Subsequently, the *Python* algorithm (Appendix L) searches all nodes' delta-strain results to find the highest absolute value (it could be negative), the mean-strain of that node, and also the node with the highest mean-strain in the ring.

7.2.4 Radial Distribution

To analyse the radial distribution, a *Python* script was created which extracts the components of CNORMF in cylindrical coordinate system for every node on the vessel surface which had a non-zero result (Appendix M). The coordinates of these nodes are also extracted. The radial contact forces could then be summed over specific zones. The radial contact forces were summed over consecutive 10° segments in the quarter cylindrical volume. The length of outer ring circumference in contact in each 10° segment was

calculated by assuming that the path of the ring in the circumferential direction follows a cosine wave of amplitude and wavelength specific to each case - both extracted from the simulation. *Mathcad 15.0* [110] was used to calculate the arc-length of the segments accordingly (Appendix N).

7.3 Sensitivity Studies

Sensitivity studies have been carried out to assess the sensitivity of analysis outputs to the following modelling assumptions and scenarios:

- Level of coefficient of friction between ring and artery
- Vessel thickness (keeping overall artery stiffness constant)
- Sensitivity to the wire diameter specification tolerance
- The effect of compaction on the resulting *in vivo* behaviour
- The effect of constraining wire ends as was applied to represent the validation test

An OLB25 R2 ring has been used for this study in a 23mm (at 100mmHg) diameter vessel with a blood pressure range of 70-130mmHg. As described in 4.3, a worst-case 52-year-old vessel model has been implemented, assuming the worst case 'high' value of parameter p_1. The datum vessel wall thickness modelled (undeformed state) is 1.4mm as per justification in 4.3. The strain and radial force results of each sensitivity study are presented and discussed in the following (7.3.1-7.3.5).

7.3.1 Coefficient of Friction (CoF)

With a lack of definitive knowledge on the coefficient of friction between stent-graft (Nitinol or polymer graft material) and arterial tissue, it was decided to assess the sensitivity and adopt a worst-case approach for further analyses. The coefficient of friction has been probed from an almost negligible value of 0.01, to a relatively high value of 0.40. A completely frictionless simulation was not probed because it can be more susceptible to instabilities.

The results in Figure 93 for the OLB25 R2 ring, show that the resulting delta-strain value is highest at the lowest CoF value ($\Delta\varepsilon$ = 0.0314% at CoF=0.01), reduces to a minimum for the case of CoF=0.2, before increasing to 0.0303% at the highest CoF value probed. The maximum strain (taken at mid cycle) in the ring had negligible variance between cases.

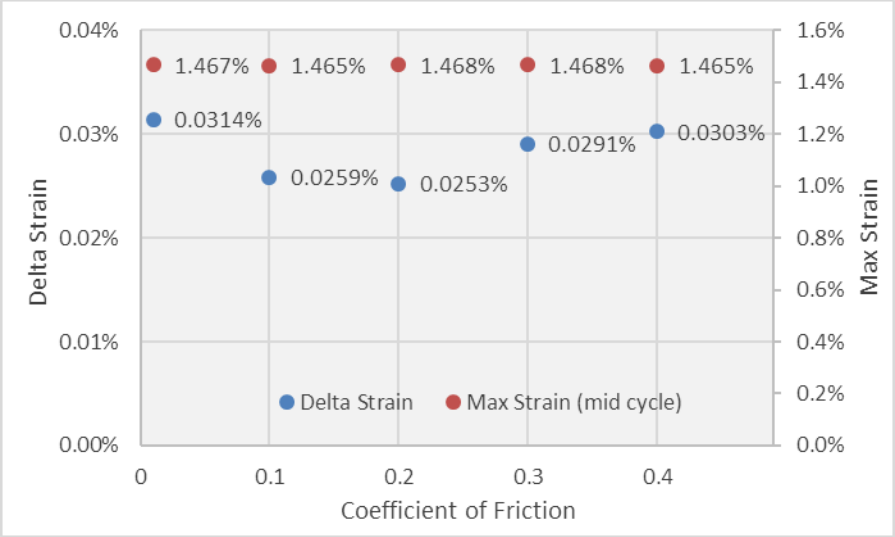

Figure 93 - Variation of delta-strain and maximum strain with the coefficient of friction implemented

The radial force exerted on the vessel at diastole and systole (70-130mmHg) are plotted with the average of these values in Figure 94. With a very low coefficient of friction there is minimal difference in radial force between diastolic and systolic, whereas this rapidly increases to be significant for the higher friction values. This gap essentially represents the frictional work in the interaction between ring and vessel between diastolic and systolic position. The average radial force decreases slightly as CoF is increased which can theoretically be attributed to a portion of the strain energy in the ring being exerted against friction in the in longitudinal and circumferential directions.

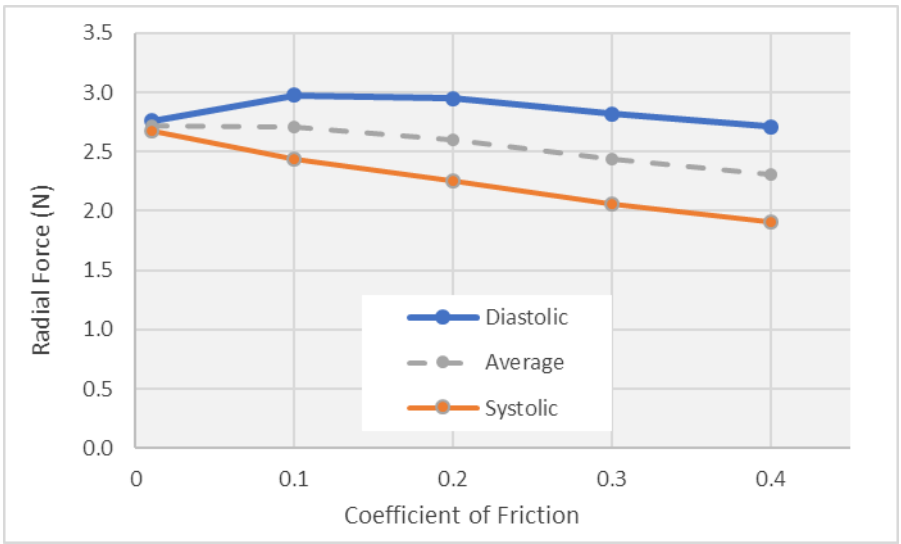

Figure 94 - Variation of radial force reading with value of coefficient of friction implemented

As a result of this sensitivity study, it was decided to apply the worst-case CoF for delta-strain results, which was the lowest friction of CoF=0.01, for later studies (7.4 and 7.5).

7.3.2 Vessel Wall Thickness

Multiple vessel models were created, through the process described in 4.3, with wall thicknesses of 0.4,0.9,1.4,1.9,2.4mm. These separate models will have differing material properties such that the same pressure-diameter response was achieved (i.e. the thickest vessel is modelled with least stiff material properties, and thinnest with the stiffest material).

Mesh density was kept roughly the same level across the study, meaning that the thicker vessels had a greater number of elements through the wall.

Results for both delta-strain and the maximum strain mid cycle are plotted in Figure 95. The maximum strain raises slightly, indicating that the ring does not result in precisely the same shape for the different vessel thicknesses, however the difference in strain levels are relatively negligible. The variance in delta-strain is slightly greater than in mean-strain, ranging from 0.051% to 0.058% at 1.9mm and 0.4mm vessel thicknesses respectively. The datum 1.4mm vessel which was the average found in literature resulted in 0.055% delta-strain.

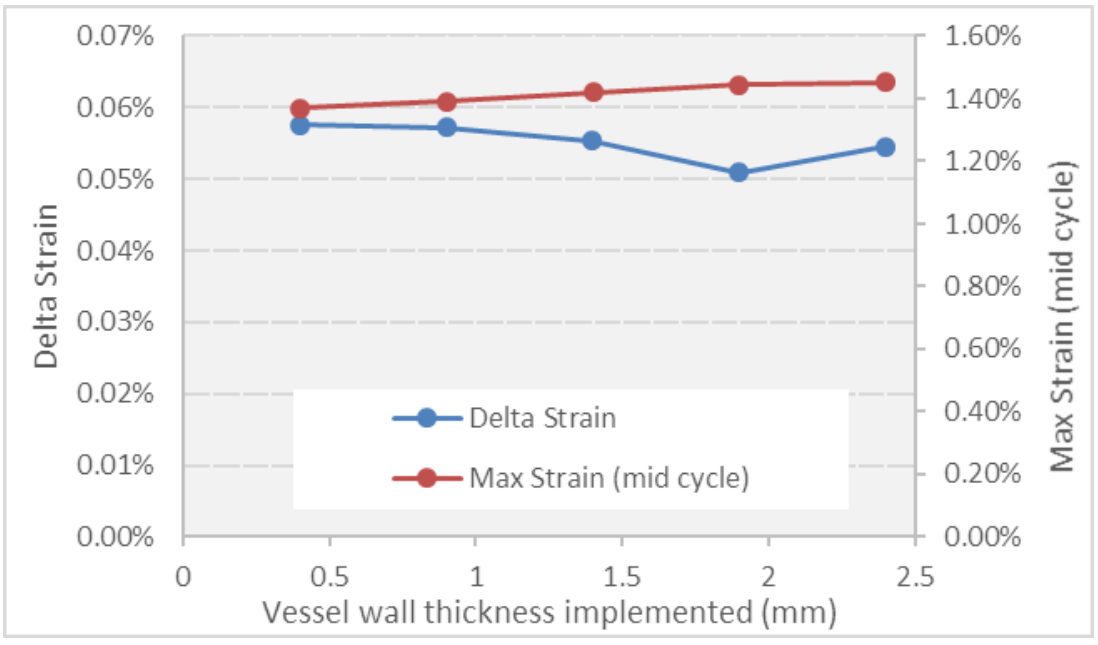

Figure 95 - Variation of delta-strain and maximum strain with vessel thickness implemented (constant compliance)

This sensitivity study shows that there is relatively little change in strain result dependent on the assumption of vessel thickness applied to the modelling approach. As a result it has been judged reasonable to assume the average vessel thickness of 1.4mm found in literature as reported in 4.3.4.2.

The vessel thickness modelled had negligible effect on the radial force results as expected.

7.3.3 Wire Diameter

The tolerance on the diameter of Nitinol wire ranges from ±0.0025mm for 0.10mm and 0.12mm wire, ±0.005mm for 0.13mm – 0.20mm wire, and ±0.0075mm for 0.22mm and 0.24mm wire [111].

It was found that for the OLB25 R2 ring, which is comprised of 0.20mm wire, reducing the diameter down to the tolerance minimum of 0.195mm raised the delta-strain result by a considerable 8.4%. While a finer wire bending the same degree as a thicker wire produces a lower delta-strain, this is countered and exceeded by the fact that the ring is significantly weaker, leading to less damping of the vessel's compliance and therefore more motion and higher delta-strains. Considering beam bending theory for circular section: the stiffness is related to the diameter raised to the 4^{th} exponential. This beam bending rule suggests that 0.195mm wire would be 9.6% less stiff than 0.20mm wire. For the non-linear ring-stent case, the FE sensitivity study results in the 0.195mm wire ring producing 8.1% less radial force than 0.20mm wire (on average in the deployed position) which leads to 33% more diametric motion, hence the increase in delta-strain reports above, of 8.4%.

These results are not negligible and for the case of fatigue, the worst-case wire diameter should be considered. However, because a key aim of this study is to gain representative radial force magnitudes from each ring, the further studies have been specified with nominal wire diameters.

7.3.4 Compaction

The effects of not fully compacting the OLB25 R2 ring to the diameter of a sheath, instead only loading to a point adequate for releasing into vessel, were as follows:

- an increase in radial force of 1.6%
- increase in maximum strain from 1.40% to 1.47%
- a 2% relative decrease in delta-strain result

Although these variances are relatively small, further models have been run with full compaction approximation included for accuracy and in aim to provide some indicative information on compacted state of the ring-stents.

7.3.5 Torsional Constraint

In section 4.5, the potential torsional constraint applied to the ring at peaks and valleys during the 'saddle pull' validation test has been discussed and probed. A ring deployed in isolation within a vessel cannot be said to have distinct torsional constraints at peak and valley, however there is perhaps some argument for this in the case of *Anaconda* proximal rings being sutured to the hook components. Therefore, an additional comparative simulation has been run with every turn torsionally constrained at both quarter ring ends. The addition of torsional constraints on the deployed OLB25 R2 ring produced the following results:

- 24% reduction in highest delta-strain
- Maximum strain in the ring (mid cycle) was raised by 15% (1.47% → 1.68%)
- 16% increase in radial force of the ring (averaged between systolic and diastolic)

It was therefore decided not to torsionally constrain the ring in further modelling as this is worst-case for a delta-strain and fatigue assessment purpose.

7.4 *Anaconda* Proximal Rings Study

The purpose of this study is first to quantify the radial strength of all *Anaconda* proximal sealing rings while deployed in vessel, in terms of units of force. Secondly, the new capability of modelling the non-linear behaviour of artery, based on Langewouters data, is incorporated and will give the first theoretical measure of ring pulsatility, and therefore fatigue relevant strain-amplitudes, in such an environment. This will be compared to the result if a linear-elastic vessel with the same diametric strain is implemented with the same methodology. Furthermore, an extended study with the mid-size OLB28 device will investigate the effect on pulsatility with varying patient age, and the sensitivity of delta strains to excessively high, or very low device oversizing. The study on OLB28 rings also provides the first quantification of how radial force is distributed along the length circumference of the ring, and how this is sensitive to oversize. This will inform future design of ring-stents particularly for sealing, and could be used to compare against the pressure distribution of competitor devices.

All *Anaconda OLB* proximal rings (R1 and R2), across the seven device sizes, have been modelled and simulated individually through ring forming, compaction approximation and deployment into Langewouters' based artery models using the methodology described in 4.4 and 7.1, with the modelling decisions applied from the sensitivity study in section 7.3. Three different artery sizes representing a lower, mean and upper recommended vessel oversizing (per the device sizing chart Appendix A) have been applied to distinct models for each ring; totalling 43 separate simulations. In each simulation, the pulsatile ring-vessel interaction has been probed over three separate blood pressure ranges: 80-120mmHg, 60-140mmHg, and 80-160mmHg which represent a normal healthy case, a worst-case treated hypertensive case and an untreated hypertensive case respectively. These ranges are derived from considering the statistically average blood pressure ranges for males >50 years from the US National Health Statistics report on blood pressure [112]. The 52 year old abdominal vessel with the worst case 'high *p1* value' (see 4.3) has been applied to each model; this being three standard deviations below the average age of *Anaconda* patients, of 76 years [97]. The mid-range OLB28 device's proximal rings have been simulated over a range of ages (52, 60, 68 and 76 years) to confirm the effect of greater compliance in younger vessels. Furthermore, the OLB28 rings have been simulated in an extended range of vessel diameters in order to probe the effect of extremely low or high oversize on the strain and radial force performance of the ring-stent.

The post-processing and analysis considers: strain levels and cyclic amplitudes for fatigue analysis, the related pulsatile ring motion and the radial force levels being exerted on the vessel. *Python* scripts have been developed to execute post processing on the output database files (.odb) in a consistent manner as described in 7.2.

A summary of the key input parameters which define each model are provided in Appendix I. Most of the results plotted here are from the 60-140mmHg because it produced the highest pulsatility for most rings. Comparison with the other blood pressure ranges are discussed where appropriate.

7.4.1 Radial Force

The radial force results are shown in Figure 96 (averaged from systolic and diastolic) for each ring at approximate device oversize levels of 10%,15% and 20%. The *Anaconda* R1 rings are shown to exert between 4.7 – 7.9N, increasing from the smallest to largest device

Figure 96 - The radial force (average of systolic and diastolic) of Anaconda R1 and R2 rings at approximately 10,15,20% device oversize

with the exception of the OLB28 which is slightly stronger than the OLB30. The slight anomaly of OLB28 was expected as it was designed with a higher 'Lutz coefficient' (see 5.4.2.1) than other devices. The same trend is observed for the R2 rings, which exert forces in the range 2.3 – 4.0N. (The reasoning for this design choice is not explicitly known, however it is thought that it was to create a device considered 'worst case' relative to the other sizes, for some types of validation testing.) The difference in radial force due to varying oversize (from 10 to 20%) is relatively small.

It is important that the ring strength is also considered relative to the size of the device or the vessel to be treated. The 'Lutz coefficient' equation (5.4.2.1) enabled the rings to be designed with similar radial strengths relative for each ring size, with the exception of OLB28 as discussed. The 'relative radial strength' has been assessed in this case by quantifying radial strength per mm length of mean ring circumference, see Figure 97. This reveals that the R1 rings exert in the range 0.068 – 0.086N/mm with the OLB25 and the OLB28 being relatively weakest and strongest respectively. The trend repeats for the R2 rings with a range of 0.035 – 0.049N/mm. The 15% oversize results suggest that the

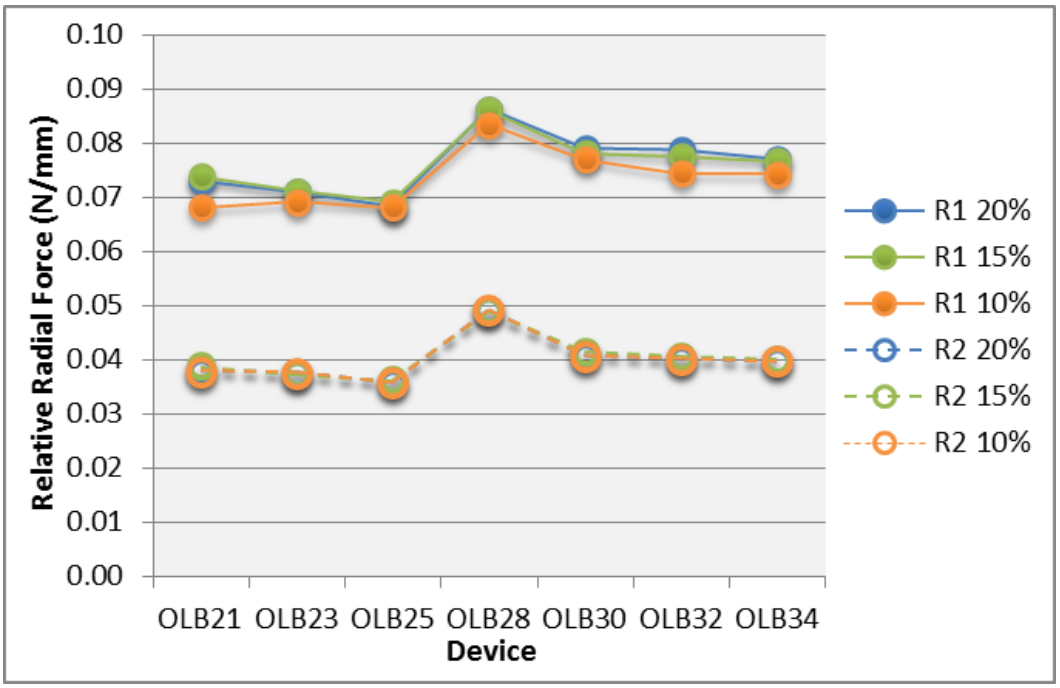

Figure 97 - Relative Radial Force (per mm ring mean circumference) of Anaconda proximal rings at approximate 10,15,20% oversize

relative force of R1s vary by ±13% (±7% if excluding OLB28) and R2s vary by ±21% (±8% if excluding OLB28).

These results represent an estimation from FE simulations based on rings acting in isolation rather than part of the *Anaconda* proximal structure: R1 and R2 rings sutured to fabric and interconnecting Nitinol hooks. The behaviour of this structure may affect the radial force levels in reality, however the rings are the key component providing radial force and therefore should be understood in isolation in the first instance. It is also considered that the ring-hook-ring structure would add stiffness and therefore be less compliant, meaning that analysing rings in isolation is a worst-case for delta-strain.

The radial force and relative radial force results are taken into consideration for the further analysis on ring motion and strain analysis. The radial force is assessed over a larger oversize range for the OLB28 rings in section 7.5.2.

7.4.2 Ring Deflection

The diastolic and systolic positional data for peaks, valleys and the mid-points of the quarter ring models have been collated for all rings by the post-processing method described in 7.2. This data on ring diameter and saddle height is subsequently used to

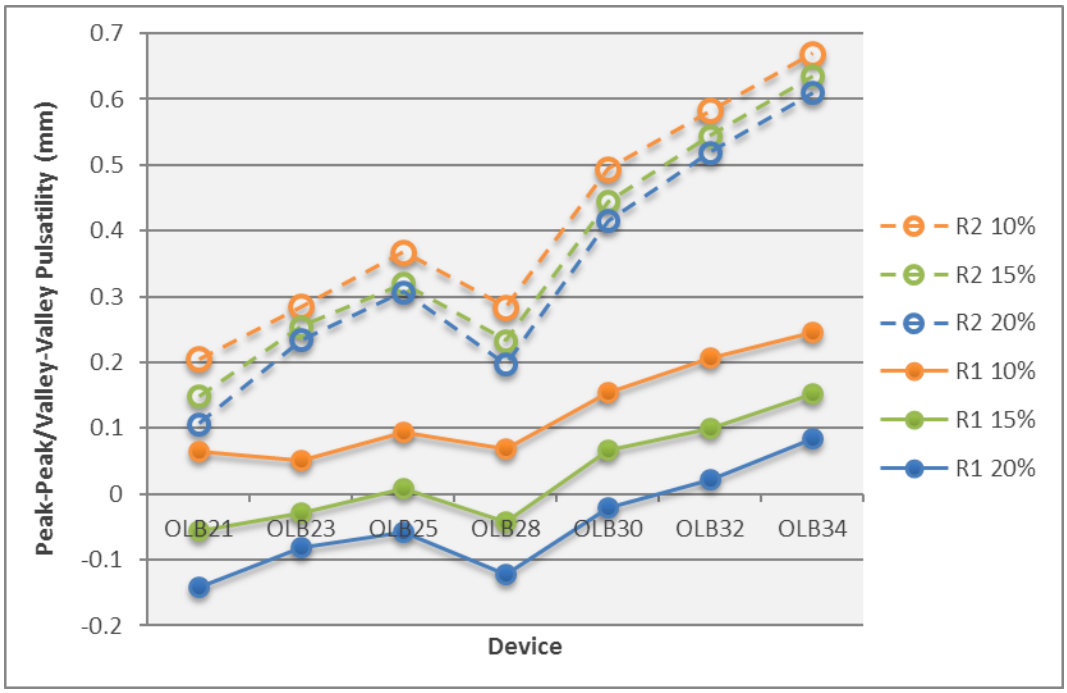

Figure 98 - The peak-to-peak/valley-to-valley pulsatility of Anaconda rings simulated at approximately 10,15,20% oversize in 52-year Langewouters model at 60-140mmHg.

calculate the 'pulsatility' of the ring which in this context will be defined as the difference in diameter or height from systolic to diastolic state.

The peak and valley location data, which vary very slightly due to differences in the bundle orientation at each end, have been averaged to provide a single value representing peak-to-peak or valley-to-valley pulsatility.

The peak-peak/valley-valley pulsatility results for all rings at 60-140mmHg are shown in Figure 98. The R2 rings show greater motion than the R1s, and are consistently being radially compressed (at peak-peak/valley-valley) during transition from systolic to diastolic state. The R1 rings, however, are not all showing a compressive movement over this blood pressure reduction: most results for the OLB21 to OLB30 at 15% and 20% (approx.) oversize result in small negative pulsatility values. The general lower pulsatility of the R1 rings can be explained by the greater damping affect which a stronger radial spring would have on the non-linear artery: locally dilating the vessel further to the stiffer, less compliant portion of the pressure-diameter curve. However, this does not explain the occurrence of negative pulsatility; increasing ring diameter with reducing blood pressure. This appears to be due to longitudinal tension in the modelled vessel (due to Poisson's effect) being reduced as pressure lowers, which in turn allows a strong ring to embed the artery wall further.

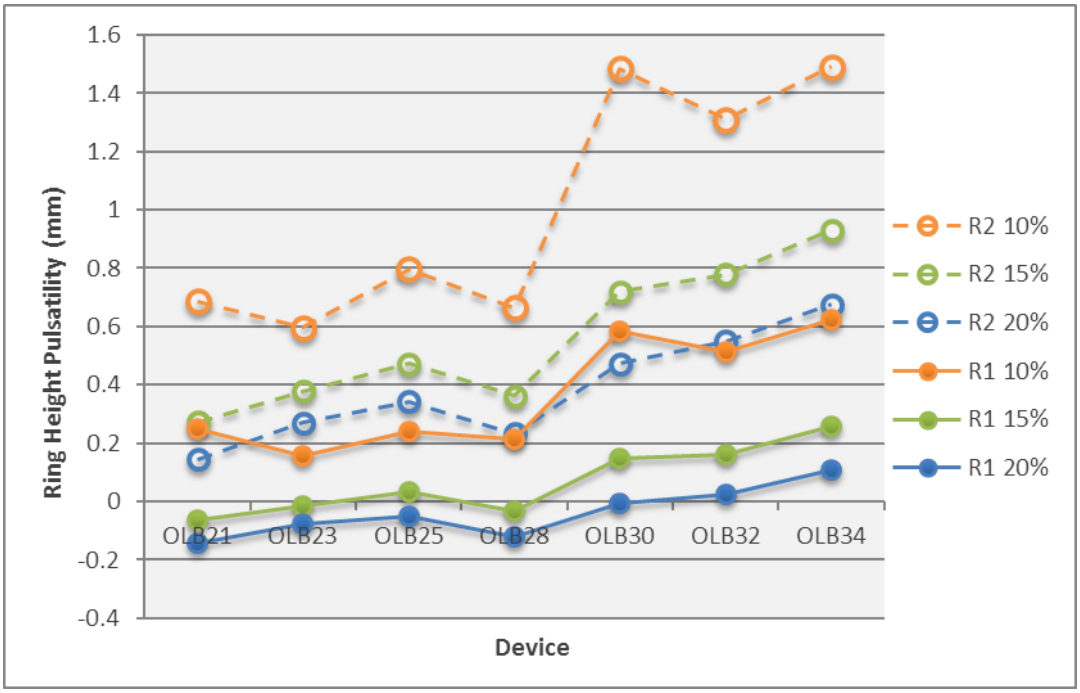

Figure 99 - Ring height pulsatility of Anaconda proximal rings at approximately 10,15,20% oversize in 52 year Langewouters model at 60-140mmHg

Regardless, the magnitudes of pulsatility of the R1s presented in Figure 98 are very small. The increasing pulsatility from small device to large is expected simply due to geometric scale. Regarding the OLB28 results which result in a dip in the cross-device trend; this correlates with the fact that both OLB28 rings have the highest relative radial strength (see Figure 97), and are therefore imparting greater vessel motion 'damping'. This suggests that the OLB28 device, with greater relative force, will be less susceptible to fatigue failure.

There is a clear and consistent trend of slightly reducing motion as the oversize is increased for any specific ring. This may be due to a greater level of motion damping because the radial force of the ring is concentrated on a smaller vessel; meaning more load per vessel circumference than the same ring in larger vessel.

The diametric pulsatility calculated from the quarter ring mid-points provide a very similar trend to that calculated from the peaks and valleys (Figure 98), however showing a lower magnitude in general: 28% lower on average.

The ring height pulsatility results, shown in Figure 99, show a similar overall trend to that of the diameter pulsatility (Figure 98) with slightly greater magnitudes. There is however a discrepancy with the OLB30 R1 and R2 rings at low oversize having significantly higher values than the general trend. This is because the recommended upper vessel diameter of

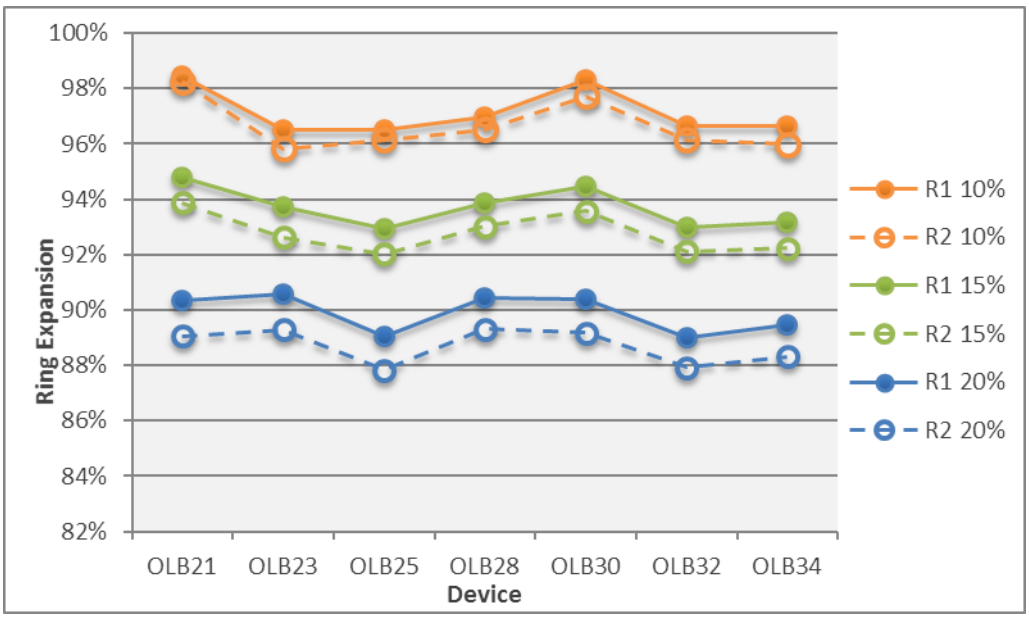

Figure 100 - Ring expansion results of Anconda proximal rings at deployed in a 52yr vessel model at approximately 10,15,20% oversize in 52 year Langewouters model at 60-140mmHg.

27.5mm for this device is proportionally the highest relative to the outer ring diameter, compared to the other devices (the 10%,15% and 20% oversizing are approximate, and the ring-to-device size ratios also have variability). This leads to the OLB30 rings sitting in a slightly flatter position, which leads to exaggerated vertical pulsatility, and an impact on the strain amplitudes as discussed in the following (7.4.3). The exaggerated height pulsatility is also, to a lesser degree, apparent for OLB21 rings at 10% oversize. The OLB21 and OLB30 having a flatter position is confirmed in Figure 100, in which 'expansion' has been calculated as a ring's diameter peak-peak/valley-valley divided by its flat mean diameter (mid cycle).

The ring diametric pulsatility plotted as a percentage of ring diameter (Figure 101) reveals that the larger device rings are resulting in the highest deflection proportionally. The rings' radial stiffness cannot be usefully compared from this study because of the ring motions being very small, sometimes negligible or even negative. However, it was proven in section 5.4.2 that absolute radial stiffness is proportional to 'relative radial force', i.e. the anaconda R1 rings will be of similar absolute stiffness. The greater 'percentage pulsatility' results found for the larger device sizes in Figure 101 could be due to the stiffness not increasing for larger devices. If the ring-stents were developed with a radial stiffness which increased linearly with device size, the resulting 'percentage pulsatility', may be more equal. This would be a shift from the current design philosophy.

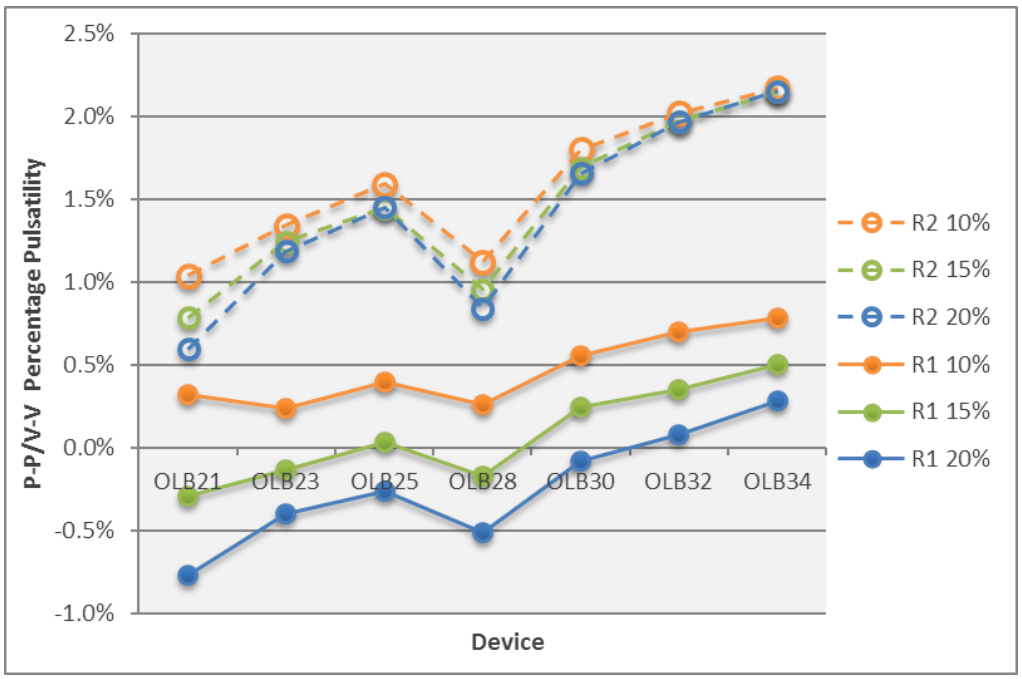

Figure 101 - Percentage pulsatility (relative to rings' flat mean diameters) of Anaconda proximal rings at approximately 10,15,20% oversize in 52 year Langewouters model at 60-140mmHg.

The above analysis is based on the 60-140mmHg blood pressure range as it produced the highest magnitude results. The pulsatility results at the other blood pressures simulated (80-120mmHg and 80-160mmHg) show the same overall trends, but with lower magnitudes. A comparison of the effect of the different blood pressure ranges is provided

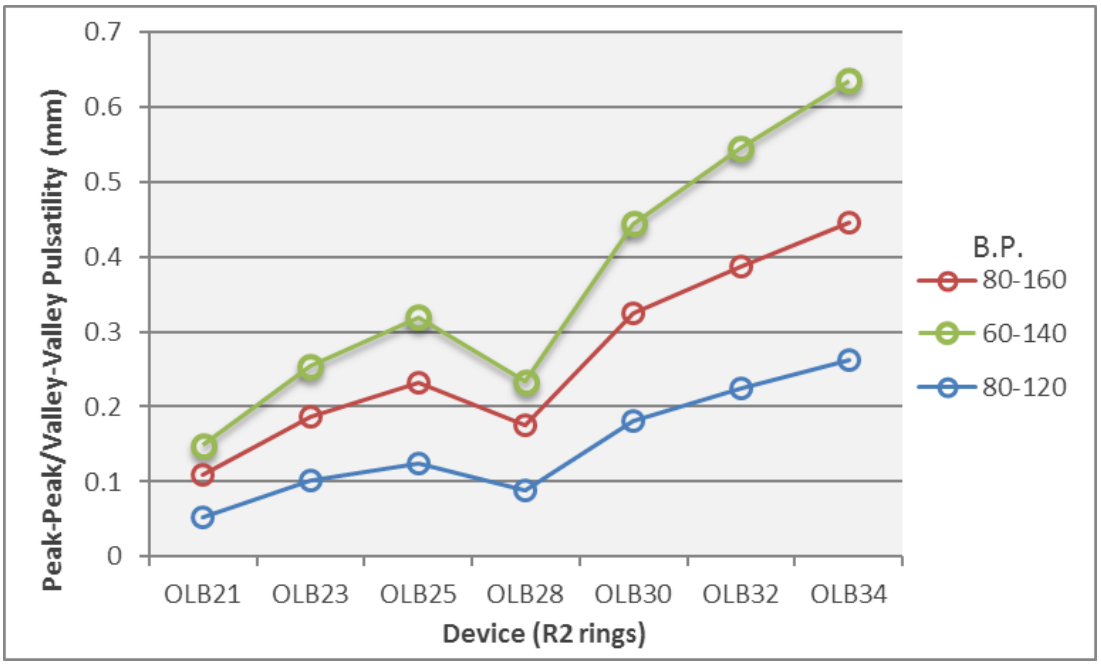

Figure 102 - Variation in peak-peak/valley-valley pulsatility at the three blood pressure ranges simulated: 80-120, 60-140, 80-160mmHg. Results plotted are from the ~15% oversize simulations.

for the R2 rings at 15% oversize in Figure 102. The 80-120mmHg range has the lowest pulsatility as expected, and the 80-160mmHg results in less motion than the 60-140mmHg due to operating at a stiffer section of the vessel's pressure-diameter curve.

7.4.3 Stress and Strain Analysis

As discussed in 2.3.2 the standard way to assess the material fatigue resistance of Nitinol is to consider the local cyclic strain oscillation, and the associated mean-strain levels, rather than consider the cyclic stress amplitudes. However, the stress distribution will be considered briefly first below (7.4.3.1).

As described in 7.2, a post-processing script has been used to calculate the delta-strain for all nodes in the model before the highest value result is searched for and exported. The mean-strain of this node is also extracted. The trends of delta-strain with oversize and device size will be considered as well as comparing the values with fatigue limits. The 'maximum strain' value exported represents the node with the highest strain at the average of systolic and diastolic positions and will therefore be referred to as 'maximum strain mid-cycle'.

7.4.3.1 Stress Distribution

The stress and strain contour plots of OLB28 R1 ring simulations at approximately 10% and 20% oversize are shown in Figure 103. Both the stress and strain are plotted as 'maximum absolute principal' which shows the greatest in magnitude of maximum principal or minimum principal values, and negative results indicate material in compression. The key observation is that the strain varies much more linearly through the wire section, from compression to tension, while the stress gradient is quite non-linear: particularly apparent in the ~20% oversize image much of the outer portion of the wire section appears at the same level of stress – i.e. these outer elements (in the bending plane) are on the Nitinol unloading plateau.

The maximum stress levels are actually at locations closer to the mid-point between peak and valley. These points while at higher stress than the maximum at the peak/valley are at lower strain levels than the peak. Such a result is only possible with a material with a significant hysteresis loop such as Nitinol. This demonstrates that the peaks/valleys have unloaded to the level of the unload plateau (350-380MPa), while central points on the wire which reached start of transformation stress levels in compaction, have only partially

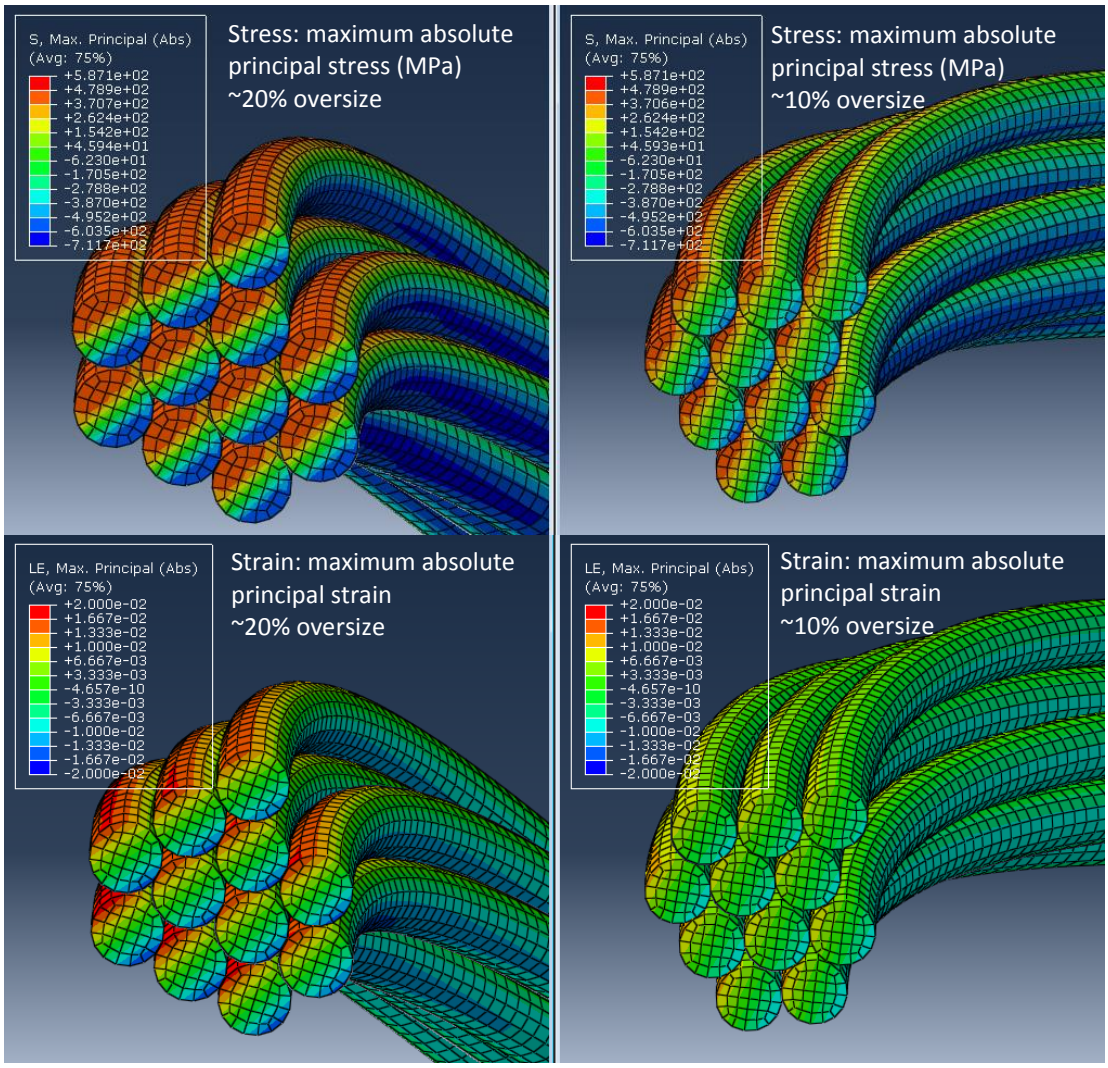

Figure 103 - Contour plots of maximum absolute principal stress (top) and strain (bottom) of the OLB28R1 ring peak at approximately 20% (left) and 10% (right) oversize. (Using the 'maximum absolute principal' plots the greatest in magnitude of Maximum/Minimum Principal value and negative results indicate material in compression.)

unloaded towards the unload plateau. In the ~20% oversize case a stress of 587MPa remains at a node near the mid-point of the wire.

7.4.3.2 Maximum Strain

Maximum strain values for the 60-140mmHg loading, plotted in Figure 104, are all in the range 1.0%-2.5% for the oversize levels probed and increase with oversize as expected. The maximum strain is essentially dependent on the level of saddle shape imposed, and the wire diameter of the Nitinol which comprises the ring. The wire diameter is predominantly responsible for the variation with device size, including the general trend of reducing max strain with increased device size: due to the wire being finer relative to ring diameter.

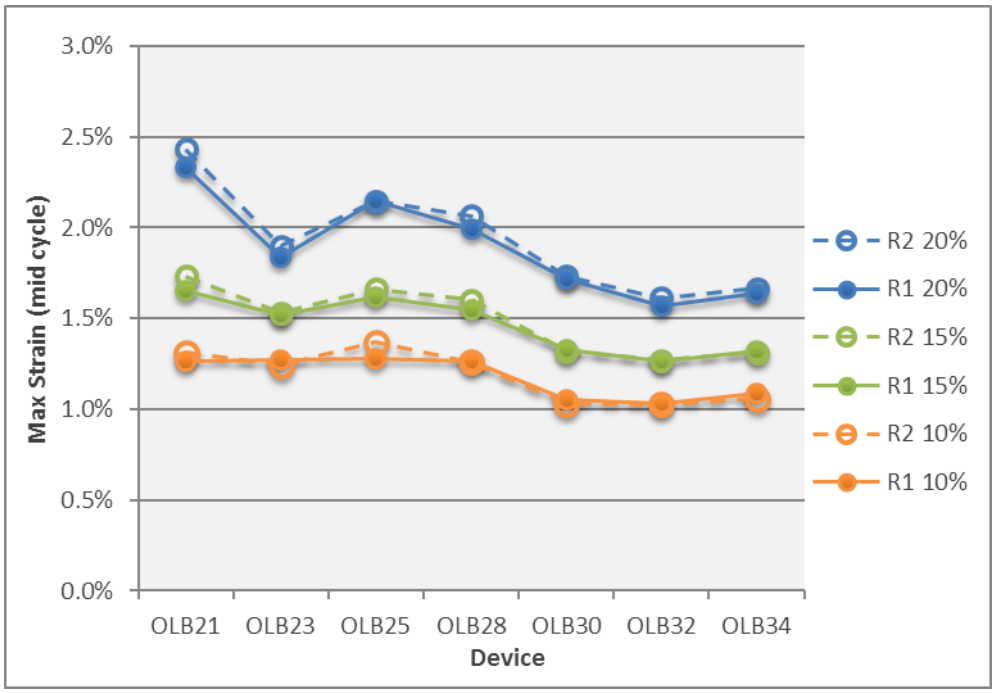

Figure 104 - Maximum Strain (mid cycle) of Anaconda proximal rings at approximately 10,15,20% oversize.

7.4.3.3 Delta-strain

The delta-strain magnitudes are obtained from the simulations for comparison with delta-strain limits. The delta-strain limits represent a level of constant cyclic straining for which the Nitinol wire has shown to be resistant to over 400 million cycles, in a loading manner similar to that *in vivo*. The delta-strain fatigue limits have been defined for three levels of mean-strain by the testing carried out at Vascutek [105], and analysis provided by the work of Chapter 6 of this thesis. The limits defined are as follows;

- 0.223% at a low mean-strain of ~0.85%
- 0.179% at a medium mean-strain of ~1.85%
- 0.165% at a high mean-strain of ~3.2%

It is assumed that linear interpolation can be used with the above data to establish delta-strain limits between the mean-strain values of 0.76% and 3.3% (this is the range of mean-strain that samples in the fatigue test actually covered because testing practicalities caused variation from the target mean-strain values above.)

The delta-strain values are plotted for the 60-140mmHg blood pressure case in Figure 105 a) and b) for R1s and R2 respectively. All results for the other blood pressure ranges (80-120mmHg and 80-160mmHg) can be found in Appendix O. In correlation with the motion results generally the 60-140mmHg results have higher delta-strain results than 80-160mmHg, with exceptions discussed below.

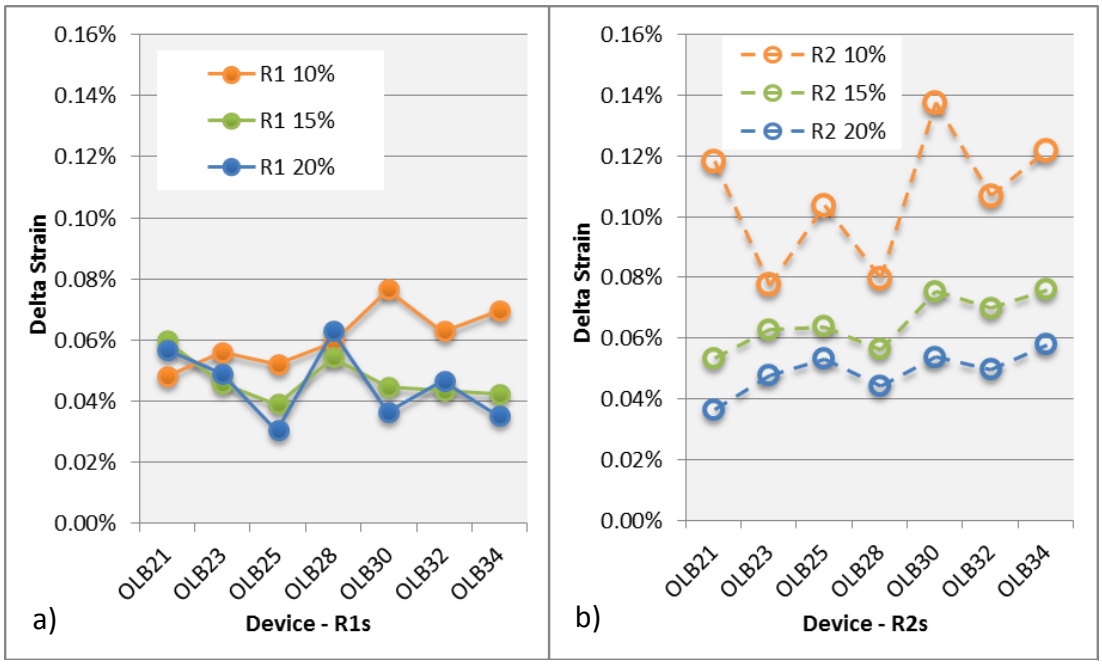

Figure 105 - a) and b) - The delta-strain results for Anaconda R1 and R2 ((a) and b) respectively) from simulations in 52yr abdominal vessel model.

The R1 delta-strain results, shown in Figure 105 a), range from 0.031% to 0.077% and do not show a consistent trend with oversize, which could be related to the motion results not showing consistency in values being negative or positive (Figure 101). No trend with device size is apparent.

The R2 delta-strain results (Figure 105 b)) range from 0.037% to 0.138% with values consistently decreasing with increased oversize. This trend correlates to the finding on pulsatility, but there is even greater variance proportionally. This is to say that the difference in motion is not purely responsible for the difference in delta-strain across the oversize range: the rings in a flatter position (low oversize) are liable to greater delta-strain per mm of diameter change, as was found in Chapter 6. The highest delta-strain of 0.138% occurred at a node with very low mean-strain of 0.07%. The delta-strain limit of 0.223% at mean-strain of ~0.85% is most relevant to compare and results in a factor of safety of 62%.

The spikes in the R2 10% results correlate to the ring height pulsatility (Figure 99), and the highest result of the OLB30 R2 at 10% will be due to the exaggerated motion which is discussed above.

The locations of the maximum delta-strains are at, or very close to, the peak or valley of the ring in the cases of 36 out of 42 simulations. The 6 remaining discrepancies always occurred within the range of R1 rings showing the lowest overall motion (OLB21-OLB30) but this was not consistent with the various oversize levels simulated. For the 6 cases, the maximum delta stain levels were located at rings' mid points between peak and valley.

In terms of which turn within a bundle resulted in highest delta-strain (e.g. inner or outer lying turns); there appeared to be no consistency, which may partially be due to the significant variability in results across the wire strands. Turn-to-turn variation was highest for the R1 rings which show the least overall motion, with a worst-case relative standard deviation (RSD) in delta-strain result of 32.6% for the OLB25 R1 at high oversize. The average RSD for all R1s was 23.9%. The R2 rings which displayed higher motion had lower relative variation between turns (RSD between 2.8% and 16%).

The high turn-to-turn variability for rings at low pulsatility is judged to be partly due to the simplified modelling method for the turn-to-turn interaction: the lack of contact being modelled allowing some variable bending from one turn to the next. This variation

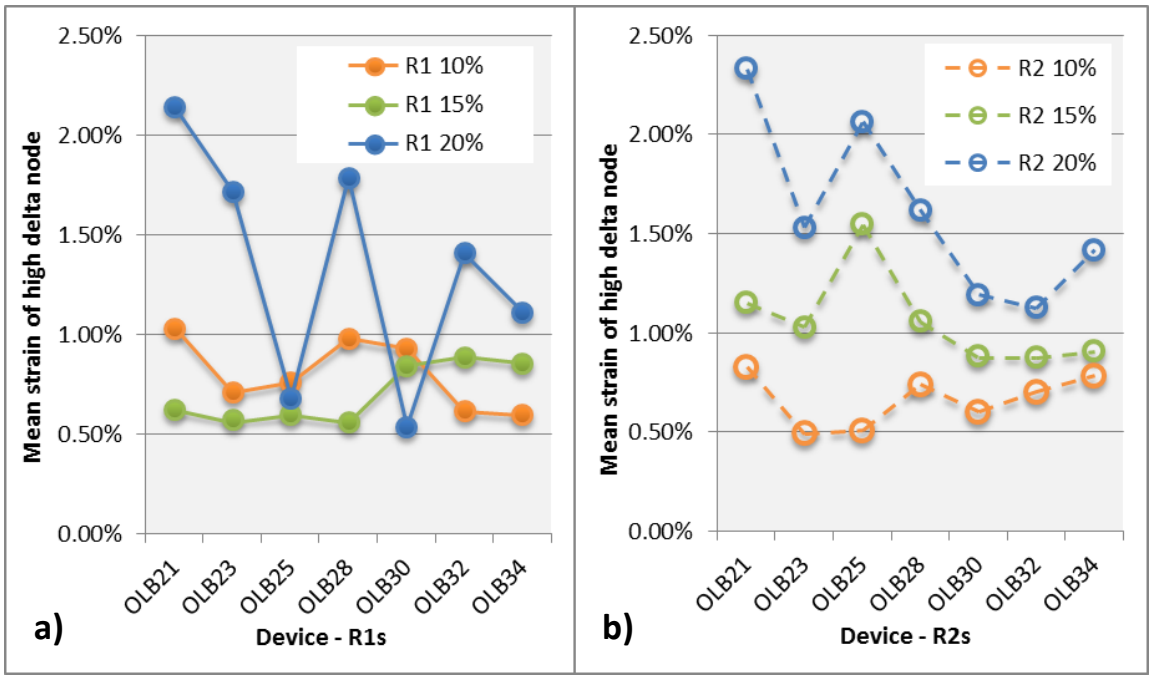

Figure 106 - a) and b) - Mean-strain of the nodes with highest delta-strain plotted for Anaconda R1 and R2 rings, (a) and b), at approximately 10,15,20% oversize

becomes less significant as bending behaviour is dominated by the motion of the entire ring bundle for larger pulsatility results. This modelling phenomenon is conservative from a fatigue prediction point of view, only increasing delta-strain result artificially if at all.

The corresponding mean-strain levels of the nodes with highest delta-strains are plotted in Figure 106, again showing a more inconsistent trend with R1 regarding oversize. The R1 ~20% oversize has two anomalies of relatively low mean-strain (OLB25 and OLB30): the location of the highest delta-strain in both these cases was mid-wire rather than the most common end of wire position, however they are not the only cases with this finding. In general, for R1 and R2s, excluding the two mentioned anomalies, mean-strains of the ~20% oversize cases are closer to the maximum strains (Figure 104) in the ring than in the ~10% oversize cases. This is due to the plane of bending during cyclic loading being unaligned with the general curve of the ring's peak/valley for the lower oversize cases, as was found in Chapter 6.

All delta-strain values are acceptably lower than the limits defined above, however it should be noted that some with very low mean-strain values are out-with the range of mean-strains defined in the ring fatigue testing.

Regarding the comparison of 60-140mmHg against 80-160mmHg: three exceptions were the OLB21 R1 ring at 10% oversize, and the OLB30 R1 and R2 at 10% oversize which showed greater delta-strains at 80-160mmHg, the OLB30 R2 having the highest result of all: delta-strain of 0.173% at a mean of 0.35%. These are all cases which see inflections in ring height pulsatility results, and significant sliding of peak/valley relative to vessel wall, which are emphasised further at the 80-160mmHg blood pressure range. This sliding behaviour, as the ring is close to becoming flat, is judged likely to be unrealistic: partly due to the worst-case 0.01 friction coefficient implemented and potentially prevented *in vivo* by the hook engagement, global structural stiffening effects, and over time the addition of biological tissue engagement with stent-graft.

7.4.3.4 Delta-Strain vs Age

As defined in 4.3, the Langewouters' based artery models (with high p_1 value) representing patient ages of 52, 60, 68 and 76 have diametric strains of 4.18%, 3.52%, 3.00% and 2.59% respectively at 80-160mmHg blood pressure range. Simulations of OLB28 R1 and R2 in the mentioned age representative artery models, at 80-160mmHg, and 15% (approximate)

device oversize confirm that the delta-strain values reduce with age, as plotted in Figure 107. The R1 showing lower delta strain relative to R2 is consistent with the general trend found earlier, which was related to the lower pulsatility of the R1.

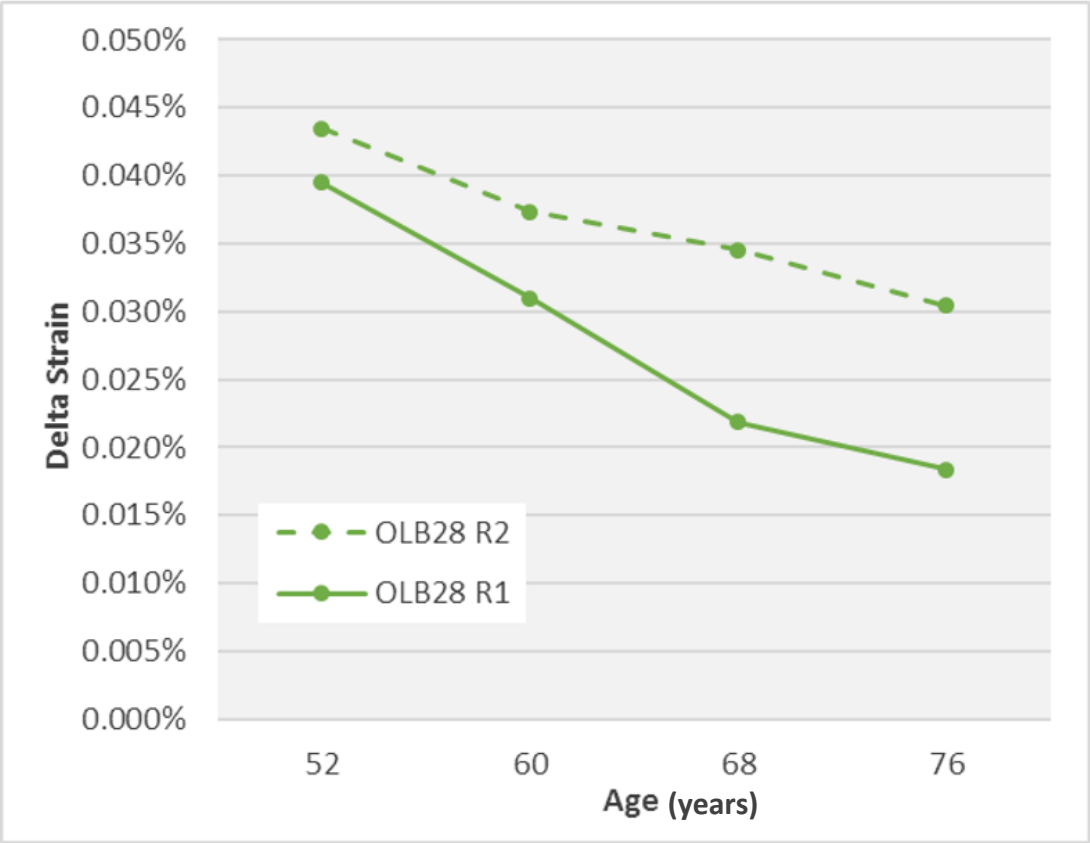

Figure 107 - Delta-Strain vs age of artery modelled for OLB28 proximal rings at approximately ~15% oversize.

7.4.4 Comparison with Simulation in Linear Elastic Vessel

The Langewouters [47] based vessel, applied to the study discussed above, has a diametric strain of 4.18% for a blood pressure range of 80-160mmHg. A linear elastic vessel was calibrated to have this diametric strain over the same pressure range. A thickness of 1.4mm was applied to an initial diameter 19.31 (from a wall thickness to diameter ratio of 0.0725 from [45]). The calibrated vessel was then scaled to have a nominal inner diameter of 24mm which is ~15% oversize for OLB28 device. The R1 and R2 of the OLB28 device were simulated separately in the linear vessel at blood pressure range of 80-160mmHg. The rest of the methodology was identical to that used in the Langewouters based models.

The peak/valley percentage pulsatility for R1 and R2 in the linear vessel was 3.73% and 3.90% respectively, which can be compared with -0.07% and 0.66% respectively for the

Langewouters model at 80-160mmHg. The linear vessel results show how little the motion of the vessel is 'dampened' in comparison with the non-linear. In fact, the diametric strain of the linear vessel with stent (averaged from contact points at rings' peak/valley and mid-point) was calculated to be 3.61% and 3.83% for R1 and R2 respectively, which when compared to the native 4.18% diametric strain, represent a reduction of 14% and 8% in magnitude respectively.

The strain results of OLB28 R1 and R2 rings simulated in the linear elastic vessel with diametric strain of 4.18% were 0.18% at 1.25% and 0.19% at 1.51% (delta-strain @ mean-strain) respectively. This compares with 0.04% at 0.60% and 0.04% at 1.24% respectively.

The stark contrast highlights how incorporating the non-linear biomechanical behaviour of aorta completely changes the fatigue safety case for ring-stents.

7.5 Variation with Oversize – OLB28

The product sizing chart (Appendix A), recommends oversizing the *Anaconda* between 10% and 20% however it is known that this guidance is sometimes ignored and oversizing beyond 30% is not uncommon [109]. The OLB28 R1 and R2 rings were simulated at an extended oversize range to probe the effect on delta-strain and radial force. The resulting deformed shape of the ring from simulations of the R1 at device oversize of 10%, 22% and 47% are shown in Figure 108.

7.5.1 Delta-Strain vs Oversize

The delta-strain results for OLB28 R1 and R2 simulations over an extended oversize range at 60-140mmHg are shown in Figure 109. All vessels have been modelled to have the same compliance, however since compliance, and diametric strain, are relative to the vessel's nominal size it should be noted that the smaller vessels (higher oversize) are changing less in magnitude of diameter.

A spike in delta-strain occurs at the simulation of 7.7% oversize (26.0mm nominal vessel ID): at this level the ring has relatively high level of ring height pulsatility in and the peak and valley are sliding considerably relative to the vessel wall. In the 5% oversize simulations the rings have flattened, embedding the vessel wall, no longer in the saddle shape pulsatile loading condition, hence the reduced delta-strains.

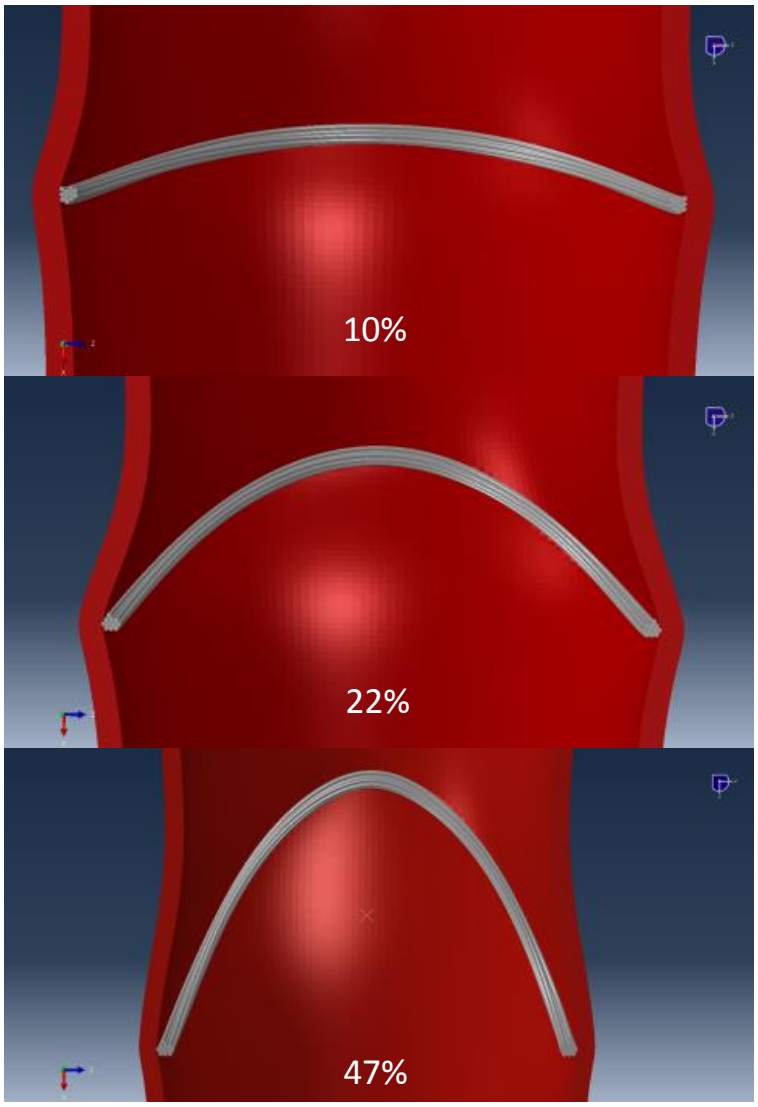

Figure 108 - The resulting position of an OLB28 R1 deployed in a 52yr vessel model at 10%,22% and 47% device oversize

The R2 has reduced to negligible delta-strains in this flat position. However, the R1 is still registering a 0.03% delta-strain - this is not reflective of the rings overall movement: detailed analysis showed that the highest 0.03% delta-strains are occurring on the outermost strand, between the bundle connection points. This suggests that the outer strand is bending between the connection points as the inward contact pressure from the vessel varies over the cycle. This reaffirms that these low-level delta-strains on the R1 rings are somewhat artificial, not representative of the true pulsatile motion of the whole ring.

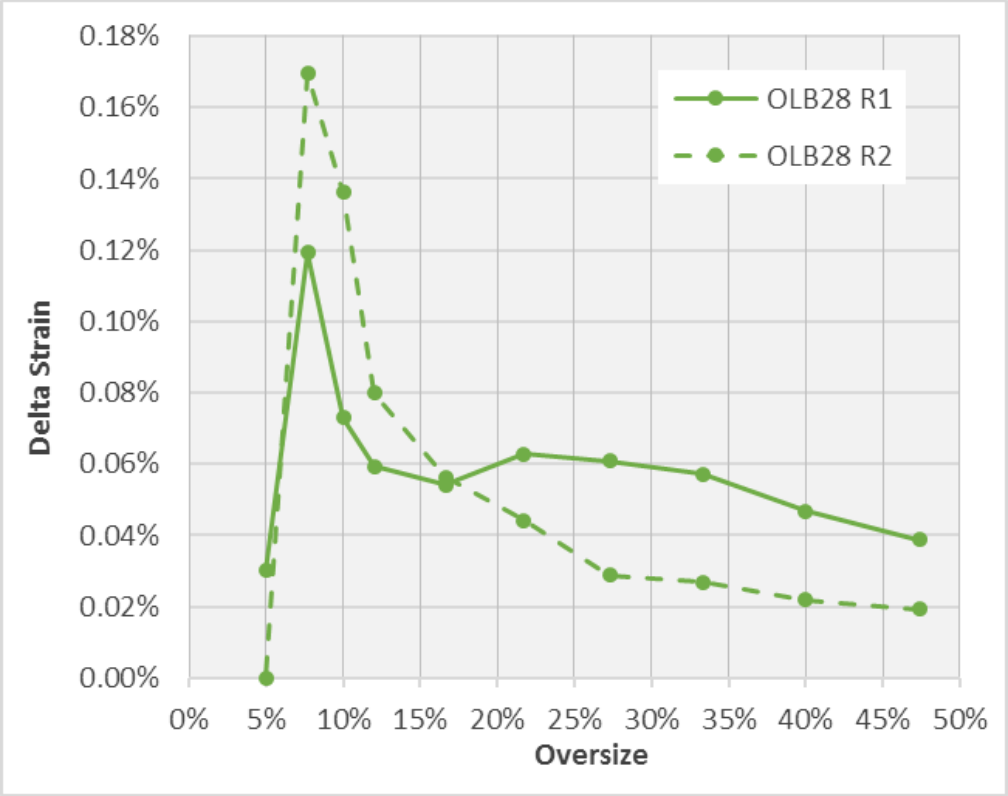

Figure 109 - Delta-strain vs. Oversize for the OLB28 proximal rings in 52yr vessel model at 60-140mmHg blood pressure

As oversize is increased from 7.7% initially both rings show sharp reduction in delta strain, followed by continual gradual reduction for the R2 and a less consistent reduction for R1 which has a second peak at ~22% oversize. However, the R1 results are judged to have some error due to the 'artificial' noise due to the methodology as discussed above.

7.5.2 Radial Force vs Oversize

The radial force results from the extended oversize range for OLB28 R1 and R2, extracted at diastolic and systolic, for the 60-140mmHg case are shown in Figure 110. Rings show slight force reductions of 14% and 17% respectively between a maximum in the 10-20% oversize window to the extremely high device 47% oversize. It is perhaps counter intuitive that the radial force does not increase with increased deformation in this range, however these rings are essentially fine wire beams bending to very high deflections; well beyond the case being considered linear. Moreover; the nonlinearity, and in particular the plateauing, of Nitinol's stress-strain response contributes to the flat curve shown. It should be noted that these results are FEA based approximations of ring-stents in isolation; the full proximal region of the *Anaconda* including hooks, fabric and suture may well influence the overall radial strength of the device. Nevertheless, the highest radial force values clearly lying

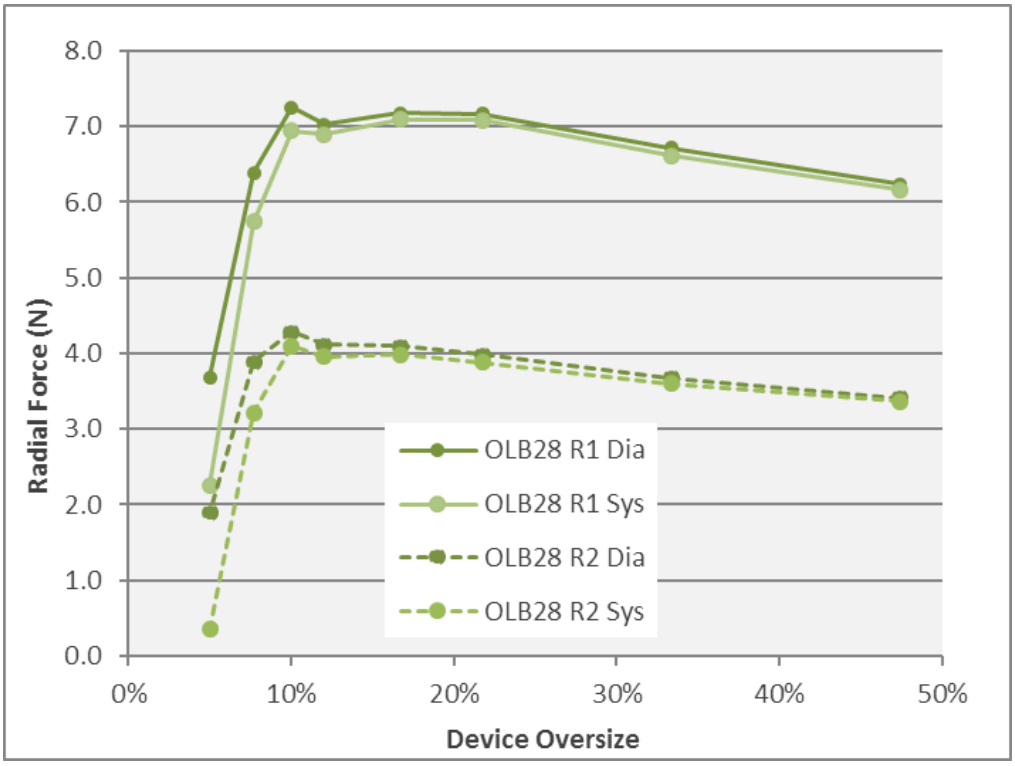

Figure 110 - Radial Force vs. Oversize for the OLB28 proximal rings in 52yr vessel models

within the 10-20% range in Figure 110 is a reinforcement of the evidence that this is the optimal range.

The significant reduction in radial force at points below 10% oversize are partly due to the relatively flexible 52yr vessel model easily deforming locally to the ring, and indeed for this case the rings are flat at the 5% device oversize level. When the R1 ring was simulated at 5% device oversize in a vessel of the average patient age of 76-years, the vessel did not

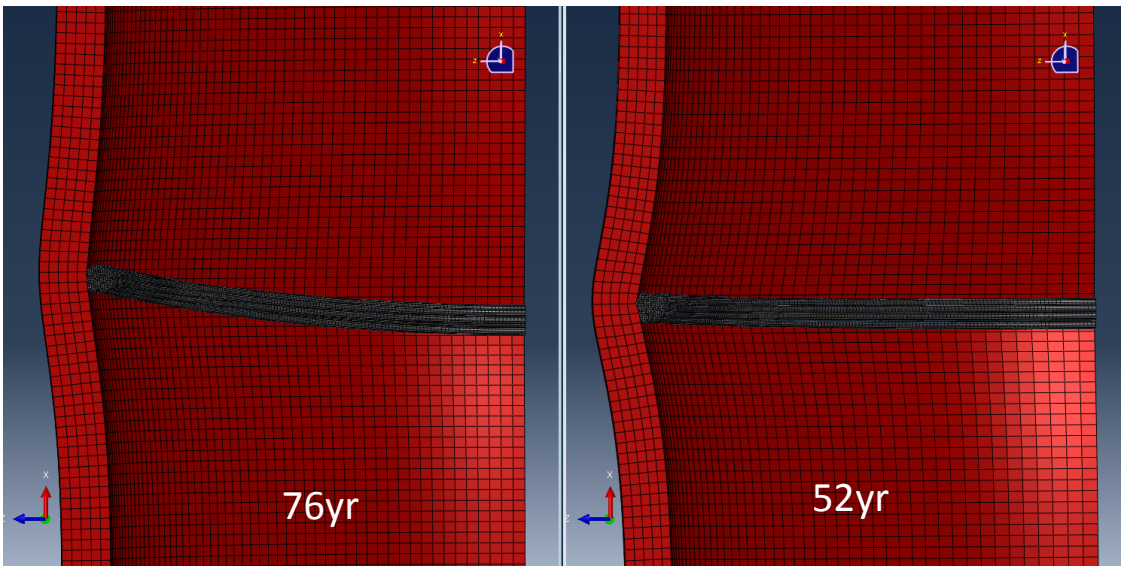

Figure 111 - The OLB28 R1 ring deployed at 5% oversize level for both a 76yr and 52yr vessel models

locally deform as much to accommodate the ring flattening, and radial force levels did not drop as low (5.14N average compared to 3.12N of the 52yr vessel model). The difference in resulting position of ring and level of embedding in the 76yr and 52yr vessel models at 5% oversize can be appreciated from Figure 111.

7.5.3 Radial Force Distribution

Contact pressure is an output parameter in *Abaqus* which could be used to quantify radial force distribution of the ring interacting with artery. However, a brief study found that the contact pressure distribution and peak magnitudes are highly dependent on the stiffness and other parameters of the contact interaction implementation, as well as the vessel element size. With a lack of confidence in the contact pressure output due to this finding and not being able to validate the results, a simpler quantification of 'radial force per mm ring circumference' has been used.

The 'radial force per mm ring circumference' was calculated as described in 7.2.4 from the final diastolic step of each simulation (80mmHg), with the addition that differences between equivalent 10° segments above and below the mid-point were averaged. The results for various oversize simulations of OLB28 R1 are plotted in Figure 112.

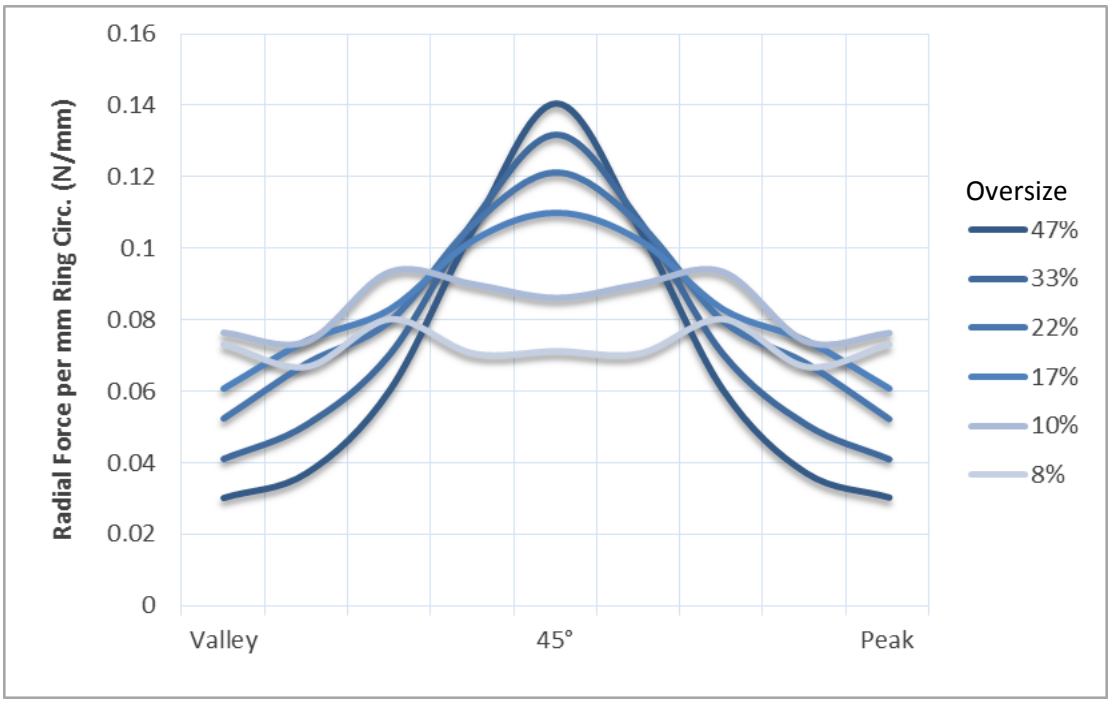

Figure 112 - Distribution of radial force of OLB28 R1 ring from peak to valley at various oversize levels. All simulations are 52yr vessel model.

The ring at lowest oversize, i.e. flattest saddle shape, shows the most consistent distribution of radial force along the length with values in the range 0.066-0.080N/mm. The ring at an excessive oversize of 47% shows significant variation in distribution with values ranging from 0.030N/mm at the peaks/valleys 0.141N/mm at the mid-point.

This quantification of radial force distribution becoming highly uneven at excessive oversize levels is a valuable confirmation that the recommended oversize range of 10-20% could provide improved apposition and therefore endo-sealing of *Anaconda* stent grafts.

7.6 Summary of Chapter 7

This work in this chapter represents the first simulations of Nitinol ring-stents interacting with non-linear vessel models under cyclic blood pressure. Due to the uniqueness of the modelling and the desired outputs, bespoke post-processing algorithms have been developed in *Python* script to assess strain state, ring motion and radial force and its distribution.

The study carried out on *Anaconda* proximal rings from all device sizes has produced the following conclusions with regards to radial force:

- The radial force of ring-stents simulated in isolation range from 4.7 – 7.9N for R1s and 2.3 – 4.0N for R2s, with negligible variance between the 10%, 15% and 20% approximate oversize levels.
- Across the device sizes, the relative radial force of R1s across the size range vary by ±13% (±7% if excluding OLB28) and R2s vary by ±21% (±8% if excluding OLB28).
- Radial force reduced slightly for a reduction in oversize from 20% - 47% for the OLB28 rings.
- Radial force dropped significantly for oversize below 10%, however this is partly dependent on the flexibility of the 52-year-old vessel model: an older, stiffer vessel model would not accommodate as much embedding and therefore the ring remains more deformed (at a higher saddle shape) and radial force levels remaining more intact.
- Radial force distribution along the length of the ring becomes significantly varied at high oversize; being concentrated at the mid-point between peak and valley.

Regarding ring motion, the simulations in the non-linear vessel result in very low levels of pulsatility when compared to the same simulation in linear vessel of the same diametric strain for the OLB28. This shows, theoretically, the significance of damping from the strength of the rings on the natural motion of the vessel. The pulsatility analysis also found the following conclusions:

- Ring pulsatility was higher for R2 rings than R1. The strength of R1 rings overpower the vessel models' natural motion, and in the case of the smaller R1s, the pulsatility in the simulations is actually showing the rings compressing slightly from diastolic to systolic – this is due to increased longitudinal tension at systolic in the vessel wall reducing the embedding of the ring.

- The larger devices in the range are showing higher relative pulsatility.

Regarding the strain state of the Anaconda rings from simulation in Langewouters arteries, the following conclusions can be made:

- The maximum strain levels in rings in deployed position are between 1.0-2.5% (taken at average of diastolic and systolic) for the 10-20% oversize range.
- Delta-strain levels for the R1 and R2 rings were in the ranges 0.031% to 0.077% and 0.037% to 0.138% respectively for the 60-140mmHg blood pressure range tested which induces the highest vessel diametric strain. These are below the current fatigue limits regardless of mean-strain level, with the highest 0.138% value having a factor of safety of 62%.
- The 80-160mmHg results were generally slightly lower in delta-strain with some anomalies including the OLB30R2 at ~10% oversize which resulted in a delta-stain of 0.173% - however this is due to significant sliding of the ring in the vessel, as the ring is on the verge of flattening, and is judged to be subdued with a more realistic friction coefficient and other factors not included in simulation such as the support provided from connected components and hook-vessel engagement.
- The delta-strain levels in R2 rings show clear reduction with increased oversize (from ~10% to ~20%). The trend is not clear with R1s.
- In the extended oversize simulations for OLB28 rings, the delta-strains have a spike in results between 10% oversize and 5% oversize (at which they reached a flat position), due to the exaggerated height pulsatility and sliding mentioned above.

Overall, the study provides a new strand of evidence that the 10-20% oversize range is optimal, and theoretically rings are fatigue safe considering that the vessels' natural motion has been 'dampened' significantly. However, the artery modelling is just one approach to capturing the tissue biomechanics and simplifies the vessel wall to be an isotropic structure. Further discussion on limitations and recommendations is provided in Chapter 9.

8

Investigating Compaction Strain

As was discussed in Chapter 2, endovascular stent-grafts such as the *Anaconda* are implanted using tubular catheter delivery systems. The devices are compacted into the flexible cylindrical sheath during device manufacture. As well as the device, the sheath must accommodate control linkage wires and a central core through which, in the case of *Anaconda*, some of the control wires are passed. When a stent-graft is compacted into a delivery sheath, the stent components (i.e. ring-stents in this case) are forced into their highest deformed state, and are competing for space with the folding fabric and other components.

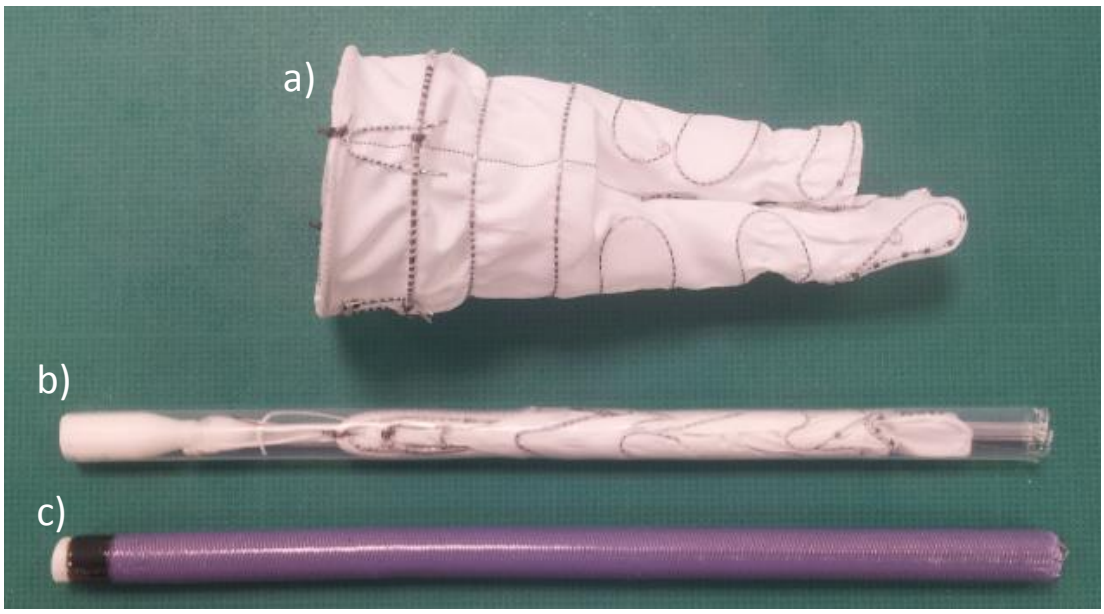

Figure 113 - Comparison of a) the OLB34 device fully expanded with compaction samples of the same device, cut to length for Micro CT scanning in b) a clear model sheath and c) the true product sheath.

The *Anaconda* body devices are delivered in sheaths with an internal diameter of 6.2mm for the device sizes 23mm and below, and 6.7mm for the larger devices. The leg components are compacted into sheaths of 5.3mm internal diameter. The Thoraflex Hybrid device's endovascular section is compacted into a less challenging 9.5mm. All devices are compacted by being pulled through funnel type geometry on mechanised equipment which measures the forces applied.

The compacted *Anaconda* OLB body devices, which are reduced to diameters as low as 20% of their nominal size, as can be seen in Figure 113. Currently, there exists a clinical desire and a commercial competitive need to reduce further the delivery system sheath diameter on the *Anaconda* product. Furthermore, the importance of compacting endovascular devices into as small a delivery system as possible is relevant for all future products being developed. The clinical requirement for delivery systems to be as slender as possible stems from firstly; the challenge of treating cases with restricted access due to narrowed or tortuous arteries, and secondly; smaller delivery systems are less likely to cause damage to the patient during operation.

The high stress/strain levels imposed on the Nitinol ring-stents is a key limitation to minimising the delivery sheath diameter. Nitinol may be 'superelastic' compared to other metal alloys, but plasticity and therefore residual strains do begin to occur beyond the phase transformation, i.e. in the fully martensitic phase. The highest deformation to the wire occurs at the peaks and valleys as the rings are essentially folded 180° into their compacted position. Obviously imposing severe plasticity throughout the bundle of wires would cause the ring to be permanently deformed on deployment. However, smaller levels of localised plasticity can go unnoticed when purely observing the deployed shape, but may still have implications on radial force and potentially fatigue durability due to the changed state of some of the material.

The settled deformed position of compacted *Anaconda* devices is complicated, unpredictable and highly variable. The competition for space between structural components, folding fabric, a central core and an 'intrinsic guidewire', as well as variations in the production process, results in random and differing compacted positions to some degree. Clearly these complexities and variation would be very challenging to simulate computationally; involving highly non-linear modelling of all other components in the stent graft and their interaction with each other through the compaction process.

Vascutek's previous comparative assessments on compaction have mainly focused on empirical measurement of the 'compaction forces': the axial pulling force required to compact devices into the sheaths. Regarding the assessment of strain levels; some previous work has used digital image measuring methods to quantify the tightest inner curvature of ring bundles from photographs of devices compacted in model transparent sheaths. However, the limitations of this method include not being able to identify individual strands, the rings themselves often being obscured by fabric, plus a risk of not measuring the curvature on the correct plane of curvature.

The deformation and resulting strain levels in compacted ring-stents have been reconsidered herein with three separate phases of analysis contributing to an improved understanding, and tools for future product development. Firstly, the fundamental problem of a ring compacted in a sheath with a central core will be considered from a geometric perspective, negating fabric and other components, and applying a simple beam bending calculation to estimate best case scenario strain levels. Secondly, Micro Computed Tomography (Micro CT) X-Ray imaging has been implemented to provide broader, more accurate assessment of the deformation and therefore strain levels enforced on *Vascutek's* ring-stents. Thirdly, an FEA study has been conducted on a number of single turn models to verify whether beam bending calculations are appropriate, and also to estimate the level of asymmetry between the tensile and compressive sides.

8.1 Simple Calculation of Beam Bending Strain and FE Verification

The compaction limits, in terms of reducing sheath diameter, can be assessed for feasibility by combining geometric calculations with the beam bending approximation for maximum strain. According to classical mechanics, for 'small deflections' [113], the maximum strain magnitude ε_{max} (at the outer tensile and inner compressive surface) of a beam in pure bending can be estimated simply by (Eq. 8.1), where h is the half-thickness of the beam in the plane of bending, and R is the radius of curvature of the beam centreline.

$$\varepsilon_{max} = h/R \qquad \textbf{(Eq. 8.1)}$$

$$\varepsilon_{max} = d/D_{curve} \qquad \textbf{(Eq. 8.2)}$$

In the case of round wire, this strain can therefore be more conveniently estimated by the ratio of wire diameter d to the centreline curvature of the deformed wire, as depicted by

Figure 114. Of course, the case in question does not fall into the 'small deflections' criteria, and the strain estimations cannot be assumed accurate. FEA, being able to take account of large deflections, will be used to assess the accuracy of the above calculation for the level of bending which ring-stent wires are subject to. In addition, the FEA will take account of the tension-compression asymmetry of Nitinol and the multi-axial loading which is occurring. A simple study using single strand rings of various wire diameters has been investigated as described in the following (8.1.1).

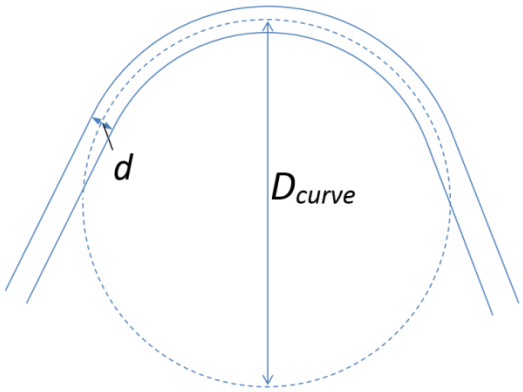

Figure 114 - Diagram of wire diameter, *d* and diameter of curvature, D_{curve} for a deformed wire

8.1.1 FE Verification Study

A simple FE study was designed to simulate Nitinol rings of various wire diameters each compacted to ten incremental sheath diameters between 12.0mm and 3.6mm. The maximum tensile and compressive true strain values were extracted from the simulations, while the deformation (curvature at the peak/valley) was extracted by the same measurement method as used on the Micro CT scans as discussed below.

Three single turn models with ring diameters representing the mean of the OLB28 R1, but with wire diameters of 0.16mm, 0.22mm and 0.28mm which broadly covers the spectrum of *wire diameter* to *ring diameter* ratio in the product range, were simulated through a compaction approximation. The models were created using the half ring methodology described in 4.2.5, with the densest mesh arrangement that was used in the earlier convergence study (60 elements in cross section) in order to provide the most accurate results (see 4.2.6). Other than the half ring, the *Abaqus* models consisted of a rigid surface representing a central core of 2.48mm (used on *Anaconda ONE-LOK*) and a cylindrical rigid

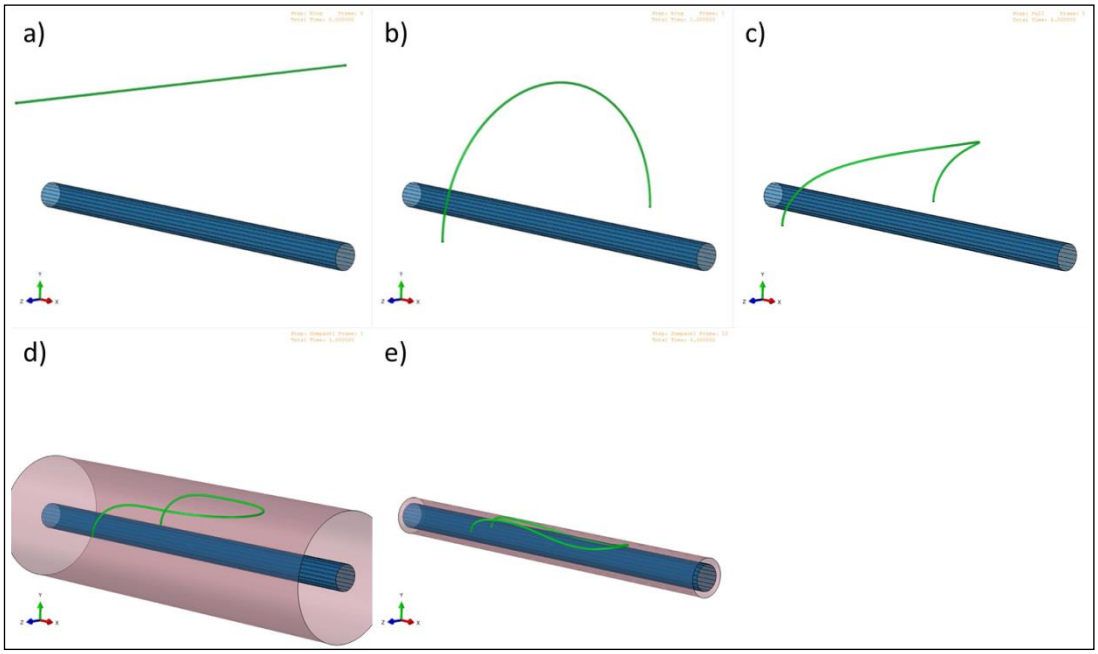

Figure 115 – Steps of single turn compaction study FE model: a) Initial straight wire and central core; b) Wire formed to half ring; c) Half ring pulled into saddle position; d) Initial compaction with 'ART' cylindrical contact surface; e) Final compaction position

surface of variable diameter created using the ART user-subroutine (see 4.2.3.2). The described components and the steps involved in each simulation are outlined in Figure 115.

The four 'general static' steps of the simulations include: 1) the forming of the half ring from straight wire; 2) the initial load applied to enforce an arbitrary saddle position; 3) an initial reduction of the ART cylinder surface to 12.0mm; and 4) final incremental reduction of the cylinder to 3.6mm.

The 'improved' Nitinol material constitutive model (see 3.3) was used for these simulations. The two contact interactions (ring to ART cylinder and ring to central core) were implemented assuming a 'hard contact' pressure-overclosure relationship using 'penalty' enforcement method, and a 0.1 friction coefficient applied in the tangential direction to aid stability.

The typical distribution of strain is shown in Figure 116, which is an image of the 0.22mm wire model compacted to 5.28mm diameter with a contour plot of 'LE, Max Principal (Abs)' with default nodal averaging criteria. The 'LE, Max Principal (Abs)' is a plot of the greater absolute magnitude of either the true (logarithmic) maximum principal strain, the true (logarithmic) minimum principal strain, i.e. the negative values plotted on the compressive side are 'minimum principal strain'. The larger absolute values on the tensile side (9.59%

compared to -8.50% in the case of Figure 116) is due to the asymmetric nitinol model: the compressive having a greater overall stiffness. This asymmetry leads to the shift of the 'neutral axis' away from the geometric beam centre, as has been thoroughly investigated in the parallel work of Brodie [26], however it is the maximum values of strain at the inner and outer surface which are of interest here.

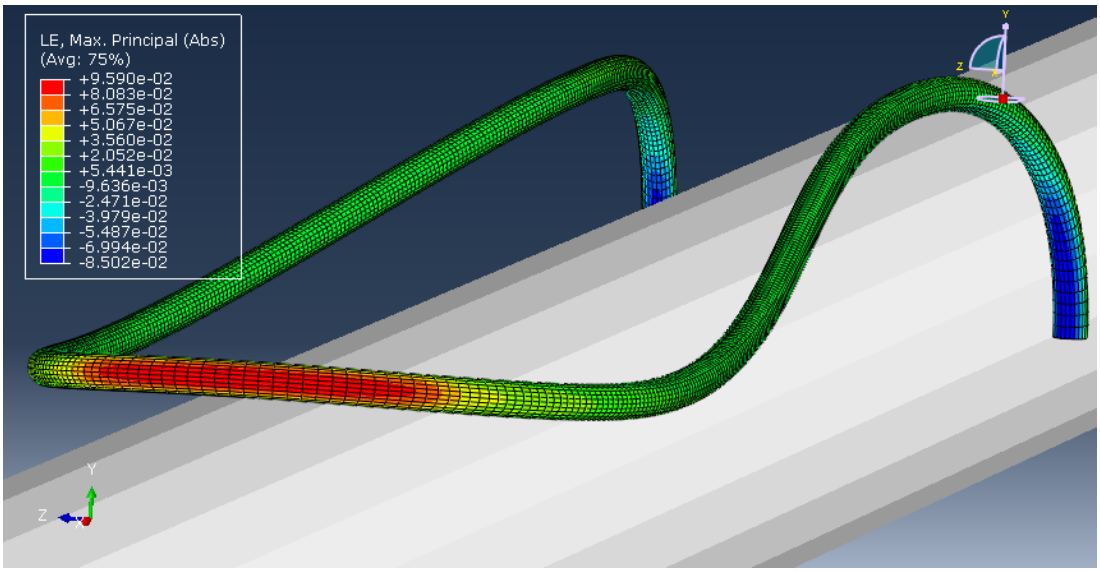

Figure 116 - A 0.22mm strand half ring model compacted to 5.28mm with a 2.48mm central core, with a contour plot of the 'absolute' maximum principal true strain.

For the measurement of curvature, the deformed geometry of the wire surface mesh was exported from *Abaqus* in 'STL' format and measured in *Creo Parametric 2.0* [114] in the same manner as the Micro CT files have been, as described in more detail in the following section 8.2. From the measurement of curvature, the strain estimation $\varepsilon_{max} = d/D_{curve}$ can be calculated (Eq. 8.2). The FE calculated maximum strain values (tensile and compressive) are plotted against the d/D_{curve} estimates in Figure 117. The trend-lines through the three separate data sets (which represented three wire thicknesses) give an indication of the level of overall asymmetry and actual maximum tensile/compressive strains relative to the measured d/D_{curve} estimate. The level of discrepancy in the results from the trend lines can be expected due to the error in measuring the diameter of curvature from the exported geometry. The region of most interest is really that beyond the superelastic transition (>~7% strain). At these levels it can be seen from Figure 117 that using curvature measurements to estimate the strain is likely to overestimate compressive strain, and under estimate tensile strain. However, the overarching conclusion from this study is that the d/D_{curve} estimate is reasonable to use in knowledge that the tensile strains

could be underestimated by up to 0.8% in strain magnitude compared to the FE predicted results.

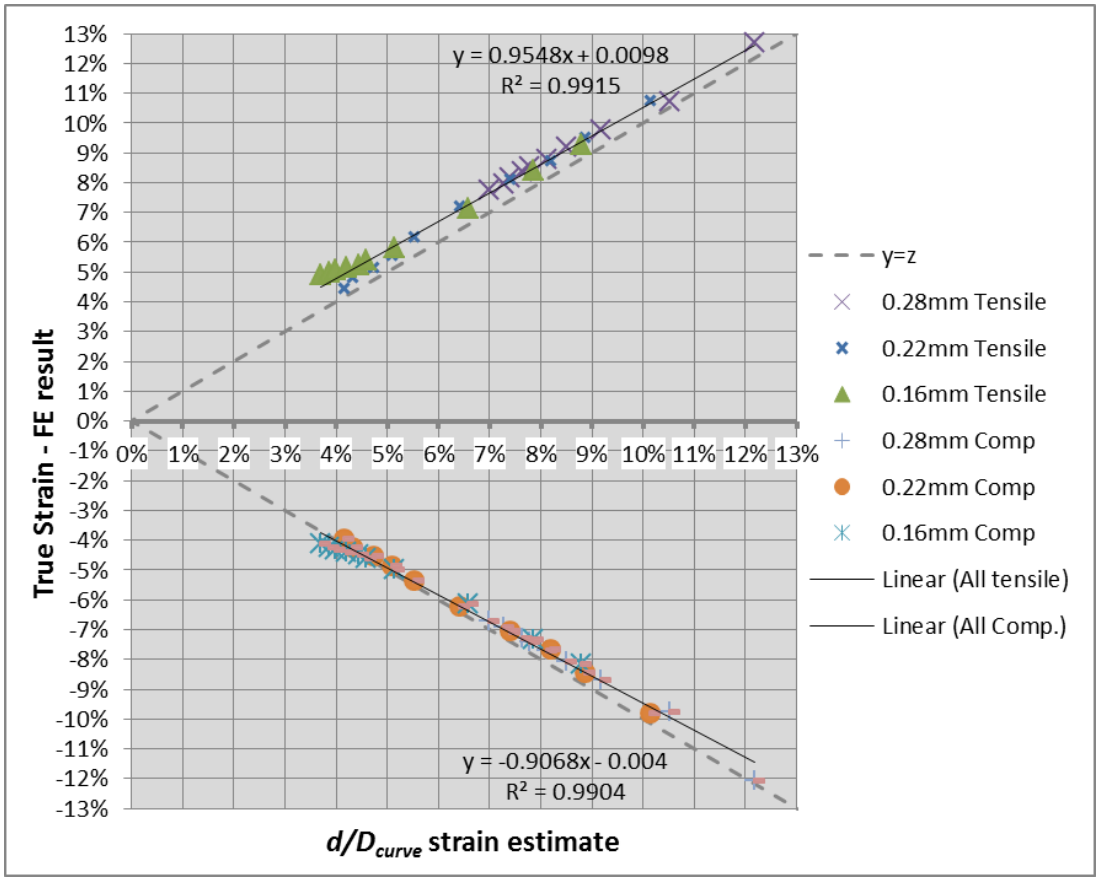

Figure 117 - FE calculated maximum tensile and compressive strain vs. d/D_{curve} estimate from curvature measurement of exported FE geometry.

8.1.2 Compaction Feasibility based on Geometric Calculations

In the knowledge that measuring the curvature to predict strain is an acceptably accurate way to analyse the strain at the peaks and valleys in the compacted state, this geometric problem can be probed mathematically to understand what is feasibly possible. A spreadsheet based model has been created which estimates strains in the inner turn of a bundle, taking account of the sheath diameter, ring bundle diameter and central core diameter. The presence of a central core inhibits the bundle from using the full diameter of the sheath to turn, as can be appreciated in Figure 118 b). Instead, the space which there is to turn can be estimated as $OD_{compaction}$ shown in Figure 118 a). Referring to Figure 119: the green right-angled triangle is used to approximate $OD_{compaction}$ where a is the bundle radius plus the central core radius and $OD_{compaction}$, which is equivalent to $2b$, is estimated by (Eq. 8.3):

$$OD_{compaction} = 2\sqrt{\left(\frac{D_{sheath}}{2}\right)^2 - \left(\frac{D_{core}}{2} + \frac{D_{bundle}}{2}\right)^2} \qquad \textbf{(Eq. 8.3)}$$

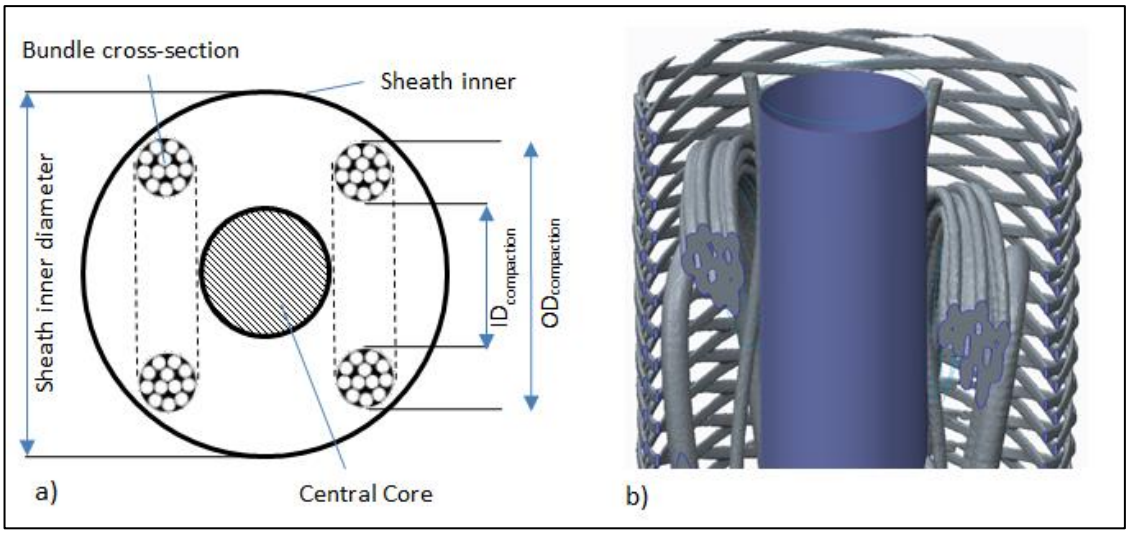

Figure 118 - a) cross-section diagram of compacted ring in sheath with a central core. The dotted lines represent the space in which the peaks will 'fold'. b) A cut view of the peaks of an OLB28 R1 ring with central core graphically represented.

The bundle diameter, D_{bundle} is estimated by circle packing theory as described in section 4.2.8. This allows an approximation of $ID_{compaction}$ and subsequently the centreline diameter of curvature of a worst-case inner strand in the bundle (assuming there is not a twist in the bundle at the peak which would allow strands to move from inner to outer position).

This geometrical calculation to estimate the inner turn strain, has been combined with ring strength calculations (see 5.4.2.1), and expanded into a spreadsheet based tool which (given the ring diameter, ring strength, sheath and core diameters as inputs) can output a

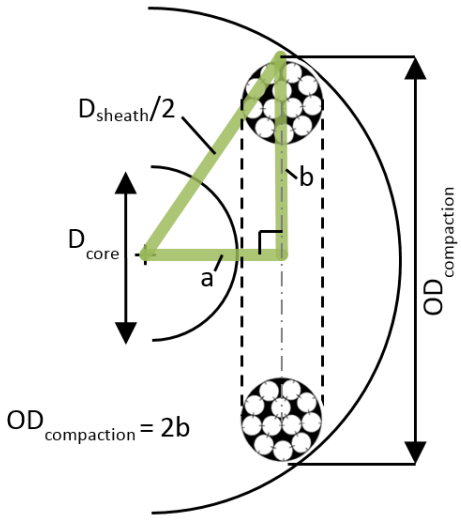

Figure 119 - Schematic of the geometric approximations used to estimate $OD_{compaction}$

range of possible bundle configurations (number of turns; wire diameter) and the estimated compaction strain of each. The accuracy of this method was compared to micro CT observations of the $OD_{curvature}$ value and found to be overestimating, because in reality there is some level of intensified curvature focused towards the apex. As such, a correction factor of 0.78 was implemented as an optional addition to the tool. While this geometric calculation is quite approximate and has shown to have significant error, it has still proven useful in investigating the trends between ring configuration and compaction strain levels or sheath/core diameters.

The most significant general finding which the above geometrical analysis has proved is that to reduce compaction strain, for most cases there exists an 'optimal window' of wire diameters: if the wire diameter is increased, less turns are required, however strain is directly proportional to wire diameter and increases due to this, and conversely if the wire diameter is reduced, a greater number of turns are required, the bundle diameter increases, in turn reducing $ID_{compaction}$ to levels which increase strain. An example of this trend, and the output of the spreadsheet tool is provided for the OLB32 R1 ring with current specification input parameters: 6.7mm sheath diameter and 2.48mm central core.

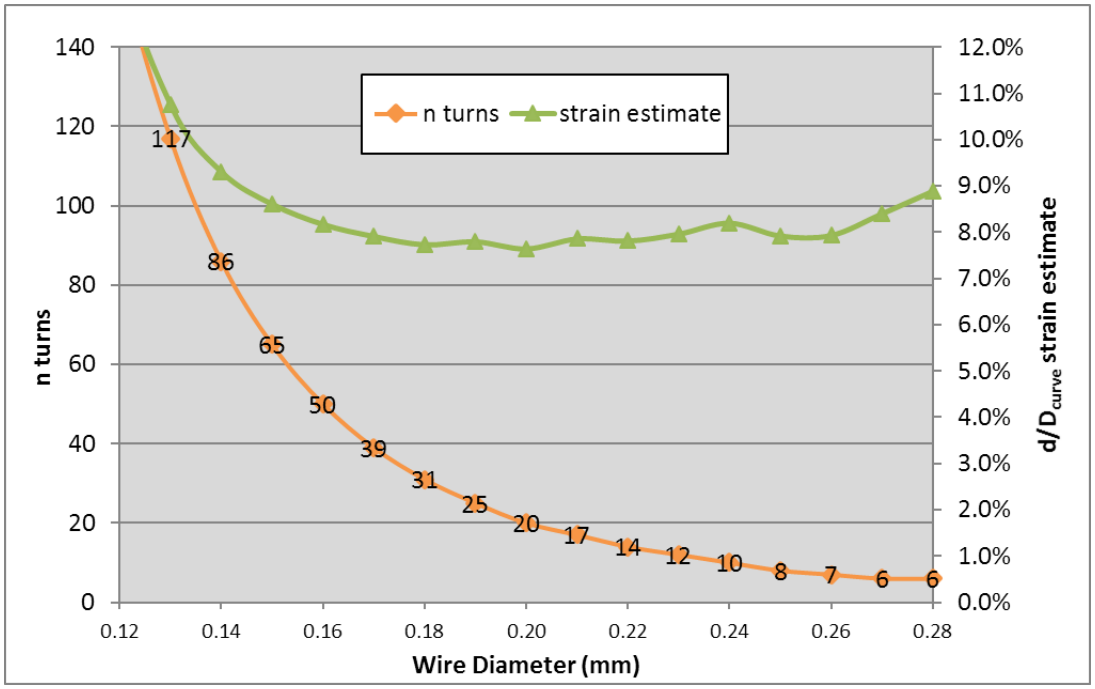

Figure 120 - The output graph from the spreadsheet tool which calculates possible bundle configurations given a ring diameter and ring strength required. Inputs: Ring ID = 29.7mm; Sheath ID = 6.7mm; Central Core D = 2.48mm; required 'Lutz' relative strength = 1.09.

To meet a 1.09 'lutz strength', for a ring of 29.7mm ID, the possible bundle configurations are shown by the orange line in Figure 120. For example 20 turns of 0.20mm or 10 turns of 0.24mm would suffice from the strength perspective. The geometrically estimated worst case (inner strand) compaction strains for a 6.7mm sheath and 2.48mm central core are given by the green line. The exponential increase at the lower end of the wire diameter scale can be seen, and a more linear increase in strain is observed beyond 0.25mm. For wire diameter values between 0.18 and 0.25mm, the curve is overall relatively flat representing the window of optimal wire diameters for this case.

8.2 Micro CT

Micro CT scanning was implemented primarily to assess the deformation and material strain levels in the Nitinol wire of the ring-stents as discussed above. The aim of the scanning was therefore to detect the Nitinol rings with enough detail to be able to identify the individual strands, particularly those on the inside of the bundle at the peaks and valleys. The scanning has also provided valuable information on hook deformation and insight to the general compaction patterns and the associated variability. The focus in this section will be purely on quantifying the compaction strains on the *Anaconda OLB* proximal rings and the *Thoraflex Hybrid* rings.

The Micro CT scanning was carried out by *Inside Matters* (Ghent, Belgium), a spin-out company from Ghent University, who develop bespoke imaging hardware and software (*Inside Matters* have now merged with company *XRE*). The '*HECTOR*' scanner [115] was used at a tube voltage of 180kV, total X-ray power of 20-25W, with a 0.5mm copper filter to reduce metal artefacts and beam hardening effects. The raw 2D image 'slices' were reconstructed to a 3D volume using their proprietary *Octopus* software. The resulting resolution was a voxel size of $25^3 \mu m^3$. Subsequently, a surface mesh (.STL) file would be determined using fixed value grey scale segmentation.

This methodology was tuned to identify the Nitinol components, however some image artefact from highly radio opaque tantalum markers was unavoidable. The stainless steel braid in the wall of the sheath is picked up as can be seen in the example Micro CT generated STL images shown in Figure 121. The bottom image in Figure 121 is 'view cut' revealing the rings and other metallic components including hooks, release wires, tantalum markers/crimps, and the tip of the 'intrinsic guide wire'.

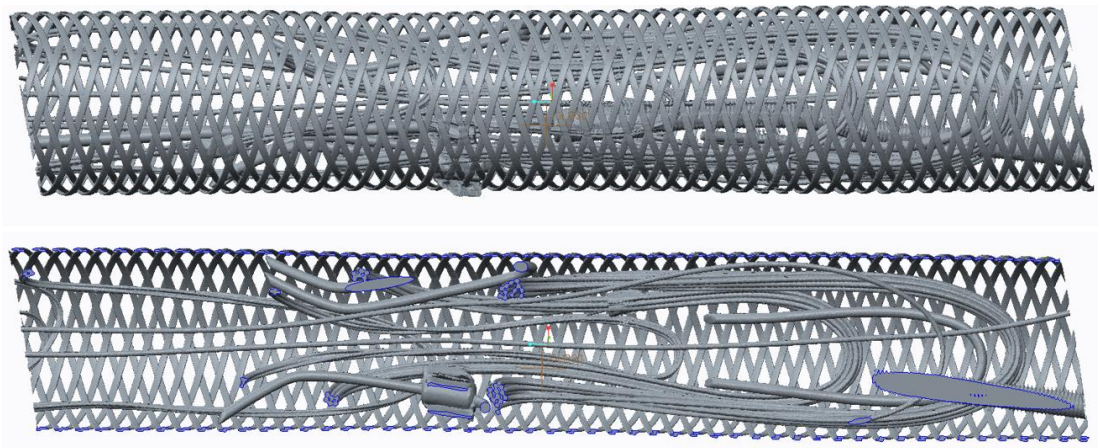

Figure 121 - An example STL image from Micro CT scan of a compacted OLB30 device in braided sheath. Top is the full image and bottom is a view cut revealing more detail of the device components.

A method was developed with *Creo Parametric 2.0* software to measure the curvature of individual strands of wire at the peaks and valleys of compacted rings. The procedure will not be fully detailed here but can be summarised as:

1. The STL image is imported and view-cut to a convenient angle for the peak or valley to be measured.
2. A plane was generated which cuts through the centre of the strand to be measured in the plane of curvature.
3. A new view cut was created with the new plane and a circle sketch tool was used to estimate the inner curvature of a single strand.
4. The centreline curvature of the strand is calculated by adding a wire diameter to the value gained in step above.

An example measurement of inner curvature of a strand at the peak of an R1 ring is shown in Figure 122, with a result of 2.43mm. All inner strands suspected of being the 'worst case' were measured for each peak and valley location.

In the initial *Anaconda* study, n=5 OLB23 and n=3 OLB34 devices were scanned because these are the largest devices, using the thickest wire, in the two respective sheath sizes (6.2mm and 6.7mm inner diameter). All other OLB body devices had a single sample prepared and scanned. The OLB23 was found to have higher strains than the OLB34, hence the increased sample size from 3 to 5.

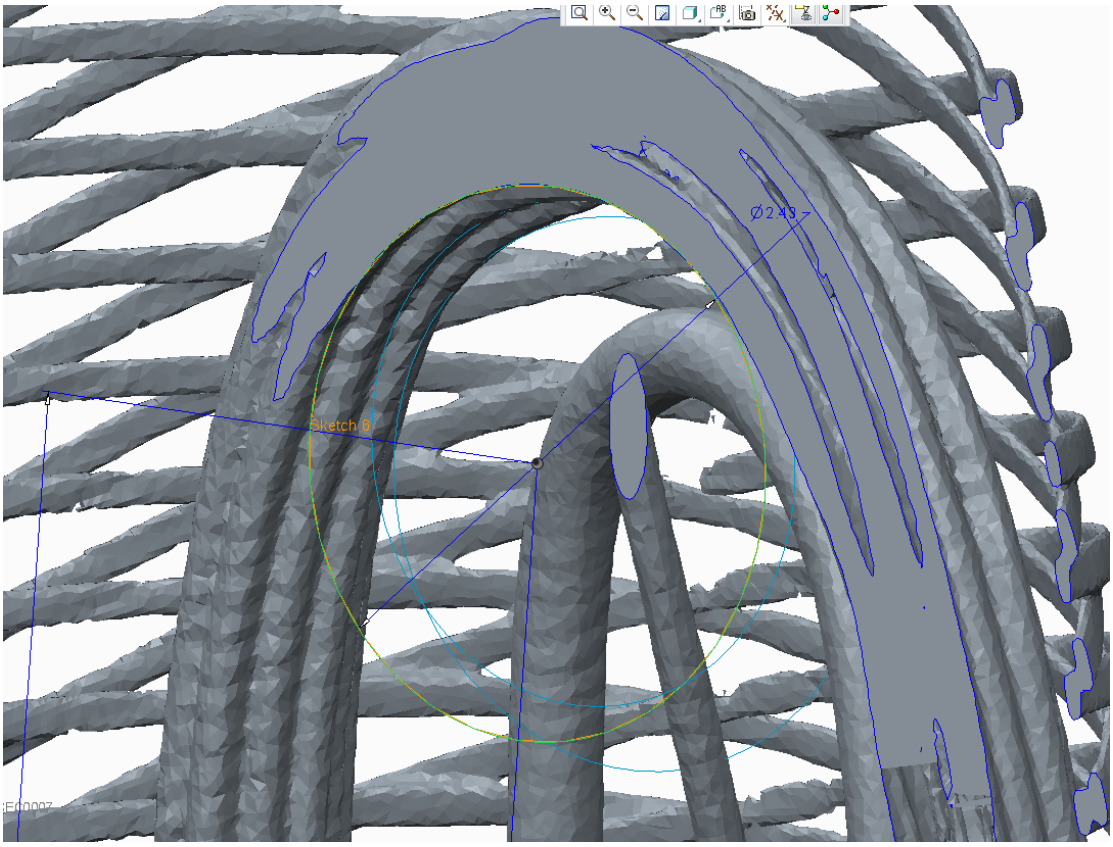

Figure 122 - An example measurement of inner strand diameter of curvature on a MicroCT generated STL image.

For validation of the scanning and image processing, two circular steel washers were both physically measured using calibrated pin gauges, and measured through the Micro-CT scan process. The washers were measured physically to have inner diameters of 2.33±0.005mm and 4.43±0.005mm each. Each washer was scanned once, converted to STL, and then measured 5 times. The average error and relative standard deviations were acceptably low at -0.004mm ±0.23% and -0.018mm ±0.10% respectively. The main source of variance is from the level of interpretation required at the step of measuring the inner curvature of a wire strand. The repeatability of measurement was therefore assessed by measuring the peaks on one sample 5 times, and found to have a relative standard deviation (RSD) of 2.95%. This was lower than the sample RSD at common locations for both the OLB23 and OLB34 (those that had multiple samples), and therefore deemed acceptable.

An example Micro CT measured set of strain results for the OLB25 device is shown in Figure 123, where each bar on the graph represents the worst-case strand (highest strain measurement) from each peak or valley. The full range of results, including one historic

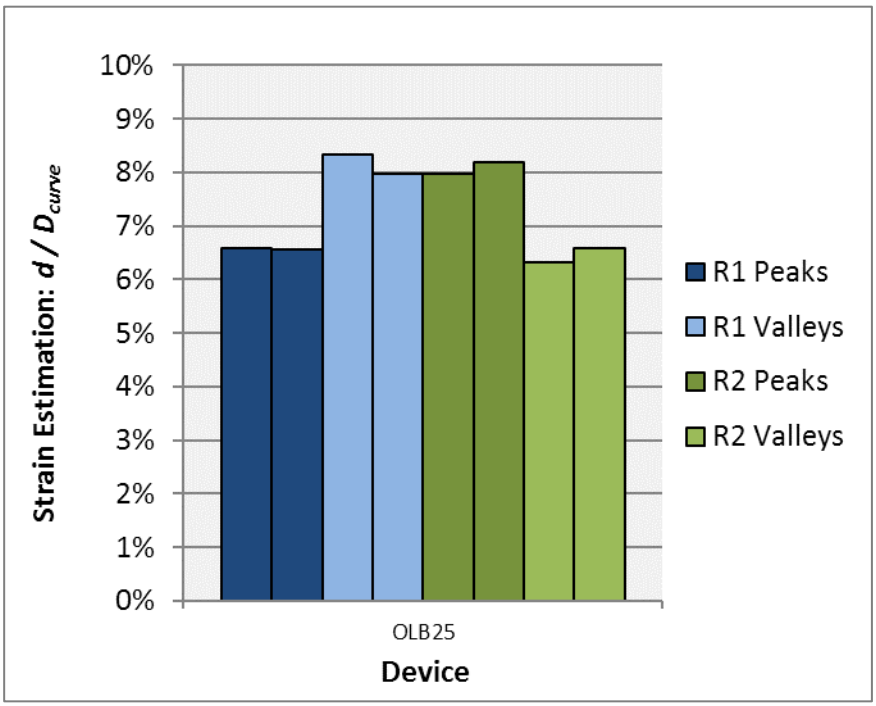

Figure 123 - MicroCT measured strain estimations from the worst-case strands from peak and valleys of the OLB25 proximal rings

B19 (previous generation) device, are plotted in Appendix P. One R1 valley result on the B19 and one R2 peak result on the OLB32 device are missing due to being obscured by artefact from the nearby tantalum markers. Across the full range, the d/D_{curve} results are in the range 4.9% – 11.4%. The R1 valleys and the R2 peaks generally show the highest strain results which can be mainly attributed to the fact that rings are overlapping in these areas; more bulk causing the respective valley or peak to fold in a smaller diameter than would be available if there were no other components to contend with. The OLB23, being the largest device in the 6.2mm sheath, produced the three highest strain results: 10.9%, 10.9% and 11.4% all at an R1 valley locations. Assessing all of the OLB23 R1 valley results provides an average 9.8% and 1.1% standard deviation. It must be kept in mind that these represent the worst-case strand at each valley location. A brief study comparing inner strands with outer strands at all locations on a single device found that outer strands were on average at 28% reduced maximum strain level. The OLB25 device appears to be under least strain, with a maximum d/D_{curve} value of 8.3% which is consistent with the fact that the OLB25 is the smallest device in the larger sheath.

Regarding the *Thoraflex Hybrid* device; the stent-graft portions are all delivered in the same 9.5mm inner diameter sheath, and therefore it was decided to scan 3 of the largest 40mm devices and compare against the results of *Anaconda*. The same methodology and

resulting resolution was applied to the distal sealing end of the *Hybrid* device, and three rings on each sample were measured (the *Thoraflex Hybrid* device is inserted pointing distally, or 'downstream' in the patients aorta, opposite to the *Anaconda* which is introduced pointing proximally). The STL produced from one scan is shown in Figure 124. The results are plotted in Appendix Q. The location of highest strain on average for the Hybrid devices was the R1 peaks with average of 10.0% and highest result of 10.2%. This result is logical: the R1 having slightly thicker wire than the 'mid rings' (0.22mm compared to 0.20mm) and the peak being in a high bulk zone with all 3 rings overlapping.

Figure 124 - An STL image from Micro CT scan of the distal end of a Thoraflex Hybrid (40mm stented section) device.

Considering the implications of the strain levels observed, the worst-case OLB23 R1 valley results was focused on. The OLB23 R1 valley worst strain d/D_{curve} measurements averaged at 9.8%±1.1% which lies in the fully martensitic phase, and if the results from the FE analysis (section 8.1.1), which were considering the effect of asymmetry, are taken into consideration this would suggest that the tensile strain could be exaggerated to 10.6% on average. Again, this is only for the tightest turn in the bundle, and the outer strands may lie at an average of 7.6% tensile (based on 28% reduction discussed above) which is just past the end of transformation. Small levels of residual strain have been observed when Nitinol has been initially strained to beyond ~7% in uniaxial loading, however the reverse transformation along the lowered plateaus is still clearly occurring. Beyond ~12% strain there is a loss of reverse transformation and significant residual strain/permanent set, as found by testing carried out by the author on behalf of Vascutek [116]. The latter case is clearly completely undesirable, and while the former may cause slight permanent set to the wire, it may not impact radial force significantly.

Nevertheless, this analysis would propose that the *Anaconda* body devices, particularly the OLB23 is fairly limited in potential for further compaction under the current configuration.

As a result of the findings here, there has been ongoing work at Vascutek to empirically assess the effect of high bending strains on the recovery of Nitinol wire, and to better

define the boundaries in which the ring-stents should operate. Such information is crucial to further development with the aim of optimising delivery device sheath diameters.

8.3 Summary of Chapter 8

Beam bending theory has been introduced to estimate the maximum strain at the inner and outer surface of a strand, given the wire diameter and diameter of curvature. An FEA study compacting single turns of various wire diameters to a range of compacted states was carried out to verify if beam bending theory is appropriate, and to assess the impact of the asymmetry of Nitinol's stress-strain relation. This found that the use of the beam bending equation is suitable for comparative analysis, however it could underestimate tensile strain by up to 0.8% strain magnitude.

A useful geometric model has been created which proves theoretically that there is often an optimal range of wire diameter for compaction. If the wire is very fine, the bundle becomes excessively large to the point that strains become high for inner turns, and in the opposite direction if the wire is very thick the strains will be increased simply due to the thickness of the beam.

The Micro CT imaging has provided more precise measurements of compacted ring-stent deformations, and subsequent strain levels. It has set a bench mark for comparative measure. However, there is a requirement to better define the compaction limits in terms of material strain.

9
Conclusions and Future Recommendations

A range of novel analysis tools and methods have been developed for assessing and optimising the mechanical performance of ring-stents from the design perspectives of: radial loading on the vessel, fatigue resistance, and ability to compact into delivery sheaths. *Vascutek's* flagship endovascular device, *Anaconda One-Lok*, has been focused on as a case study to provide new knowledge in these areas. However, the tools and methods are also being used to optimise new products at the company.

First of all, the FEA methods which have been developed will be reflected on here, followed by a summary of the knowledge gained and lastly the recommendations for improvements and further work.

9.1 Methodologies Developed

The single-turn approach of van Zyl [7] was adopted and progressed by solving instabilities, adding methods to radially load and fully compact a ring, verifying the accuracy of the quarter-ring symmetry conditions by comparing with a half-ring model and justifying an appropriate mesh and element type through a mesh convergence study. Subsequently, a novel method of representing the 'full bundle' of the ring-stent has been developed which provides realistic geometry and mechanical stiffness using a simplification of the turn-to-turn interaction instead of modelling contact between the wires. The simplification, adding connector elements between the axes of adjacent wires, took significant iterative efforts to find the most appropriate solution in terms of connector element properties. Early attempts caused issues with solution stability, and the bundle could become somewhat tangled through the compaction process. A satisfactory solution was found through repeating sensitivity studies carried out on *Anaconda* OLB25 R2 ring simulations, however

the full study on all *Anaconda* proximal rings revealed that the method still has vulnerabilities. Most significantly, at low levels of ring pulsatility, there was significant variation in the delta-strains in individual turns. While these delta-strains were low in relation to the fatigue limit, they may be adding an artificial level of strain amplitude ultimately due to the turn-to-turn interaction simplification.

A new method to model the non-linear stiffness of human aortic artery in FEA has been produced. The most challenging part of this is finding data which can be applied to represent a specific age or location of artery with confidence. The more complex artery structural models such as the Holzapfel-Gasser-Ogden (see section 2.4) do not currently have the level and consistency of data required to apply the model for product development. Interpreting the Langewouters data to produce average or worst-case pressure-diameter curves for specific ages of abdominal or thoracic artery is the approach applied here, however it is only one solution and future efforts will need to be made to compare with other methods of modelling human aorta.

The combination of the full bundle modelling and the Langewouters' based artery definitions provides the first FEA simulations of ring-stents reducing the natural vessel motion due to the applied radial load stressing the vessel locally to stiffer regions of its pressure-displacement curve. The method has also provided the first look at how radial force is distributed along the circumference of the ring.

The application of 'circle packing theory' coefficients is an effective way to estimate bundle diameters given wire thickness and number of turns. This has been implemented in the standard ring design tools at *Vascutek* to estimate ring mean diameter from manufactured inner diameter, from which the relative ring strength, or 'Lutz value', of rings are now calculated. The 'circle packing theory' coefficients were also used in the spreadsheet based geometric model for compaction strain estimation, which itself has provided a method to quickly assess what ring configuration may be theoretically optimal to reduce compaction strains. This tool lead to the realisation and quantification of how reducing the diameter of the delivery systems' central core could reduce compaction strains, or allow for reduction of sheath diameter. Implementation of a reduced core is underway at *Vascutek* as part of product development.

The ‘Lutz coefficient’, used to standardise the radial strength of rings, was provided to the company without a proper derivation when the intellectual property for the ring-stent was acquired. A derivation from beam bending theory has been provided here, and the approach has been verified with FEA simulations, and therefore continues to be used.

Due to the complexities and variability of ring-stent devices compacting, Micro CT imaging and measurement was introduced, as opposed to simulation, to assess deformation and therefore strain levels in the Nitinol wire. This method has benchmarked the current devices in terms of worst-case compaction strain in rings, and is a standard part of the development process.

9.2 Knowledge Gained

Early simulations, using single-turn modelling, provided design relevant insight into trends of how mean-strain and delta-strain vary with oversize and pulsatility of a ring. Regarding ‘ring strength’, the beam bending equation based derivation of ‘absolute radial force’ and ‘relative radial force’, have provided understanding and validation for applying the ‘Lutz value’ approach as mentioned above. The relation of a ring-stent’s ‘radial stiffness’ to its wire diameter and ring diameter was also derived, which provides a new parameter by which to consider ring design. The plateauing radial force vs. displacement behaviour was introduced and shown to be common for various ratios of wire diameter to ring diameter.

The simulations of the physical ring fatigue tests were essential for creating the new ‘strain-life’ fatigue limit for the current grade wire. This collective work is ‘non- zero’ mean-strain material fatigue analysis on Nitinol wire, an example of which could not be found in literature. It provides the basis on which the fatigue life of ring-stents deployed in vessel can be assessed, and has been necessary to update the fatigue safety case for current devices.

The study involving ‘full bundle’ rings deployed in artery has provided evidence of optimal device oversizing, from radial force and distribution perspective. The work of Chapter 7 also provides a theoretical proof of the ‘damping’ behaviour and resulting low level delta-strains, caused by the ring forcing the artery locally to the stiffer region of its pressure-diameter curve. This suggests fatigue safety for the *Anaconda* rings in the vessel age-range studied, however further validation is required, and comparison with other vessel biomechanical models would be recommended as they become available. The artery

modelling method is an interpretation of 'passive' response observations from empirical testing; it does not consider the 'active' biological response, such as remodelling growth.

The geometric calculation model of ring-stents in compacted positions has revealed that often there is an optimal range in terms of wire diameter: increasing wire thickness inherently increases strain, while conversely very fine wire results in excessive bundle diameter and inner turns which would theoretically have increased strain. The FE study on single-turn models of various wire diameters being forced into various levels of compacted deformations provided evidence that using the 'd/D_{curve}' measurement is a reasonable estimation of strain, however tensile strains could be underestimated by up to 0.8% in strain magnitude. As mentioned above the Micro CT method introduced has provided benchmark data on worst-case compaction strain, and confirmation of which device sizes see the highest strain levels.

9.3 Recommendations

The quarter-ring approach, which assumes two planes of symmetry, is limited to simulating idealised circular vessels and assumes perfectly straight deployment, i.e. both peaks at an equal axial position in the vessel. If the impacts of adverse factors such as lopsided deployment or elliptical vessel lumens are to be assessed, then the quarter-ring method is not applicable. Half-ring or full-ring modelling would need to be implemented, which will clearly add to the computational expense. The current full-bundle, ring-in-artery modelling is perhaps already at the limit of being convenient to run simulations on a desktop simulation computer within reasonable timescales (over 1 day for some rings). Furthermore, there is a desire to model full-device systems, i.e. multiple ring-stents interconnected with some representation of fabric, and interacting with other components. It is therefore a recommendation that a computationally lighter method be investigated, by implementing beam element theory, and comparing results with the continuum element approach presented here.

Regarding validation of ring-stent models, it is recommended that radial force levels are compared with empirical results from known physical test methods such as the 'segmented head' testers or the 'sling method' described in 4.2.4. The former can be outsourced at stent testing laboratories, and the latter is currently being developed at *Vascutek*.

While the results presented in Chapter 7 include the first quantification of how ring-stent loading varies circumferentially, it was beyond the scope of the project to acquire accurate contact pressures. This is because the reported local contact pressures at the interaction between ring and vessel are sensitive to the mesh density and the specifics of the contact interaction properties implemented. It is intended that a sensitivity study will be carried out to find an adequate mesh and contact properties to capture pressures accurately. Validation would also be possible by comparing with pressure sensor equipment, which is another test method being developed at *Vascutek*.

It is recommended that as well as radial force, the rings' radial stiffness should be considered in future design, and in particular whether the 'absolute radial stiffness' should be constant over a range of ring sizes, or vary in relation to the ring diameter.

The strain state of a ring-stent depends on its geometric proportions (i.e. wire diameter and ring diameter), its deformed position, and to some degree the deformation history. It is envisaged that a spreadsheet based tool could instantly provide the mean-strain and delta-strain of any ring-stent give the above variables. To enable this, a broad FE parametric study is intended to be carried out in order to populate the data field required.

Regarding vessel modelling, it is suggested that the method presented here (from Langewouters data [47]) is compared and verified against other characterisations of human aortic artery which may be identified or become available. As mentioned above, the Langewouters data is from cadaveric aortic samples taken out the body, and therefore does not take account of the structural stiffness added by surrounding tissue, organs and the spine. The separate layers of the artery tissue are not modelled, nor are their complex composite structures, or the natural levels of residual strain which are known to exist in healthy human aorta. This could affect the true ring-artery interaction and particularly the level of embedding which occurs. Future modelling of the artery could attempt to take this into account if data is available.

A realistic value of coefficient of friction between stent and vessel was not implemented here because of lack of data. Instead, the worst-case condition of an extremely low coefficient of friction of 1% was implemented. However, this caused significant sliding between ring and vessel for rings which were on the verge of flattening. This was judged to

be unrealistic, and it is recommended that a more realistic coefficient of friction be implemented if it can be justified or gained through empirical testing.

A possible route to validating the full-bundle, ring in artery methodology is by comparison with Dynamic Electrocardiogram gated (ECG) CT scanning. A project nearing completion, led by the *Univeristy of Twente* in collaboration with *Vascutek*, is not only providing Dynamic CT 3D volume data averaged for 10 points in the cardiac cycle from numerous patients, but quantification of ring pulsatility levels at numerous time points post-operation. This data could be used to validate the motion of rings in simulations, and guide how remodelling of tissue should be taken account of, as rings are being observed generally flattening somewhat overtime, from results so far.

Regarding Nitinol modelling, limitations of the constitutive model are being addressed by further research at the *University of Strathclyde*. The most obvious addition which could provide another use to simulation would be the ability to accurately model the residual strain, and unload plateau reduction effects of high pre-strains (>~10%). Implementing such would potentially allow the compaction to be optimised further by understanding whether small amounts of a ring-stent being exposed to high strains would be acceptable or completely detrimental to the rings' recovery.

A method to measure the compaction deformation and strain levels in individual strands has been developed, however the compaction strain limits need to be better defined. The method of measuring Micro CT scans is vulnerable to variability caused by user interpretation. If the procedure to measure curvature could be automated with an algorithm it would remove this risk.

References

[1] T. McGloughlin, Ed., *Biomechanics and Mechanobiology of Aneurysms*, vol. 7. Berlin, Heidelberg, Heidelberg: Springer Berlin Heidelberg, 2011.

[2] T. Duerig, A. Pelton, and D. Stöckel, "An overview of nitinol medical applications," *Mater. Sci. Eng. A*, vol. 273–275, pp. 149–160, Dec. 1999.

[3] BSI, "ISO 25539-1:2017 Cardiovascular implants — Endovascular devices Part 1: Endovascular prostheses." BSI, 2017.

[4] BSI, "ISO 25539-2:2012 Cardiovascular implants — Endovascular devices Part 2 : Vascular stents." BSI, 2012.

[5] W. C. Young and R. G. Budynas, *Roark's Formulas for Stress and Strain*, 7th ed. McGraw-Hill, 2002.

[6] E. McCummiskey, "The Development of an Analysis Tool for the Design of Endovascular Devices," Univesity of Strathclyde, 2008.

[7] M. van Zyl, "The Development of an Integrated Modelling Framework to Aid with the Design of Endovascular Devices," University of Strathclyde, 2015.

[8] "Cook Zenith." [Online]. Available: https://aortic.cookmedical.com/abdominal/. [Accessed: 01-Jan-2018].

[9] "Gore Excluder." [Online]. Available: http://www.goremedical.com/products/excluder. [Accessed: 01-Jan-2018].

[10] "Medtronic Endurant." [Online]. Available: http://global.medtronic.com/xg-en/healthcare-professionals/products/cardiovascular/aortic-stent-grafts/endurantii.html. [Accessed: 01-Jan-2018].

[11] D. Perrin, P. Badel, L. Orgeas, C. Geindreau, S. rolland du Roscoat, J. N. Albertini, and S. Avril, "Patient-specific simulation of endovascular repair surgery with tortuous aneurysms requiring flexible stent-grafts," *J. Mech. Behav. Biomed. Mater.*, vol. 63, no. July, pp. 86–99, 2016.

[12] S. W. Robertson, A. R. Pelton, and R. O. Ritchie, "Mechanical fatigue and fracture of Nitinol," *Int. Mater. Rev.*, vol. 57, no. 1, pp. 1–37, Jan. 2012.

[13] D. Stoeckel, A. Pelton, and T. Duerig, "Self-expanding nitinol stents: material and design considerations.," *Eur. Radiol.*, vol. 14, no. 2, pp. 292–301, Feb. 2004.

[14] Y. Liu, Z. Xie, J. Van Humbeeck, and L. Delaey, "Asymmetry of stress–strain curves under tension and compression for NiTi shape memory alloys," *Acta Mater.*, vol. 46, no. 12, pp. 4325–4338, 1998.

[15] E. Henderson, D. H. Nash, and W. M. Dempster, "On the experimental testing of fine Nitinol wires for medical devices.," *J. Mech. Behav. Biomed. Mater.*, vol. 4, no. 3, pp. 261–8, Apr. 2011.

[16] B. Reedlunn, C. B. Churchill, E. E. Nelson, J. a. Shaw, and S. H. Daly, "Tension, compression, and bending of superelastic shape memory alloy tubes," *J. Mech. Phys. Solids*, Jan. 2013.

[17] A. R. Pelton, J. Dicello, and S. Miyazaki, "Optimisation of processing and properties of medical grade Nitinol wire," *Minim. Invasive Ther. Allied Technol.*, vol. 9, no. 2, pp. 107–118, Jan. 2000.

[18] A. R. Pelton, N. Rebelo, T. W. Duerig, and A. Wick, “Experimental and FEM Analysis of the Bending Behaviour of Superelastic Tubing 1994,” *1st Int’l Conf. Shape Mem. Superelastic Technol.*, pp. 353–358, 1994.

[19] A. R. Wick, A., Vohringer, O., Pelton, “The Bending Behavior of NiTi,” *J. Phys. IV. Colloq.*, vol. 5, p. C8:789-794, 1995.

[20] T. W. Duerig, K. N. Melton, D. Stöckel, C. M. Wayman, and S. M. Fisher, *Engineering Aspects of Shape Memory Alloys*. Elsevier, 1990.

[21] D. Siddons and R. J. Moon, “Tensile and compression performance of superelastic NiTi tubing,” *Mater. Sci. Technol.*, vol. 17, no. September, pp. 1073–1078, 2001.

[22] D. S. Ford and S. R. White, “Thermomechanical behavior of 55Ni45Ti nitinol,” *Acta Mater.*, vol. 44, no. 6, pp. 2295–2307, 1996.

[23] W. W. Chen, Q. Wu, J. H. Kang, and N. A. Winfree, “Compressive superelastic behavior of a NiTi shape memory alloy at strain rates of 0.001-750 s-1,” *Int. J. Solids Struct.*, vol. 38, no. 50–51, pp. 8989–8998, 2001.

[24] J. Yang, F., Wu, H., K., Pu, Z., “The effect of strain rate and sample size effect on the superelastic behaviour of superelastic alloys,” in *Proceedings of the Second International Conference on Shape Memory and Superelastic Technologies*, 1997.

[25] S. Nemat-Nasser and J. Y. Choi, “Strain rate dependence of deformation mechanisms in a Ni–Ti–Cr shape-memory alloy,” *Acta Mater.*, vol. 53, no. 2, pp. 449–454, Jan. 2005.

[26] R. Brodie, “Characterization of Superelastic Nitinol Wire for Application to Aortic Stent Graft Design,” University of Strathclyde, 2018.

[27] M. Schlun, A. Zipse, G. Dreher, and N. Rebelo, “Effects of cyclic loading on the uniaxial behavior of nitinol,” *J. Mater. Eng. Perform.*, vol. 20, no. 4–5, pp. 684–687, 2011.

[28] D. Stevenson and P. Campbell, “Vascutek Report: Accelerate Body Fatigue Test Rev 04 (Design File 009).” Vascutek, 2002.

[29] R.Brodie, “Vascutek Report: 1985, Rev 01 - NTF - BDC-TP-1761 Test Protocol, Anaconda Low Profile Radial Durability (Design File 119, Section 2.21).” Vascutek, 2016.

[30] Vascutek, “Vascutek Report: Rotary Bend Fatigue Testing Rev 02, Vascutek.” Vascutek, 2010.

[31] M. M. Patel and R. F. Gordon, “An Investigation of Diverse Surface Finishes on Fatigue Properties of Superelastic Nitinol Wire,” *Fort Wayn Met.*, no. May, pp. 1–6, 2006.

[32] M. M. Patel, D. L. Plumley, R. J. Bouthot, and J. L. Proft, “The Significance of Melt Practice on Fatigue Properties of Superelastic NiTi Fine Diameter Wire,” *Wire*, no. May, pp. 1–6, 2006.

[33] M. M. Patel, M. R. Mitchell, K. Jerina, and S. W. Dean, “Characterizing Fatigue Response of Nickel-Titanium Alloys by Rotary Beam Testing,” *J. ASTM Int.*, vol. 4, no. 6, p. 100390, 2007.

[34] A. Runciman, D. Xu, A. R. Pelton, and R. O. Ritchie, “The influence of melt practice on final fatigue properties of superelastic NiTi wires,” *Biomaterials*, vol. 32, no. 22, pp. 4987–93, 2011.

[35] J. E. Schaffer and D. L. Plumley, “Fatigue performance of nitinol round wire with varying cold work reductions,” *J. Mater. Eng. Perform.*, vol. 18, no. 5–6, pp. 563–568, 2009.

[36] “Nitinol Devices and Components (now Confluent Inc.).” [Online]. Available: www.nitinol.com. [Accessed: 01-Jan-2018].

[37] A. Wick, X.-Y. Gong, J. Fino, J. Sheriff, and A. R. Pelton, “Bending fatigue characteristics of Nitinol,” *Proc. SMST*, vol. 683, pp. 361–366, 2006.

[38] B. James, J. Foulds, and L. Eiselstein, “Failure analysis of NiTi wires used in medical applications,” *J. Fail. Anal. Prev.*, vol. 5, no. 5, pp. 82–87, 2005.

[39] R. Klabunde, *Cardiovascular Physiology Concepts*, vol. 3. Lippincott Williams & Wilkins, 2011.

[40] J. D. Humphrey and G. A. Holzapfel, “Mechanics, mechanobiology, and modeling of human abdominal aorta and aneurysms,” *J. Biomech.*, vol. 45, no. 5, pp. 805–814, Mar. 2012.

[41] C. S. Roy, “The Elastic Properties of the Arterial Wall,” *J. Physiol.*, vol. 3, no. 2, pp. 125–159, Jan. 1881.

[42] P. Hallock and I. C. Benson, “Studies on the Elastic Properties of Human Isolated Aorta,” *J. Clin. Invest.*, vol. 16, no. 4, pp. 595–602, Jul. 1937.

[43] G. M. Hass, “Elastic tissue. II. A study of the elasticity and tensile strength of elastic tissue isolated from the human aorta,” *Am. Heart J.*, vol. 25, no. 6, p. 842, Jun. 1943.

[44] D. H. Bergel, “The static elastic properties of the arterial wall,” *J. Physiol.*, vol. 156, pp. 445–457, 1961.

[45] B. M. Learoyd and M. G. Taylor, “Alterations with age in the viscoelastic properties of human arterial walls.,” *Circ. Res.*, vol. 18, no. 3, pp. 278–92, Mar. 1966.

[46] T. Nakashima and J. Tanikawa, “A Study of Human Aortic Distensibility With Relation To Atherosclerosis and Aging,” *Angiology*, vol. 22, no. 8, pp. 477–490, Jan. 1971.

[47] G. J. Langewouters, K. H. Wesseling, and W. J. Goedhard, “The static elastic properties of 45 human thoracic and 20 abdominal aortas in vitro and the parameters of a new model.,” *J. Biomech.*, vol. 17, no. 6, pp. 425–35, Jan. 1984.

[48] T. Länne, B. Sonesson, D. Bergqvist, H. Bengtsson, and D. Gustafsson, “Diameter and compliance in the male human abdominal aorta: influence of age and aortic aneurysm.,” *Eur. J. Vasc. Surg.*, vol. 6, no. 2, pp. 178–84, Mar. 1992.

[49] B. Sonesson, T. Länne, E. Vernersson, and F. Hansen, “Sex difference in the mechanical properties of the abdominal aorta in human beings.,” *J. Vasc. …*, vol. 20, no. 6, pp. 959–69, Dec. 1994.

[50] B. Sonesson, F. Hansen, H. Stale, and T. Länne, “Compliance and diameter in the human abdominal aorta--the influence of age and sex.,” *Eur. J. Vasc. Surg.*, vol. 7, no. 6, pp. 690–7, Nov. 1993.

[51] L. H. Peterson, R. E. Jensen, and J. Parnell, “Mechanical Properties of Arteries in Vivo,” *Circ. Res.*, vol. 8, no. 3, pp. 622–639, May 1960.

[52] “Institute of Biomechanics, T.U. Graz.” [Online]. Available: http://www.biomech.tugraz.at/. [Accessed: 01-Jan-2018].

[53] R. W. Ogden, G. Saccomandi, and I. Sgura, “Fitting hyperelastic models to

experimental data," *Comput. Mech.*, vol. 34, no. 6, pp. 484–502, Aug. 2004.

[54] R. W. Ogden, "Large Deformation Isotropic Elasticity - On the Correlation of Theory and Experiment for Incompressible Rubberlike Solids," *Proc. R. Soc. A Math. Phys. Eng. Sci.*, vol. 326, no. 1567, pp. 565–584, Feb. 1972.

[55] G. A. Holzapfel, T. C. Gasser, and R. W. Ogden, "A New Constitutive Framework for Arterial Wall Mechanics and a Comparative Study of Material Models," *J. Elast.*, vol. 61, no. 1/3, pp. 1–48, 2000.

[56] T. C. Gasser, R. W. Ogden, and G. A. Holzapfel, "Hyperelastic modelling of arterial layers with distributed collagen fibre orientations," *J. R. Soc. Interface*, vol. 3, no. 6, pp. 15–35, Feb. 2006.

[57] C. A. J. Schulze-Bauer, C. Mörth, and G. A. Holzapfel, "Passive Biaxial Mechanical Response of Aged Human Iliac Arteries," *J. Biomech. Eng.*, vol. 125, no. 3, p. 395, 2003.

[58] G. A. Holzapfel, G. Sommer, C. T. Gasser, and P. Regitnig, "Determination of layer-specific mechanical properties of human coronary arteries with nonatherosclerotic intimal thickening and related constitutive modeling.," *Am. J. Physiol. Heart Circ. Physiol.*, vol. 289, no. 5, pp. H2048-58, Nov. 2005.

[59] G. A. Holzapfel, G. Sommer, and P. Regitnig, "Anisotropic Mechanical Properties of Tissue Components in Human Atherosclerotic Plaques," *J. Biomech. Eng.*, vol. 126, no. 5, p. 657, 2004.

[60] G. A. Holzapfel, G. Sommer, M. Auer, P. Regitnig, and R. W. Ogden, "Layer-specific 3D residual deformations of human aortas with non-atherosclerotic intimal thickening.," *Ann. Biomed. Eng.*, vol. 35, no. 4, pp. 530–45, Apr. 2007.

[61] A. J. Schriefl, G. Zeindlinger, D. M. Pierce, P. Regitnig, and G. a Holzapfel, "Determination of the layer-specific distributed collagen fibre orientations in human thoracic and abdominal aortas and common iliac arteries," *J. R. Soc. Interface*, vol. 9, no. 71, pp. 1275–1286, Jun. 2011.

[62] G. A. Holzapfel and R. W. Ogden, "Modelling the layer-specific three-dimensional residual stresses in arteries, with an application to the human aorta," *J. R. Soc. Interface*, vol. 7, no. 46, pp. 787–799, May 2009.

[63] H. Weisbecker, D. M. Pierce, P. Regitnig, and G. a Holzapfel, "Layer-specific damage experiments and modeling of human thoracic and abdominal aortas with non-atherosclerotic intimal thickening.," *J. Mech. Behav. Biomed. Mater.*, vol. 12, pp. 93–106, Aug. 2012.

[64] L. Cardamone, a Valentín, J. F. Eberth, and J. D. Humphrey, "Origin of axial prestretch and residual stress in arteries.," *Biomech. Model. Mechanobiol.*, vol. 8, no. 6, pp. 431–46, Dec. 2009.

[65] J. D. Humphrey, J. F. Eberth, W. W. Dye, and R. L. Gleason, "Fundamental role of axial stress in compensatory adaptations by arteries.," *J. Biomech.*, vol. 42, no. 1, pp. 1–8, Jan. 2009.

[66] L. A. Taber and J. D. Humphrey, "Stress-Modulated Growth, Residual Stress, and Vascular Heterogeneity," *J. Biomech. Eng.*, vol. 123, no. 6, p. 528, 2001.

[67] J. Ferruzzi, D. A. Vorp, and J. D. Humphrey, "On constitutive descriptors of the biaxial mechanical behaviour of human abdominal aorta and aneurysms," *J. R. Soc.*

Interface, vol. 8, no. 56, pp. 435–450, Mar. 2011.

[68] A. Valentín, J. D. Humphrey, and G. Holzapfel, "A Multi-Layered Computational Model of Coupled Elastin Degradation, Vasoactive Dysfunction, and Collagenous Stiffening in Aortic Aging," *Ann. Biomed. Eng.*, vol. 39, no. 7, pp. 2027–2045, Jul. 2011.

[69] D. A. Vorp, M. L. Raghavan, and M. W. Webster, "Mechanical wall stress in abdominal aortic aneurysm: influence of diameter and asymmetry.," *J. Vasc. Surg.*, vol. 27, no. 4, pp. 632–9, Apr. 1998.

[70] M. L. Raghavan, D. A. Vorp, M. P. Federle, M. S. Makaroun, and M. W. Webster, "Wall stress distribution on three-dimensionally reconstructed models of human abdominal aortic aneurysm," *J. Vasc. Surg.*, vol. 31, no. 4, pp. 760–769, Apr. 2000.

[71] A. K. Venkatasubramaniam, M. J. Fagan, T. Mehta, K. J. Mylankal, B. Ray, G. Kuhan, I. C. Chetter, and P. T. McCollum, "A comparative study of aortic wall stress using finite element analysis for ruptured and non-ruptured abdominal aortic aneurysms.," *Eur. J. Vasc. Endovasc. Surg.*, vol. 28, no. 2, pp. 168–76, Aug. 2004.

[72] D. A. Vorp, "Biomechanics of abdominal aortic aneurysm," *J. Biomech.*, vol. 40, no. 9, pp. 1887–1902, Jan. 2007.

[73] D. Roy, G. A. Holzapfel, C. Kauffmann, and G. Soulez, "Finite element analysis of abdominal aortic aneurysms: geometrical and structural reconstruction with application of an anisotropic material model," *IMA J. Appl. Math.*, vol. 79, no. 5, pp. 1011–1026, 2014.

[74] Y. C. Fung, K. Fronek, and P. Patitucci, "Pseudoelasticity of arteries and the choice of its mathematical expression.," *Am. J. Physiol.*, vol. 237, no. 5, pp. H620-31, Nov. 1979.

[75] J. D. Humphrey, "Mechanics of the arterial wall: review and directions.," *Crit. Rev. Biomed. Eng.*, vol. 23, no. 1–2, pp. 1–162, 1995.

[76] M. Raghavan and D. A. Vorp, "Toward a biomechanical tool to evaluate rupture potential of abdominal aortic aneurysm: identification of a finite strain constitutive model and evaluation of its applicability," *J. Biomech.*, vol. 33, no. 4, pp. 475–482, Apr. 2000.

[77] J. P. Vande Geest, M. S. Sacks, and D. A. Vorp, "The effects of aneurysm on the biaxial mechanical behavior of human abdominal aorta," *J. Biomech.*, vol. 39, no. 7, pp. 1324–1334, Jan. 2006.

[78] W. Dempster and D. Forbes, "Analysis Methods for Vascutek Stent Designs," 2001.

[79] G. J. Langewouters, K. H. Wesseling, and W. J. Goedhard, "The static elastic properties of 45 human thoracic and 20 abdominal aortas in vitro and the parameters of a new model.," *J. Biomech.*, vol. 17, no. 6, pp. 425–35, Jan. 1984.

[80] D. Bow, "Vascutek Report: Mathmodel Critique (KTP8620_2.2_v3)." Vascutek, 2012.

[81] W. Dempster, "Integration of FE analysis with the Srathclyde Anaconda/Thoracic Bundle Model." University of Strathclyde, 2009.

[82] ASTM F2063 Standard, "F2063 Standard Specification for Wrought Nickel-Titanium Shape Memory Alloys for Medical Devices and Surgical Implants 1," *Annu. B. ASTM Stand.*, no. C, pp. 1–6, 2012.

[83] A. Boukis and R. Brodie, "Vascutek Report: RD 2107R Tensile Testing of Nitinol Wire

using Instron with Bullhorn Grips and Video Extensometer." Vascutek.

[84] F. Auricchio and R. L. Taylor, "Shape-memory alloys: modelling and numerical simulations of the finite-strain superelastic behavior," *Comput. Methods Appl. Mech. Eng.*, vol. 143, no. 1–2, pp. 175–194, Apr. 1997.

[85] F. Auricchio, R. L. Taylor, and J. Lubliner, "Shape-memory alloys: macromodelling and numerical simulations of the superelastic behavior," *Comput. Methods Appl. Mech. Eng.*, vol. 146, no. 3–4, pp. 281–312, Jul. 1997.

[86] J. Lubliner, "A simple model of generalized plasticity," *Int. J. Solids Struct.*, vol. 8, pp. 769–778, 1991.

[87] R. Thomas, "Improving Medical Devices Using Computational Modeling," 2012. [Online]. Available: https://www.asme.org/engineering-topics/articles/performance-test-codes/improving-medical-devices-using-computational-mode. [Accessed: 01-Jun-2017].

[88] O. C. Zienkiewicz, R. L. Taylor, and J. Z. Zhu, *The Finite Element Method: Its Basis & Fundamentals*, 7th ed. Butterworth-Heinemann, 2013.

[89] T. K. Hellen and A. A. Becker, *Finite Element Analysis for Engineers - A Primer*. NAFEMS, 2013.

[90] S. Moaveni, *Finite Element Analysis: Theory and Application with Ansys*. Prentice Hall, 2003.

[91] "Abaqus 6.13 Online Documentation." Dassault Systemes, 2013.

[92] ASTM, "ASTM F3067 Guide for Radial Loading of Balloon Expandable and Self Expanding Vascular Stents," 2014.

[93] R. L. Graham, B. D. Lubachevsky, K. J. Nurmela, and P. R. J. Ostergard, "Dense packings of congruent circles in a circle," *Discrete Math.*, vol. 181, pp. 139–154, 1998.

[94] B. D. Lubachevsky and R. L. Graham, "Curved Hexagonal Packings of Equal Disks in a Circle," *Discrete Comput. Geom.*, vol. 18, pp. 179–194, 1997.

[95] G. E. Reis, "Dense Packing of Equal Circles within a Circle," *Math. Mag.*, vol. 48, no. 1, pp. 33–37, 1975.

[96] S. Kravitz, "Packing Cylinders into Cylindrical Containers," *Math. Mag.*, vol. 40, no. 2, p. 65, Mar. 1967.

[97] Vascutek, "Vascutek Clinical Report: Evaluation of the Use of the Vascutek Anaconda Stent Graft System." Vascutek, 2013.

[98] Vascutek, "Thoraflex™ Hybrid Device Post-Market Surveillance Registry - Annual Report." Vascutek, 2015.

[99] R. S. Marlow, "A general first-invariant hyperelastic constitutive model," *Const. Model. Rubber III*, pp. 157–160, 2003.

[100] W. Flügge, *Stresses in Shells*. Berlin, Heidelberg: Springer Berlin Heidelberg, 1960.

[101] C. K. Zarins, C. Xu, and S. Glagov, "Atherosclerotic enlargement of the human abdominal aorta.," *Atherosclerosis*, vol. 155, no. 1, pp. 157–64, Mar. 2001.

[102] M. R. Labrosse, C. J. Beller, T. Mesana, and J. P. Veinot, "Mechanical behavior of human aortas: Experiments, material constants and 3-D finite element modeling

including residual stress.," *J. Biomech.*, vol. 42, no. 8, pp. 996–1004, May 2009.

[103] D. Roy, C. Kauffmann, S. Delorme, S. Lerouge, G. Cloutier, and G. Soulez, "A literature review of the numerical analysis of abdominal aortic aneurysms treated with endovascular stent grafts.," *Comput. Math. Methods Med.*, vol. 2012, p. 820389, Jan. 2012.

[104] C. Matthews, "Engineers' Data Book," in *Engineers's Data Book*, 3rd ed., Professional Engineering Publishing, 2004, p. 77.

[105] R. Brodie, "Vascutek Report: R&D 1601P Nitinol Ring Fatigue Material Characterisation Testing Protocol." Vascutek, 2015.

[106] R. Brodie, "Vascutek Report: RD 1601R Nitinol Ring Fatigue Material Characterisation Testing Report." Vascutek, 2016.

[107] European Network of Transmission System Operators for Electricity, "P1: Load-Frequency Control and Performance," 2009.

[108] British Standard Institute, "Metallic materials, fatigue testing, statistical planning and analysis of data," *BS ISO 12107*. 2012.

[109] J. van Prehn, F. J. V Schlösser, B. E. Muhs, H. J. M. Verhagen, F. L. Moll, and J. A. van Herwaarden, "Oversizing of Aortic Stent Grafts for Abdominal Aneurysm Repair: A Systematic Review of the Benefits and Risks," *Eur. J. Vasc. Endovasc. Surg.*, vol. 38, no. 1, pp. 42–53, 2009.

[110] PTC, "Mathcad 15.0." PTC, Needham, MA. USA, 2010.

[111] Vascutek, "Nitinol Wire Specification, Drawings 208 (-001,-002,-003,-004,-006,-007,-008,-009,-019)."

[112] J. D. Wright, J. P. Hughes, Y. Ostchega, S. S. Yoon, and T. Nwankwo, "Mean systolic and diastolic blood pressure in adults aged 18 and over in the United States, 2001-2008.," *Natl. Health Stat. Report.*, no. 35, pp. 1–22, 24, Mar. 2011.

[113] J. Hannah and M. J. Hillier, *Applied Mechanics*, 3rd ed. Pearson Education Ltd, 1995.

[114] PTC, "Creo Parametric 2.0." Needham, MA. USA, 2012.

[115] B. Masschaele, M. Dierick, D. Van Loo, M. N. Boone, L. Brabant, E. Pauwels, V. Cnudde, and L. Van Hoorebeke, "HECTOR: A 240kV micro-CT setup optimized for research," *J. Phys. Conf. Ser.*, vol. 463, p. 012012, Oct. 2013.

[116] D. Bow, "Vascutek Report: RD 2574 - Investigating Permanent Set and Kinking in Nitinol Wires Subject to High Bending." Vascutek, 2018.

List of Appendices

Appendix A

Anaconda Sizing Chart

Device Selection Procedure

1. SELECT THE BODY

a. Measure the native aortic maximum neck diameter* at the deployment site. **D1**
b. Select the appropriate size of bifurcate body from the Body Sizing Table (page 3).

2. SELECT THE RIGHT LEG

a. Measure the right native iliac diameter† at the deployment site. **D5a**
b. Measure the total device effective length needed ie. the peak of the bifurcate body proximal ring stent to the distal iliac leg deployment site. **L4a**
c. Select the Catalogue Number(s) needed using the Leg Sizing Table (page 4).

3. SELECT THE LEFT LEG

a. Measure the left native iliac diameter† at the deployment site. **D5b**
b. Measure the total device effective length needed ie. the peak of the bifurcate body proximal ring stent to the distal iliac leg deployment site. **L4b**
c. Select the Catalogue Number(s) needed using the Leg Sizing Table (page 4).

Please Note:
a) All dimensions are based upon the internal vessel diameter. If external diameters are used then an allowance must be made for the vessel wall thickness.
b) Other component combinations may be used for more complex anatomy. For advice please contact your Anaconda™ Clinical Support Specialist.
c) Where the maximum total device length needed is between those quoted in the leg sizing tables the shorter leg should be selected.
d) Minimum leg-to-leg overlap and length of deployment site 20mm.

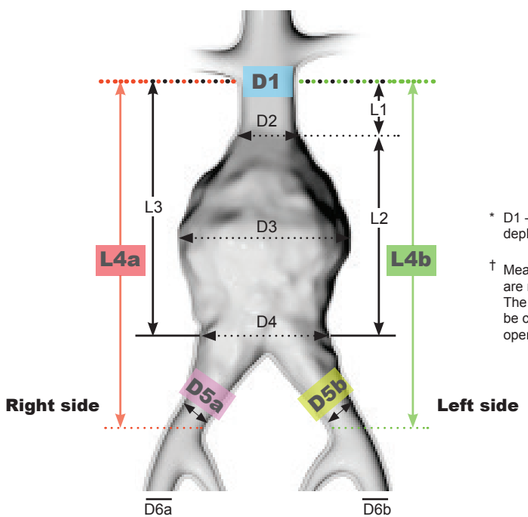

* D1 - Maximum neck diameter at the deployment site.

† Measurements highlighted in colour are needed for correct device selection. The other measurements shown should be considered at the patient pre-operative assessment stage.

ONE-LOK™ Body Sizing Table

Aortic Vessel Internal Diameter Range - D1 (mm)	Catalogue Number	Device Proximal Diameter (OD mm) A
17.5 - 19.5	OLB21	21.5
19.5 - 21.0	OLB23	23.5
21.0 - 23.0	OLB25	25.5
23.0 - 25.0	OLB28	28.0
25.0 - 27.5	OLB30	30.5
26.5 - 29.0	OLB32	32.0
28.5 - 31.0	OLB34	34.0

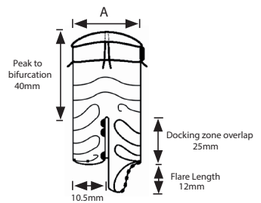

ONE-LOK™ Compatible Legs

Straight

Catalogue Number	Diameter (mm) A	B	Length L (mm)
L12x060	12	12	60
L12x080	12	12	80
L12x100	12	12	100
L12x120	12	12	120
L12x140	12	12	140
L12x160	12	12	160
L12x180	12	12	180

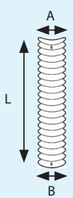

Tapered

Catalogue Number	Diameter (mm) A	B	Length L (mm)
TL1210x080	12	10	80
TL1210x110	12	10	110
TL1210x130	12	10	130
TL1210x150	12	10	150
TL1210x170	12	10	170

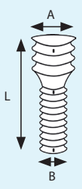

Flared

Catalogue Number	Diameter (mm) A	B	Length L (mm)
FL1213x080	12	13	80
FL1213x110	12	13	110
FL1213x130	12	13	130
FL1213x150	12	13	150
FL1213x170	12	13	170
FL1215x080	12	15	80
FL1215x110	12	15	110
FL1215x130	12	15	130
FL1215x150	12	15	150
FL1215x170	12	15	170
FL1217x080	12	17	80
FL1217x110	12	17	110
FL1217x130	12	17	130
FL1217x150	12	17	150
FL1217x170	12	17	170

Catalogue Number	Diameter (mm) A	B	Length L (mm)
FL1219x085	12	19	85
FL1219x110	12	19	110
FL1219x130	12	19	130
FL1219x150	12	19	150
FL1219x170	12	19	170
FL1221x085	12	21	85
FL1221x110	12	21	110
FL1221x130	12	21	130
FL1221x150	12	21	150
FL1221x170	12	21	170
FL1223x090	12	23	90
FL1223x110	12	23	110
FL1223x130	12	23	130
FL1223x150	12	23	150
FL1223x170	12	23	170

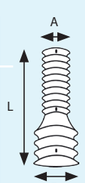

ONE-LOK™ Leg Sizing Table

Measure the Iliac Artery Diameter (mm) (D5a & D5b)	Determine the Total Device Length Needed* (mm) (L4a & L4b)	Select Appropriate Catalogue Number(s)
8.5 - 9.5mm	120mm	TL1210X080
	150mm	TL1210X110
	170mm	TL1210X130
	190mm	TL1210X150
	210mm	TL1210X170
10.0 - 11.5mm	100mm	L12X060
	120mm	L12X080
	140mm	L12X100
	160mm	L12X120
	180mm	L12X140
	200mm	L12X160
	220mm	L12X180
11.0 - 12.5mm	120mm	FL1213X080
	150mm	FL1213X110
	170mm	FL1213X130
	190mm	FL1213X150
	210mm	FL1213X170
12.5 - 14.0mm	120mm	FL1215X080
	150mm	FL1215X110
	170mm	FL1215X130
	190mm	FL1215x150
	210mm	FL1215x170
13.5 - 15.0mm	120mm	FL1217X080
	150mm	FL1217X110
	170mm	FL1217X130
	190mm	FL1217X150
	210mm	FL1217X170
15.5 - 17.0mm	125mm	FL1219X085
	150mm	FL1219X110
	170mm	FL1219X130
	190mm	FL1219X150
	210mm	FL1219X170
16.5 - 19.0mm	125mm	FL1221X085
	150mm	FL1221X110
	170mm	FL1221X130
	190mm	FL1221X150
	210mm	FL1221X170
18.5 - 21.0mm	130mm	FL1223X090
	150mm	FL1223X110
	170mm	FL1223X130
	190mm	FL1223X150
	210mm	FL1223X170

* Peak of the bifurcate body proximal ring stent to the distal iliac leg deployment site

Appendix B

UMAT for Superelasticity and Plasticity of Shape Memory Alloys

UMAT for Superelasticity and Plasticity of Shape Memory Alloys

Superelastic-plastic behavior is based on the uniaxial behavior shown here:

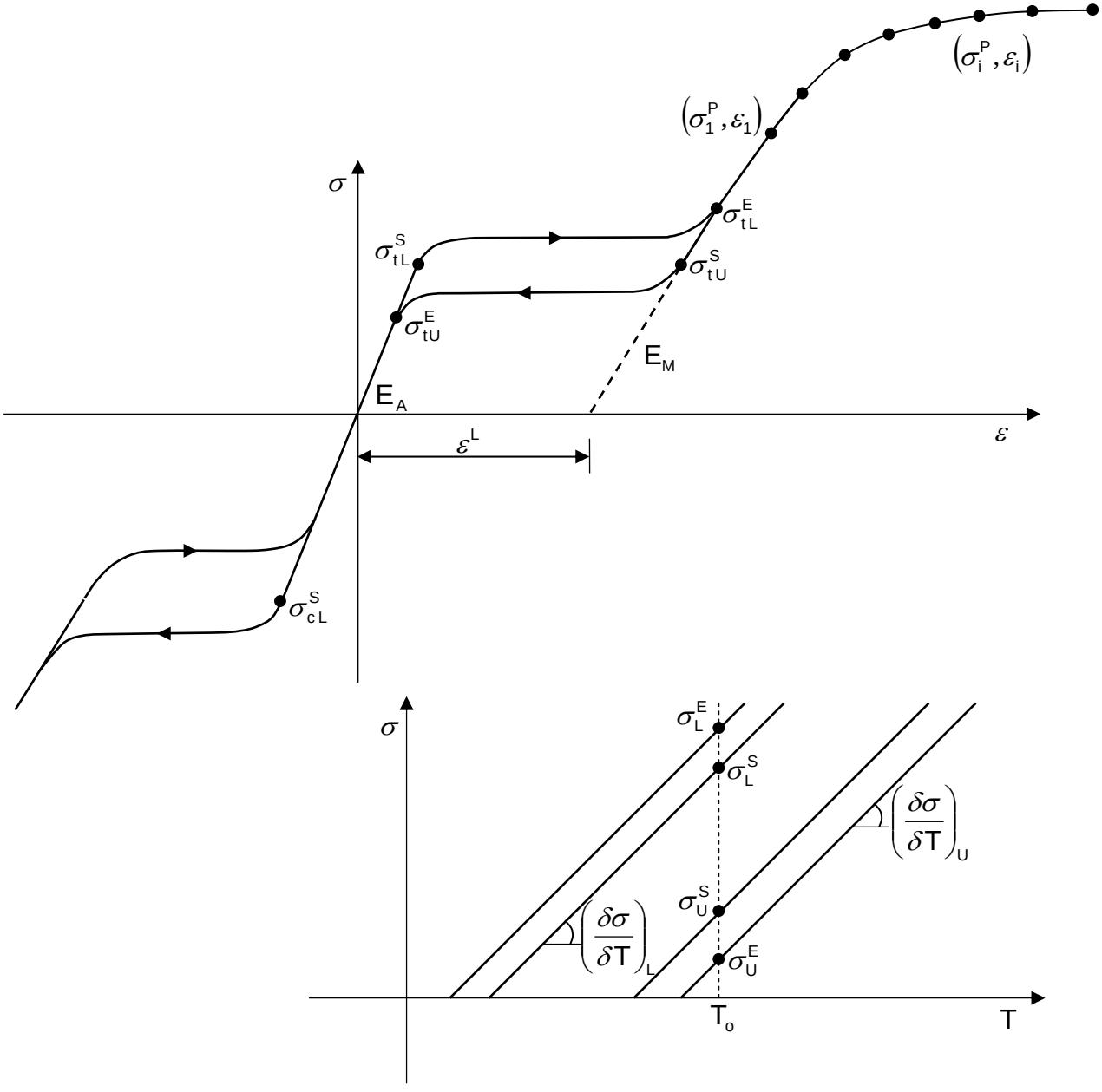

Usage

Superelastic only behavior

```
*MATERIAL, NAME=name
*USER MATERIAL, CONSTANTS=15 + N_A
```

E_A, ν_A, E_M, ν_M, ε^L, $\left(\frac{\delta\sigma}{\delta T}\right)_L$, σ_L^S, σ_L^E

T_O, $\left(\frac{\delta\sigma}{\delta T}\right)_U$, σ_U^S, σ_U^E, σ_{CL}^S, ε_V^L, N_A, N_{S1}, ...N_{SNA}

```
*DEPVAR
 24,
```

Superelastic-plastic behavior

```
*MATERIAL, NAME=name
*USER MATERIAL, CONSTANTS=16 + N_A + 2N_P
```

E_A, ν_A, E_M, ν_M, ε^L, $\left(\frac{\delta\sigma}{\delta T}\right)_L$, σ_L^S, σ_L^E

T_O, $\left(\frac{\delta\sigma}{\delta T}\right)_U$, σ_U^S, σ_U^E, σ_{CL}^S, ε_V^L, N_A, N_{S1}, ...N_{SNA}, N_P, σ_1^P, ε_1...σ_{NP}^P, ε_{NP} *(8 values per line)*

```
*DEPVAR
 31,
```

Note that for both the elastic and elastic-plastic behaviors, the name parameter on `*MATERIAL` must start with `ABQ_SUPER_ELASTIC`.

Input to Superelasticity UMAT

E_A	Austenite elasticity
ν_A	Austenite Poisson's ratio
E_M	Martensite elasticity
ν_M	Martensite Poisson's ratio
ε^L	Transformation strain
$\left(\frac{\delta\sigma}{\delta T}\right)_L$	$\delta\sigma/\delta T$ loading
σ_L^S	Start of transformation loading
σ_L^E	End of transformation loading
T_O	Reference temperature
$\left(\frac{\delta\sigma}{\delta T}\right)_U$	$\delta\sigma/\delta T$ unloading
σ_U^S	Start of transformation unloading
σ_U^E	End of transformation unloading
σ_{CL}^S	Start of transformation stress during loading in compression, as a positive value
ε_V^L	Volumetric transformation strain. If $\varepsilon_V^L = \varepsilon^L$, an associated flow algorithm is used, with ε_V^L computed based on σ_L^S and σ_{CL}^S. For all other cases, a nonassociated flow algorithm is used, which produces an unsymmetric Jacobian matrix. The `USYMM` parameter is thus required on the `*USER MATERIAL` keyword
N_A	Number of annealings to be performed during the analysis
N_{S1} - N_{SNA}	Step numbers at which all state dependent variable are set to zero
N_P	Number of stress-strain pairs to define yield curve
$\sigma_1^P, \varepsilon_1 ... \sigma_{NP}^P, \varepsilon_{NP}$	Stress-strain points in the yield curve

Output from Superelasticity UMAT

SDV1 – 6	Linear elastic strains
SDV7 – 12	Transformation strains
SDV19	Equivalent transformation strain
SDV20	Volumetric transformation strain
SDV21	Fraction of Martensite
SDV22	Equivalent uniaxial tensile stress
SDV23	Equivalent uniaxial tensile transformation strain
SDV24	Equivalent uniaxial tensile total strain
SDV26 – 31	Plastic strains[1]
SENER, ELSE, ALLSE	Linear elastic strain energy variables[2]
PENER, ELPD, ALLPD	Transformation strain energy variables[2]

1. Available for superelastic-plastic behavior
2. See the Output Table in ABAQUS User's Manual for definitions

Appendix C

PythonScript – Unifrom Radial Force Application

```
### Apply the Uniform Radial Load with cartesian components

# Select the nodes in in centre of the wire
nodes=mdb.models[modelname].rootAssembly.instances['Wire-1'].edges[0].getNodes()
#set constants
c=0
Zpositionlist=[]
#Count the number of nodes
Nlength=len(nodes)
# Load on each node:
Fradialnode = F_Radial/(Nlength-2)
# Allows limits on the nodes selected, as a ratio of the length, from each end:
Zminratio=(0.0001)
Zmaxratio=(0.0001)
# loop over nodes for ratio calcs
for i in range(0,len(nodes)):
    Zpositionlist.append(nodes[i].coordinates[2])

Zpositionlist.sort()
z1=Zpositionlist[0]
z2=Zpositionlist[Nlength-1]
Zref=Zpositionlist[Nlength-1]-Zpositionlist[0]

#calculate placing of nodes'region based on ratios
Zmin=z1+Zminratio*Zref
Zmax=z2-Zmaxratio*Zref

# loop over nodes to apply bc
for i in range(0,Nlength):
    c+=1
    b=i
    x=b+1
    node=nodes[(b):(x)]
    print node[0]
    noderegion = regionToolset.Region(nodes=node)
    nodecountstr=str(x)
    nodelabel="node"+nodecountstr
    if nodes[i].coordinates[2] >= Zmin:
        if nodes[i].coordinates[2] <= Zmax:
            Centerpinednode="node"+nodecountstr
            ratio=(z2-nodes[i].coordinates[2])/Zref
            BCz=-cos(ratio*pi/2)*Fradialnode
            BCy=-sin(ratio*pi/2)*Fradialnode
            #Apply force to node
            mdb.models[modelname].ConcentratedForce(amplitude=UNSET,
createStepName=
                'Pull', localCsys=None,
                name=nodelabel, region=noderegion, cf1=UNSET, cf2=BCy,
                cf3=BCz)
```

Appendix D

PythonScript – Half Model Single Strand

```
##Abaqus modules:
# -*- coding: mbcs -*-
from part import *
from material import *
from section import *
from assembly import *
from step import *
from interaction import *
from load import *
from mesh import *
from job import *
from sketch import *
from visualization import *
from connectorBehavior import *
import regionToolset
import math

# Define Wire Parameters
# rd = Ring Diameter, wd = wire diamter
#Base constants
rd = 26.74
wd = 0.22

#  Define Loads
#Axial Force on quarter wire
F_Axial = 0.2
#Total Uniform Radial Force on quater wire
F_Radial = 0.2

#calculated parameters
rr = rd/2
wr = wd/2
l = (pi)*(rr)

#Seeds in Quarter Circumference of cross section
Nseed = 6
#els in cross:
Xseed = 4
#Element Length
elSize = 0.375*wd

###Create Steps
##Ring Step
mdb.models['Model-1'].StaticStep(name='Ring', previous='Initial')
mdb.models['Model-1'].steps['Ring'].setValues(nlgeom=ON)
mdb.models['Model-1'].steps['Ring'].setValues(initialInc=0.05,
    maxInc=0.05)

##Pull Step
mdb.models['Model-1'].StaticStep(name='Pull', previous= 'Ring')
mdb.models['Model-1'].steps['Pull'].setValues(initialInc=0.05, maxInc=
    0.05, maxNumInc=400, minInc=1e-07, stabilizationMagnitude=0.0002,
        stabilizationMethod=DAMPING_FACTOR, continueDampingFactors=False,
        adaptiveDampingRatio=None)

###Create Part
mdb.models['Model-1'].ConstrainedSketch(name='__profile__', sheetSize=200.0)
mdb.models['Model-1'].sketches['__profile__'].CircleByCenterPerimeter(center=(0.
0, 0.0), point1=(0, wr))

mdb.models['Model-1'].Part(dimensionality=THREE_D, name='Wire', type=
    DEFORMABLE_BODY)
mdb.models['Model-1'].parts['Wire'].BaseSolidExtrude(depth=l, sketch=
    mdb.models['Model-1'].sketches['__profile__'])
del mdb.models['Model-1'].sketches['__profile__']
#Create Datum
mdb.models['Model-1'].parts['Wire'].DatumPlaneByPrincipalPlane(offset=0.0,
    principalPlane=XYPLANE)
```

```
mdb.models['Model-1'].parts['Wire'].DatumPlaneByPrincipalPlane(offset=0.0,
    principalPlane=YZPLANE)
mdb.models['Model-1'].parts['Wire'].DatumPlaneByPrincipalPlane(offset=0.0,
    principalPlane=XZPLANE)
# create partition
mdb.models['Model-1'].parts['Wire'].PartitionCellByDatumPlane(cells=
    mdb.models['Model-1'].parts['Wire'].cells.getSequenceFromMask(('[#1 ]', ),
    ), datumPlane=mdb.models['Model-1'].parts['Wire'].datums[3])

mdb.models['Model-1'].parts['Wire'].PartitionCellByDatumPlane(cells=
    mdb.models['Model-1'].parts['Wire'].cells.getSequenceFromMask(('[#3 ]', ),
    ), datumPlane=mdb.models['Model-1'].parts['Wire'].datums[4])

## Nitinol Create Material
mdb.models['Model-1'].Material(name='ABQ_SUPER_ELASTIC_1')
mdb.models['Model-1'].materials['ABQ_SUPER_ELASTIC_1'].Depvar(n=24)
mdb.models['Model-1'].materials['ABQ_SUPER_ELASTIC_1'].UserMaterial(
    mechanicalConstants=(64000.0, 0.435, 40000.0, 0.435, 0.06, 4.3, 660,
   680, 0, 5.03, 400, 350, 1100, 0.06, 0.0))
# create section
mdb.models['Model-1'].HomogeneousSolidSection(material='ABQ_SUPER_ELASTIC_1',
name=
    'wire', thickness=None)
# Assign section to part
mdb.models['Model-1'].parts['Wire'].SectionAssignment(offset=0.0, offsetField=
    '', offsetType=MIDDLE_SURFACE, region=Region(
    cells=mdb.models['Model-1'].parts['Wire'].cells.getSequenceFromMask(mask=(
    '[#f ]', ), )), sectionName='wire', thicknessAssignment=FROM_SECTION)


## Import of instance and meshing
mdb.models['Model-1'].rootAssembly.DatumCsysByDefault(CARTESIAN)
mdb.models['Model-1'].rootAssembly.Instance(dependent=OFF, name='Wire-1', part=
    mdb.models['Model-1'].parts['Wire'])
# Rotate and move instance
mdb.models['Model-1'].rootAssembly.translate(instanceList=('Wire-1', ), vector=
    (0.0, rr, 0.0))
mdb.models['Model-1'].rootAssembly.translate(instanceList=('Wire-1', ), vector=
    (0.0, 0.0, -l/2))
# Seed instance
mdb.models['Model-1'].rootAssembly.seedEdgeByNumber(constraint=FINER, edges=

mdb.models['Model-1'].rootAssembly.instances['Wire-1'].edges.getSequenceFromMask
(
    ('[#20418 ]', ), ), number=Xseed)
mdb.models['Model-1'].rootAssembly.seedEdgeByNumber(constraint=FINER, edges=

mdb.models['Model-1'].rootAssembly.instances['Wire-1'].edges.getSequenceFromMask
(
    ('[#101a00 ]', ), ), number=Nseed)
# Find and define the centre edge of the wire
centre_edge=mdb.models['Model-1'].rootAssembly.instances['Wire-1'].edges.findAt(
((0.,rr,0.),),)
# Create an edge set for that edge
mdb.models['Model-1'].rootAssembly.Set(name='CentreEdge', edges=centre_edge)
# Seed the central edge with an even number
n_els = (pi*rd/2)/elSize
# Round to an even number:
n_els_even = int(8*round(n_els/8))
#seed
mdb.models['Model-1'].rootAssembly.seedEdgeByNumber(constraint=FINER,
edges=centre_edge, number=n_els_even)
#seed the other long edges (seems necessary in some cases)
a = mdb.models['Model-1'].rootAssembly
e1 = a.instances['Wire-1'].edges
pickedEdges = e1.getSequenceFromMask(mask=('[#100 ]', ), )
a.seedEdgeByNumber(edges=pickedEdges, number=n_els_even, constraint=FINER)
a = mdb.models['Model-1'].rootAssembly
```

```
e1 = a.instances['Wire-1'].edges
pickedEdges = e1.getSequenceFromMask(mask=('[#20 ]', ), )
a.seedEdgeByNumber(edges=pickedEdges, number=n_els_even, constraint=FINER)
a = mdb.models['Model-1'].rootAssembly
e1 = a.instances['Wire-1'].edges
pickedEdges = e1.getSequenceFromMask(mask=('[#4 ]', ), )
a.seedEdgeByNumber(edges=pickedEdges, number=n_els_even, constraint=FINER)
a = mdb.models['Model-1'].rootAssembly
e1 = a.instances['Wire-1'].edges
pickedEdges = e1.getSequenceFromMask(mask=('[#40000 ]', ), )
a.seedEdgeByNumber(edges=pickedEdges, number=n_els_even, constraint=FINER)
#mesh instance
#Linear Elements selection
mdb.models['Model-1'].rootAssembly.setElementType(elemTypes=(ElemType(
    elemCode=C3D8, elemLibrary=STANDARD), ElemType(elemCode=C3D6,
    elemLibrary=STANDARD), ElemType(elemCode=C3D4, elemLibrary=STANDARD)),
    regions=(

mdb.models['Model-1'].rootAssembly.instances['Wire-1'].cells.getSequenceFromMask
(
    ('[#f ]', ), ), ))
#mesh
mdb.models['Model-1'].rootAssembly.generateMesh(regions=(
    mdb.models['Model-1'].rootAssembly.instances['Wire-1'], ))

###Identify the Middle Node 1 and hold in X direction
# select all wire nodes
allWireNodes = mdb.models['Model-1'].rootAssembly.instances['Wire-1'].nodes
#create a bounding box
delta = 0.001
xmin = 0 - delta
ymin = rr - delta
zmin = l/4 - delta
xmax = 0 + delta
ymax = rr + delta
zmax = l/4 + delta

# Get nodes that lie inside the bounding box
midnode1 = allWireNodes.getByBoundingBox(xmin, ymin, zmin, xmax, ymax, zmax)
#create node set for the node
mdb.models['Model-1'].rootAssembly.Set(name='MiddleNode1', nodes=midnode1)
# Pinning the middle node of the wire for all steps(after meshing)
# Pin the middle node in X-direction:
myRegion = regionToolset.Region(nodes=midnode1)
mdb.models['Model-1'].DisplacementBC(amplitude=UNSET, createStepName=
        'Initial', distributionType=UNIFORM, fieldName='', fixed=OFF,
        localCsys=None, name="pinmiddle1", region=myRegion, u1=0.0, u2=UNSET,
u3=UNSET, ur1=UNSET, ur2=UNSET,ur3=UNSET)

###Identify the Middle Node 2 and hold in X direction
# select all wire nodes
allWireNodes = mdb.models['Model-1'].rootAssembly.instances['Wire-1'].nodes
#create a bounding box
delta = 0.001
xmin = 0 - delta
ymin = rr - delta
zmin = -l/4 - delta
xmax = 0 + delta
ymax = rr + delta
zmax = -l/4 + delta
# Get nodes that lie inside the bounding box
midnode2 = allWireNodes.getByBoundingBox(xmin, ymin, zmin, xmax, ymax, zmax)
#create node set for the node
mdb.models['Model-1'].rootAssembly.Set(name='MiddleNode2', nodes=midnode2)
# Pinning the middle node of the wire for all steps(after meshing)
# Pin the middle node in X-direction:
myRegion = regionToolset.Region(nodes=midnode2)
mdb.models['Model-1'].DisplacementBC(amplitude=UNSET, createStepName=
```

```
        'Initial', distributionType=UNIFORM, fieldName='', fixed=OFF,
        localCsys=None, name="pinmiddle2", region=myRegion, u1=0.0, u2=UNSET,
u3=UNSET, ur1=UNSET, ur2=UNSET,ur3=UNSET)

#create a node set for the centre edge
mdb.models['Model-1'].rootAssembly.Set(name='CentreNodes',
nodes=mdb.models['Model-1'].rootAssembly.sets['CentreEdge'].nodes)

###Identify the Top Node
# select all wire nodes
allWireNodes = mdb.models['Model-1'].rootAssembly.instances['Wire-1'].nodes
#create a bounding box
delta = 0.001
xmin = 0 - delta
ymin = rr - delta
zmin = 0 - delta
xmax = 0 + delta
ymax = rr + delta
zmax = 0 + delta

# Get nodes that lie inside the bounding box
topnode = allWireNodes.getByBoundingBox(xmin, ymin, zmin, xmax, ymax, zmax)

#create node set for the node
mdb.models['Model-1'].rootAssembly.Set(name='PeakNode', nodes=topnode)

### Wire Surface:
# Create Wire Surface which will be used to define the contact interaction
mdb.models['Model-1'].parts['Wire'].Surface(name='WireSurf', side1Faces=
    mdb.models['Model-1'].parts['Wire'].faces.getSequenceFromMask(('[#3014 ]',
    ), ))

# Create Wire Ends' surfaces for output analysis purpose
mdb.models['Model-1'].parts['Wire'].Surface(name='Wire_End_YZplane', side1Faces=
    mdb.models['Model-1'].parts['Wire'].faces.getSequenceFromMask(('[#4888 ]',
    ), ))
mdb.models['Model-1'].parts['Wire'].Surface(name='Wire_End_XZplane', side1Faces=
    mdb.models['Model-1'].parts['Wire'].faces.getSequenceFromMask(('[#8460 ]',
    ), ))


###Create a node set at the peak
# select all wire nodes
allWireNodes = mdb.models['Model-1'].rootAssembly.instances['Wire-1'].nodes

# Get nodes that lie inside the bounding box
boundrad = rr + delta
PeakNodes =
allWireNodes.getByBoundingCylinder((0.0,rr,-delta),(0.0,rr,delta),boundrad)

#create node set for the node
mdb.models['Model-1'].rootAssembly.Set(name='Peak_Nodes', nodes=PeakNodes)

# Pin the Peak Node in the Z direction:
myRegion = regionToolset.Region(nodes=topnode)
mdb.models['Model-1'].DisplacementBC(amplitude=UNSET, createStepName=
        'Initial', distributionType=UNIFORM, fieldName='', fixed=OFF,
        localCsys=None, name="PinTopZ", region=myRegion, u1=UNSET, u2=UNSET,
u3=0.0, ur1=UNSET, ur2=UNSET,ur3=UNSET)

# Pin the peak node in the Y direction for Ring Step
mdb.models['Model-1'].DisplacementBC(amplitude=UNSET, createStepName=
        'Initial', distributionType=UNIFORM, fieldName='', fixed=OFF,
        localCsys=None, name="HoldTopTemp", region=myRegion, u1=UNSET, u2=0.0,
u3=UNSET, ur1=UNSET, ur2=UNSET,ur3=UNSET)
mdb.models['Model-1'].boundaryConditions['HoldTopTemp'].deactivate('Pull')

### Apply wire forming displacement BCs Y direction:
```

```
#End 1
#select facenodes top end and create the region
facenodes1=mdb.models['Model-1'].rootAssembly.instances['Wire-1'].faces[11].getN
odes()
facenodes2=mdb.models['Model-1'].rootAssembly.instances['Wire-1'].faces[3].getNo
des()
facenodes3=mdb.models['Model-1'].rootAssembly.instances['Wire-1'].faces[14].getN
odes()
facenodes4=mdb.models['Model-1'].rootAssembly.instances['Wire-1'].faces[7].getNo
des()
facenodes=facenodes1+facenodes2+facenodes3+facenodes4

#set constants
c=0
Xpositionlist=[]
Nlenght=len(facenodes)
#Cycle over nodes
c=0
for i in range(0,Nlenght):
    c+=1
    b=i
    x=b+1
    node=facenodes[(b):(x)]
    print node[0]
    region = regionToolset.Region(nodes=node)
    nodecountstr=str(c)
    nodelabel="WireEnd1_"+nodecountstr
    BCy= -facenodes[i].coordinates[1]
    mdb.models['Model-1'].DisplacementBC(amplitude=UNSET, createStepName=
        'Ring', distributionType=UNIFORM, fieldName='', fixed=OFF,
        localCsys=None, name=nodelabel, region=region, u1=UNSET, u2=BCy,
u3=UNSET, ur1=UNSET, ur2=UNSET,ur3=UNSET)

#End 2
#select facenodes bottom end and create the region
facenodes1=mdb.models['Model-1'].rootAssembly.instances['Wire-1'].faces[15].getN
odes()
facenodes2=mdb.models['Model-1'].rootAssembly.instances['Wire-1'].faces[6].getNo
des()
facenodes3=mdb.models['Model-1'].rootAssembly.instances['Wire-1'].faces[10].getN
odes()
facenodes4=mdb.models['Model-1'].rootAssembly.instances['Wire-1'].faces[5].getNo
des()
facenodes=facenodes1+facenodes2+facenodes3+facenodes4
#set constants
c=0
Xpositionlist=[]
Nlenght=len(facenodes)
#Cycle over nodes
c=1000
for i in range(0,Nlenght):
    c+=1
    b=i
    x=b+1
    node=facenodes[(b):(x)]
    print node[0]
    region = regionToolset.Region(nodes=node)
    nodecountstr=str(c)
    nodelabel="WireEnd2"+nodecountstr
    BCy= -facenodes[i].coordinates[1]
    mdb.models['Model-1'].DisplacementBC(amplitude=UNSET, createStepName=
        'Ring', distributionType=UNIFORM, fieldName='', fixed=OFF,
        localCsys=None, name=nodelabel, region=region, u1=UNSET, u2=BCy,
u3=UNSET, ur1=UNSET, ur2=UNSET,ur3=UNSET)


##Apply Linear Pull Load
a = mdb.models['Model-1'].rootAssembly
```

```
v1 = a.instances['Wire-1'].vertices
verts1 = v1.getSequenceFromMask(mask=('[#3 ]', ), )
Ends = regionToolset.Region(vertices=verts1)
mdb.models['Model-1'].ConcentratedForce(name='PullLoad-1',
createStepName='Pull',
    region=Ends, cf1=-0.2, distributionType=UNIFORM, field='',
    localCsys=None)

a = mdb.models['Model-1'].rootAssembly
Peak = a.sets['PeakNode']
mdb.models['Model-1'].ConcentratedForce(name='PullLoad-2',
createStepName='Pull',
    region=Peak, cf1=0.2, distributionType=UNIFORM, field='',
    localCsys=None)

### Set output requests
mdb.models['Model-1'].fieldOutputRequests['F-Output-1'].setValues(variables=(
'S', 'MISES','E', 'NE', 'LE', 'U', 'RF', 'CF','VF', 'CSTRESS',
'CDISP','CFORCE', 'SDV'), timeInterval=1.0, timeMarks=OFF)
#Set output frequency
mdb.models['Model-1'].fieldOutputRequests['F-Output-1'].setValuesInStep(
        stepName='Pull', timeInterval=0.1)
```

Appendix E

Langewouters' Parameters

Parameters Extracted from Langewouters Paper

The derivation and the use of the p_0 and p_1 parameters in this document are provided in the Langewouters paper. The parameter values here, for the abdominal and thoracic regions, have been extracted directly from the paper. (Langewouters et al. 1984):

Langewouters, G.J., Wesseling, K.H. & Goedhard, W.J., 1984. The static elastic properties of 45 human thoracic and 20 abdominal aortas in vitro and the parameters of a new model. *Journal of biomechanics*, 17(6), pp.425–35. Available at: http://www.sciencedirect.com/science/article/pii/0021929084900344 [Accessed July 5, 2012].

Abdominal Parameter Values

Age	P0	P1
30	39.300	35.700
39	21.5	27.400
40	19	31.900
46	11.7	26.100
46	12.9	21.400
50	9	29.100
53	7.5	20.500
54	8.6	29.300
57	1.8	26.600
58	-2	24.300
59	-4.4	31.500
63	-0.5	23.700
64	8.1	25.000
66	8.3	20.000
70	-5.8	20.400
73	-18.7	22.800
75	-29.2	28.500
76	-16.9	33.600
76	-40.3	23.700
78	-7.7	24.700

Thoracic Parameter Values

Age	P0	P1
30	50.400	42.300
39	41.3	36.800
45	36.5	36.000
45	27.7	39.700
46	24.9	41.000
47	31.7	44.400
50	38.5	45.700
50	20.3	32.100
50	26	29.600
53	27.1	36.800
54	23.9	29.400
56	25.7	33.200
57	29.5	28.800
57	21.4	26.000
58	21.1	31.500
59	18.3	26.700
60	21.2	29.500
63	25.7	38.800
64	12.7	28.000
65	23.4	30.700
66	12.2	22.200
66	18.7	27.900
66	19.6	30.100
66	15.9	27.000
68	20.3	35.000
68	5.5	19.400
71	16.4	27.100
71	11.4	17.100
72	12.6	23.100
72	6.5	27.500
73	11.6	26.000
75	-1.3	13.100
76	2.1	15.900
76	2.1	29.600
76	7.7	23.000
79	-2.3	21.600
80	-11.7	18.500
81	3.7	18.900
82	-14.4	20.700
85	1.8	15.100
85	10.8	26.300
87	-0.4	20.700
87	1.1	14.400
88	-0.4	29.500
88	1.3	23.100

Appendix F

Script Flow Diagram – Ring-in-Artery Model

Full-Bundle, Ring-in-Artery Script Top Level Flow Diagram

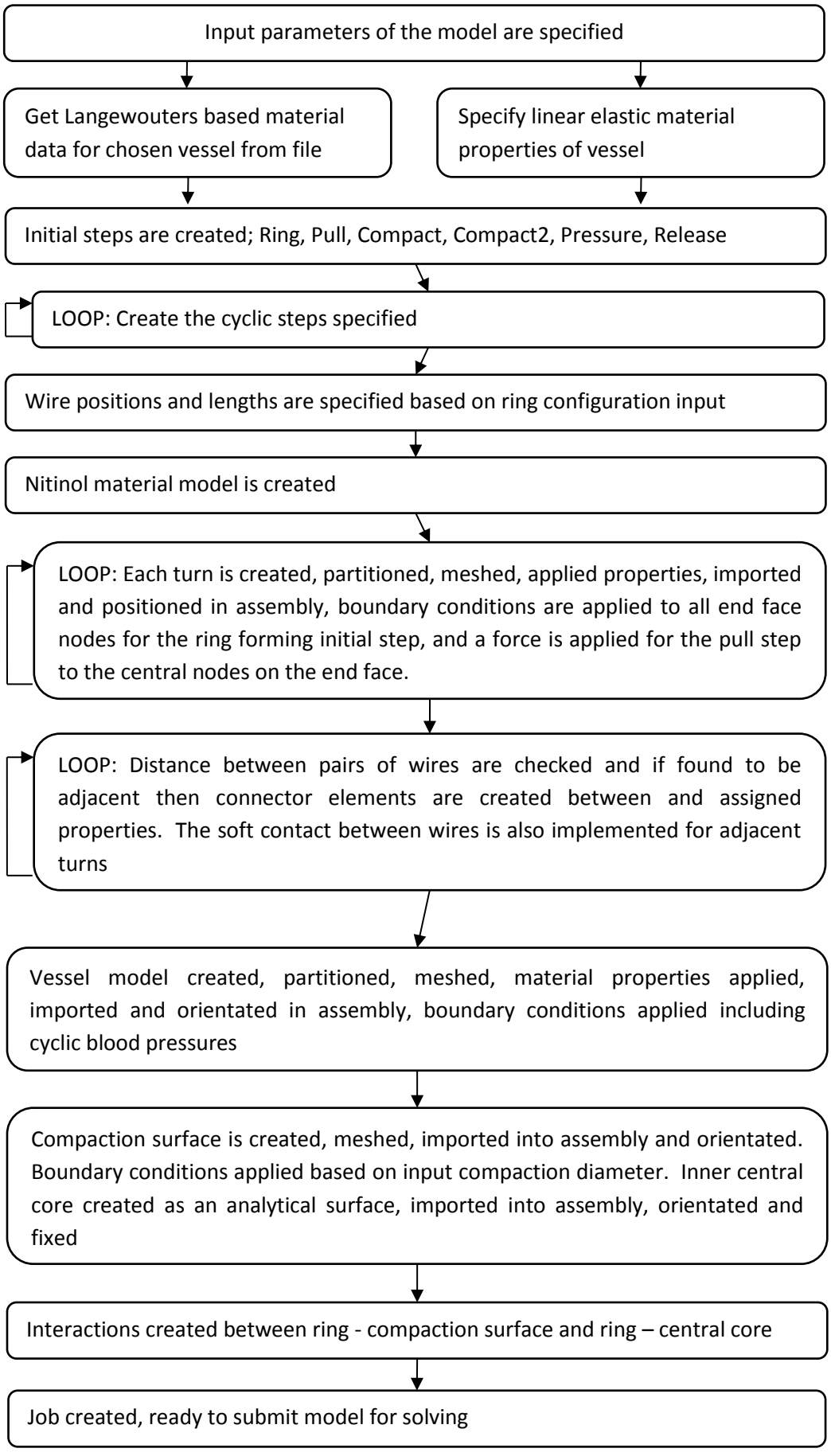

Appendix G

Powerpro Line Tensile Test Results

019mm powerpro line test2 Test Report

Product	: 019 poerpro line	**Stress Range**	: 40.00 MPa
Batch	: 1 37c	**Strain Range**	: 30.00 %
Date	: 25/05/12	**Until Extn**	: 7.00 mm
Operator	: rb	**Until Extn**	: 0.0100 mm

No.	Diameter mm	Maximum N
1	0.1900	40.90
	Mean	40.90
	Median	40.90
	Std. Dev.	-
	Coe. Var.	-
	Minimum	40.90
	Maximum	40.90

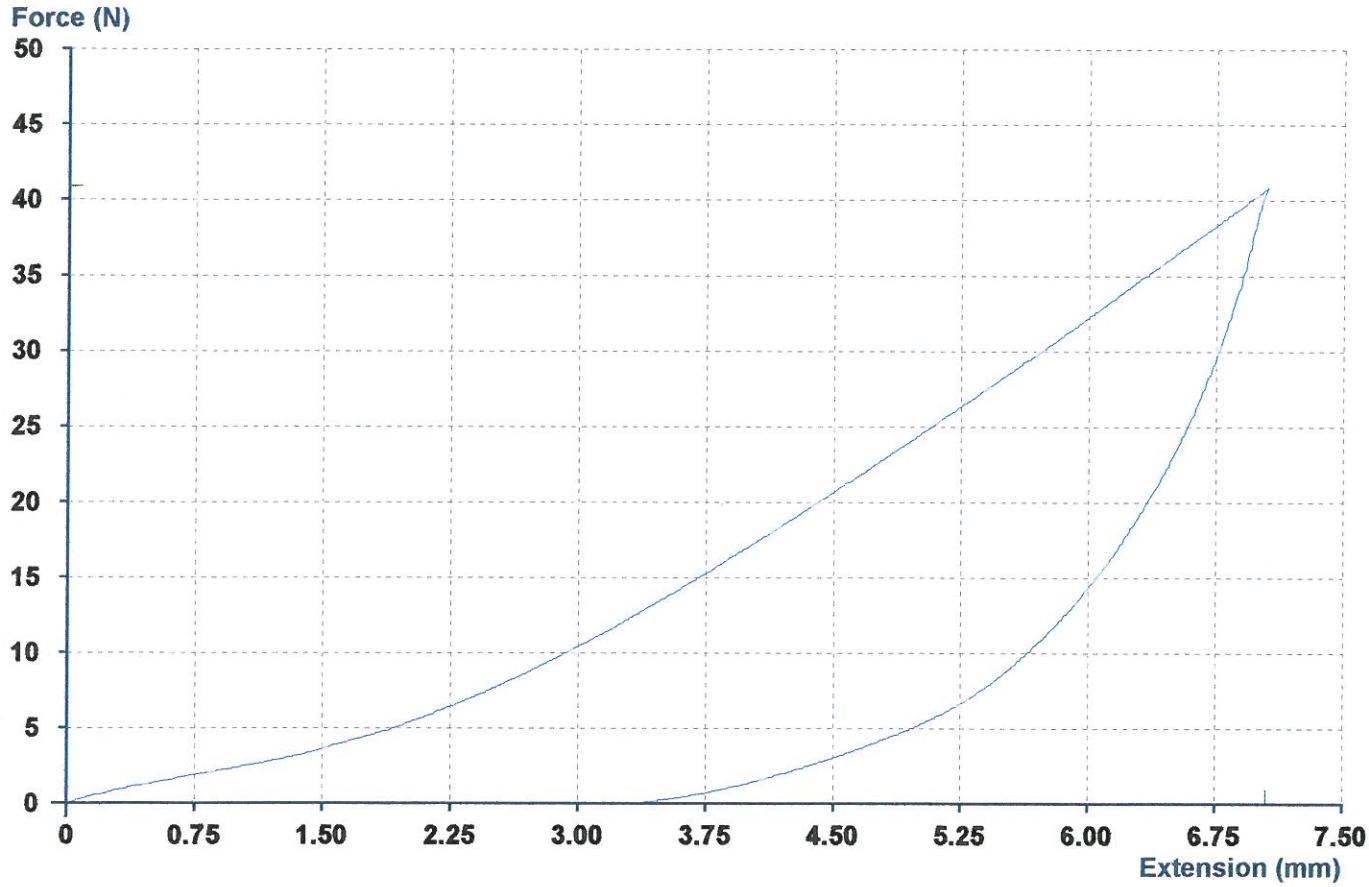

019mm powerpro line test2 Test Report

Product	: 019 poerpro line	**Stress Range**	: 40.00 MPa
Batch	: 1 37c	**Strain Range**	: 30.00 %
Date	: 25/05/12	**Until Extn**	: 7.00 mm
Operator	: rb	**Until Extn**	: 0.0100 mm

No.	Diameter mm	Maximum N
1	0.1900	[illegible]
	Mean	[illegible]
	Median	40.90
	Std. Dev.	-
	Coe. Var.	-
	Minimum	40.50
	Maximum	40.90

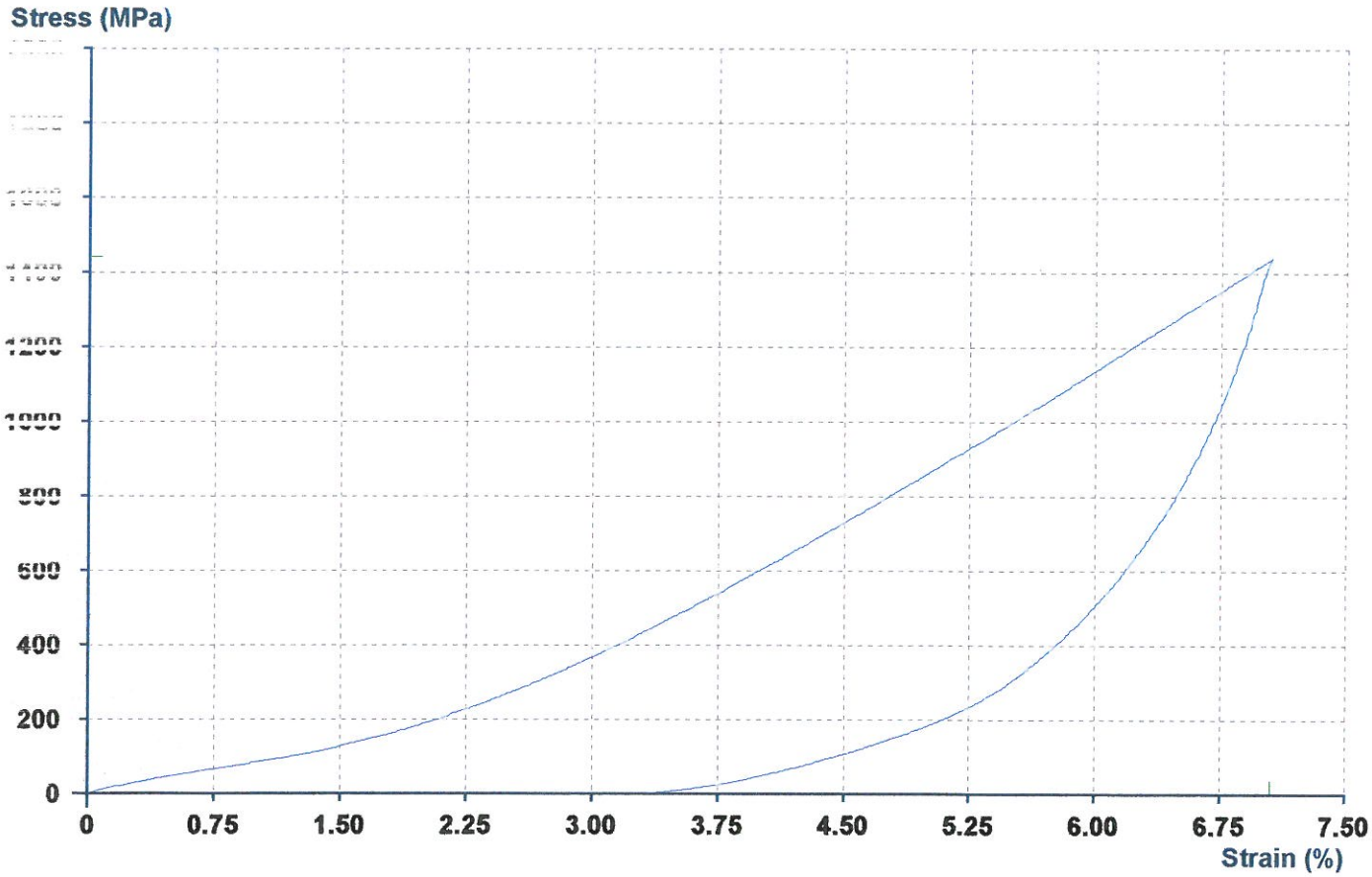

019mm powerpro line test2 Test Report

Product	: 019 poerpro line	**Load Range**	: 40.00 N
Batch	: 2 37c	**Extension Range**	: 30.00 mm
Date	: 25/05/12	**Until Extn**	: 7.00 mm
Operator	: rb	**Until Extn**	: 0.0100 mm

No.	Diameter mm	Maximum N
1	0.1900	38.84
	Mean	38.84
	Median	38.84
	Std. Dev.	-
	Coe. Var.	-
	Minimum	38.84
	Maximum	38.84

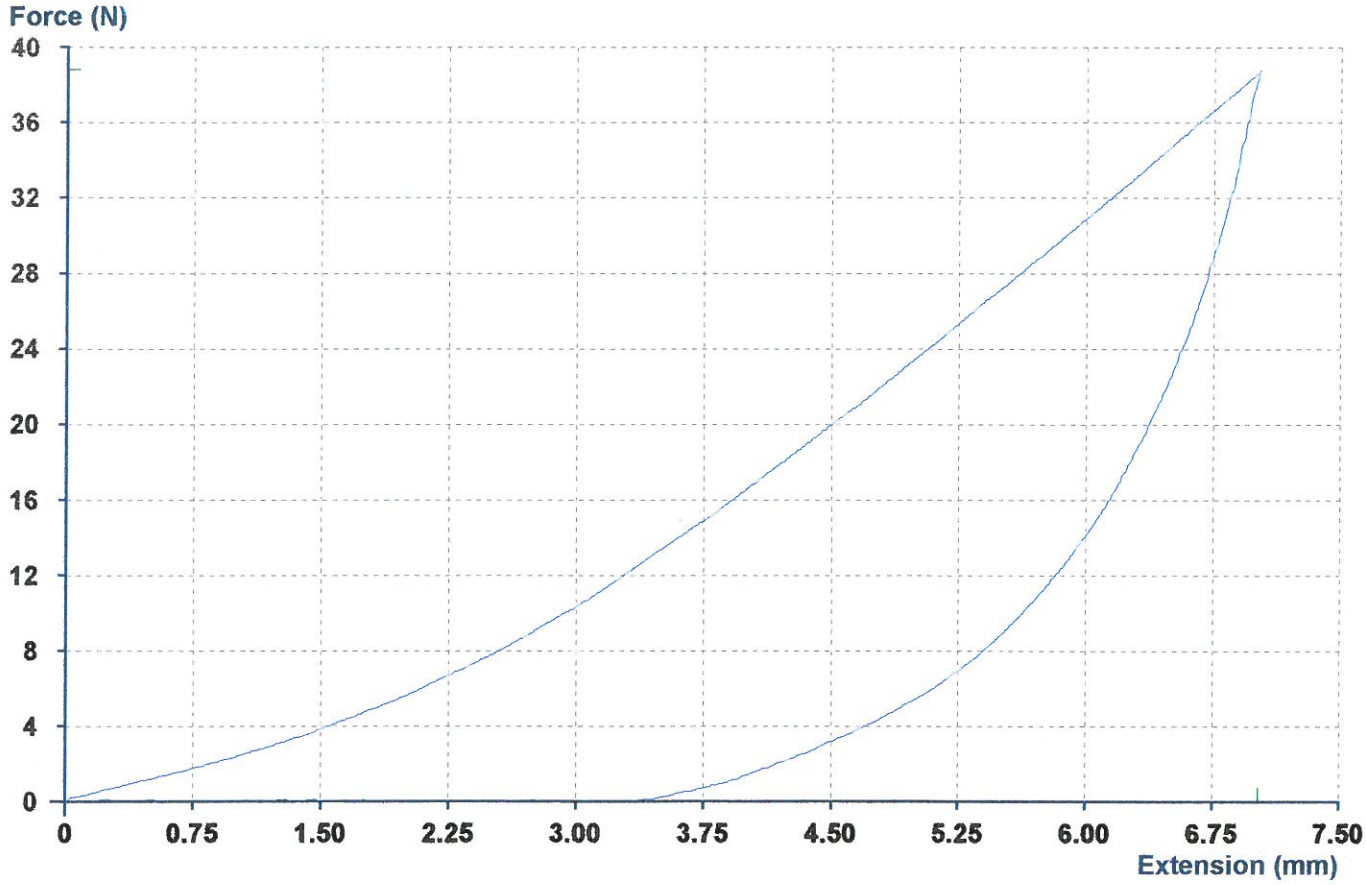

019mm powerpro line test2 Test Report

Product	: 019 poerpro line	**Load Range**	: 40.00 N
Batch	: 2 37c	**Extension Range**	: 30.00 mm
Date	: 25/05/12	**Until Extn**	: 7.00 mm
Operator	: rb	**Until Extn**	: 0.0100 mm

No.	Diameter mm	Maximum N
1	0.1900	38.84
	Mean	38.84
	Median	38.84
	Std. Dev.	-
	Coe. Var.	-
	Minimum	38.84
	Maximum	38.84

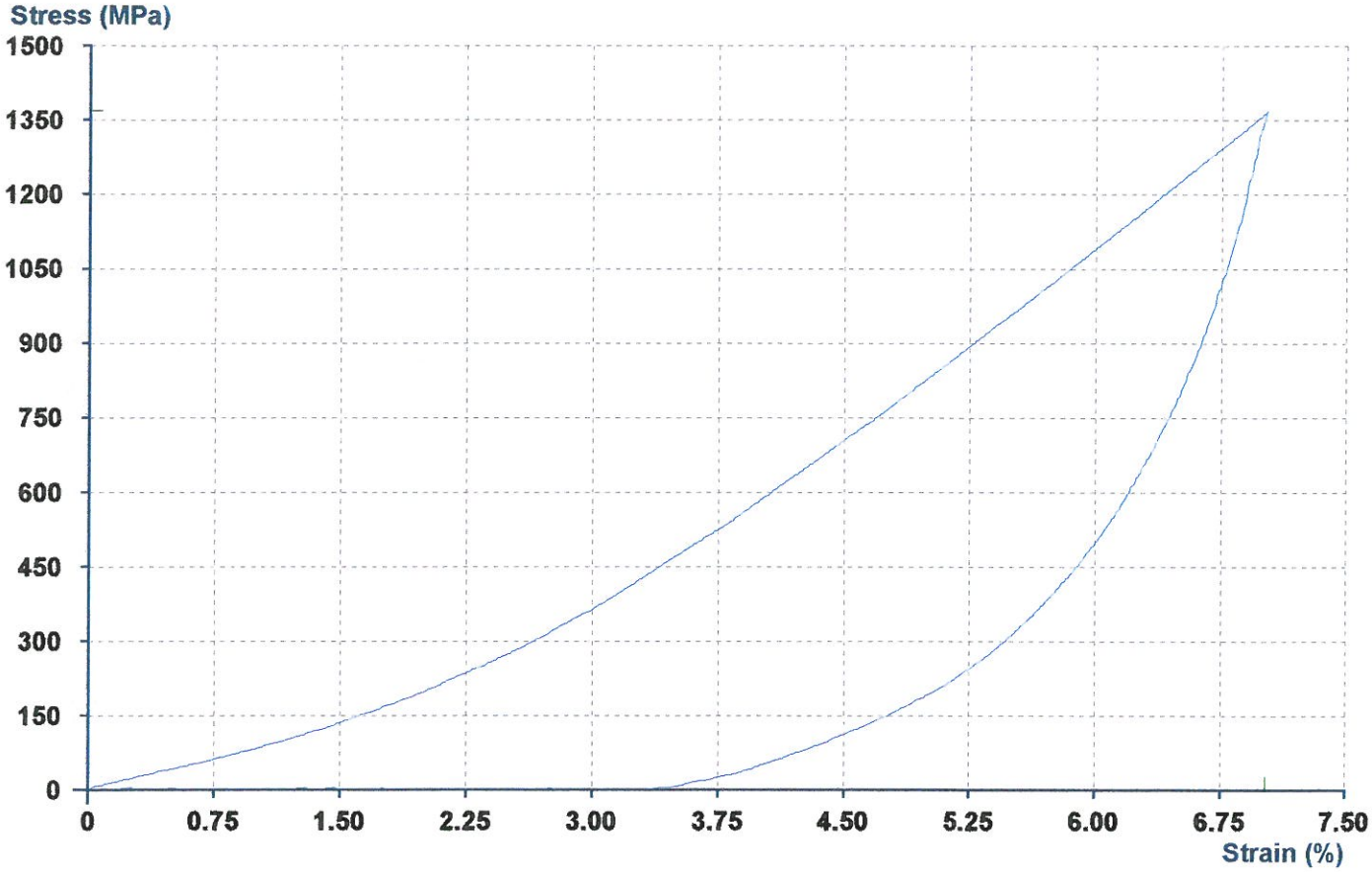

019mm powerpro line test2 Test Report

Product	: 019 poerpro line	**Stress Range**	: 40.00 MPa
Batch	: 3 37c	**Strain Range**	: 30.00 %
Date	: 25/05/12	**Until Extn**	: 7.00 mm
Operator	: rb	**Until Extn**	: 0.0100 mm

No.	Diameter mm	Maximum N
1	0.1900	39.88
	Mean	39.88
	Median	39.88
	Std. Dev.	-
	Coe. Var.	-
	Minimum	39.88
	Maximum	39.88

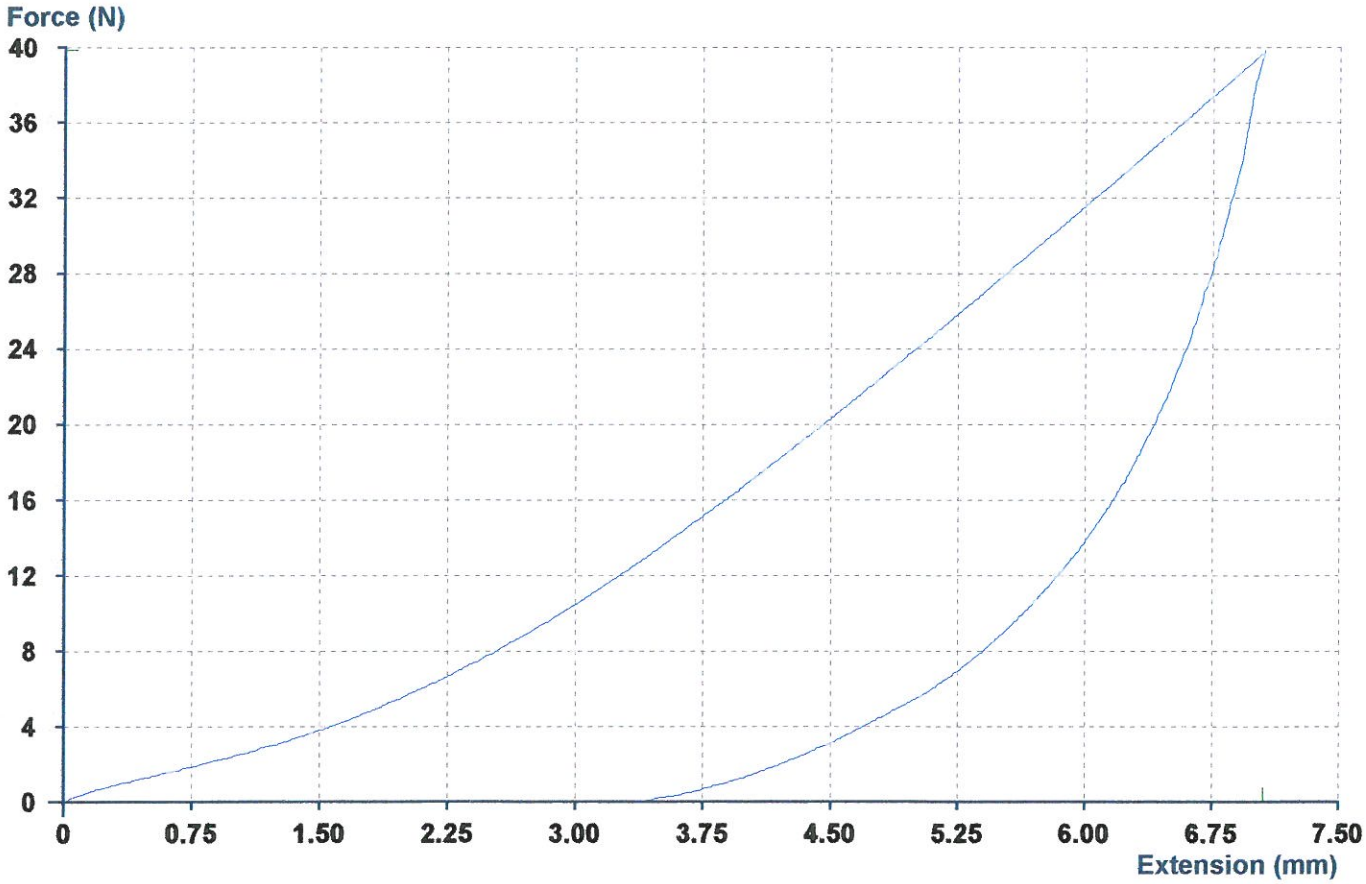

019mm powerpro line test2 Test Report

Product	: 019 poerpro line	**Load Range**	: 40.00 N
Batch	: 3 37c	**Extension Range**	: 30.00 mm
Date	: 25/05/12	**Until Extn**	: 7.00 mm
Operator	: rb	**Until Extn**	: 0.0100 mm

No.	Diameter mm	Maximum N
1	0.1900	39.88
Mean		39.88
Median		39.88
Std. Dev.		-
Coe. Var.		-
Minimum		39.88
Maximum		39.88

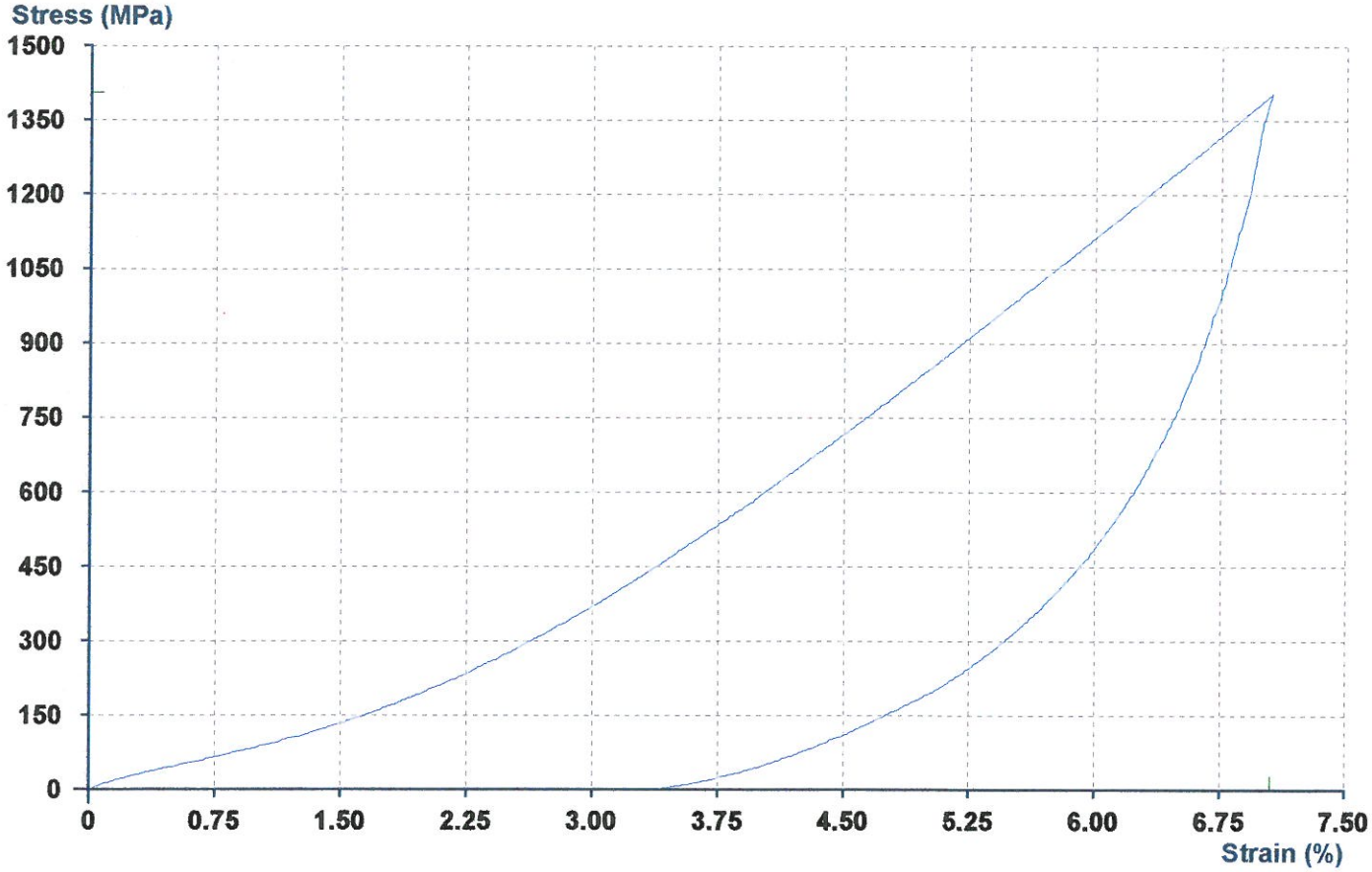

Appendix H

Connector Line Stiffness Assessment

0.19mm 'Power Pro' Line Stiffness Assessment

Length of samples = 100mm

Stiffness in terms of Newton Force per mm of extension for the 100mm samples ranges from 2.33N/mm to 7.41N/mm, dependent on which part of the curve is used. Values below were estimated from tensile plots (Appendix G).

37C Tests, 100mm sample length	Initial Elasticity (N/mm)	Settled Elasticity (N/mm)
Sample1	2.22	7.55
Sample2	2.29	7.11
Sample3	2.48	7.56
Average	**2.33**	**7.41**

The lines between the ring and pull point are approximately 170mm, which would give them a stiffness in the range of: 1.37N/mm – 4.35N/mm (from average above/1.7)

There are 8 lines in the physical test attached to the ring. Only quarter of the ring is being modelled, and likewise only 2 of the 8 lines are being modelled. The stiffness of the modelled line for a full ring should be the same as above: 1.37N/mm – 4.35N/mm

If a single line at peak and valley are used for each turn of the model is used as the method (for simplicity), then each line should have a stiffness value of 1/n of above value range, where n is the number of turns. e.g. for B28R1 which has 11 turns: 0.125N/mm – 0.395N/mm

It is decided that the best approach is to take the 'settled modulus' because it is thought that the slack in the weave of the line is taken out when force is applied to tie the knots. Therefore, 0.395N/mm should be applied in the model for each 170mm line between quarter ring peak/valley and a pull point.

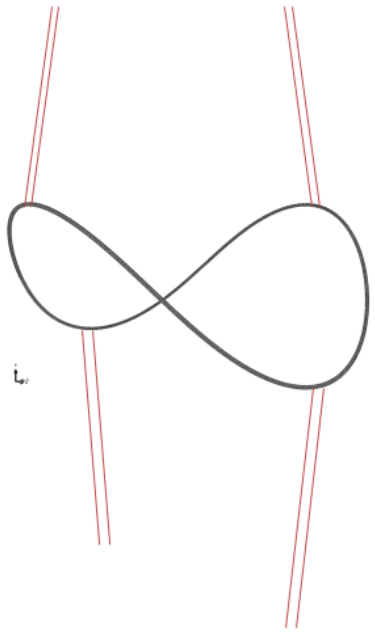

Appendix I

Summary of Input Parameters for Anaconda Study

Input Data for Anaconda Proximal Ring FEA Study

Device	Sheath ID (mm)	Ring	Mean Ring Dia. (mm)	Wire diameter (mm)	n turns	Ves. ID (mm)	Mod. Name
OLB21	6.2	R1	20.39	0.18	10	17.50	OLB21_R1_52_V17-5_Comp_SUR
						18.50	OLB21_R1_52_V18-5_Comp_SUR
						19.50	OLB21_R1_52_V19-5_Comp_SUR
		R2	20.19	0.18	5	17.50	OLB21_R2_52_V17-5_Comp_SUR
						18.50	OLB21_R2_52_V18-5_Comp_SUR
						19.50	OLB21_R2_52_V19-5_Comp_SUR
OLB23	6.2	R1	22.43	0.18	12	19.50	OLB23_R1_52_V19-5_Comp_SUR
						20.25	OLB23_R1_52_V20-25_Comp_SUR
						21.00	OLB23_R1_52_V21-0_Comp_SUR
		R2	22.24	0.18	6	19.50	OLB23_R2_52_V19-5_Comp_SUR
						20.25	OLB23_R2_52_V20-25_Comp_SUR
						21.00	OLB23_R2_52_V21-0_Comp_SUR
OLB25	6.7	R1	24.46	0.20	10	21.00	OLB25_R1_52_V21-0_Comp_SUR
						22.00	OLB25_R1_52_V22-0_Comp_SUR
						23.00	OLB25_R1_52_V23-0_Comp_SUR
		R2	24.24	0.20	5	21.00	OLB25_R2_52_V21-0_Comp_SUR
						22.00	OLB25_R2_52_V22-0_Comp_SUR
						23.00	OLB25_R2_52_V23-0_Comp_SUR
OLB28	6.7	R1	26.56	0.22	11	23.00	OLB28_R1_52_V23-0_Comp_SUR
						24.00	OLB28_R1_52_V24-0_Comp_SUR
						25.00	OLB28_R1_52_V25-0_Comp_SUR
		R2	26.36	0.22	6	23.00	OLB28_R2_52_V23-0_Comp_SUR
						24.00	OLB28_R2_52_V24-0_Comp_SUR
						25.00	OLB28_R2_52_V25-0_Comp_SUR
OLB30	6.7	R1	28.59	0.22	12	25.00	OLB30_R1_52_V25-0_Comp_SUR
						26.25	OLB30_R1_52_V26-25_Comp_SUR
						27.50	OLB30_R1_52_V27-5_Comp_SUR
		R2	28.36	0.22	6	25.00	OLB30_R2_52_V25-0_Comp_SUR
						26.25	OLB30_R2_52_V26-25_Comp_SUR
						27.50	OLB30_R2_52_V27-5_Comp_SUR
OLB32	6.7	R1	30.65	0.22	14	26.50	OLB32_R1_52_V26-5_Comp_SUR
						27.75	OLB32_R1_52_V27-75_Comp_SUR
						29.00	OLB32_R1_52_V29-0_Comp_SUR
		R2	30.36	0.22	7	26.50	OLB32_R2_52_V26-5_Comp_SUR
						27.75	OLB32_R2_52_V27-75_Comp_SUR
						29.00	OLB32_R2_52_V29-0_Comp_SUR
OLB34	6.7	R1	32.67	0.24	12	28.50	OLB34_R1_52_V28-5_Comp_SUR
						29.75	OLB34_R1_52_V29-75_Comp_SUR
						31.00	OLB34_R1_52_V31-0_Comp_SUR
		R2	32.42	0.24	6	28.50	OLB34_R2_52_V28-5_Comp_SUR
						29.75	OLB34_R2_52_V29-75_Comp_SUR
						31.00	OLB34_R2_52_V31-0_Comp_SUR

Appendix J

PythonScript – Radial Force Post Processing

```
## Radial Force Extraction Script
from odbAccess import *
from abaqusConstants import *
import math
import os
import regionToolset
import csv

odbnamelist = ['model_name_1','model_name_2']

data = [["ODB_Name","BP_80-120 Dia","BP_80-120 Sys","BP_60-140 Dia","BP_60-140
Sys","BP_80-160 Dia","BP_80-160 Sys"]]
writepath = "[Insert path to write outputs to here]"
os.chdir(writepath)
out_file = 'Radial_Force.csv'
with open(out_file, 'ab') as fp:
    a = csv.writer(fp, delimiter=',')
    a.writerows(data)

for odbname in odbnamelist:
    path = "[insert location of ODBs]"
    odbfile = path+ '\\'+ odbname+ '.odb'
    odb=openOdb(odbfile)
    ###Select a frame
    D10lastframe = odb.steps['D10'].frames[-1]
    S10lastframe = odb.steps['S10'].frames[-1]
    ###Field Output
    ContactForceD10 = D10lastframe.fieldOutputs['CNORMF']
    ContactForceS10 = S10lastframe.fieldOutputs['CNORMF']
    ## Region and subset:
    region = odb.rootAssembly.instances['VESSEL-1']
    fieldD10 = ContactForceD10.getSubset(region=region, position = NODAL)
    fieldS10 = ContactForceS10.getSubset(region=region, position = NODAL)
    ## Create Cylindrical Coordinate System
    scratchOdb = session.ScratchOdb(odb)
    scratchOdb.rootAssembly.DatumCsysByThreePoints(name='CSYS-1',
        coordSysType=CYLINDRICAL, origin=(0.0, 0.0, 0.0), point1=(0.0, 1.0,
        0.0), point2=(0.0, 0.0, 1.0))
    ##convert results:
    dtm = scratchOdb.rootAssembly.datumCsyses['CSYS-1']
    field_cylindircal_D10 = fieldD10.getTransformedField(datumCsys= dtm)
    field_cylindircal_S10 = fieldS10.getTransformedField(datumCsys= dtm)
    Vessel_CNORMF_Values_D10 = field_cylindircal_D10.values
    Vessel_CNORMF_Values_S10 = field_cylindircal_S10.values
    ##Cycle through to total the CNORMF magnitude
    ## and radial values (data[0])
    ##Contact_Magnitude = 0
    Contact_Radial_Total_D10 = 0
    Contact_Radial_Total_S10 = 0
    for x in Vessel_CNORMF_Values_D10:
        ##Contact_Magnitude = Contact_Magnitude + x.magnitude
        Contact_Radial_Total_D10 = Contact_Radial_Total_D10 + x.data[0]
    for x in Vessel_CNORMF_Values_S10:
        Contact_Radial_Total_S10 = Contact_Radial_Total_S10 + x.data[0]
    data = [[odbname, Contact_Radial_Total_D10, Contact_Radial_Total_S10]]
    ## Write Device and Contact Force Results to CSV format:
    ##Location for Result spreadsheet:
    os.chdir(writepath)
    with open(out_file, 'ab') as fp:
        a = csv.writer(fp, delimiter=',')
        a.writerows(data)
    session.odbs[odbfile].close()
```

Appendix K

PythonScript – Ring Motion Post Processing

```
from odbAccess import *
from abaqusConstants import *
import math
import os
import csv
from odbAccess import *
from abaqusConstants import *
import math
import os
import regionToolset
import csv
from numpy import array

odbnamelist = ['model_name_1','model_name_2']


##Create a CSV file to collate data witha header:
data = [["ODB_Name","Initial Mean Diameter","PV Diameter @80","PV Diameter
@120","PV Pulsatility 80-120",
        "MidPoint Diameter @80","MidPoint Diameter @120","MidPoint Pulsatility
80-120",
        "Height @80","Height @120","Delta Height 80-120",
        "PV Diameter @60","PV Diameter @140","PV Pulsatility 60-140",
        "MidPoint Diameter @60","MidPoint Diameter @140","MidPoint Pulsatility
60-140",
        "Height @60","Height @140","Delta Height 60-140",
        "PV Diameter @80","PV Diameter @160","PV Pulsatility 80-160",
        "MidPoint Diameter @80","MidPoint Diameter @160","MidPoint Pulsatility
80-160",
        "Height @80","Height @160","Delta Height 80-160"]]
writepath = "[Insert path to write outputs to here]"
os.chdir(writepath)
out_file = 'Ring_Motion.csv'
with open(out_file, 'ab') as fp:
    a = csv.writer(fp, delimiter=',')
    a.writerows(data)

for odbname in odbnamelist:
    path = "[insert location of ODBs]"
    odbfile = path+ '\\'+ odbname+ '.odb'
    odb=openOdb(odbfile)
    TurnCount = 0
    # Find the number of turns
    for instanceName in odb.rootAssembly.instances.keys():
        if "TURN" in instanceName:
            TurnCount = TurnCount + 1
    ##Num of turns:
    n = TurnCount
    ###Create cylindrical coordinate system
    scratchOdb = session.ScratchOdb(odb)
    scratchOdb.rootAssembly.DatumCsysByThreePoints(name='CSYS-1',
        coordSysType=CYLINDRICAL, origin=(0.0, 0.0, 0.0), point1=(0.0, 1.0,
        0.0), point2=(0.0, 0.0, 1.0))
    dtm = scratchOdb.rootAssembly.datumCsyses['CSYS-1']
    #####End Nodes INITIAL Diameter ####
    frame = odb.steps['Ring'].frames[-1]
    U_fieldData = frame.fieldOutputs['U']
    ##U_fieldData_Cylindrical = U_fieldData.getTransformedField(datumCsys= dtm)
    Rad_End1_Initial_all = []
    Rad_End2_Initial_all = []
    for x in range(n):
        ###End1
        node = odb.rootAssembly.nodeSets['TURN'+ str(x+1)+ '_END1NODE']
        nodeSubset = U_fieldData.getSubset(region=node)
        Rad_Disp_Initial_node = nodeSubset.values[0].data[1]  ### data[1] is Y
which is Radial for End1
        nodeNum = nodeSubset.values[0].nodeLabel
        initial = odb.rootAssembly.instances['TURN'+
```

```
str(x+1)].nodes[nodeNum-1].coordinates[1]  ### data[1] is Y which is Radial for
End1
        Rad_Pos_Initial_node = initial + Rad_Disp_Initial_node
        Rad_End1_Initial_all.append(Rad_Pos_Initial_node)
        ###End2
        node = odb.rootAssembly.nodeSets['TURN'+ str(x+1)+ '_END2NODE']
        nodeSubset = U_fieldData.getSubset(region=node)
        Rad_Disp_Initial_node = nodeSubset.values[0].data[2]### data[2] is Z
which is Radial for End2
        nodeNum = nodeSubset.values[0].nodeLabel
        initial = odb.rootAssembly.instances['TURN'+
str(x+1)].nodes[nodeNum-1].coordinates[2]  ### data[2] is Z which is Radial for
End2
        Rad_Pos_Initial_node = initial + Rad_Disp_Initial_node
        Rad_End2_Initial_all.append(Rad_Pos_Initial_node)
    End1_Diameter_Initial =
(sum(Rad_End1_Initial_all)/len(Rad_End1_Initial_all))*2
    End2_Diameter_Initial =
(sum(Rad_End2_Initial_all)/len(Rad_End2_Initial_all))*2
    ########   S10   ######
    frame = odb.steps['S10'].frames[-1]
    U_fieldData = frame.fieldOutputs['U']
    U_fieldData_Cylindrical = U_fieldData.getTransformedField(datumCsys= dtm)
    Rad_End1_all = []
    Rad_End2_all = []
    MidNode_Rad_Disp_all = []
    Height_Disp_End1_all = []
    Height_Disp_End2_all = []
    for x in range(n):
        ###End1
        ###Radial
        node = odb.rootAssembly.nodeSets['TURN'+ str(x+1)+ '_END1NODE']
        nodeSubset = U_fieldData.getSubset(region=node)
        Rad_Disp_node = nodeSubset.values[0].data[1]### data[1] is Y which is
Radial for End1
        nodeNum = nodeSubset.values[0].nodeLabel
        initial = odb.rootAssembly.instances['TURN'+
str(x+1)].nodes[nodeNum-1].coordinates[1]  ### data[1] is Y which is Radial for
End1
        Rad_Pos_node = initial + Rad_Disp_node
        Rad_End1_all.append(Rad_Pos_node)
        ###Ring Height Data
        X_Disp_node = nodeSubset.values[0].data[0]
        Node_initial_X = odb.rootAssembly.instances['TURN'+
str(x+1)].nodes[nodeNum-1].coordinates[0]
        X_Position = X_Disp_node + Node_initial_X
        Height_Disp_End1_all.append(X_Position)
        ###End2
        ###Radial
        node = odb.rootAssembly.nodeSets['TURN'+ str(x+1)+ '_END2NODE']
        nodeSubset = U_fieldData.getSubset(region=node)
        Rad_Disp_node = nodeSubset.values[0].data[2]## data[2] is Z which is
Radial for End2
        nodeNum = nodeSubset.values[0].nodeLabel
        initial = odb.rootAssembly.instances['TURN'+
str(x+1)].nodes[nodeNum-1].coordinates[2] ## data[2] is Z which is Radial for
End2
        Rad_Pos_node = initial + Rad_Disp_node
        Rad_End2_all.append(Rad_Pos_node)
        ###Ring Height Data
        X_Disp_node = nodeSubset.values[0].data[0]
        Node_initial_X = odb.rootAssembly.instances['TURN'+
str(x+1)].nodes[nodeNum-1].coordinates[0]
        X_Position = X_Disp_node + Node_initial_X
        Height_Disp_End2_all.append(X_Position)
        ###MidNode
        node1 = odb.rootAssembly.nodeSets['TURN'+ str(x+1)+ '_MIDNODE_LOW']
        node2 = odb.rootAssembly.nodeSets['TURN'+ str(x+1)+ '_MIDNODE_HIGH']
```

```
        nodeSubset1 = U_fieldData_Cylindrical.getSubset(region=node1)
        nodeSubset2 = U_fieldData_Cylindrical.getSubset(region=node2)
        Rad_Disp_node1 = nodeSubset1.values[0].data[0]
        Rad_Disp_node2 = nodeSubset2.values[0].data[0]
        MidNode_Rad_Disp = (Rad_Disp_node1+Rad_Disp_node2)/2
        MidNode_Rad_Disp_all.append(MidNode_Rad_Disp)
    End1_Diameter_S10 = (sum(Rad_End1_all)/n)*2
    End2_Diameter_S10 = (sum(Rad_End2_all)/n)*2
    All_MidNode_Rad_Pos_S10 =
array(Rad_End1_Initial_all)+array(MidNode_Rad_Disp_all)
    MidNode_Diameter_S10 = (sum(All_MidNode_Rad_Pos_S10)/n)*2
    Height_S10 = ((sum(Height_Disp_End2_all)/n)-(sum(Height_Disp_End1_all)/n))
    ########   D10   ######
    frame = odb.steps['D10'].frames[-1]
    U_fieldData = frame.fieldOutputs['U']
    U_fieldData_Cylindrical = U_fieldData.getTransformedField(datumCsys= dtm)
    Rad_End1_all = []
    Rad_End2_all = []
    MidNode_Rad_Disp_all = []
    Height_Disp_End1_all = []
    Height_Disp_End2_all = []
    for x in range(n):
        ###End1
        ###Radial
        node = odb.rootAssembly.nodeSets['TURN'+ str(x+1)+ '_END1NODE']
        nodeSubset = U_fieldData.getSubset(region=node)
        Rad_Disp_node = nodeSubset.values[0].data[1]### data[1] is Y which is
Radial for End1
        nodeNum = nodeSubset.values[0].nodeLabel
        initial = odb.rootAssembly.instances['TURN'+
str(x+1)].nodes[nodeNum-1].coordinates[1]  ### data[1] is Y which is Radial for
End1
        Rad_Pos_node = initial + Rad_Disp_node
        Rad_End1_all.append(Rad_Pos_node)
        ###Ring Height Data
        X_Disp_node = nodeSubset.values[0].data[0]
        Node_initial_X = odb.rootAssembly.instances['TURN'+
str(x+1)].nodes[nodeNum-1].coordinates[0]
        X_Position = X_Disp_node + Node_initial_X
        Height_Disp_End1_all.append(X_Position)
        ###End2
        ###Radial
        node = odb.rootAssembly.nodeSets['TURN'+ str(x+1)+ '_END2NODE']
        nodeSubset = U_fieldData.getSubset(region=node)
        Rad_Disp_node = nodeSubset.values[0].data[2]## data[2] is Z which is
Radial for End2
        nodeNum = nodeSubset.values[0].nodeLabel
        initial = odb.rootAssembly.instances['TURN'+
str(x+1)].nodes[nodeNum-1].coordinates[2] ## data[2] is Z which is Radial for
End2
        Rad_Pos_node = initial + Rad_Disp_node
        Rad_End2_all.append(Rad_Pos_node)
        ###Ring Height Data
        X_Disp_node = nodeSubset.values[0].data[0]
        Node_initial_X = odb.rootAssembly.instances['TURN'+
str(x+1)].nodes[nodeNum-1].coordinates[0]
        X_Position = X_Disp_node + Node_initial_X
        Height_Disp_End2_all.append(X_Position)
        ###MidNode
        node1 = odb.rootAssembly.nodeSets['TURN'+ str(x+1)+ '_MIDNODE_LOW']
        node2 = odb.rootAssembly.nodeSets['TURN'+ str(x+1)+ '_MIDNODE_HIGH']
        nodeSubset1 = U_fieldData_Cylindrical.getSubset(region=node1)
        nodeSubset2 = U_fieldData_Cylindrical.getSubset(region=node2)
        Rad_Disp_node1 = nodeSubset1.values[0].data[0]
        Rad_Disp_node2 = nodeSubset2.values[0].data[0]
        MidNode_Rad_Disp = (Rad_Disp_node1+Rad_Disp_node2)/2
        MidNode_Rad_Disp_all.append(MidNode_Rad_Disp)
    End1_Diameter_D10 = (sum(Rad_End1_all)/n)*2
```

```
    End2_Diameter_D10 = (sum(Rad_End2_all)/n)*2
    All_MidNode_Rad_Pos_D10 =
array(Rad_End1_Initial_all)+array(MidNode_Rad_Disp_all)
    MidNode_Diameter_D10 = (sum(All_MidNode_Rad_Pos_D10)/n)*2
    Height_D10 = ((sum(Height_Disp_End2_all)/n)-(sum(Height_Disp_End1_all)/n))
    ########   S15   ######
    frame = odb.steps['S15'].frames[-1]
    U_fieldData = frame.fieldOutputs['U']
    U_fieldData_Cylindrical = U_fieldData.getTransformedField(datumCsys= dtm)
    Rad_End1_all = []
    Rad_End2_all = []
    MidNode_Rad_Disp_all = []
    Height_Disp_End1_all = []
    Height_Disp_End2_all = []
    for x in range(n):
        ###End1
        ###Radial
        node = odb.rootAssembly.nodeSets['TURN'+ str(x+1)+ '_END1NODE']
        nodeSubset = U_fieldData.getSubset(region=node)
        Rad_Disp_node = nodeSubset.values[0].data[1]### data[1] is Y which is
Radial for End1
        nodeNum = nodeSubset.values[0].nodeLabel
        initial = odb.rootAssembly.instances['TURN'+
str(x+1)].nodes[nodeNum-1].coordinates[1]  ### data[1] is Y which is Radial for
End1
        Rad_Pos_node = initial + Rad_Disp_node
        Rad_End1_all.append(Rad_Pos_node)
        ###Ring Height Data
        X_Disp_node = nodeSubset.values[0].data[0]
        Node_initial_X = odb.rootAssembly.instances['TURN'+
str(x+1)].nodes[nodeNum-1].coordinates[0]
        X_Position = X_Disp_node + Node_initial_X
        Height_Disp_End1_all.append(X_Position)
        ###End2
        ###Radial
        node = odb.rootAssembly.nodeSets['TURN'+ str(x+1)+ '_END2NODE']
        nodeSubset = U_fieldData.getSubset(region=node)
        Rad_Disp_node = nodeSubset.values[0].data[2]## data[2] is Z which is
Radial for End2
        nodeNum = nodeSubset.values[0].nodeLabel
        initial = odb.rootAssembly.instances['TURN'+
str(x+1)].nodes[nodeNum-1].coordinates[2] ## data[2] is Z which is Radial for
End2
        Rad_Pos_node = initial + Rad_Disp_node
        Rad_End2_all.append(Rad_Pos_node)
        ###Ring Height Data
        X_Disp_node = nodeSubset.values[0].data[0]
        Node_initial_X = odb.rootAssembly.instances['TURN'+
str(x+1)].nodes[nodeNum-1].coordinates[0]
        X_Position = X_Disp_node + Node_initial_X
        Height_Disp_End2_all.append(X_Position)
        ###MidNode
        node1 = odb.rootAssembly.nodeSets['TURN'+ str(x+1)+ '_MIDNODE_LOW']
        node2 = odb.rootAssembly.nodeSets['TURN'+ str(x+1)+ '_MIDNODE_HIGH']
        nodeSubset1 = U_fieldData_Cylindrical.getSubset(region=node1)
        nodeSubset2 = U_fieldData_Cylindrical.getSubset(region=node2)
        Rad_Disp_node1 = nodeSubset1.values[0].data[0]
        Rad_Disp_node2 = nodeSubset2.values[0].data[0]
        MidNode_Rad_Disp = (Rad_Disp_node1+Rad_Disp_node2)/2
        MidNode_Rad_Disp_all.append(MidNode_Rad_Disp)
    End1_Diameter_S15 = (sum(Rad_End1_all)/n)*2
    End2_Diameter_S15 = (sum(Rad_End2_all)/n)*2
    All_MidNode_Rad_Pos_S15 =
array(Rad_End1_Initial_all)+array(MidNode_Rad_Disp_all)
    MidNode_Diameter_S15 = (sum(All_MidNode_Rad_Pos_S15)/n)*2
    Height_S15 = ((sum(Height_Disp_End2_all)/n)-(sum(Height_Disp_End1_all)/n))
    ########   D15   ######
    frame = odb.steps['D15'].frames[-1]
```

```
    U_fieldData = frame.fieldOutputs['U']
    U_fieldData_Cylindrical = U_fieldData.getTransformedField(datumCsys= dtm)
    Rad_End1_all = []
    Rad_End2_all = []
    MidNode_Rad_Disp_all = []
    Height_Disp_End1_all = []
    Height_Disp_End2_all = []
    for x in range(n):
        ###End1
        ###Radial
        node = odb.rootAssembly.nodeSets['TURN'+ str(x+1)+ '_END1NODE']
        nodeSubset = U_fieldData.getSubset(region=node)
        Rad_Disp_node = nodeSubset.values[0].data[1]### data[1] is Y which is
Radial for End1
        nodeNum = nodeSubset.values[0].nodeLabel
        initial = odb.rootAssembly.instances['TURN'+
str(x+1)].nodes[nodeNum-1].coordinates[1]  ### data[1] is Y which is Radial for
End1
        Rad_Pos_node = initial + Rad_Disp_node
        Rad_End1_all.append(Rad_Pos_node)
        ###Ring Height Data
        X_Disp_node = nodeSubset.values[0].data[0]
        Node_initial_X = odb.rootAssembly.instances['TURN'+
str(x+1)].nodes[nodeNum-1].coordinates[0]
        X_Position = X_Disp_node + Node_initial_X
        Height_Disp_End1_all.append(X_Position)
        ###End2
        ###Radial
        node = odb.rootAssembly.nodeSets['TURN'+ str(x+1)+ '_END2NODE']
        nodeSubset = U_fieldData.getSubset(region=node)
        Rad_Disp_node = nodeSubset.values[0].data[2]## data[2] is Z which is
Radial for End2
        nodeNum = nodeSubset.values[0].nodeLabel
        initial = odb.rootAssembly.instances['TURN'+
str(x+1)].nodes[nodeNum-1].coordinates[2] ## data[2] is Z which is Radial for
End2
        Rad_Pos_node = initial + Rad_Disp_node
        Rad_End2_all.append(Rad_Pos_node)
        ###Ring Height Data
        X_Disp_node = nodeSubset.values[0].data[0]
        Node_initial_X = odb.rootAssembly.instances['TURN'+
str(x+1)].nodes[nodeNum-1].coordinates[0]
        X_Position = X_Disp_node + Node_initial_X
        Height_Disp_End2_all.append(X_Position)
        ###MidNode
        node1 = odb.rootAssembly.nodeSets['TURN'+ str(x+1)+ '_MIDNODE_LOW']
        node2 = odb.rootAssembly.nodeSets['TURN'+ str(x+1)+ '_MIDNODE_HIGH']
        nodeSubset1 = U_fieldData_Cylindrical.getSubset(region=node1)
        nodeSubset2 = U_fieldData_Cylindrical.getSubset(region=node2)
        Rad_Disp_node1 = nodeSubset1.values[0].data[0]
        Rad_Disp_node2 = nodeSubset2.values[0].data[0]
        MidNode_Rad_Disp = (Rad_Disp_node1+Rad_Disp_node2)/2
        MidNode_Rad_Disp_all.append(MidNode_Rad_Disp)
    End1_Diameter_D15 = (sum(Rad_End1_all)/n)*2
    End2_Diameter_D15 = (sum(Rad_End2_all)/n)*2
    All_MidNode_Rad_Pos_D15 =
array(Rad_End1_Initial_all)+array(MidNode_Rad_Disp_all)
    MidNode_Diameter_D15 = (sum(All_MidNode_Rad_Pos_D15)/n)*2
    Height_D15 = ((sum(Height_Disp_End2_all)/n)-(sum(Height_Disp_End1_all)/n))
    ########   S20   ######
    frame = odb.steps['S20'].frames[-1]
    U_fieldData = frame.fieldOutputs['U']
    U_fieldData_Cylindrical = U_fieldData.getTransformedField(datumCsys= dtm)
    Rad_End1_all = []
    Rad_End2_all = []
    MidNode_Rad_Disp_all = []
    Height_Disp_End1_all = []
    Height_Disp_End2_all = []
```

```
    for x in range(n):
        ###End1
        ###Radial
        node = odb.rootAssembly.nodeSets['TURN'+ str(x+1)+ '_END1NODE']
        nodeSubset = U_fieldData.getSubset(region=node)
        Rad_Disp_node = nodeSubset.values[0].data[1]### data[1] is Y which is
Radial for End1
        nodeNum = nodeSubset.values[0].nodeLabel
        initial = odb.rootAssembly.instances['TURN'+
str(x+1)].nodes[nodeNum-1].coordinates[1]  ### data[1] is Y which is Radial for
End1
        Rad_Pos_node = initial + Rad_Disp_node
        Rad_End1_all.append(Rad_Pos_node)
        ###Ring Height Data
        X_Disp_node = nodeSubset.values[0].data[0]
        Node_initial_X = odb.rootAssembly.instances['TURN'+
str(x+1)].nodes[nodeNum-1].coordinates[0]
        X_Position = X_Disp_node + Node_initial_X
        Height_Disp_End1_all.append(X_Position)
        ###End2
        ###Radial
        node = odb.rootAssembly.nodeSets['TURN'+ str(x+1)+ '_END2NODE']
        nodeSubset = U_fieldData.getSubset(region=node)
        Rad_Disp_node = nodeSubset.values[0].data[2]## data[2] is Z which is
Radial for End2
        nodeNum = nodeSubset.values[0].nodeLabel
        initial = odb.rootAssembly.instances['TURN'+
str(x+1)].nodes[nodeNum-1].coordinates[2] ## data[2] is Z which is Radial for
End2
        Rad_Pos_node = initial + Rad_Disp_node
        Rad_End2_all.append(Rad_Pos_node)
        ###Ring Height Data
        X_Disp_node = nodeSubset.values[0].data[0]
        Node_initial_X = odb.rootAssembly.instances['TURN'+
str(x+1)].nodes[nodeNum-1].coordinates[0]
        X_Position = X_Disp_node + Node_initial_X
        Height_Disp_End2_all.append(X_Position)
        ###MidNode
        node1 = odb.rootAssembly.nodeSets['TURN'+ str(x+1)+ '_MIDNODE_LOW']
        node2 = odb.rootAssembly.nodeSets['TURN'+ str(x+1)+ '_MIDNODE_HIGH']
        nodeSubset1 = U_fieldData_Cylindrical.getSubset(region=node1)
        nodeSubset2 = U_fieldData_Cylindrical.getSubset(region=node2)
        Rad_Disp_node1 = nodeSubset1.values[0].data[0]
        Rad_Disp_node2 = nodeSubset2.values[0].data[0]
        MidNode_Rad_Disp = (Rad_Disp_node1+Rad_Disp_node2)/2
        MidNode_Rad_Disp_all.append(MidNode_Rad_Disp)
    End1_Diameter_S20 = (sum(Rad_End1_all)/n)*2
    End2_Diameter_S20 = (sum(Rad_End2_all)/n)*2
    All_MidNode_Rad_Pos_S20 =
array(Rad_End1_Initial_all)+array(MidNode_Rad_Disp_all)
    MidNode_Diameter_S20 = (sum(All_MidNode_Rad_Pos_S20)/n)*2
    Height_S20 = ((sum(Height_Disp_End2_all)/n)-(sum(Height_Disp_End1_all)/n))
    ########   D20   ######
    frame = odb.steps['D20'].frames[-1]
    U_fieldData = frame.fieldOutputs['U']
    U_fieldData_Cylindrical = U_fieldData.getTransformedField(datumCsys= dtm)
    Rad_End1_all = []
    Rad_End2_all = []
    MidNode_Rad_Disp_all = []
    Height_Disp_End1_all = []
    Height_Disp_End2_all = []
    for x in range(n):
        ###End1
        ###Radial
        node = odb.rootAssembly.nodeSets['TURN'+ str(x+1)+ '_END1NODE']
        nodeSubset = U_fieldData.getSubset(region=node)
        Rad_Disp_node = nodeSubset.values[0].data[1]### data[1] is Y which is
Radial for End1
```

```
        nodeNum = nodeSubset.values[0].nodeLabel
        initial = odb.rootAssembly.instances['TURN'+
str(x+1)].nodes[nodeNum-1].coordinates[1]  ### data[1] is Y which is Radial for
End1
        Rad_Pos_node = initial + Rad_Disp_node
        Rad_End1_all.append(Rad_Pos_node)
        ###Ring Height Data
        X_Disp_node = nodeSubset.values[0].data[0]
        Node_initial_X = odb.rootAssembly.instances['TURN'+
str(x+1)].nodes[nodeNum-1].coordinates[0]
        X_Position = X_Disp_node + Node_initial_X
        Height_Disp_End1_all.append(X_Position)
        ###End2
        ###Radial
        node = odb.rootAssembly.nodeSets['TURN'+ str(x+1)+ '_END2NODE']
        nodeSubset = U_fieldData.getSubset(region=node)
        Rad_Disp_node = nodeSubset.values[0].data[2]## data[2] is Z which is
Radial for End2
        nodeNum = nodeSubset.values[0].nodeLabel
        initial = odb.rootAssembly.instances['TURN'+
str(x+1)].nodes[nodeNum-1].coordinates[2] ## data[2] is Z which is Radial for
End2
        Rad_Pos_node = initial + Rad_Disp_node
        Rad_End2_all.append(Rad_Pos_node)
        ###Ring Height Data
        X_Disp_node = nodeSubset.values[0].data[0]
        Node_initial_X = odb.rootAssembly.instances['TURN'+
str(x+1)].nodes[nodeNum-1].coordinates[0]
        X_Position = X_Disp_node + Node_initial_X
        Height_Disp_End2_all.append(X_Position)
        ###MidNode
        node1 = odb.rootAssembly.nodeSets['TURN'+ str(x+1)+ '_MIDNODE_LOW']
        node2 = odb.rootAssembly.nodeSets['TURN'+ str(x+1)+ '_MIDNODE_HIGH']
        nodeSubset1 = U_fieldData_Cylindrical.getSubset(region=node1)
        nodeSubset2 = U_fieldData_Cylindrical.getSubset(region=node2)
        Rad_Disp_node1 = nodeSubset1.values[0].data[0]
        Rad_Disp_node2 = nodeSubset2.values[0].data[0]
        MidNode_Rad_Disp = (Rad_Disp_node1+Rad_Disp_node2)/2
        MidNode_Rad_Disp_all.append(MidNode_Rad_Disp)
    End1_Diameter_D20 = (sum(Rad_End1_all)/n)*2
    End2_Diameter_D20 = (sum(Rad_End2_all)/n)*2
    All_MidNode_Rad_Pos_D20 =
array(Rad_End1_Initial_all)+array(MidNode_Rad_Disp_all)
    MidNode_Diameter_D20 = (sum(All_MidNode_Rad_Pos_D20)/n)*2
    Height_D20 = ((sum(Height_Disp_End2_all)/n)-(sum(Height_Disp_End1_all)/n))
    ####End 1 - Valley Calulations
    End1_Systolic_Diameters = array([End1_Diameter_S10, End1_Diameter_S15,
End1_Diameter_S20])
    End1_Diastolic_Diameters = array([End1_Diameter_D10, End1_Diameter_D15,
End1_Diameter_D20])
    Pulsatilities_End1 = End1_Systolic_Diameters - End1_Diastolic_Diameters
    ####End 2 - Valley Calulations
    End2_Systolic_Diameters = array([End2_Diameter_S10, End2_Diameter_S15,
End2_Diameter_S20])
    End2_Diastolic_Diameters = array([End2_Diameter_D10, End2_Diameter_D15,
End2_Diameter_D20])
    Pulsatilities_End2 = End2_Systolic_Diameters - End2_Diastolic_Diameters
    ##### Average End1,End2 (Valley,Peak) calcs:
    Average_ValleyPeak_Systolic_Diameters = (End1_Systolic_Diameters +
End2_Systolic_Diameters)/2
    Average_ValleyPeak_Diastolic_Diameters = (End1_Diastolic_Diameters +
End2_Diastolic_Diameters)/2
    Average_ValleyPeak_Pulsatility = (Pulsatilities_End1 + Pulsatilities_End2)/2
    ##### Mid Node Calculations
    Mid_Systolic_Diameters = array([MidNode_Diameter_S10, MidNode_Diameter_S15,
MidNode_Diameter_S20])
    Mid_Diastolic_Diameters = array([MidNode_Diameter_D10, MidNode_Diameter_D15,
MidNode_Diameter_D20])
```

```
    Pulsatilities_Mid = Mid_Systolic_Diameters - Mid_Diastolic_Diameters
    ###### Hieght Calulations
    Systolic_Heights = array([Height_S10, Height_S15, Height_S20])
    Diastolic_Heights = array([Height_D10, Height_D15, Height_D20])
    Delta_Heights = Diastolic_Heights - Systolic_Heights
    AllData = [[odbname, End1_Diameter_Initial,
Average_ValleyPeak_Diastolic_Diameters[0],Average_ValleyPeak_Systolic_Diameters[
0],

Average_ValleyPeak_Pulsatility[0],Mid_Diastolic_Diameters[0],Mid_Systolic_Diamet
ers[0],

Pulsatilities_Mid[0],Diastolic_Heights[0],Systolic_Heights[0],Delta_Heights[0],

Average_ValleyPeak_Diastolic_Diameters[1],Average_ValleyPeak_Systolic_Diameters[
1],

Average_ValleyPeak_Pulsatility[1],Mid_Diastolic_Diameters[1],Mid_Systolic_Diamet
ers[1],

Pulsatilities_Mid[1],Diastolic_Heights[1],Systolic_Heights[1],Delta_Heights[1],

Average_ValleyPeak_Diastolic_Diameters[2],Average_ValleyPeak_Systolic_Diameters[
2],

Average_ValleyPeak_Pulsatility[2],Mid_Diastolic_Diameters[2],Mid_Systolic_Diamet
ers[2],

Pulsatilities_Mid[2],Diastolic_Heights[2],Systolic_Heights[2],Delta_Heights[2]]]
    ####Write results to spreadsheet:
    os.chdir(writepath)
    with open(out_file, 'ab') as fp:
        a = csv.writer(fp, delimiter=',')
        a.writerows(AllData)
    session.odbs[odbfile].close()
```

Appendix L

PythonScript – Strain Analysis Post Processing

```
### STRAIN ANALYSIS SCRIPT

from odbAccess import *
from abaqusConstants import *
import math
import os
import regionToolset
import csv
from numpy import array

odbnamelist = ['model_name_1','model_name_2']

####Create a CSV file to collate data witha header:
data = [["ODB_Name","Delta","@ Mean of:","Node","Turn","Max Strain Mid Cycle","@
Node","Turn"]]
writepath = "[Insert path to write outputs to here]"
os.chdir(writepath)
out_file = 'Strain_Analysis.csv'
with open(out_file, 'ab') as fp:
    a = csv.writer(fp, delimiter=',')
    a.writerows(data)

for odbname in odbnamelist:
    path = "[insert location of ODBs]"
    odbfile = path+ '\\'+ odbname+ '.odb'
    odb=openOdb(odbfile)
    TurnCount = 0
    # Find the number of turns
    for instanceName in odb.rootAssembly.instances.keys():
        if "TURN" in instanceName:
            TurnCount = TurnCount + 1
    high_Delta = 0
    high_MeanStrain = 0
    for x in range(TurnCount):
        ###Select a frame
        D10lastframe = odb.steps['D10'].frames[-1]
        S10lastframe = odb.steps['S10'].frames[-1]
        ##########################################
        ####  Calculate delta strain
        StrainD10 = D10lastframe.fieldOutputs['LE']
        StrainS10 = S10lastframe.fieldOutputs['LE']
        region = odb.rootAssembly.instances['TURN'+ str(x+1)]
        ####Extrapolate Nodal Values from calculated integration point strains
through the region
        #### (still in vector form)
        StrainD10subset = StrainD10.getSubset(region=region, position =
ELEMENT_NODAL)
        StrainS10subset = StrainS10.getSubset(region=region, position =
ELEMENT_NODAL)
        ##Get Scalars:
        MaxP_StrainD10subset =
StrainD10subset.getScalarField(invariant=MAX_PRINCIPAL)
        MaxP_StrainS10subset =
StrainS10subset.getScalarField(invariant=MAX_PRINCIPAL)
        ##Delta and Mean calc on each SCALAR:
        Delta_maxP = MaxP_StrainD10subset - MaxP_StrainS10subset
        Mean_maxP = (MaxP_StrainD10subset + MaxP_StrainS10subset)/2
        b = -1
        for a in Delta_maxP.values:
            ##count:
            b = b+1
            m = a.data
            if abs(m) > abs(high_Delta):
                high_Delta = m
                node = a.nodeLabel
                part = a.instance.name
                MeanStrain = Mean_maxP.values[b].data
        ## Find the highest mean strain, mid-cycle in ring:
```

```
        for d in Mean_maxP.values:
            p = d.data
            if p > high_MeanStrain:
                high_MeanStrain = p
                HighMean_Node = d.nodeLabel
                HighMean_Part = d.instance.name
    print "Delta:",high_Delta,"@",MeanStrain,"mean strain, Loaction:
Node",node,part
    print "Max Strain:",high_MeanStrain,"@ Node", HighMean_Node, HighMean_Part

##############################################################################
    high_Delta2 = 0
    high_MeanStrain2 = 0
    for x in range(TurnCount):
        ###Select a frame
        D15lastframe = odb.steps['D15'].frames[-1]
        S15lastframe = odb.steps['S15'].frames[-1]
        ##########################################
        ####  Calculate delta strain
        StrainD15 = D15lastframe.fieldOutputs['LE']
        StrainS15 = S15lastframe.fieldOutputs['LE']
        region = odb.rootAssembly.instances['TURN'+ str(x+1)]
        ####Extrapolte Nodel Values from calculated integration point strains
through the region
        #### (still in vector form)
        StrainD15subset = StrainD15.getSubset(region=region, position =
ELEMENT_NODAL)
        StrainS15subset = StrainS15.getSubset(region=region, position =
ELEMENT_NODAL)
        ##Get Scalars:
        MaxP_StrainD15subset =
StrainD15subset.getScalarField(invariant=MAX_PRINCIPAL)
        MaxP_StrainS15subset =
StrainS15subset.getScalarField(invariant=MAX_PRINCIPAL)
        ##Delta and Mean calc on each SCALAR:
        Delta_maxP = MaxP_StrainD15subset - MaxP_StrainS15subset
        Mean_maxP = (MaxP_StrainD15subset + MaxP_StrainS15subset)/2
        b = -1
        for a in Delta_maxP.values:
            ##count:
            b = b+1
            m = a.data
            if abs(m) > abs(high_Delta2):
                high_Delta2 = m
                node2 = a.nodeLabel
                part2 = a.instance.name
                MeanStrain2 = Mean_maxP.values[b].data
        ## Find the highest mean strain, mid-cycle in ring:
        for d in Mean_maxP.values:
            p = d.data
            if p > high_MeanStrain2:
                high_MeanStrain2 = p
                HighMean_Node2 = d.nodeLabel
                HighMean_Part2 = d.instance.name
    print "Delta:",high_Delta2,"@",MeanStrain2,"mean strain, Loaction:
Node",node2,part2
    print "Max Strain:",high_MeanStrain2,"@ Node", HighMean_Node2,
HighMean_Part2
##    ##########################################
    high_Delta3 = 0
    high_MeanStrain3 = 0
    for x in range(TurnCount):
        ###Select a frame
        D20lastframe = odb.steps['D20'].frames[-1]
        S20lastframe = odb.steps['S20'].frames[-1]
        ##########################################
        ####  Calculate delta strain
        StrainD20 = D20lastframe.fieldOutputs['LE']
```

```
        StrainS20 = S20lastframe.fieldOutputs['LE']
        region = odb.rootAssembly.instances['TURN'+ str(x+1)]
        ####Extrapolte Nodel Values from calculated integration point strains
through the region
        #### (still in vector form)
        StrainD20subset = StrainD20.getSubset(region=region, position =
ELEMENT_NODAL)
        StrainS20subset = StrainS20.getSubset(region=region, position =
ELEMENT_NODAL)
        ##Get Scalars:
        MaxP_StrainD20subset =
StrainD20subset.getScalarField(invariant=MAX_PRINCIPAL)
        MaxP_StrainS20subset =
StrainS20subset.getScalarField(invariant=MAX_PRINCIPAL)
        ##Delta and Mean calc on each SCALAR:
        Delta_maxP = MaxP_StrainD20subset - MaxP_StrainS20subset
        Mean_maxP = (MaxP_StrainD20subset + MaxP_StrainS20subset)/2
        b = -1
        for a in Delta_maxP.values:
            ##count:
            b = b+1
            m = a.data
            if abs(m) > abs(high_Delta3):
                high_Delta3 = m
                node3 = a.nodeLabel
                part3 = a.instance.name
                MeanStrain3 = Mean_maxP.values[b].data
        ## Find the highest mean strain, mid-cycle in ring:
        for d in Mean_maxP.values:
            p = d.data
            if p > high_MeanStrain3:
                high_MeanStrain3 = p
                HighMean_Node3 = d.nodeLabel
                HighMean_Part3 = d.instance.name
    print "Delta:",high_Delta3,"@",MeanStrain3,"mean strain, Loaction:
Node",node3,part3
    print "Max Strain:",high_MeanStrain3,"@ Node", HighMean_Node3,
HighMean_Part3
    ############
    data = [[odbname, high_Delta, MeanStrain, node, part,
    high_MeanStrain, HighMean_Node, HighMean_Part, high_Delta2,
    MeanStrain2, node2, part2, high_MeanStrain2, HighMean_Node2,
    HighMean_Part2, high_Delta3, MeanStrain3, node3, part3, high_MeanStrain3,
    HighMean_Node3, HighMean_Part3]]
##    data = [[odbname, high_Delta, MeanStrain, node, part,
##    high_MeanStrain, HighMean_Node, HighMean_Part, high_Delta2,
##    MeanStrain2, node2, part2, high_MeanStrain2, HighMean_Node2,
##    HighMean_Part2]]
    with open(out_file, 'ab') as fp:
        a = csv.writer(fp, delimiter=',')
        a.writerows(data)
    session.odbs[odbfile].close()
```

Appendix M

PythonScript – Radial Force Distribution Post Processing

```
from odbAccess import *
from abaqusConstants import *
import math
import os
import regionToolset
import csv

odbname = 'model_name'

data = [["Node","R Coord","Theta Coord","Z Coord","R_Force","Force Mag"]]
writepath = "[Insert path to write outputs to here]"
os.chdir(writepath)
out_file = 'Radial_Dist.csv'
with open(out_file, 'ab') as fp:
    a = csv.writer(fp, delimiter=',')
    a.writerows(data)


path = "[insert location of ODBs]"
odbfile = path+ '\\'+ odbname+ '.odb'
odb=openOdb(odbfile)
###Select a frame
frame = odb.steps['D10'].frames[2]
###Field Output
ContactForceD10 = frame.fieldOutputs['CNORMF']
Coords = frame.fieldOutputs['COORD']
## Region and subset:
region = odb.rootAssembly.instances['VESSEL-1']
ContactSubset = ContactForceD10.getSubset(region=region, position = NODAL)
CoordsSubset = Coords.getSubset(region=region, position = NODAL)
CoordValues = CoordsSubset.values

## Create Cylindrical Coordinate System
scratchOdb = session.ScratchOdb(odb)
scratchOdb.rootAssembly.DatumCsysByThreePoints(name='CSYS-1',
    coordSysType=CYLINDRICAL, origin=(0.0, 0.0, 0.0), point1=(0.0, 0.0,
    1.0), point2=(0.0, 1.0, 0.0))
##convert results:
dtm = scratchOdb.rootAssembly.datumCsyses['CSYS-1']
Contact_Transfomed_Values = ContactSubset.getTransformedField(datumCsys=
dtm).values
ContactForceList = []

a = 0
for a in Contact_Transfomed_Values:
    if a.data[0] != 0:
        nodeLabel = a.nodeLabel
        R_Force = a.data[0]
        Mag_Force = a.magnitude
        b = 0
        for b in CoordValues:
            if b.nodeLabel == nodeLabel:
                X_coord = b.data[0]
                Y_coord = b.data[1]
                Z_coord = b.data[2]
                R_coord = ((Y_coord**2)+(Z_coord**2))**0.5
                Theta_coord = atan(Z_coord/Y_coord)
                Z_cyl_coord = X_coord
                break
        ContactForceList.append((nodeLabel, R_coord, Theta_coord, Z_cyl_coord,
R_Force, Mag_Force), )


# Write Device and Contact Force Results to CSV format:
##Location for Result spreadsheet:
os.chdir(writepath)
with open(out_file, 'ab') as fp:
    a = csv.writer(fp, delimiter=',')
```

```
    a.writerows(ContactForceList)

session.odbs[odbfile].close()
```

Appendix N

Ring Contact Length Calculations (PDF of Mathcad file)

Input the assumed ring radius and amplitude:

$Radius := 10.251$ Amplitude $a := 6.51$

Wavelength (half a ring) $\lambda := \pi \cdot Radius = 32.20447$

$$k := \frac{2\pi}{\lambda} = 0.1951$$

If the ring shape is approximated by a cos wave of: a cos (kx), the arc length of a segment of that line from a to b in the wave length direction can be calculated by

$\int_a^b \sqrt{1 - (a \cdot k \cdot \sin(k \cdot x))^2}\, dx$ which is derived from the standard arc length of a line

formula: s= $\int_a^b \sqrt{1 + \left(\frac{dy}{dx}\right)^2}\, dx$

Define n number of segments in quarter ring:

$n := 9$ $L := \frac{\lambda}{2} = 16.10223$ L = quarter ring length

Define the a and b points for seperate calculations:

$$q := \frac{L}{n}, \frac{2L}{n} .. L$$

$q =$	$q - \frac{L}{n} =$
1.78914	0
3.57827	1.78914
5.36741	3.57827
7.15655	5.36741
8.94569	7.15655
10.73482	8.94569
12.52396	10.73482
14.3131	12.52396
16.10223	14.3131

Arc length equation:

$$s(q) := \int_{q-\frac{L}{n}}^{q} \sqrt{1 + (-a \cdot k \cdot \sin(k \cdot x))^2}\, dx$$

Quarter ring contact length:

$$S := \int_0^L \sqrt{1 + (-a \cdot k \cdot \sin(k \cdot x))^2}\, dx = 21.35952$$

Arc length results for each segment:

$s(q) =$
1.84481
2.12299
2.49237
2.77801
2.88318
2.77801
2.49237
2.12299
1.84481

Quick Check with flat ring OD:

$RingOD := 27.43$

$ContactCirc := RingOD\pi = 86.17389$

Compare with:

$4S = 85.43806$

$$Error := \frac{(ContactCirc - 4 \cdot S)}{ContactCirc} = 0.85388 \cdot \%$$

Appendix O

FEA Delta Strain Results – Anaconda Study

FEA Delta Strain Results from Anaconda Proximal Ring Study in 52yr Langewouters Vessel at various pressure ranges

At 80-120mmHg

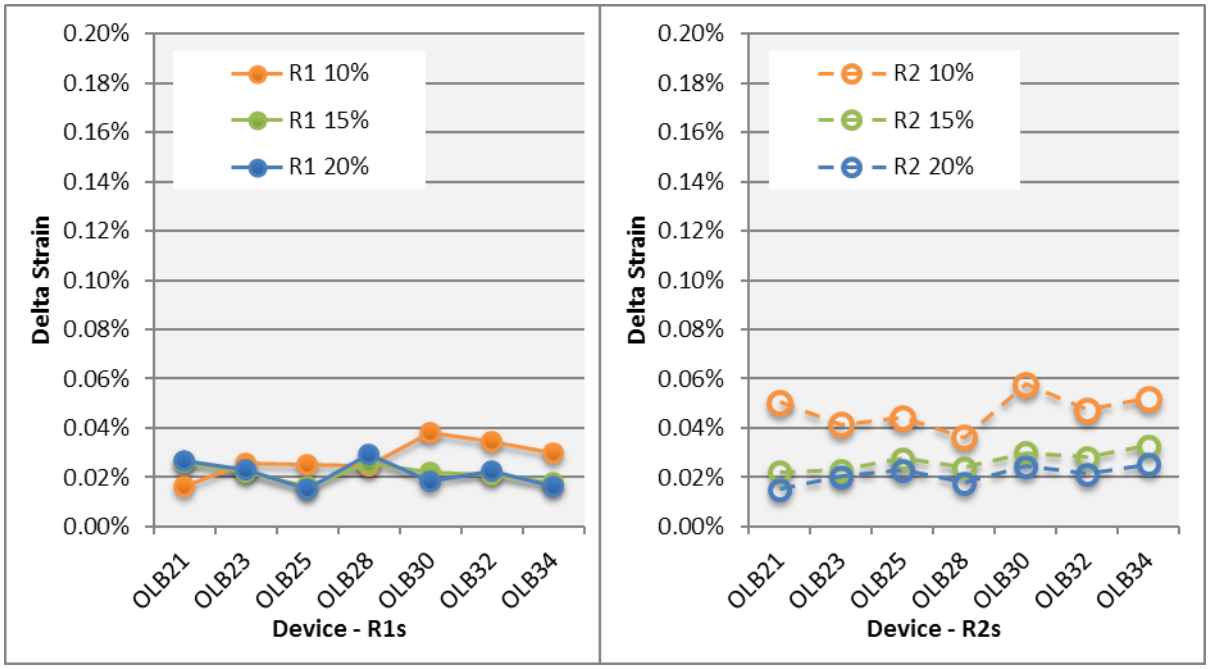

At 60-140mmHg

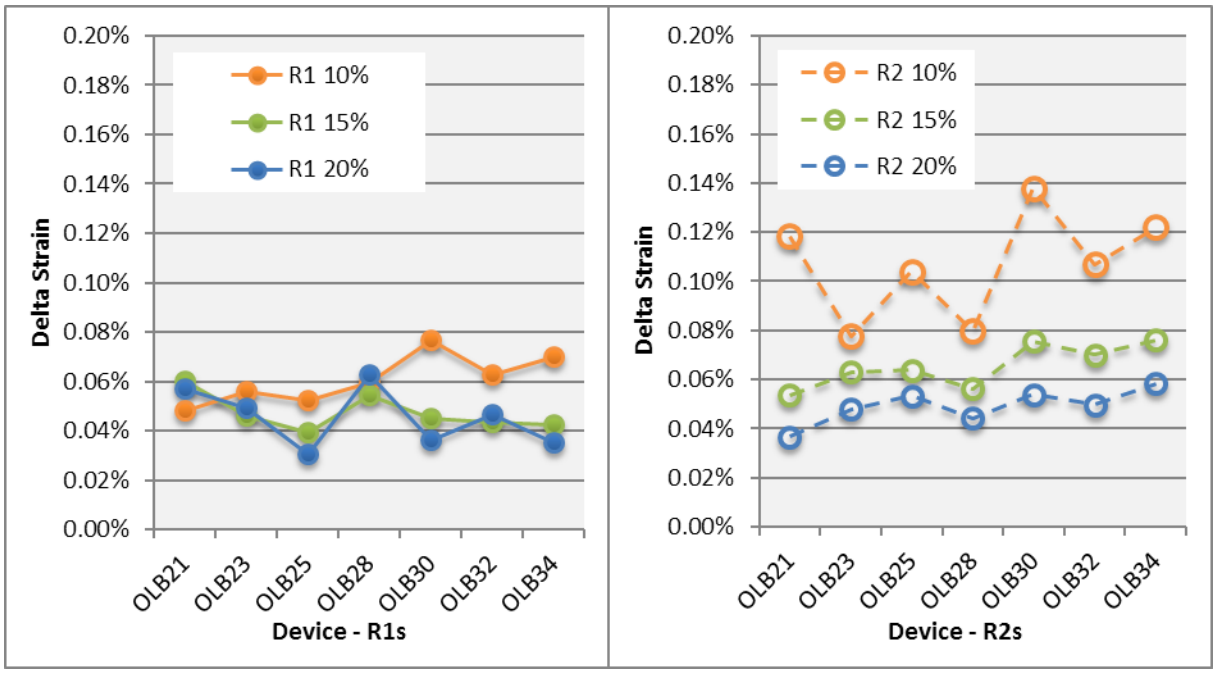

At 80-160mmHg

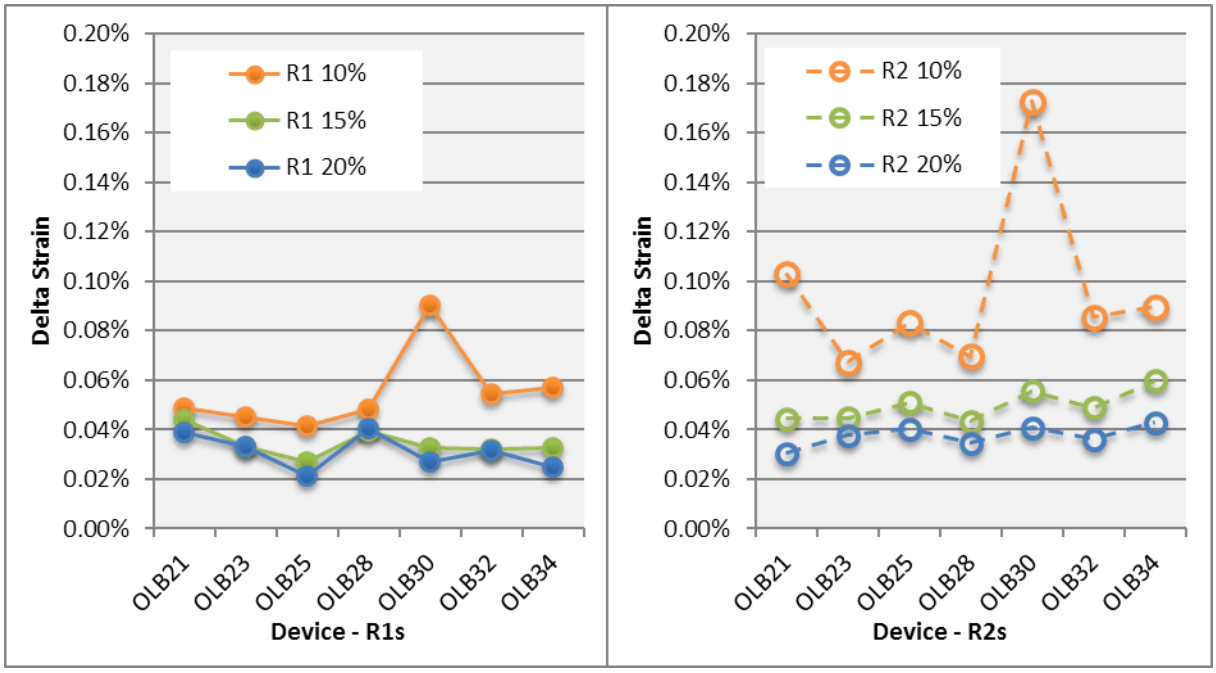

Appendix P

MicroCT based ring compaction strain measurements – Anaconda

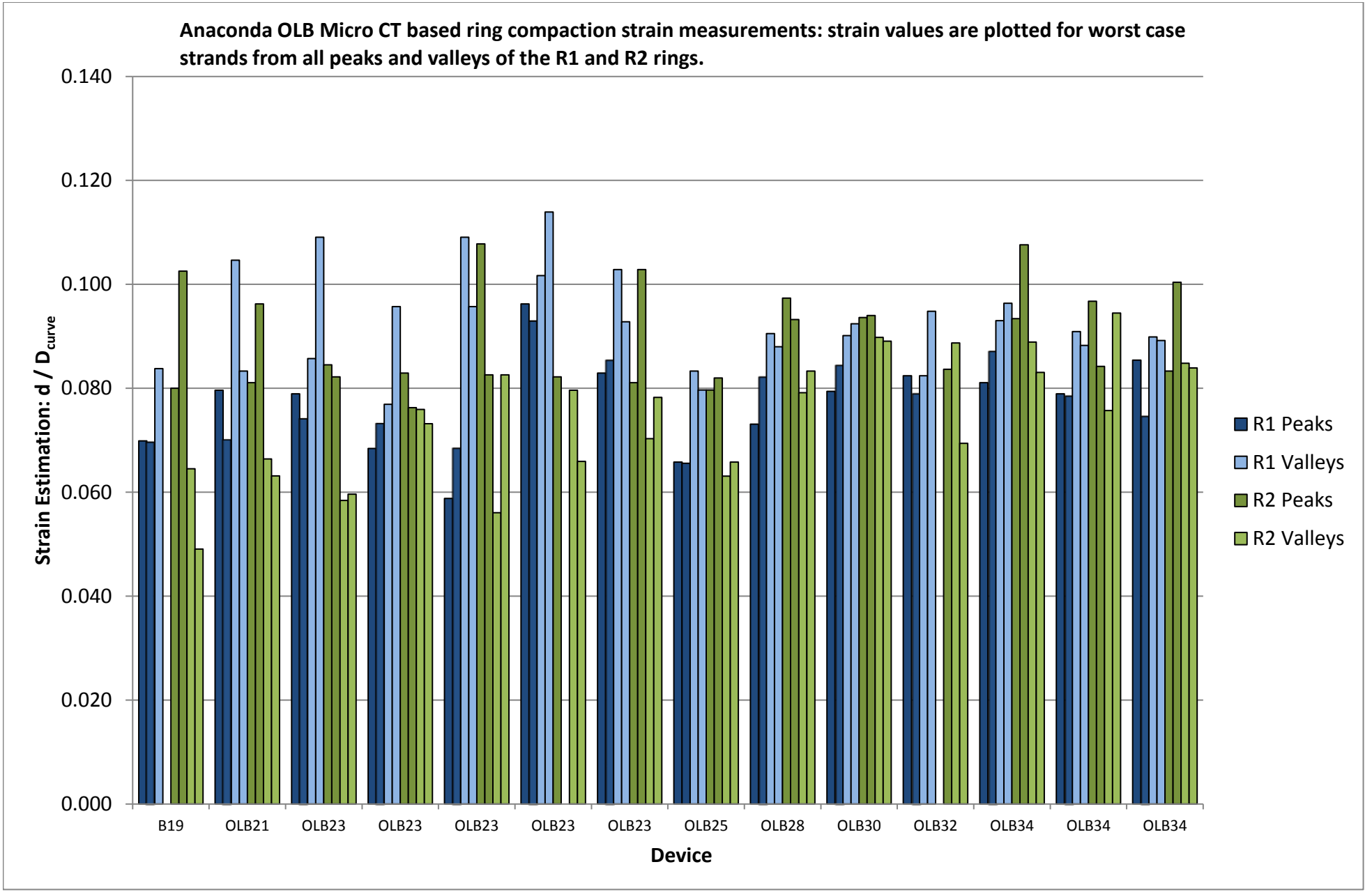
Anaconda OLB Micro CT based ring compaction strain measurements: strain values are plotted for worst case strands from all peaks and valleys of the R1 and R2 rings.
0.140
0.120
0.100
0.080
0.060
0.040
0.020
0.000
Strain Estimation: d / D curve
B19
OLB21
OLB23
OLB23
OLB23
OLB23
OLB23
OLB25
OLB28
OLB30
OLB32
OLB34
OLB34
OLB34
Device
R1 Peaks
R1 Valleys
R2 Peaks
R2 Valleys

Appendix Q

MicroCT based ring compaction strain measurements – Thoraflex Hybrid

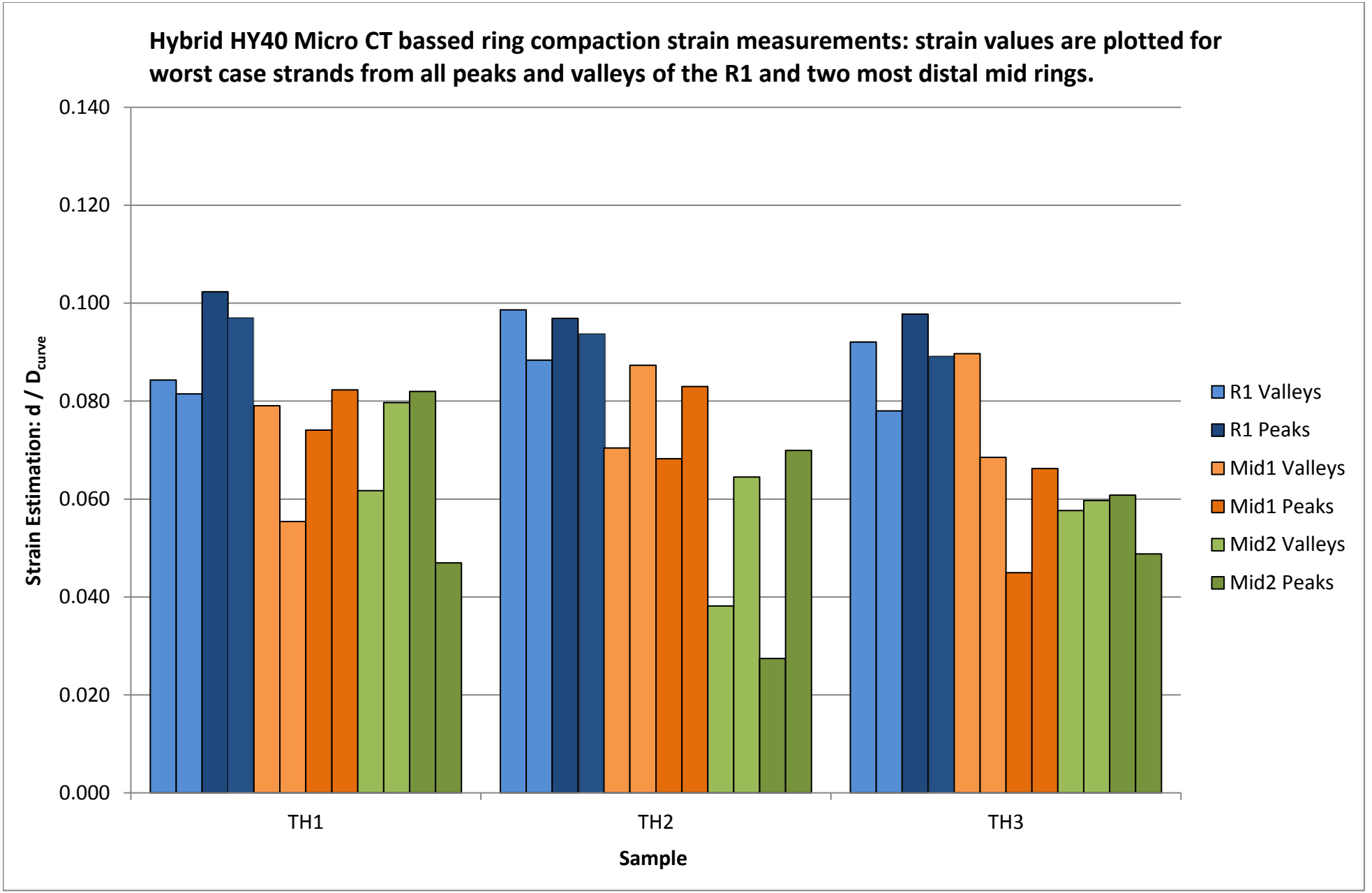
Hybrid HY40 Micro CT bassed ring compaction strain measurements: strain values are plotted for worst case strands from all peaks and valleys of the R1 and two most distal mid rings.
0.140
0.120
0.100
0.080
0.060
0.040
0.020
0.000
Strain Estimation: d / D curve
TH1
TH2
TH3
Sample
R1 Valleys
R1 Peaks
Mid1 Valleys
Mid1 Peaks
Mid2 Valleys
Mid2 Peaks